High sensitivity matter-wave interferometry : towards a determination of the fine structure constant below 10-10

Léo Morel

THÈSE DE DOCTORAT
DE SORBONNE UNIVERSITÉ

Spécialité : Physique

École doctorale n°564: Physique en Île-de-France

réalisée

au Laboratoire Kastler Brossel

sous la direction de Saïda Guellati-Khelifa

présentée par

Léo Morel

pour obtenir le grade de :

DOCTEUR DE SORBONNE UNIVERSITÉ

Sujet de la thèse :

High sensitivity matter-wave interferometry: towards a determination of the fine structure constant at the level of 10^{-10}

soutenue le 23 septembre 2019

devant le jury composé de :

M^{me}	Caroline Champenois	Rapporteuse
M.	Albert Roura	Rapporteur
M.	Arnaud Landragin	Président du jury
M.	Achim Peters	Examinateur
M^{me}	Saïda Guellati-Khelifa	Directrice de thèse
M.	Pierre Cladé	Invité

Remerciements

J'ai effectué mon travail de thèse au Laboratoire Kastler Brossel d'octobre 2016 à septembre 2019, dirigé par Antoine Heidmann *que je remercie pour son accueil au sein de l'unité.*

Je souhaite remercier chaleureusement Saïda Guellati-Khelifa*, ma directrice de thèse, pour m'avoir mené lors de ces premières années de jeune chercheur. Je ne me souviens pas de toutes les questions que je suis venu te poser dans ton bureau, ni de leur nombre, mais je sais que les réponses que tu y a apportées m'ont toujours permis d'avancer dans ma compréhension de notre sujet de recherche. Tu m'as aussi transmis beaucoup de ton savoir expérimental, et surtout une certaine pugnacité et exigence envers la performance du dispositif. Enfin, merci pour les questions que tu m'as posées sur ce que je faisais. Ces questions, toujours pertinentes, ont eu la constance de me pousser vers plus de rigueur et de compréhension.*

Mes remerciements vont également à Pierre Cladé *qui a co-encadré ces travaux, notamment pour avoir accompagné mes premiers pas sur le dispositif expérimental. Cependant, je crois que ce n'est pas sur la maîtrise informatique et électronique du dispositif que je retiendrais le plus de ce que tu m'as appris. C'est plutôt la manière que tu as de penser les phénomènes physiques que nous étudions: un savant mélange entre une formulation efficace et un pragmatisme expérimental.*

Je remercie aussi tous les membres de l'équipe Métrologie des systèmes simples et tests fondamentaux *du laboratoire.* François Biraben *pour l'intérêt que tu as*

porté à nos travaux lors des repas du midi où l'on se croisait, François Nez *pour les discussions que nous avons eu ainsi que leur large spectre. J'ai souvenir d'une explication pas à pas du laser titane:saphir sur laquelle je me suis greffé et dont les détails m'ont permis d'entrapercevoir ses principes de fonctionnement et de remarquer la beauté d'un tel agencement. Je remercie aussi* Lucile Julien *pour le recul que tu m'as apporté que ce soit sur des aspects recherche, mais aussi quelques autres.*

Un grand merci aussi aux doctorant·e ·s qui m'ont précédé au sein de l'équipe. Merci à Hélène Fleurbaey *qui finissait sa thèse sur l'expérience Hydrogène quand je débutais la mienne d'avoir été là pour mes débuts de thèse et de m'avoir écouté décrire mes échecs et réussites. Merci aussi à* Clément Courvoisier *qui m'a précédé sur le dispositif expérimental. Nous avons eu peu de recouvrement, mais je te remercie pour ton accueil chaleureux et ta franchise. Enfin, tu as su par la clarté de ton manuscrit me passer de nombreux détails de l'expérience. Enfin, je remercie* Manuel Andia *et* Raphaël Jannin *que j'ai rencontré pendant ma thèse pour leur sympathie et l'intérêt qu'ils ont porté à mes travaux.*

Je pense aussi aux deux doctorants qui assurent la suite. Thomas Simon *sur l'expérience Hydrogène, je te remercie pour le plaisir que j'ai eu à échanger avec toi et je te souhaite de très beaux succès sur la fin de ta thèse. Et* Zhibin Yao*, qui prend la suite sur l'expérience d'interférométrie. Merci pour ta patience et curiosité sur tous les aspects du dispositif.*

J'aimerais aussi remercier toutes les personnes qui ont travaillé dans le laboratoire avec moi, à commencer par Satya Bade *qui a commencé son post-doc à peu près que j'ai commencé ma thèse et qui a su attirer mon attention sur un certains nombre de points que je pensais avoir compris et de m'avoir montré d'abord que les choses étaient plus complexes et ensuite d'avoir réfléchi ensemble pour affiner notre compréhension à tous les deux. Je remercie aussi* Jun Sun *qui a pris la suite de* Satya*. Enfin je remercie les stagiaires qui ont contribué à l'expérience,*

Paul, Alice, Renaud *et en particulier* Lionel Djadaojee *qui, en plus de sa bonne humeur et son entrain a monté avec brio de la table de détection.*

Je remercie de plus Holger Müller *et son équipe de m'avoir accueilli pendant deux semaines dans leur laboratoire à Berkeley.*

Je remercie également les membres du jury ma thèse. Caroline Champenois *et* Albert Roura *qui l'ont rapporté avec beaucoup d'exigence et qui m'ont permis à la fois de l'améliorer et aussi de prendre du recul. J'aimerais aussi remercier* Achim Peters *d'avoir examiné mon travail, et* Arnaud Landragin *d'avoir accepté la charge de présidence du jury. Mes remerciements sincères pour l'intérêt que vous avez porté à mes travaux.*

Je tiens aussi à remercier tous les membres des services administratifs du laboratoire. Läetitia Morel, Romain Rybka *et* Thierry Tardieu *au secrétariat pour la rapidité avec laquelle mes demandes ont été traitées et leur patience lors de leurs explications. J'aimerais en particulier remercier* Valérie Revelut *pour sa bonne humeur communicative.*

La recherche en physique expérimentale ne pourrait se faire sans les services techniques du laboratoire. Carou Doré, Gaël Coupin *et* Sébastien Colinot *à l'atelier mécanique ont toujours su réaliser les pièces que je leur demandais avec beaucoup de rapidité et de précision. Je les en remercie, ainsi que pour le partage de leur savoir et les discussions que nous avons eu. Les membres de l'atelier d'électronique,* Loïc Garcia *et en particulier* Brigitte Delamour*, m'ont été d'une aide extraordinaire. J'ai appris dans votre atelier bien plus que la réalisation de circuits, mais aussi la capacité à développer des solutions expérimentales simples à des problèmes compliqués.*

J'aimerais remercier toutes et tous les doctorant·e ·s qui ont réalisé ou réalisent leur thèse en même temps que moi au laboratoire. Je garderai un excellent souvenir des moments passés à discuter de physique et d'autres choses.

Enfin, je remercie chaleureusement mes amis et ma famille qui ont été là à mes côtés pendant ces trois années. Vous m'avez écouté parler de choses parfois incompréhensibles, parfois juste trop techniques avec patience et gentillesse. Ainsi, un immense merci à Mathilde, Victor, Nathan*, à mes parents* Pascale *et* Pierrick *et à mon frère* Marc*.*

Nina*, je ne peux exprimer avec des mots tout ce que ce travail te doit. Merci de m'avoir porté pendant ces trois ans, dans les moments de joie et tous les autres.*

Contents

Chapter 1

General Introduction

The measurement of the ratio h/m_X of any particle has long drawn attention as the Rydberg constant R_∞ defined as:

$$R_\infty = \frac{m_e c \alpha^2}{2h}, \tag{1.0.1}$$

where m_e is the mass of the electron, c the speed of light, h the Planck constant, can be rewritten as:

$$\alpha^2 = \frac{2R_\infty}{c}\frac{m_X}{m_e}\frac{h}{m_X} \tag{1.0.2}$$

allowing for a determination of α, the fine structure constant, first introduced by A. Sommerfeld in 1916, which writes:

$$\alpha = \frac{e^2}{4\pi\epsilon_0 \hbar c}. \tag{1.0.3}$$

In equation (1.0.2), the relative uncertainty on R_∞ is $5.9 \cdot 10^{-12}$ with the 2014 CODATA adjustment[Mohr, 2016]. The mass of the electron is known with a recently improved measurement method[Sturm, 2014] to $2.9 \cdot 10^{-11}$ in atomic units. The mass of X is determined through precision measurement of cyclotrons frequencies in a Penning trap. For example, the relative atomic mass of ^{87}Rb is known to $6.9 \cdot 10^{-11}$[Wang, 2017].

On the other hand, the relative precision on the ratios h/m_X for ^{87}Rb and ^{133}Cs evaluate respectively to $1.3 \cdot 10^{-9}$[Bouchendira, 2011] and $4.0 \cdot 10^{-10}$[Parker, 2018], making this term the limiting factor in the α determination based on equation (1.0.2).

The first measurements of h/m_X for an α determination were performed with neutrons, and based on the measurement of their de Broglie wavelength through

their scattering on silicon crystals[Kruger, 1999]. In the 1990s, the development of atom interferometry techniques has led to a renewed interest in the h/m_X determinations with atomic masses[Wicht, 2002].

Nowadays, the h/m_X determinations are useful in two contexts. Firstly, the α determination deduced from h/m_X allows a computation of the anomalous moment of the electron a_e using Quantum ElectroDynamics (QED) calculations, with contributions from the Standard Model (SM). The comparison with an experimental value of a_e[Hanneke, 2008] then provides a stringent test of the SM[Parker, 2018]. The second interest is linked to the redefinition of the kilogram in the frame of the new Système International d'Unités (SI). We start by presenting the latter before returning to the test of the SM.

1.1 Redefinition of the kilogram - New SI

The redefinition of the SI, implemented in May 2019, fixed the values of fundamental constants to define units. In particular, the Planck constant h as been fixed and a mass is measured through the ratio h/m_X. The relative atomic mass is defined by

$$A_r(m_X) = \frac{m_X}{m_u}, \tag{1.1.1}$$

where m_u is the unified atomic mass. This quantity is known with relative uncertainty lower than 10^{-10} for most atomic species such as ^{87}Rb. The measurement of h/m_X then allows to link the m_u to the SI through the relation:

$$\frac{h}{m_u} = A_r(m_X)\frac{h}{m_X} \tag{1.1.2}$$

Moreover, the elementary charge e has also been fixed for the definition of the ampere. As the speed of light c is also fixed for the definition of the meter, a determination of α allows to determine as well the vacuum permittivity ϵ_0 (or the vacuum permeability μ_0) from equation (1.0.3).

1.2 Test of the Standard Model

QED expresses the anomalous moment of the electron as a power series of the fine structure constant α:

$$a_e = \frac{g_e - 2}{2} = \sum_n C^{(2n)} \left(\frac{\alpha}{2\pi}\right)^n, \tag{1.2.1}$$

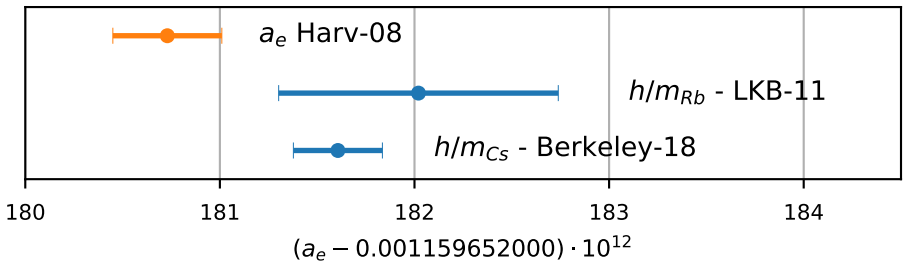

Figure 1.1: Comparison between values of a_e obtained by a direct measurement[Hanneke, 2008](in orange) and the combination of an h/m_X determination and QED+SM calculations(LKB[Bouchendira, 2011], Berkeley[Parker, 2018])(in blue)

where g_e is the electron Landé factor. The power series coefficients are given through QED calculations and the leptons mass ratio[Aoyama, 2019] as following:

$$C^{(2n)} = A_1^{(2n)} + A_2^{(2n)}\left(\frac{m_e}{m_\mu}\right) + A_2^{(2n)}\left(\frac{m_e}{m_\tau}\right) + A_3^{(2n)}\left(\frac{m_e}{m_\mu}, \frac{m_e}{m_\mu}\right) \tag{1.2.2}$$

Up to now five terms have been computed. The latest term A_1^{10} requires the computation of more than $12,000$ Feynman diagrams and can only be determined numerically.

In addition to this power series expansion, the theoretical prediction of a_e accounts for a hadronic and a weak contribution:

$$a_e(\text{th}) = a_e\,(\text{QED}) + a_e\,(\text{Hadron}) + a_e\,(\text{Weak}) \tag{1.2.3}$$

Moreover, a_e has been measured with extreme precision at Harvard in 2008[Hanneke, 2008] in the group of G. Gabrielse. We plot in figure (1.1) the comparison between this experimental value and the values obtained from the theoretical calculations presented above[Aoyama, 2019] and the experimental determinations of h/m_X from our team with ^{87}Rb [Bouchendira, 2011] and the group of H. Müller at Berkeley with ^{133}Cs [Parker, 2018].

The precision of theoretical calculations is better than the experimental determinations involved in the α/a_e comparison, such that in 2011, the experimental value a_e was used to extract the most precise value of α by inverting equation (1.2.3) and yielded a relative precision of $2.3 \cdot 10^{-10}$ on α. The measurement of

our team, with relative uncertainty of $6.6 \cdot 10^{-10}$ was important as it performed a test of QED calculations, thus validating the α value[1].

This situation has changed in 2018 with the measurement of h/m_{Cs} by the group of H. Müller at Berkeley obtained by atom interferometry. The achieved relative precision is $2.0 \cdot 10^{-10}$ on α. Moreover, the comparison with the Harvard measurement exhibits a discrepancy of 2.5σ, which raises the question of contributions beyond the SM in expansion series (1.2.3).

Search for new physics beyond the SM is nowadays a pressing matter. Although SM has great success, among them the prediction of the magnetic moment of the electron g_e at the part per trillion level (figure (1.1)), the SM cannot explain the matter/antimatter asymmetry that our world exhibit. Moreover, cosmological observations suggest the existence of not yet directly observed matter and energy known respectively as *Dark Matter* (DM) and *Dark Energy*.

Recently, atomic and molecular physics have drawn the attention as a platform to test the SM in a multitude of ways. A recent review[Safronova, 2018] quotes a large number of experiments in this field. We can quote experiments aiming at measuring the electron electric dipole moment with molecular beams[ACME Collaboration, 2018] or searching for variations of fundamental constants with space and/or time with the comparison of atomic clocks[Huntemann, 2014].

In the context of the search of DM, the α/a_e comparison is of particular interest as a discrepancy would indicate the coupling between the electron with a not yet observed particle. However, the current 2.5σ discrepancy is not yet sufficient to conclude on that matter. The group of G. Gabrielse now at Northwestern University has recently announced their plans towards a new measurement of a_e[Gabrielse, 2019].

Moreover, we have worked in our team towards a new determination on α with a competitive uncertainty with respect to the Berkeley determination. During my thesis, I worked on this measurement with ^{87}Rb on the new experimental setup of our team, which I contributed to develop.

1.3 New experimental setup for the determination of h/m_{Rb}

The principle of our determination of h/m_{Rb} is based on the measurement of the recoil velocity v_r of an atom, *i.e.* the velocity an atom acquires when it absorbs

[1] We should note that in 2011, the errorbars of the Harvard measurement and the h/m_{Rb} determination overlapped. The situation changed with CODATA fundamental constants reevaluation in 2014 and corrections in the computation of a_e.

a photon. As a photon carries a momentum $\hbar k$, where k is its wavevector, and through momentum conservation, we obtain:

$$v_r = \frac{\hbar}{m} k \tag{1.3.1}$$

For a plane wave in vacuum, we have $k = 2\pi\nu/c$, where ν is the frequency of the laser that drives the momentum transfer process. Thanks to the technology of frequency combs[Diddams, 2000], ν can be known with a better precision than the recoil velocity. Then, the combined measurement of v_r and of ν allows for the determination of h/m.[2]

The recoil velocity is measured through the measurement of the acquired velocity by the atom upon the photon absorption in a differential velocity sensor based on the compensation of Doppler effect.

With the absorption of a single photon, the atom ends in an excited state and decays incoherently through spontaneous emission. In order to avoid this effect, we use two-photon transitions in a Λ scheme: the atom absorbs a photon from a laser field and decays through stimulated emission in a second laser field. The process is now coherent and the atomic motion controlled. We place ourselves in counterpropagating configuration for the two laser fields, such that the two-photon transitions are sensitive to Doppler effect.

First, Raman transitions (see section 2.1) couple the two hyperfine states of the ^{87}Rb atom and are used to build the differential velocity sensor. With these transitions, the recoil velocity $v_r \sim 5.9$ mm $\cdot$ s^{-1} translates into a Doppler shift of ~ 15 kHz.

With 30 ms interferometric interrogations, where the effective duration on the velocity measurement is $T_{\text{Ramsey}} = 10$ ms, the Ramsey duration, we typically obtain precision on the recoil velocity of $\frac{1}{1000}\frac{1}{T_{\text{Ramsey}}} \sim 0.1$ Hz, which corresponds to a relative precision of $\sim 7 \cdot 10^{-6}$ on the recoil velocity. This corresponds to a velocity sensitivity of ~ 40 nm$\cdot$s^{-1}. The duration of interrogation imposes the use of laser cooled atoms.

Secondly, Bloch Oscillations (BO) (see section 2.3) transfer an even number of recoils to the atoms while leaving their internal state unchanged. We typically transfer a 1000 recoils, which corresponds to an enhancement in the measurement performance up to $\sim 7 \cdot 10^{-9}$. Moreover, the atoms acquire a velocity of 6 m $\cdot$ s^{-1} with the BO process. With the 30 ms interrogation duration above, the magnetic field should be controlled on a few tens of centimeters.

[2]We now drop the subscript Rb, which is the atom used in our experiments.

This is one of the major improvement of the new experimental setup, described in section 3.3.3. The excellent magnetic field control that extends over 45 cm allows for the reduction of this contribution to systematic errors, which was one of the largest in the latest measurement of our team[Bouchendira, 2011].

This also allowed us to increase the interrogation duration with $T_{\mathrm{Ramsey}} = 20$ ms, thus doubling the sensitivity of our determination. Combined with a better control of vibration noise induced by a simpler vibration isolation setup, we exhibited unprecedented statistical uncertainty on h/m (see chapter 5).

The other major error source of the latest measurement is related to the gaussian beam correction to the wavevector k. Indeed, the photon wavevector is perfectly known only in the case of a plane wave in vacuum. In order to reduce the effect, an as such the error, we increase the waist of the laser beams as they tend to a plane wave.

However, the intensity of the beam scales as P/w^2 with P the laser power. In order to maintain the intensity constant and as such increase the laser power, our team has worked with a new laser technology based on high power lasers at 1.5 μm that are doubled in PPLN crystals[Andia, 2015b]. This technology, now fully deployed on the new setup, allows for larger beams but also increased the stability of the setup.

Finally, as the α/a_e comparison promises to yield useful information in the search for new physics, the new experimental setup is also intended to run next generation interferometers with even increased sensitivity[Cladé, 2009]. Such interferometers are very sensitive to intensity inhomogeneities induced by the atomic motion in the laser beams.

In order to implement them, the setup is equipped with a Bose Einstein Condensate (BEC) production setup in an optical dipole trap. Indeed, BEC sources present a smaller velocity spread and as such reduced sensitivity to intensity inhomogeneities. The setup has been described in [Jannin, 2015a] and [Courvoisier, 2016], and the effect of interactions in a BEC on an interferometer modeled in [Jannin, 2015b]. In this work we have improved the BEC production process and observed experimentally the effect of atom-atom interactions (see section 4.1).

1.4 Outlook of this manuscript

Aiming at providing precise determinations of the fine structure constant α, our work aims to a new determination with competitive uncertainty in order to provide an alternative value to the comparison α/a_e in order to confirm the recent discrepancy. While working on the installation of the interferometry laser system of our new experimental setup, we have worked on the long term BEC use.

In order to present this work, the remaining of the manuscript is divided in two parts and five chapters. The first part contains two chapters and is focused on the presentation of the experiment:

- In **chapter 2**, we will explain the fundamental concepts underlying our experiment: stimulated Raman transitions, atom interferometry and Bloch Oscillations.

- **Chapter 3** presents the implementation of these concepts on the experiment.

The second part presents the results that we have obtained during this thesis work:

- In **chapter 4**, we discuss the difficulties that arise when using either BEC as an atom source or atoms at the output of an optical molasse. This discussion allows us to defend our choice of atomic source for the h/m measurement.

- **Chapter 5** presents the exact protocol for the measurement of the h/m ratio and the data analysis associated. We also discuss the statistical performance of the setup, which has not been reached in another experiment to the best of our knowledge.

- In **chapter 6**, we detail our study of systematic error sources. This study, although yet incomplete, shows that the current measurement campaigns can allow to reach a competitive uncertainty.

Part I

The experiment

Chapter 2

Fundamentals

Introduction

A few tools are needed in order to measure the recoil velocity of an atom. The aim of this chapter is to present in detail these tools, and their associated concepts. In a few words, we simply need to transfer photon momenta to atoms and measure the velocity they have acquired.

We start by studying *stimulated Raman transitions* which are two-photon transitions in a Λ scheme: a particle is subjected to two laser beams, absorbs a photon from one, and emits through stimulated emission another photon in the second laser beam, thus reaching its final state.

Immediately following, *counterpropagating Raman transitions*, a particular case, will be detailed. This will allow us to introduce the concepts of *atom interferometry*. In the frame of this thesis, this part is essential as it will introduce a core part of our work.

Finally, we will present the phenomenon of Bloch Oscillations which is responsible for the transfer of a large number of recoils to the atoms.

2.1 Stimulated Raman transitions

2.1.1 General considerations

Two-photon transitions have proven to be extremely useful in spectroscopy. They may be used to either suppress or enhance Doppler effect. Using Raman transitions, we are able to control the atomic wavefunction between two electronic ground states, which allows us to reach coherent manipulation of the atoms quantum states.

In order to present the features of these transitions, we assume that we can describe atoms through a three level system with two ground states $|\alpha\rangle$, $|\beta\rangle$ and an excited state $|e\rangle$. Its internal Hamiltonian can be written:

$$H_{internal} = \hbar\omega_{HFS} |\beta\rangle \langle\beta| + \hbar\omega_e |e\rangle \langle e| , \tag{2.1.1}$$

with the energy of $|\alpha\rangle$ taken as reference and $\omega_e > \omega_{HFS}$ as the couplings between the ground states and the excited state are induced by optical transitions. The notation ω_{HFS} is related to the hyperfine structure of the atom (see next paragraph).

An energy level diagram of a Raman transition is displayed on figure (2.1, left). Two laser fields $\left\{\left(\omega_1, \vec{k}_1\right), \left(\omega_2, \vec{k}_2\right)\right\}$ couple the excited state $|e\rangle$ to the ground states. A realistic atomic model would assume that the excited state spontaneously decays. In order to prevent such a process, the one-photon laser coupling is detuned from resonance by an amount Δ ($\Delta \sim 60$ GHz in our experiment), such that the excited state is not populated.

The geometric configuration of the beams is given by the two beam wavevectors $\vec{k}_1$ and $\vec{k}_2$. At this point, we make no assumptions on the relative orientations of the beams. As we shall see in section 2.1.3, two particular configurations are of interest: the two beams are aligned and travel whether in the same direction (*co-propagating*) or in opposite directions (*counterpropagating*).

2.1.1.1 Justification of the three level atom

We work with ^{87}Rb atom, which is an alkali atom. In the electronic ground state ($5^2S_{1/2}$), the total angular momentum of the electrons is $J = 1/2$. The coupling with the nuclear magnetic moment $I = 3/2$ induces a hyperfine structure in the atomic levels. Then the total angular momentum of the atom in the ground state is $F = 1$ or $F = 2$, and we have:

$$E_{F=2} - E_{F=1} = \hbar\omega_{HFS}. \tag{2.1.2}$$

Each of these atom angular momentum values contains $2F + 1$ Zeeman sublevels, for which the degeneracy can be lifted by the application of a constant magnetic field. Typically, a 30 mG magnetic field separates the levels by 42 kHz[Steck, 2001].

As we will see in the following, the frequency linewidth of Raman transitions that we use is typically $\lesssim 5$ kHz such that the Zeeman sublevels are resolved. As a consequence, we can choose for each hyperfine level a Zeeman sublevel to address. For interferometry, we choose $|\alpha\rangle = |F = 1, m_F = 0\rangle$ and $|\beta\rangle = |F = 2, m_F = 0\rangle$ as they are insensitive to magnetic field at the first order.

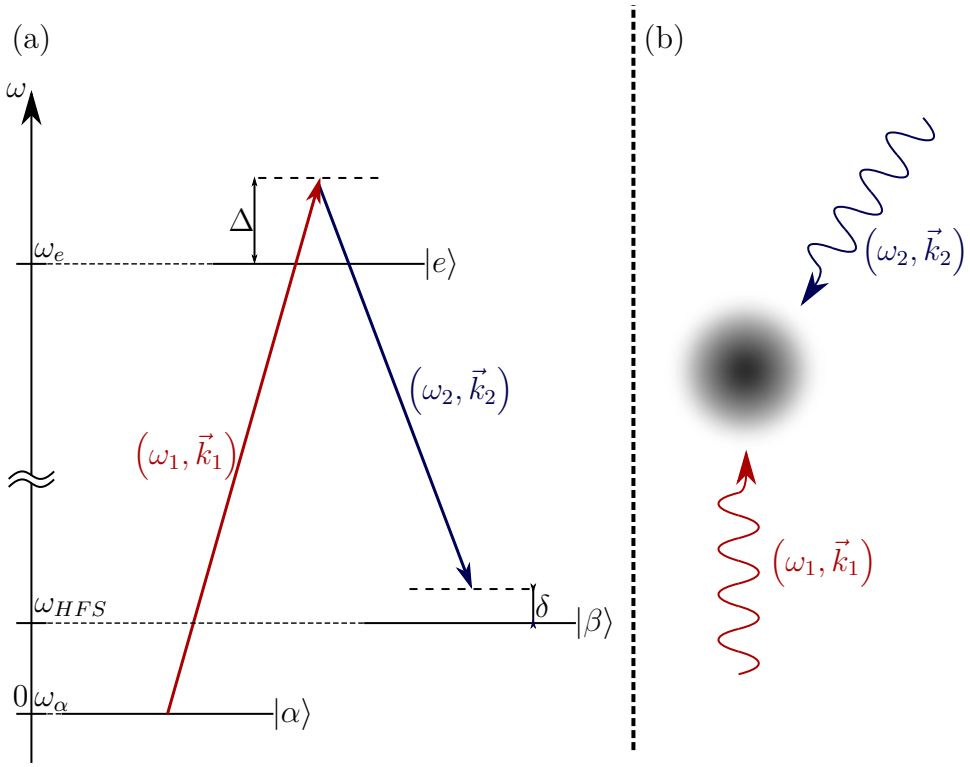

Figure 2.1: (a): Three level system for the description of Raman transitions. The excited state is coupled to the two ground states through two beams that are detuned by Δ from the one photon transition. The mismatch between the two-photon frequency $\omega_1 - \omega_2$ and the atomic internal energy ω_{HFS} is written δ. The scaling with respect to our experimental conditions is not respected since $\Delta \sim 60$ GHz, $\omega_{HFS} \sim 6.8$ GHz and $\delta \sim 0 - 20$ MHz.
(b): Example of a geometric configuration where an atom is subjected to two beams.

The excited state that we adress is $5^2P_{3/2}$ (D_2 line) for which the total angular momentum of the electron is $J' = 3/2$. Its hyperfine structure displays four energy levels ($F' = 0, 1, 2, 3$). The reduction of this complex structure to a single level is an approximation that will be shortly treated after the reduction of the three level system to a two level system, and the computation of their transition probabilities. This treatment reveals the selection rules of the Raman process.

2.1.1.2 Resonance condition

Before turning to the explicit writing of the coupling Hamiltonian of the system, we write the resonance condition of the Raman process. To this aim, we consider the system $\Big\{\text{atom} + \text{field}\Big\}$ as quantized.

We assume that initially, the atom is in state $|\alpha, \vec{p_i}\rangle$, where $\vec{p_i}$ is the momentum of the atom, placing ourselves in a plane wave modeling. Moreover, there are n_1 and n_2 photons in each field. The initial state is then defined by the ket: $|\psi_i\rangle = |\alpha, \vec{p_i}, n_1, n_2\rangle$.

The Raman process is defined as follows: the atom absorbs a photon from field (1) and emits one in field (2) while its quantum state changes to $|\beta, \vec{p_f}\rangle$, where $\vec{p_f}$ is the final momentum of the atom. The final state of the system is then: $|\psi_f\rangle = |\beta, \vec{p_f}, n_1 - 1, n_2 + 1\rangle$.

The resonance condition is given by verifying both momentum and energy conservation. The former simply writes:

$$\vec{p_f} = \vec{p_i} + \hbar\vec{k_1} - \hbar\vec{k_2}. \tag{2.1.3}$$

For the latter, we start by writing the free Hamiltonian of the system:

$$H_0 = H_{internal} + \frac{\hat{\vec{p}}^2}{2m} + \hbar\omega_1\hat{N}_1 + \hbar\omega_2\hat{N}_2, \tag{2.1.4}$$

where $\hat{N}_\iota$ is the number operator for each field. Writing $\langle\psi_i| H_0 |\psi_i\rangle = \langle\psi_f| H_0 |\psi_f\rangle$, we obtain energy conservation:

$$\frac{\vec{p_i}^2}{2m} + \hbar\Big(n_1\omega_1 + n_2\omega_2\Big) = \frac{\vec{p_f}^2}{2m} + \hbar\omega_{HFS} + \hbar\Big((n_1 - 1)\omega_1 + (n_2 + 1)\omega_2\Big). \tag{2.1.5}$$

By injecting equation (2.1.3), we obtain the *resonance condition*:

$$\delta = \omega_1 - \omega_2 - \omega_{HFS} = \frac{\vec{p_i} \cdot \vec{k}_e}{m} + \frac{\hbar\vec{k}_e^2}{2m}, \tag{2.1.6}$$

where $\vec{k}_e = \vec{k}_1 - \vec{k}_2$ is the Raman transition effective wavevector and δ the *two-photon detuning* has also been defined on figure (2.1).

The interpretation of this equation is straightforward: by controlling the frequencies of the lasers and thus the detuning δ, one can address the Raman transition to atoms with a given velocity. In other words, one can associate the atomic internal state to information on the atomic velocities.

In particular, if we assume that all atoms have the same velocity, by scanning the detuning and observing the transition, one can measure this given velocity. The effective wavevector $\vec{k}_e$ controls the properties of this measurement as its direction controls the measured component of the velocity. In order to characterize precisely this measurement method, and discuss in detail its sensitivity, we first need to describe the coupling operator associated to Raman transitions.

Remark In equation (2.1.6), it is worth pointing out that the detuning δ and the effective wavevector $\vec{k}_e$ are not independent parameters. Indeed, for each laser, we have in vacuum $k_\iota = \omega_\iota/c$, with c the speed of light $\sim 3 \cdot 10^8$ m $\cdot$ s^{-1}.

Taking into account the variations of the wavevectors, we find corrections of the order of $p_i/(mc) = v_i/c$. The typical atomic velocities in our experiment do not exceed 10 m $\cdot$ s^{-1}, such that this correction can be considered negligible when treating Raman transitions. In the following of the development, we assume that the wavevectors are constant and consider their variations as a refinement (see section 5.1.5).

2.1.2 Quantum mechanical description of the coupling

We model the ideal case described in figure (2.1). The field (1) couples the atomic state $|\alpha\rangle$ with the excited state $|e\rangle$, and the field (2) couples $|\beta\rangle$ with $|e\rangle$. A more realistic model would take into account the action of field (1) on $|\beta\rangle$ and vice versa. Such treatment has been presented in previous works[Cladé, 2005; Bouchendira, 2012; Andia, 2015a]. We choose not to do so here to simplify the equations. However, they will be taken into account in the model that considers the hyperfine structure of the excited state (section 2.1.2.2, equation (2.1.40)), that replicates the results reported in [Battesti, 2003].

We place ourselves in the *dressed atom* picture, and we consider the initial state $|\psi_i\rangle$ with initial momentum $\vec{p_i} = \vec{p}$. Then the following set of states forms a almost resonant subset under the action of the Raman Hamiltonian due to momentum conservation:

$$|\alpha\rangle = |\alpha, \vec{p}, n_1, n_2\rangle \tag{2.1.7}$$

$$|\beta\rangle = \left|\beta, \vec{p} + \hbar\vec{k}_e, n_1 - 1, n_2 + 1\right\rangle \tag{2.1.8}$$

$$|e\rangle = \left|e, \vec{p} + \hbar\vec{k}_1, n_1 - 1, n_2\right\rangle, \tag{2.1.9}$$

where the left hand side of each equation are simplified notations for the remaining of this section.

In this frame, the free Hamiltonian of the subset $\{|\alpha\rangle, |\beta\rangle, |e\rangle\}$ reads:

$$H_0 = \hbar \begin{pmatrix} \delta + \frac{\vec{p}^2}{2m} & 0 & 0 \\ 0 & \frac{\left(\vec{p}+\hbar\vec{k}_e\right)^2}{2m} & 0 \\ 0 & 0 & \Delta + \frac{\left(\vec{p}+\hbar\vec{k}_1\right)^2}{2m} \end{pmatrix} \tag{2.1.10}$$

In experimental situations, the first two diagonal terms differ by less than a few MHz. On the contrary, $\Delta \sim 60$ GHz in order to avoid spontaneous emission. This hierarchy on the energy levels indicates that the excited state can be eliminated from the problem, and as such that we can reduce the system to a two level system. We detail this treatment in the following lines:

The coupling induced by the laser fields is described with the dipole interaction:

$$\hat{V} = -\hat{\vec{d}} \cdot \hat{\vec{E}} \tag{2.1.11}$$

where $\hat{\vec{d}}$ is the dipole operator associated to the atom and $\hat{\vec{E}}$ the electric field operator associated to the field which can be written[Grynberg, 2010]:

$$\hat{\vec{E}} = \sum_{i=1,2} \vec{\mathcal{E}}_i \left(e^{ik_i\hat{x}} a_i - e^{-ik_i\hat{x}} a_i^\dagger \right), \tag{2.1.12}$$

where a_i are the annihilition operator of laser mode i.

We write the *Rabi frequencies* describing the coupling:

$$\frac{\mathbf{\Omega}_1}{2} = \frac{1}{\hbar} \langle e| \hat{V} |\alpha\rangle \tag{2.1.13}$$

$$\frac{\mathbf{\Omega}_2}{2} = \frac{1}{\hbar} \langle e| \hat{V} |\beta\rangle \tag{2.1.14}$$

which are complex numbers[1]. The amplitude of the Rabi frequencies is of the order of 10 MHz, which is also small compared to the one photon detuning Δ.

This leads to the following coupling Hamiltonian $\hat{V}$:

$$\hat{V} = \hbar \begin{pmatrix} 0 & 0 & \mathbf{\Omega}_1/2 \\ 0 & 0 & \mathbf{\Omega}_2/2 \\ \mathbf{\Omega}_1^*/2 & \mathbf{\Omega}_2^*/2 & 0 \end{pmatrix} \tag{2.1.15}$$

[1]This is indicated by the bold font

The total Hamiltonian is then given by:

$$H = H_0 + \hat{V} \tag{2.1.16}$$

$$= \hbar \begin{pmatrix} \delta + \frac{\vec{p}^2}{2m} & 0 & \mathbf{\Omega}_1/2 \\ 0 & \frac{\left(\vec{p}+\hbar\vec{k}_e\right)^2}{2m} & \mathbf{\Omega}_2/2 \\ \mathbf{\Omega}_1^*/2 & \mathbf{\Omega}_2^*/2 & \Delta + \frac{\left(\vec{p}+\hbar\vec{k}_1\right)^2}{2m} \end{pmatrix} \tag{2.1.17}$$

The procedure to reduce of the three level Hamiltonian to an effective Hamiltonian H_e on the two ground states subset $\{|\alpha\rangle, |\beta\rangle\}$ is given by [CohenTannoudji, 2001] (equation (26) of complement $\mathbf{B_I}$). In our case, with Δ dominating over the other terms of the Hamiltonian, we obtain:

$$\langle\kappa| H_e |\iota\rangle = \langle\kappa| H_0 |\iota\rangle - \frac{1}{\Delta} \langle\kappa| \hat{V} |e\rangle \langle e| \hat{V} |\iota\rangle \tag{2.1.18}$$

for κ, ι being either α or β.

Using this formula, and with a redefinition of the energy origin, we obtain the effective Hamiltonian:

$$H_e = \hbar \begin{pmatrix} \delta + \Omega_\alpha^{\mathrm{LS}} & \mathbf{\Omega}/2 \\ \mathbf{\Omega}^*/2 & \Omega_\beta^{\mathrm{LS}} + \delta_{\mathrm{Doppler}} \end{pmatrix}, \tag{2.1.19}$$

where we have introduced different terms:

$$\Omega_\alpha^{\mathrm{LS}} = -\frac{|\mathbf{\Omega}_1|^2}{4\Delta} \tag{2.1.20}$$

$$\Omega_\beta^{\mathrm{LS}} = -\frac{|\mathbf{\Omega}_2|^2}{4\Delta} \tag{2.1.21}$$

are the *light shifts* which correspond to the energy shift induced by an off resonant coupling and

$$\mathbf{\Omega} = -\frac{\mathbf{\Omega}_1 \mathbf{\Omega}_2^*}{2\Delta} \tag{2.1.22}$$

is the *two-photon complex Rabi frequency.* Finally,

$$\delta_{\mathrm{Doppler}} = \frac{1}{\hbar} \left(\frac{\left(\vec{p} + \hbar\vec{k}_e\right)^2}{2m} - \frac{\vec{p}^2}{2m} \right) \tag{2.1.23}$$

$$= \frac{\vec{k}_e \cdot \vec{p}}{m} + \frac{\hbar\vec{k}_e^2}{2m} = \vec{k}_e \cdot \vec{v} + \frac{\hbar\vec{k}_e^2}{2m} \tag{2.1.24}$$

exhibits the Doppler sensitivity of the transition.

We have now reduced the Raman Hamiltonian to a two level system. This simplification allows us to detail the transition probabilities associated to the Raman coupling.

2.1.2.1 Transition probabilities

In order to simplify the discussion, we redefine the detuning δ with an *extended detuning* $\delta_t(\vec{v})$ that accounts for the Doppler effect and light shifts:

$$\delta_t(\vec{v}) = \delta + \Omega_\alpha^{\mathrm{LS}} - \Omega_\beta^{\mathrm{LS}} - \delta_{\mathrm{Doppler}}(\vec{v}), \tag{2.1.25}$$

and the two-photon complex Rabi frequency that we split in modulus and phase:

$$\mathbf{\Omega} = \Omega e^{-i\phi}, \tag{2.1.26}$$

where Ω is the *Rabi frequency* and ϕ the *phase of the transition*. The phase sign convention is guided by the definition of the Pauli matrices:

$$\sigma_x = \begin{pmatrix} 0 & 1 \\ 1 & 0 \end{pmatrix}, \sigma_y = \begin{pmatrix} 0 & -i \\ i & 0 \end{pmatrix} \text{ and } \sigma_z = \begin{pmatrix} 1 & 0 \\ 0 & -1 \end{pmatrix}, \tag{2.1.27}$$

and it evaluates to:

$$\phi = \phi_2 - \phi_1, \tag{2.1.28}$$

where ϕ_i describes the intrinsic phase of the two lasers.

Finally, we set an appropriate energy origin such that the total Hamiltonian is written under the simple form:

$$\frac{H}{\hbar} = \begin{pmatrix} \delta_t(\vec{v})/2 & \Omega e^{-i\phi}/2 \\ \Omega e^{i\phi}/2 & -\delta_t(\vec{v})/2 \end{pmatrix} \tag{2.1.29}$$

$$= \frac{\delta_t(\vec{v})}{2}\sigma_z + \frac{\Omega}{2}\Big(\cos(\phi)\sigma_x + \sin(\phi)\sigma_y\Big). \tag{2.1.30}$$

The evolution operator of the total Hamiltonian can be simply expressed using the formula

$$\exp(ia\vec{n}\cdot\vec{\sigma}) = \cos(a)\mathbf{1} + i\sin(a)\vec{n}\cdot\vec{\sigma}, \tag{2.1.31}$$

where a is real and $\vec{n}$ is a normal vector. We get from equation (2.1.30):

$$U(\tau) = \cos\left(\frac{\Omega_e\tau}{2}\right)\mathbf{1} - i\frac{\sin\left(\frac{\Omega_e\tau}{2}\right)}{\Omega_e}\begin{pmatrix} \delta_t(\vec{v}) & \Omega e^{-i\phi} \\ \Omega e^{i\phi} & -\delta_t(\vec{v}) \end{pmatrix}, \tag{2.1.32}$$

$$\text{with} \quad \Omega_e = \sqrt{\Omega^2 + \delta_t(\vec{v})^2}, \text{ the effective Rabi pulsation} \tag{2.1.33}$$

With an initial state $|\psi_i\rangle = |\alpha\rangle$, we can compute the transition probability:

$$P_{|\alpha\rangle\to|\beta\rangle} = \left| \langle\beta| U(\tau) |\alpha\rangle \right|^2 \tag{2.1.34}$$

$$= \frac{\Omega^2}{\Omega^2 + \delta_t (\vec{v})^2} \sin^2 \left(\sqrt{\Omega^2 + \delta_t (\vec{v})^2} \frac{\tau}{2} \right) \tag{2.1.35}$$

Scaling the above formula with the Rabi frequency by defining the reduced detuning $\delta'_t (\vec{v}) = \delta_t (\vec{v}) / \Omega$ and the pulse area $\theta = \Omega\tau$, we can rewrite it:

$$P_{|\alpha\rangle\to|\beta\rangle} = \frac{1}{1 + \delta'_t (\vec{v})^2} \sin^2 \left(\frac{\theta}{2} \sqrt{1 + \delta'_t (\vec{v})^2} \right) \tag{2.1.36}$$

The above formula is plotted on figure (2.2) for two particular pulse areas that we will encounter in the following section discussing atom interferometry. This formula (2.1.36) and the figure exhibit that the width of the coupling in terms of agreement with the resonance condition scales proportionally with Ω.

In term of Doppler effect, we have seen in equation (2.1.25) that the detuning scales linearly with atomic velocity such that the width of the Raman transition in velocity space is given by:

$$\Delta v \sim \frac{\Omega}{k_e}, \tag{2.1.37}$$

where k_e is the norm of the effective wavevector which depends on the geometry of the laser beams.

2.1.2.2 Selection rules

The excited state of the D_2 line splits in four hyperfine states, with for each a Zeeman sublevels substructure. As a consequence, a complete treatment of the Raman transitions should take into account all the excited states $|F', m_{F'}\rangle$.

The formula (2.1.18) becomes:

$$\langle\kappa| H_e |\iota\rangle = \langle\kappa| H_0 |\iota\rangle - \sum_{F',m_{F'}} \frac{1}{\Delta_{F',m_{F'}}} \langle\kappa| H_c |F', m_{F'}\rangle \langle F', m_{F'}| H_c |\iota\rangle . \tag{2.1.38}$$

This sum simplifies by considering that the $\Delta_{F',m_{F'}} \sim \Delta$ as the hyperfine structure energies extends over 500 MHz $\ll \Delta$. Moreover, as $\hat{V} = -\hat{\vec{d}} \cdot \hat{\vec{E}}$, one can account for the laser polarizations in the computation.

The calculation of this effective Hamiltonian as been performed in Rémy Battesti PhD thesis[Battesti, 2003]. Its conclusions are the following for copropagating and counterpropagating transitions (see next section):

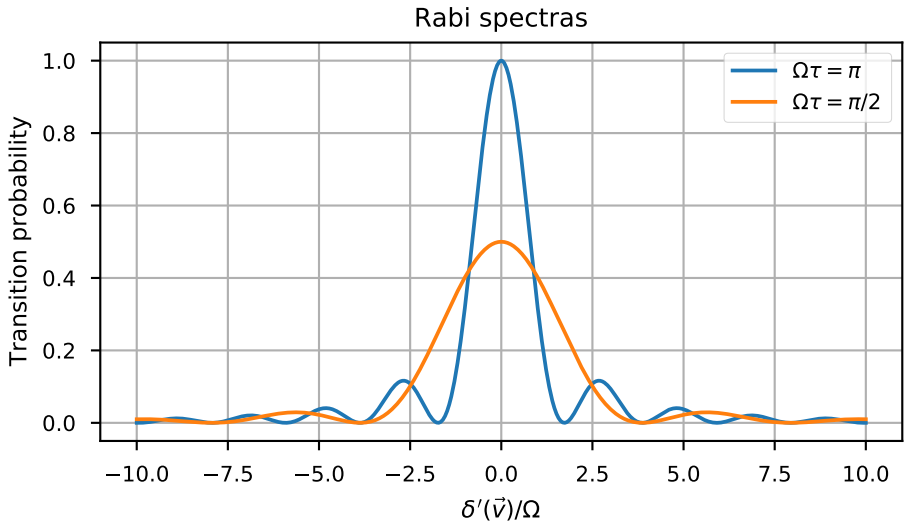

Figure 2.2: The transition probability of a single Raman pulse for given pulse duration.

1. The selection rules states that only two hyperfine sublevels of same m_F ($\Delta m_F = 0$) can be coupled with two linearly polarized lasers if their polarizations are orthogonal, provided the bias magnetic field is aligned along the propagation direction of the laser beams.

2. The effective two photon Rabi frequency of the $|F = 1, m_F = 0\rangle \leftrightarrow |F = 2, m_F = 0\rangle$ coupling writes:

$$\Omega = \frac{\sqrt{I_1 I_2}}{I_s} \frac{\Gamma^2}{16\Delta}, \tag{2.1.39}$$

   where I_i represents the intensity of each laser i seen by the atoms, $\Gamma = 2\pi \cdot 6.06$ MHz is the natural line width of the excited state and $I_s = 2.50\,\mathrm{mW{\cdot}cm^{-2}}$ is the saturation intensity of D_2 line for linearly polarized light[Steck, 2001].

3. The light shifts are also extracted. For each laser present in the system and for each level:

$$\Omega_i^{\mathrm{LS}} = \frac{I_i}{I_s} \frac{\Gamma^2}{8\Delta}, \tag{2.1.40}$$

where the detuning Δ depends on the considered hyperfine level. Thus, we are sensitive the differential displacement between the two levels:

$$\Omega^{\mathrm{LS}}_{\mathrm{diff},i} = \frac{I_i}{I_s}\frac{\Gamma^2}{8(\Delta-\omega_{HFS})} - \frac{I_i}{I_s}\frac{\Gamma^2}{8\Delta} \tag{2.1.41}$$

$$\simeq \frac{I_i}{I_s}\frac{\Gamma^2}{8\Delta} \times \frac{\omega_{HFS}}{\Delta}, \tag{2.1.42}$$

when the detuning Δ is large with respect to the hyperfine structure splitting.

We point out that the selection rule $\Delta m_F = 0$ is a consequence of the approximation $\Delta_{F',m_{F'}} \sim \Delta$ which amounts to not resolving the hyperfine structure of the excited state. Strictly speaking, transitions with $\Delta m_F = \pm 2$ are not strictly forbidden. As we restrict ourselves to the subspace $\{|F=1,m_F=0\rangle, |F=2,m_F=0\rangle\}$ for interferometry, it is interesting to compute the order of magnitude of the Rabi frequency of the $|F=1,m_F=0\rangle \rightarrow |F=2,m_F=\pm 2\rangle$ transitions.

This calculation, which is a generalization of the one presented in [Battesti, 2003], states that:

$$\frac{\Omega(|F=1,m_F=0\rangle \leftrightarrow |F=2,m_F=\pm 2\rangle)}{\Omega} \sim \frac{A_{5^2P_{3/2}}}{h\Delta} \sim 10^{-3}, \tag{2.1.43}$$

where $A_{5^2P_{3/2}}$ is the magnetic dipole constant of the considered excited state and evaluates to $h\cdot 84.7$ MHz[Steck, 2001] and Ω defined by equation (2.1.39) represents the coupling constant between the magnetically insensitive states ($m_F = 0$). The numerical value is given for our experimental parameters ($\Delta \sim 60$ GHz).

In our experimental setup, we apply a bias magnetic field that displaces the states $|F=2,m_F=\pm 2\rangle$ by $\sim \pm 40$ kHz by Zeeman effect such that the transitions $|F=1,m_F=0\rangle \rightarrow |F=2,m_F=\pm 2\rangle$ are off resonance. As a consequence, the amplitudes of probability associated with these couplings are negligible. Moreover, the light shifts on the $|F=1,m_F=0\rangle$ state induced by this coupling evaluate below the mHz range with our experimental conditions, and thus can also be safely neglected.

2.1.3 Co- and counter-propagating transitions

Two geometrical configurations show a particular interest when using Raman transitions: the *co-propagating* and the *counterpropagating*. Their name are quite straightforward: in the first case the two laser beams propagate in the same direction, or in opposite direction for the second one. We denote them respectively with the superscripts $\downarrow\downarrow$ and $\downarrow\uparrow$.

Their respective effective wavevector are given by:

$$k_e^{\downarrow\downarrow} = k_1 - k_2 \tag{2.1.44}$$
$$k_e^{\downarrow\uparrow} = k_1 + k_2, \tag{2.1.45}$$

Using the resonance condition, we can link those two effective wavevectors to the atomic energy levels:

$$k_e^{\downarrow\downarrow} \simeq \frac{\omega_{HFS}}{c} \tag{2.1.46}$$
$$k_e^{\downarrow\uparrow} \simeq 2\frac{\omega_e}{c}, \tag{2.1.47}$$

where c is the speed of light, and we have reused the three level system notations. For ^{87}Rb, we have $\omega_\beta \simeq 2\pi \cdot (6.8 \text{ GHz})$ and $\omega_e \simeq 2\pi \cdot (384 \text{ THz})$. From these numbers we can estimate the velocity difference between the two coupled states given by $\hbar k_e/m$. For copropagating transitions, this yield $\sim 100 \text{ nm} \cdot \text{s}^{-1}$. The typical durations involved in our experiment being less than a second, we can neglect this difference.

However for counterpropagating transitions, the velocity difference evaluates to $v_R \sim 1.2 \text{ cm} \cdot \text{s}^{-1}$. Using them, an atomic wavefunction can then be put in a superposition between two states whose spatial separation is given by $v_R \delta t$. For $\delta t = 1$ ms, the separation is 12 μm, macroscopic with respect to the atomic size. As such counterpropagating transitions appear as excellent candidates to prepare atoms in a spatially separated superpositions.

In order to evaluate the width of the transferred velocity class, translating our ability to address atom gases, we need to compare those wavevectors to the Rabi frequency Ω of the coupling. In our experimental conditions, $\Omega \sim 2\pi \cdot (5 \text{ kHz})$. We can now compute order of magnitude for the width of the transition in velocity space for those two cases:

$$\Delta v^{\downarrow\downarrow} \sim 220 \text{ m} \cdot \text{s}^{-1} \qquad \Longleftrightarrow T^{\downarrow\downarrow} \sim 505 \text{ K} \tag{2.1.48}$$
$$\Delta v^{\downarrow\uparrow} \sim 2 \cdot 10^{-3} \text{ m} \cdot \text{s}^{-1} \Longleftrightarrow T^{\downarrow\uparrow} \sim 40 \text{ nK}, \tag{2.1.49}$$

where we have also expressed the width using the one dimensional temperature ($\frac{1}{2}m\Delta v^2 = \frac{1}{2}kT$).

In the laboratory, as we will see in chapter 3, we produce atom gases using the optical molasses techniques, which allows to reach temperatures of ~ 4 μK. Alternatively, we can produce Bose-Einstein condensate which exhibits a temperature ~ 100 nK. In this context, copropagating transitions can address to whole atomic sample, while counterpropagating transitions are extremely velocity selective.

However, copropagating transitions are not completely insensitive to the Doppler effect. The Doppler shift $\vec{k}_e \cdot \vec{v}$ evaluates to $\sim 2 \cdot \pi \cdot (20 \text{ Hz}) / (\text{m} \cdot \text{s}^{-1})$. Performing a Rabi spectrum whose width is of the order of the Rabi frequency, a few kHz, this shift is almost undetectable. Using the Ramsey clock technique that are presented in next section, one may reach sub-Hertz precision and observe this Doppler shift.

Thus, as copropagating transitions allow to address a large velocity class, and their associated Doppler shift is small with respect to the Rabi frequency, we can use them to probe the atomic internal states. Nevertheless, they cannot be considered as completely Doppler insensitive.

On the other hand, the two-photon wavevector of counterpropagating transitions exhibit a Doppler shift of $\sim 2.6 \text{ MHz} / (\text{m} \cdot \text{s}^{-1})$. For lasers in vertical configuration, and with atoms subjected to the gravitational acceleration $g = 9.81 \text{ m} \cdot \text{s}^{-2}$, the frequency sweep that is necessary to maintain the resonance condition evaluates to $\sim 25 \text{ MHz} \cdot \text{s}^{-1}$. This number is large compared to typical Rabi frequencies: gravity sets the atoms out of resonance in a few hundreds of microseconds. Operating counterpropagating Raman transitions requires a careful compensation of this shift. This also exhibits that these transitions can be used to measure the gravitational acceleration.

Moreover, the small width of the transition in velocity space allows to select a narrow velocity class from an atomic sample, or to measure its velocity distribution. This technique has been used by our team in the earlier stages of the experiment to implement a velocity sensor based on two π-pulses[Cladé, 2006]. The principle of operation goes as follow:

After the production and release of a sample from optical molasses, one applies a narrow Raman pulse ($\Omega < 2\pi \cdot (1 \text{ kHz})$) to select a sub-recoil velocity class. Following, a given number of Bloch Oscillations (see section 2.3) is applied to the selected atoms to transfer a known number of atomic recoils. Finally, a final Raman pulse is applied to atoms. By repeating the process and scanning the frequency of this last pulse, one performs a measurement of the velocity distribution at the output of the Bloch Oscillations process. The velocity transferred by Bloch Oscillations can then be extracted from the comparison of this measurement and the knowledge of the initially selected velocity class.

This method has now been supplanted by *atom interferometry* since 2008[Cadoret, 2008b] following the proposal by the team of S. Chu[Wicht, 2002]. This technique takes advantage of the already announced property of velocity transfer induced by counterpropagating Raman transitions in order to prepare atoms in a superposition of spatially separated states.

2.2 Atom Interferometry

In a very general scope, atom interferometry denotes the experimental techniques that prepare atoms in a superposition of internal and/or momentum (or external) states in order to perform measurements.

The development that is presented here takes the form of a few stages: we first discuss Ramsey sequences which will allow us to present the basic concepts of the technique. Immediately following, the optical Mach-Zehnder analog of external atom interferometry will be introduced.

To refine this presentation, we will consider the effect of gravity which will lead us to the presentation of the path integral formalism for the computation of the output state of the interferometer.

This exposition of the basic concepts will allow us to present our differential velocity sensor, which is also called Ramsey-Bordé interferometer. This interferometer is used for the measurement of the recoil velocity.

Finally we will discuss the noise sensitivity of the interferometric based measurement process.

However, before we get to the heart of the matter, let me present and discuss an approximation that we use along this part.

π and $\pi/2$ pulses

Two particular pulses deduced from equation (2.1.32) have a particular interest. At resonance ($\delta_t(\vec{v}) = 0$):

- The π-pulse ($\Omega\tau = \pi$):

$$U_\pi = \begin{pmatrix} 0 & -ie^{-i\phi} \\ -ie^{i\phi} & 0 \end{pmatrix} \tag{2.2.1}$$

- The $\frac{\pi}{2}$-pulse ($\Omega\tau = \frac{\pi}{2}$):

$$U_{\pi/2} = \frac{1}{\sqrt{2}} \begin{pmatrix} 1 & -ie^{-i\phi} \\ -ie^{i\phi} & 1 \end{pmatrix} \tag{2.2.2}$$

In the first case, the initial state is flipped and the transformation can be seen as a *mirror*, while the second case corresponds to a *beam splitter*: if the initial state can be described $|\psi_i\rangle = |\alpha\rangle$ or $|\beta\rangle$, then the final state will be a superposition between those two states. Inversely, if the input state is a superposition:

$$|\psi_i\rangle = c_\alpha |\alpha\rangle + c_\beta |\beta\rangle , \tag{2.2.3}$$

then we can write the output state:

$$|\psi_f\rangle = \frac{1}{\sqrt{2}}\left\{\left(c_\alpha - ie^{-i\phi}c_\beta\right)|\alpha\rangle + \left(-ie^{i\phi}c_\alpha + c_\beta\right)|\beta\rangle\right\}, \tag{2.2.4}$$

such that the probability to be projected in either $|\alpha\rangle$ or $|\beta\rangle$ exhibits an interference pattern which depends on the phase of the quantum coefficients and the phase associated to the transition.

Infinitely short pulses hypothesis
The above pulse are simplifications of equation (2.1.32) but, as we will see below, they contain the heart of atom interferometry signals.

In order to use them, we first assume that $\delta_t(\vec{v}) \ll \Omega$, which places us in the case of resonant pulses. With our experimental parameters this hypothesis can be seen as unjustified in particular because the light shifts are of the same order of magnitude than the Rabi frequency. Our method is to treat them as a perturbation from the ideal case given by the infinitely short pulses. These perturbations are treated both theoretically and experimentally in section 4.2.

Finally, we assume *infinitely short pulses* $\tau \to 0$, such that the laser pulses happen at a very well defined timing. This corresponds to $\Omega \to \infty$, so that the pulse area $\theta = \Omega\tau$ is constant. We detail in this part a treatement beyond the infinitely short pulses hypothesis (section 2.2.5) that justifies it.

2.2.1 Ramsey sequences

Until section 2.2.3, we will suppose that the atoms are not subjected to gravity.

We consider an atomic two level system whose free Hamiltonian can be written:

$$H_0 = \frac{\delta_0(\vec{v})}{2}\sigma_z \tag{2.2.5}$$

in the lasers frame. The detuning $\delta_0(\vec{v})$ takes into account the internal energy and the Doppler sensitivity. It simply expresses:

$$\delta_0(\vec{v}) = \delta - \delta_{\text{Doppler}} \tag{2.2.6}$$

$$= \omega_1 - \omega_2 - \left(\omega_{HFS} + \vec{k_e}\cdot\vec{v} + \frac{\hbar\vec{k}_e^2}{2m}\right). \tag{2.2.7}$$

The interferometric sequence that we consider is a *Ramsey sequence*: the initial atomic state is either $|\alpha\rangle$ or $|\beta\rangle$ and it is subjected to two $\frac{\pi}{2}$ separated by a duration T_{Ramsey}. We then measure the transition probability of the sequence.

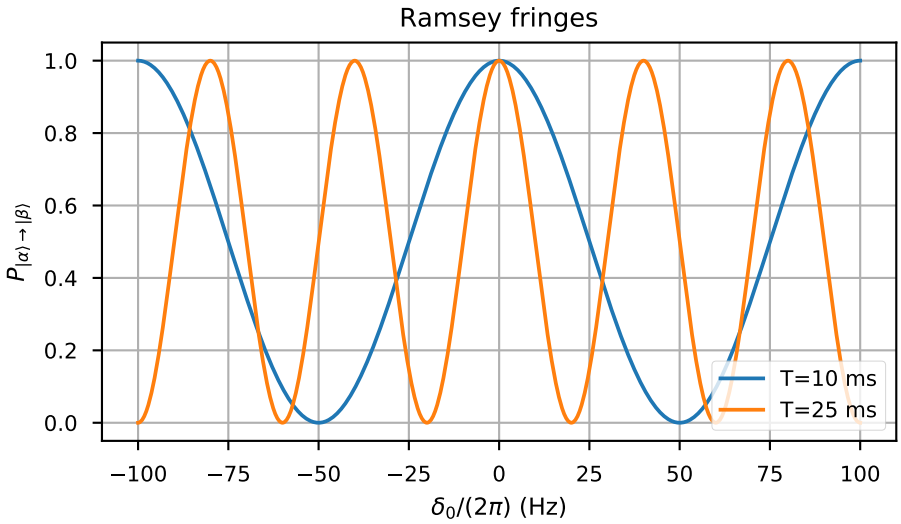

Figure 2.3: Ramsey fringes for two interferometer duration. The x axis has been scaled such that its unit is in Hertz. We notice that in this unit the period of the fringes is indeed T_{Ramsey}^{-1}. Moreover, only the central fringe exhibits a superposition of the maxima.

We identify the two pulses by index I and II. By composition of the evolution operators we can compute the total evolution operator of the sequence:

$$U_{\text{Ramsey}} = U_{\pi/2,II} U_0 \left(T_{\text{Ramsey}}\right) U_{\pi/2,I}, \tag{2.2.8}$$

where U_0 is easily obtained from H_0:

$$U_0(t) = \begin{pmatrix} \exp\left(-i\frac{\delta_0(\vec{v})}{2}t\right) & 0 \\ 0 & \exp\left(i\frac{\delta_0(\vec{v})}{2}t\right) \end{pmatrix} \tag{2.2.9}$$

The transition probability:

$$P_{|\alpha\rangle\to|\beta\rangle} = \left|\langle\beta| U_{\text{Ramsey}} |\alpha\rangle\right|^2, \tag{2.2.10}$$

is independent of the input state and writes:

$$P_{|\alpha\rangle\to|\beta\rangle}\left(\vec{v}\right) = \frac{1}{4}\left|1 + \exp\left(-i\left(\delta_0\left(\vec{v}\right) T_{\text{Ramsey}} + \phi_I - \phi_{II}\right)\right)\right|^2 \tag{2.2.11}$$

$$= \frac{1 + \cos\left(\delta_0\left(\vec{v}\right) T_{\text{Ramsey}} + \phi_I - \phi_{II}\right)}{2} \tag{2.2.12}$$

We can define the phase of the Ramsey sequence: $\Phi_{\text{Ramsey}} = \delta_0\left(\vec{v}\right) T_{\text{Ramsey}} + \phi_I - \phi_{II}$. For the following discussion, we assume $\phi_I = \phi_{II}$ for simplicity.

The central fringe is defined as $\Phi_{\text{Ramsey}} = \delta_0(\vec{v})\, T_{\text{Ramsey}} = 0$, *i.e.* $\delta_0(\vec{v}) = 0$ where we recover the resonance condition (equation (2.1.6)).

We plotted equation (2.2.12) on figure (2.3) for a Ramsey duration of 10 and 25 ms. The period of the signal scales as T_{Ramsey}^{-1}, such that we observe a succession of maxima. With a single T_{Ramsey}, one cannot discriminate the central fringe and the ones for which $\Phi_{\text{Ramsey}} = n2\pi$ for $n \neq 0$. However, combining the measurement from two T_{Ramsey} allows to lift this undetermination.

In our experiment, the typical performance of our interferometers allow a determination of the central fringe with a sensitivity of $\delta\phi = 5$ mrad. In terms of $\delta_0(\vec{v})$, this yields a precision of $\delta\phi/T_{\text{Ramsey}} \sim 2\pi \cdot (100\text{ mHz})$ for $T_{\text{Ramsey}} = 10$ ms. The interferometric method allows for more precise measurements than the single pulse measurement, by means of an increased interrogation duration.

Additionally, in the infinitely short duration hypothesis, it is insensitive to the light shifts $\Omega_{\text{diff}}^{\text{LS}}$. If we were to take into account their contribution, we would expect the correction to scale as $\sim \Omega_{\text{diff}}^{\text{LS}}\tau/T_{\text{Ramsey}}$. In the single pulse configuration, this correction would simply be given by $\Omega_{\text{diff}}^{\text{LS}}$. Typically, using Ramsey sequences this effect is reduced by a factor 100.

Thus, not only Ramsey sequences allow for more precise determinations due to increased interaction duration, but the quantity that is measured presents less perturbation induced by the transitions.

By performing this measurement, one compares two quantities of equation (2.2.7):

1. $\omega_{\text{laser}} = \omega_1 - \omega_2$, which is an experimental parameter, usually controlled by a phase lock of the beatnote signal of the two lasers. In our experiment, this phase lock is performed with respect to a stable microwave reference, itself referenced to the atomic clock signal from SYRTE.

2. $\omega_{\text{atom}} = \omega_{HFS} + \vec{k_e} \cdot \vec{v} + \frac{\hbar \vec{k_e}^2}{2m}$ is the energy difference between the two atomic levels and characterizes both the atomic internal and external states.

Placing ourselves in the frame of the atom, we can interpret a Ramsey sequence as a phase matching experiment over the phase difference between the atomic states induced by free evolution during the interrogation duration:

$$\Phi_{\text{atom}} = \int_0^{T_{\text{Ramsey}}} dt\ \omega_{\text{atom}}(t), \tag{2.2.13}$$

and the accumulated phase of the lasers for the same duration:

$$\Phi_{\text{laser}} = \int_0^{T_{\text{Ramsey}}} dt\ \omega_{\text{laser}}(t). \tag{2.2.14}$$

Assuming no time dependence and $\Phi_{\text{atom}} = \Phi_{\text{laser}}$, one recovers the expression of the central fringe.

Let us now suppose that we run this sequence with copropagating transitions on an atomic sample produced from optical molasses. The width in velocity space of the transition allows to address all the atoms. Moreover, the Doppler term linear in velocity induces inhomogeneous phase shifts of the order $\sigma_v k_e^{\downarrow\downarrow} T_{\text{Ramsey}}$ over the atomic sample, where σ_v is the width of its velocity distribution. Typically $\sigma_v \sim 3$ cm $\cdot$ s^{-1}, yielding phase shifts of $\sigma_\Phi \sim 4$ mrad per ms of interrogation. These phase shifts may result in a loss of contrast but at this order of magnitude, they do not damage the fringes signal. Moreover, assuming that the mean velocity of the cloud is 0, this term does not shift the central fringe.

Alternatively, if the Ramsey sequence is ran in counterpropagating configuration, we would expect that the Doppler sensitivity of transition to allow for a precise measurement of the atomic velocity. However, we should also estimate the phase shifts over the atomic sample. Since the transitions are now velocity selective, the width of the atomic sample in velocity space is given by the width of the Raman transition $\Omega/k_e^{\downarrow\uparrow}$. We then obtain that the inhomogeneous phase shifts over the selected atomic sample scale as ΩT_{Ramsey}, a few radians per ms of interrogation, which completely washes out the fringes. As a consequence no interferometric signal would be observed using a single Ramsey sequence in counterpropagating configuration.

In order to implement interferometry on atomic external states, we should use more elaborate schemes that we present in the following sections.

2.2.2 Atom interferometry: Mach-Zehnder configuration

We start by describing the Mach-Zehnder interferometer whose name comes from its close analogy to the optical Mach-Zehnder. Although rarely used in our experiment, the conceptual simplicity of this interferometer eases the presentation of interferometry principles. It is represented in figure (2.4, top). The pulse sequence goes as follow:

1. The atomic initial state $|\psi_i\rangle = |\alpha, \vec{p_i}\rangle$ is split by a $\pi/2$ counterpropagating Raman transition. After this pulse, the state is:

$$\frac{1}{\sqrt{2}}\left(|\alpha, \vec{p_i}\rangle - ie^{-i\phi_I}\left|\beta, \vec{p_i} + \hbar\vec{k_e}\right\rangle\right) \tag{2.2.15}$$

2. After a duration T, a π-pulse which flips the quantum states is applied. For this duration the free Hamiltonian has governed the evolution of the

wavefunction such that the incoming state before the π pulse writes:

$$\frac{1}{\sqrt{2}}\left(e^{i\delta_0(\vec{v})T/2}\left|\alpha,\vec{p_i}\right\rangle - ie^{-i(\phi_I+\delta_0(\vec{v})T/2)}\left|\beta,\vec{p_i}+\hbar\vec{k_e}\right\rangle\right) \tag{2.2.16}$$

After applying the pulse, the state is:

$$\frac{-i}{\sqrt{2}}\left(e^{i(\delta_0(\vec{v})T/2-\phi_{II})}\left|\beta,\vec{p_i}+\hbar\vec{k_e}\right\rangle - ie^{-i(\phi_I+\delta_0(\vec{v})T/2-\phi_{II})}\left|\alpha,\vec{p_i}\right\rangle\right) \tag{2.2.17}$$

3. After a second waiting period of the same amount T, the two states overlap in space and can interfere with one another. Once again, we start by writing the wavefunction after the free evolution:

$$\begin{aligned}\frac{-i}{\sqrt{2}}\Big(&e^{i(\delta_0(\vec{v})T/2-\phi_{II}-\delta_0(\vec{v})T/2)}\left|\beta,\vec{p_i}+\hbar\vec{k_e}\right\rangle\\ &- ie^{-i(\phi_I+\delta_0(\vec{v})T/2-\phi_{II}-\delta_0(\vec{v})T/2)}\left|\alpha,\vec{p_i}\right\rangle\Big)\end{aligned} \tag{2.2.18}$$

We immediately see that the terms corresponding to the free evolution cancel out. This result can be expected from the symmetry of the interferometer: the two arms spend the same duration in each state. After the application of the third pulse, the state is given by:

$$\begin{aligned}\frac{-i}{2}\Big\{&\left(e^{-i\phi_{II}}-e^{-i(\phi_I-\phi_{II}+\phi_{III})}\right)\left|\beta,\vec{p_i}+\hbar\vec{k_e}\right\rangle\\ &- i\left(e^{-i(\phi_I-\phi_{II})}+e^{-i(\phi_{II}-\phi_{III})}\right)\left|\alpha,\vec{p_i}\right\rangle\Big\}\end{aligned} \tag{2.2.19}$$

Now that we have obtained the state at the output of the three pulses sequence, we can compute the transition probability as we did for the Ramsey sequence:

$$P_{|\alpha\rangle\to|\beta\rangle}\left(\vec{v}\right) = \frac{1-\cos\left(\phi_I-2\phi_{II}+\phi_{III}\right)}{2}, \tag{2.2.20}$$

where, compared to the single Ramsey sequence, the phase of the output is displaced by π which is a consequence of the fact that this interferometer correspond to two concatenated Ramsey sequences.

The main result of this analysis is that the output state of this interferometer does not depend on the atomic velocity but only on the relative phases of the lasers during the pulses.

In particular, when using counterpropagating Raman transitions, we have seen that the Doppler sensitivity washes out the fringes of a Ramsey transitions. The

Mach-Zehnder configuration compensates these inhomogeneous phases and allows to recover the interferometric signal.

This result will still be verified when we will take into account for constant gravity in the atomic equation of motion. Moreover, gravitational acceleration will govern the laser phases through the atom positions (term $\vec{k_e} \cdot \vec{z}$) during the interferometer.

Pulse area imperfections

Before taking into account gravity, I would like to discuss the situations where the pulse area of the beam-splitters and mirrors are not perfectly $\pi/2$ and π. In the infinitely short pulse hypothesis, for a pulse area θ, the evolution operator of a pulse is given by (equation (2.1.32)):

$$U(\theta, \phi) = \begin{pmatrix} \cos(\theta/2) & -ie^{-i\phi}\sin(\theta/2) \\ -ie^{i\phi}\sin(\theta/2) & \cos(\theta/2) \end{pmatrix} \tag{2.2.21}$$

Considering that the free evolution terms cancel, we are left to multiply the evolution operators to get the transition probability of the pulse sequence. However, we should be careful with the middle pulse:

At the temperature of 2 μK, the de Broglie wavelength is of the order of 300 nm. The wavepacket separation at the time of the middle pulse is given by $(\hbar k_e/m) \cdot T$, and is typically greater that 100 μm. Thus, the two wavepackets can not interfere with each other and we should apply the pulse evolution operator separately.

Another possibility is to define a *ad hoc* evolution operator for with the diagonal terms are set to 0:

$$U'(\theta) = \begin{pmatrix} 0 & -ie^{-i\phi^{(A)}}\sin(\theta/2) \\ -ie^{i\phi^{(B)}}\sin(\theta/2) & 0 \end{pmatrix}, \tag{2.2.22}$$

where we distinguish the two laser phases to take into account for the spatial shift between the two arms. This operator is not unitary, so that the norm of the wavefunction is not conserved. This loss can be interpreted as a loss of atomic signal (dashed lines of figure 2.4). Experimentally, this will appear as a loss of contrast in the fringes signal. The evolution operator of the three pulse sequence is then:

$$U = U(\theta_{III}) \cdot U'(\theta_{II}) \cdot U(\theta_I), \tag{2.2.23}$$

for which the transition probability reads:

$$P_{|\alpha\rangle\to|\beta\rangle} = \frac{\sin^2(\frac{\theta_{II}}{2})}{2}\Bigg(1 + \cos(\theta_I)\cos(\theta_{III}) - \sin(\theta_I)\sin(\theta_{III})\cos\left(\phi_I - \phi_{II}^{(A)} - \phi_{II}^{(B)} + \phi_{III}\right)\Bigg) \tag{2.2.24}$$

When replacing $\theta_I = \theta_{III} = \pi/2$ and $\theta_{II} = \pi$, we find the previous formula (2.2.20).

This analysis allows us to exhibit the impact of the spatial splitting between the two arms on the interferometric phase since the term $2\phi_{II}$ was replaced by $\phi_{II}^{(A)} + \phi_{II}^{(B)}$. However, the pulse area imperfections do not contribute to the interferometric phase, but modify the contrast of the fringes.

First, the $\sin^2(\frac{\theta_{II}}{2})$ prefactor is a consequence of the non-unitarity of the *ad hoc* middle pulse evolution operator. The atom loss induced by the imperfect pulse area of this pulse limits the amplitude of the fringe signal.

We can then define the contrast of the interferometer:

$$\mathcal{C} = P^{\text{max.}}_{|\alpha\rangle\to|\beta\rangle} - P^{\text{min.}}_{|\alpha\rangle\to|\beta\rangle}, \tag{2.2.25}$$

which corresponds to twice the amplitude of the fringes[2]. With the input of equation (2.2.24), we find:

$$\mathcal{C} = \sin^2\left(\frac{\theta_{II}}{2}\right)\sin(\theta_I)\sin(\theta_{III}) \tag{2.2.26}$$

To conclude this discussion on the pulse area imperfections, let us develop this formula around the nominal values of the pulse, and then assume that the pulse area imperfections have a common origin (such as low frequency laser intensity variation), and write the imperfection $\delta\theta$ for a $\pi/2$ pulse. The contrast them becomes:

$$\mathcal{C} = 1 - 2\delta\theta^2 \tag{2.2.27}$$

Assuming a normal distribution with width $\sigma_{\delta\theta}$, we find the contrast mean and standard deviation:

$$\langle\mathcal{C}\rangle = 1 - 2\sigma^2_{\delta\theta} \text{ and } \sigma_{\mathcal{C}} = 2\sqrt{2}\sigma^2_{\delta\theta} \tag{2.2.28}$$

To give an order of magnitude of the contrast fluctuations, we can consider an upper bound of 5% of laser intensity fluctuations. Since the Rabi frequency and thus the pulse area is proportional to the intensity, we can estimate $\delta\theta \sim 80$ mrad. This yield $\sigma_{\mathcal{C}} < 2\%$.

This study shows that, at least in simple scheme Raman based interferometry, pulse area imperfections do not shift the central fringe. Moreover, the scaling of their contribution to noise indicates that, in a certain limit, interference fringes are shielded from shot to shot pulse area fluctuations.

[2]In optical interferometry, the contrast (or visibility) is usually defined as the ratio between the amplitude and the mean optical intensity. In quantum mechanics based interferometry, we deal with probabilities whose sum is one. As a consequence, the contrast of an atom interferometer reduces to twice the fringes amplitude.

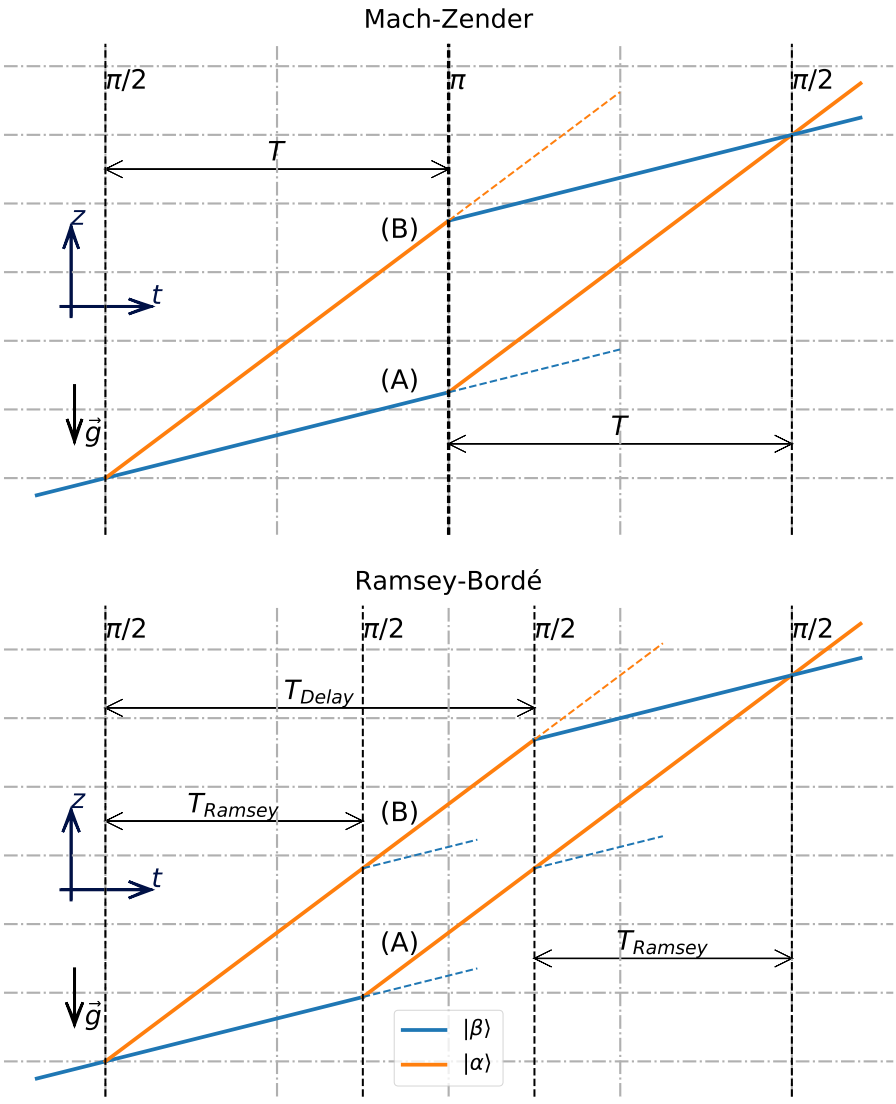

Figure 2.4: Top: the Mach Zehnder interferometer. Bottom: a Ramsey Bordé interferometer in differential velocity sensor configuration. The black vertical dashed lines indicates the optical pulses with their associated pulse area. The colored lines display the atomic trajectories. The dashed colored lines show the loss channels. The effect of gravity has not been represented for clarity.

2.2.3 Interferometry in a gravitational field

When treating the motion of atoms, gravity is not negligible such that a treatment of atom interferometry should take it into account. The starting point of such a treatment is to use the action of Lagrangian dynamics. In a constant gravitational field:

$$\mathcal{L}\left(\vec{r},\vec{v}\right)=\frac{m\vec{v}^2}{2}-mgz, \tag{2.2.29}$$

where $\vec{v}$ the velocity of the considered particle and z its position on the vertical direction. For simplicity, we will restrict ourselves to a one dimensional treatment along the vertical direction.

In classical Lagrangian mechanics, the principle of least action states that considering a particle which passes through the space-time points (z_a,t_a) and (z_b,t_b), then the path Γ_{cl} that is taken by the particle is the one that extremizes the action $\mathcal{S}\left(\Gamma\right)$:

$$\mathcal{S}\left(\Gamma\right)=\int_{t_a}^{t_b}\mathcal{L}(z(t),v_z(t))dt. \tag{2.2.30}$$

This principle leads to Newton equation of dynamics through Euler-Lagrange equations.

Additionally, in the quantum regime, we want to give an expression of the evolution operator that allow to compute the state $|\psi(t_f)\rangle$ from the initial state $|\psi(t_i)\rangle$:

$$|\psi(t_f)\rangle=U(t_i,t_f)\,|\psi(t_i)\rangle \tag{2.2.31}$$

Projecting on the position basis and inserting a completeness relation, we obtain:

$$\langle z_b|\psi(t_f)\rangle=\int \mathrm{d}z_i\,\langle z_b|\,U(t_i,t_f)\,|z_i\rangle\,\langle z_i|\psi(t_i)\rangle \tag{2.2.32}$$

The term $K(z_i\ t_i,z_f\ t_f)=\langle z_b|\,U(t_i,t_f)\,|z_i\rangle$ is the quantum propagator. The composition property of the evolution operator $U(t_f,t_i)=U(t_f,t)U(t,t_i)$ extends to the propagation operator through the insertion of a completeness relation in equation (2.2.32).

Moreover, by dividing the space-time interval (z_i,t_i) to (z_f,t_f) in infinitesimal steps, one builds a path Γ and its corresponding action.[Feynman, 1965]

The Feynman formulation of quantum mechanics proves that the quantum propagator can be written:

$$K(z_i\ t_i,z_f\ t_f)=\mathcal{N}\sum_{\Gamma}\exp\left(-i\frac{\mathcal{S}(\Gamma)}{\hbar}\right), \tag{2.2.33}$$

where $\mathcal{N}$ is a normalization factor.

In the classical limit, *i.e.* when $\mathcal{S}(\Gamma_{cl}) \gg \hbar$, the phase of the exponential term varies very rapidly with the paths variations and vanish in the sum, except for the classical path contribution which extremizes the action. We then obtain:

$$\langle z_f|\psi(t_f)\rangle = e^{-i\frac{\mathcal{S}(\Gamma_{cl})}{\hbar}} \langle z_i|\psi(t_i)\rangle \tag{2.2.34}$$

2.2.3.1 Classical limit

With initial conditions (z_0, v_0) at $t = 0$, the equation of motions $v(t) = v_0 - gt$ and $z(t) = z_0 + v_0 t - gt^2/2$ leads to the classical action for a duration T:

$$\mathcal{S}(\Gamma_{cl}) = \int_0^T dt \frac{m}{2}(v_0 - gt)^2 - mg(z_0 + v_0 t - gt^2/2) \tag{2.2.35}$$

$$= mT\left(\frac{v_0^2}{2} - gz_0 - v_0 gT + \frac{g^2T^2}{3}\right) \tag{2.2.36}$$

In our experimental conditions, typical values are $T = 10$ ms and $v_0 = 1\ \mathrm{m\cdot s^{-1}}$, we obtain $\mathcal{S}(\Gamma_{cl})/\hbar \sim 5 \cdot 10^6$ rad such that the classical limit is indeed reached.

As a consequence, we perform a semi-classical treatment of the interferometers where the external state of the atom is treated classically and the transition pulses are treated through quantum mechanics. We then treat the atoms external motion as a classical trajectory, *i.e.* with complete knowledge of position and velocity.

The equation of motion for the two arms of the Mach-Zehnder, taking into account the atomic recoil induced by the laser transitions, are given by:

$$\begin{aligned} z^{(A)}(t) &= z_0 + v_0 t - \frac{gt^2}{2} + \frac{\hbar k_e}{m}(t - T)\Theta(t - T) \\ z^{(B)}(t) &= z_0 + \left(v_0 + \frac{\hbar k_e}{m}\right)t - \frac{gt^2}{2} - \frac{\hbar k_e}{m}(t - T)\Theta(t - T), \end{aligned} \tag{2.2.37}$$

where Θ is the Heaviside function.

In order to integrate the Lagrangian on each path, one separates them in two around the π pulse time T. After carrying each integral, we find $\mathcal{S}^{(A)} = \mathcal{S}^{(B)}$, and:

$$\phi^{propagation} = 0 \tag{2.2.38}$$

Because the propagation induced differential phase cancels, it is independent of the initial position and velocity of the atoms. The consequence of which is that, again, this contribution to the output phase of the interferometer is identical over the atomic sample.

This result holds even in the non classical limit for Lagrangian that are at most quadratic in position and velocity. First, the phase shift due to propagation was

computed in [Storey, 1994] and applied to atom interferometry. This work was then extended in [Wolf, 2011] where it is shown that the differential phase shift in a Mach-Zehnder atom interferometer cancels.

2.2.3.2 Laser phases

The phase difference induced by the wavefunction propagation in a gravitational field cancels, so that we are left with evaluating the phase shift induced by the imprinted laser phases (equation (2.2.20)). We can write the laser phase at all times:

$$\phi(z(t),t) = k_e z(t) - \int_0^t \omega(t')dt' + \phi^0, \tag{2.2.39}$$

where ϕ^0 is an arbitrary phase. By taking the phase reference at the start of the interferometer, we have $\phi^0 = 0$

Due to gravitational acceleration, the resonance condition of Raman transitions will not be met if the frequency difference is not swept along the interferometer. We assume a linear sweep:

$$\omega(t) = \omega(0) - k_e g_0 t, \tag{2.2.40}$$

where $g_0 > 0$ is an experimental parameter which corresponds to an estimation of the gravitational acceleration. With this linear sweep, the frequency contribution to the laser phase is:

$$-\int_0^t \omega(t')dt' = -\omega(0)t + \frac{1}{2}k_e g_0 t^2 \tag{2.2.41}$$

On the other hand, the wavepackets positions are governed by the gravity acceleration. Using the formulas (2.2.37), we have for the two arms:

$$\begin{aligned}\phi^{(A)} &= \phi(z^{(A)}(T),T) \\ &= k_e\left(z_0 + v_0 T - \frac{gT^2}{2}\right) - \omega(0)T + \frac{1}{2}k_e g_0 T^2,\end{aligned} \tag{2.2.42}$$

and

$$\begin{aligned}\phi^{(B)} &= \phi(z^{(B)}(2T),2T) - \phi(z^{(B)}(T),T) + \phi(z^{(B)}(0),0) \\ &= k_e\left(z_0 + v_0 T - \frac{3gT^2}{2}\right) - \omega(0)T + \frac{3}{2}k_e g_0 T^2\end{aligned} \tag{2.2.43}$$

The phase difference between the two arms is hence:

$$\phi^{lasers} = -k_e T^2\left(g - g_0\right) \tag{2.2.44}$$

The interpretation of this formula is quite straightforward. The term $(g - g_0)$ displays the physical quantity to be measured g and an experimental parameter g_0 to which it is compared. Similarly to the discussion on Ramsey sequences where the frequency of a local oscillator was compared to the atomic internal frequency, the Mach-Zehnder interferometer measurement can be interpreted as a comparison between the local oscillator sweep rate and the atomic resonance condition sweep induced by their external motion.

The sensitivity of the measurement scales with $k_e T^2 = k_e T \cdot T$, and is proportional to the space-time area that the interferometer arms enclose.

In terms of performance, for a given detectable phase shift $\delta\phi$, the smallest detectable gravity variation is given by

$$\delta g = \frac{\delta\phi}{k_e T^2}. \tag{2.2.45}$$

For typical values $\delta\phi = 5$ mrad and $T = 100$ ms, at 780 nm, one finds a relative sensitivity on g of $\sim 10^{-8}$ illustrating the long known performance of gravimetry based on atom interferometry[Ménoret, 2018].

2.2.3.3 Perturbative Lagrangians

In the presence of a perturbative Lagrangian $\mathcal{L}_{pert} \ll \mathcal{L}$ small enough such that the trajectories are unperturbed, the phase shift relative to a path is given by [Storey, 1994]:

$$\phi^{path} = \frac{1}{\hbar}\int_{\Gamma_{cl}} \mathrm{d}t \mathcal{L}_{pert} \tag{2.2.46}$$

In order to apply this formalism to atom interferometry, one would imagine subdivide the path between the optical pulses. Then, one should propagate the initial and final positions for each sub-path. This procedure promises to be cumbersome. However, it is possible to write an effective Lagrangian that factorizes the sub-paths and allows to evaluate the effect of the perturbation by writing a single integral.

Let us consider a single path with a velocity kick in the middle, result of an optical transition (see figure (2.5)). Then the phase shift of the wavefunction along this path is given by:

$$\phi^{path} = \frac{\mathcal{S}(\Gamma_1) + \mathcal{S}(\Gamma_2)}{\hbar} + \phi^{laser}(t_{pulse}), \tag{2.2.47}$$

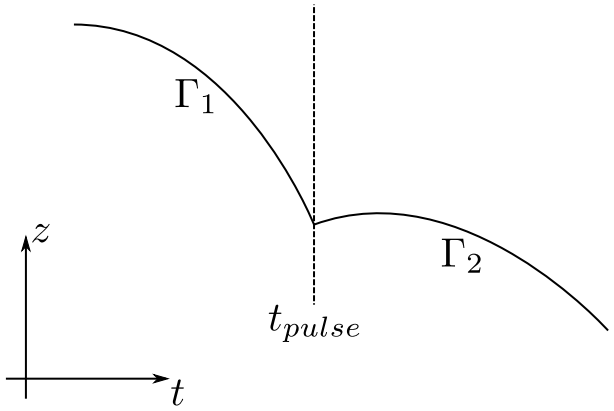

Figure 2.5: Division of a path Γ around a laser pulse that performs a velocity kick.

where $\phi^{laser} = k_e z$. Writing the action in integral form, we find:

$$\phi^{path} = \frac{1}{\hbar}\int_{\Gamma} \mathrm{d}t \left(\mathcal{L} + \hbar\phi^{laser}\left(t_{pulse}\right)\delta\left(t - t_{pulse}\right)\right), \tag{2.2.48}$$

where δ is the Dirac delta.

From this equation, we define the effective Lagrangian $\mathcal{L}_{eff}$:

$$\mathcal{L}_{eff} = \mathcal{L} + \hbar \sum_{\text{pulses}} \phi^{laser}(t_{pulse})\delta(t - t_{pulse}), \tag{2.2.49}$$

where the sum is carried on the pulses that induced a velocity kick.

First, with this Lagrangian, the Euler Lagrange equation is written:

$$\frac{\mathrm{d}}{\mathrm{d}t}\left(\frac{\partial\mathcal{L}}{\partial v}\right) = \frac{\partial\mathcal{L}}{\partial z} + \hbar\frac{\partial\phi^{laser}}{\partial z}\delta\left(t - t_{pulse}\right) \tag{2.2.50}$$

$$m\frac{\mathrm{d}v}{\mathrm{d}t} = \frac{\partial\mathcal{L}}{\partial z} + \hbar k_e\delta\left(t - t_{pulse}\right), \tag{2.2.51}$$

where the most right-handed term displays the velocity kick. In particular, the integration of this equation exhibits a Heaviside function that we have already encountered in equation (2.2.37).

Secondly, in the treatment of the interferometric phases that we have made above, we separated the phase shift induced by the propagation of the wavefunction and by the laser beams. With this effective Lagrangian, both terms appear.

Example: linear gravity gradient

As an application, we treat a simple perturbation case: the linear gravity gradient. Assume that the gravity acceleration is not constant but varies with the position:

$$g(z) = g_c - \gamma z. \tag{2.2.52}$$

Then the potential associated is given by:

$$-mg_c z + m\frac{\gamma}{2}z^2, \tag{2.2.53}$$

where we have the usual gravity term of the Lagrangian and the perturbation:

$$\mathcal{L}_{pert} = m\frac{\gamma}{2}z^2 \tag{2.2.54}$$

The phase induced by the perturbation is given by the phase difference between the two paths:

$$\phi^{\text{perturbation}} = \phi^{path(B)} - \phi^{path(A)} \tag{2.2.55}$$

$$= \int_{\Gamma_{cl}^{(B)}} \mathrm{d}t\ m\frac{\gamma}{2}z^2(t) - \int_{\Gamma_{cl}^{(A)}} \mathrm{d}t\ m\frac{\gamma}{2}z^2(t) \tag{2.2.56}$$

The trajectories correspond to the unperturbed ones, given by equations (2.2.37). Before including these solutions, we manipulate the above expression:

$$\phi^{\text{perturbation}} = m\gamma \int_{t=0}^{2T} \mathrm{d}t \frac{1}{2}\left(z^{(B)}(t)^2 - z^{(A)}(t)^2\right) \tag{2.2.57}$$

$$= m\gamma \int_{t=0}^{2T} \mathrm{d}t \frac{z^{(B)}(t) + z^{(A)}(t)}{2}\left(z^{(B)}(t) - z^{(A)}(t)\right) \tag{2.2.58}$$

The interpretation of this formula is quite straightforward: the phase shift induced by gravity gradients is proportional to the integral of the product of the mean interferometer position with the position difference between the two arms. The first term controls the local value of the gravity acceleration. For the second, it is intuitive that the phase shift induced by a linear spatial inhomogeneity scales with the relative difference of the two positions.

With the input of equations (2.2.37):

$$\begin{cases} z^{(B)}(t) - z^{(A)}(t) &= \frac{\hbar k_e}{m}\Big(t - (t-T)\Theta(t-T)\Big) \\ \frac{z^{(B)}(t)+z^{(A)}(t)}{2} &= z_0 + \left(v_0 + \frac{\hbar k_e}{2m}\right)t - \frac{g_c t^2}{2} \end{cases} \tag{2.2.59}$$

The Heaviside function requires to split the integral. After performing the calculation we find:

$$\phi^{\text{perturbation}} = \gamma k_e T^2 \left(z_0 + \left(v_0 + \frac{\hbar k_e}{2m}\right)T - \frac{7}{12}g_c T^2\right), \tag{2.2.60}$$

which agrees with the literature[3]. In particular, it is in agreement with the exact result derived in [Peters, 1998] at the first order in γ.

[3]The $\frac{\hbar k_e}{2m}$ is sometimes not present, thanks to an alternative definition of the initial velocity that was not followed here

We are now able to treat perturbations that we can express in a Lagrangian form. Moreover, we have provided an effective Lagrangian that allows to reduce the amount of computation necessary to obtain formula or estimates.

2.2.4 Ramsey-Bordé in differential velocity sensor configuration

As we have already exposed, the aim of our research is the measurement of the velocity transferred by optical transitions (section 2.3).

To build an interferometer sensitive to such a transfer, it is sufficient to split the Mach-Zehnder π pulse in two $\pi/2$ and separate them for a duration $T_{\text{delay}} - T_{\text{Ramsey}}$ (see figure (2.4, bottom)).

In this context the parameter T_{delay} represents the delay between the two Ramsey sequences that now form the interferometer. Because this interferometer is built out of two Ramsey sequences, the nature of the signal is modified. However, it conserves the Mach-Zehnder property that the phase shift at the output of the sequence depends only on the phases imprinted during the Raman transitions, such that we can write:

$$\begin{aligned}\Phi^{\text{interferometer}} &= \phi^{(B)}(T_{\text{Ramsey}} + T_{\text{delay}}) - \phi^{(B)}(T_{\text{delay}}) + \phi^{(B)}(0) \\ &\quad - \phi^{(A)}(T_{\text{Ramsey}})\end{aligned} \tag{2.2.61}$$

In order to exhibit the differential velocity sensitivity of this interferometer, let us suppose that the atoms are subjected to a process in between the Ramsey sequences that induced a velocity shift Δv and a position shift Δz at time $T_{\text{Ramsey}} < t' < T_{\text{delay}}$. For example, for a constant additional acceleration a between t_a and $t_a + T_a$, with $\Delta v = aT_a$, $\Delta z = aT_a^2/2$ and $t' = (t_a + T_a)/2$.

Such a process changes the positions at the second Ramsey sequence by an amount:

$$\delta z(t > t') = \Delta z + \Delta v(t - t'), \tag{2.2.62}$$

We can then extract the $k_e z$ contribution to the interferometric phase:

$$k_e \left(\Delta v T_{\text{Ramsey}} - g T_{\text{Ramsey}} T_{\text{delay}}\right), \tag{2.2.63}$$

where we observe that the interferometer signal retains only the amount of transferred velocity.

Additionally, we need to keep the Raman resonance condition along the interferometer. Similarly to the Mach-Zehnder case, we assume a linear ramp for each of the Ramsey sequences and treat them separately. Indeed the velocity transfer

process leads to an additional frequency jump (or sweep, ...) on which we make no assumption. Computing the contribution of this term, we get:

$$\omega(0)T_{\text{Ramsey}} - \frac{k_e g_0 T_{\text{Ramsey}}^2}{2} - \left(\omega(T_{\text{delay}})T_{\text{Ramsey}} - \frac{k_e g_0 T_{\text{Ramsey}}^2}{2}\right) \tag{2.2.64}$$

$$= -\delta\omega T_{\text{Ramsey}}, \text{ where } \delta\omega = \omega(T_{\text{delay}}) - \omega(0). \tag{2.2.65}$$

Unlike the case of the Mach-Zehnder, the signal at the output of this interferometer is independent of the explicit value of the frequency ramp, *i.e.* it is not limited by our *a priori* knowledge of the gravitational acceleration.

The total phase of the interferometer can then be expressed:

$$\Phi^{\text{interferometer}} = T_{\text{Ramsey}}\Big(k_e(\Delta v - gT_{\text{delay}}) - \delta\omega\Big) \tag{2.2.66}$$

By scanning the parameter $\delta\omega$ and determining the value for which the phase shift is 0, one measures the velocity difference between the first and second Ramsey sequence. This behavior justifies the denomination *differential velocity sensor configuration*.

The g sensitivity of this interferometer scales as $k_e T_{\text{Ramsey}} T_{\text{delay}}$, where we find that it is proportional to the space-time area enclosed by the interferometers are, similarly to the Mach-Zehnder case. However, the sensitivity of the Δv measurement scales proportionally with the distance between the two arms $k_e T_{\text{Ramsey}}$.

We can interpret the Ramsey-Bordé measurement process as a comparison between the Doppler effect induced by the atomic external motion ($\Delta v - gt$) and the laser frequency difference ($\delta\omega$) between the two Ramsey sequences. We exhibit here the main difference between the Ramsey-Bordé and Mach-Zehnder, which compares the atomic acceleration to a sweep rate.

However, this signal still depends on the gravitational acceleration. If it is possible to reverse the direction of the velocity transfer, one may finally eliminate the contribution of gravity by combining the output of two interferometers.

Eliminating the contribution of gravitational acceleration from the signal, one meets the condition to be sensitive to a velocity transfer process.

In terms of performance, with typical values $T_{\text{Ramsey}} = 10$ ms, $\delta\phi = 5$ mrad, we get a velocity sensitivity of $\sim 10^{-7}$ m $\cdot$ s^{-1}. In terms of recoil velocity $v_r \sim 1.2$ cm $\cdot$ s^{-1}, this correspond to a 10^{-5} relative sensitivity. In practice, we are able to transfer a thousand atomic recoils in between the interferometer. We are then to expect a relative sensitivity better than 10^{-8} for each measured spectra.

Atomic survival and contrast

Because the Ramsey-Bordé interferometer combines four beam splitters, there are 12 paths[4] at the output of the interferometer. We first reduce this number to 6 by applying at the output of the first Ramsey sequence an optical pulse resonant with atoms in the internal state $|\beta\rangle$, which is the initial intral state. This pulse projects the atoms on the $\left\{ |\alpha\rangle\,,\ |\beta\rangle \right\}$ basis and removes the atoms that were projected onto $|\beta\rangle$. It does not affect the spatial superposition coherence in state $|\alpha\rangle$.

After this pulse, if the pulse areas of the beam splitters were perfectly $\pi/2$, half the initial atoms are removed from the interferometer. They will not be detected simultaneously with the remaining atoms and will not affect the contrast of the fringes. However, when running the differential velocity sensor, we lose by construction half the input atoms.

Let us move along to the computation of the contrast considering pulse area imperfections. When computing the contrast of the Mach-Zehnder interferometer, we wrote the complete output probability formula. Because there are now four pulses in the interferometer, as well as suppressed paths, this approach is cumbersome. We then follow an alternative method:

The idea is to write the projection of the atomic wavefunction on one of the outputs as the sum of the two path dependent amplitudes. For instance: $\langle\alpha|\psi_f\rangle = \boldsymbol{c}^{(A)} + \boldsymbol{c}^{(B)}$.[5] Computing the norm of this coefficient:

$$|\langle\alpha|\psi_f\rangle|^2 = \left|\boldsymbol{c}^{(A)}\right|^2 + \left|\boldsymbol{c}^{(B)}\right|^2 + \left|\boldsymbol{c}^{*(A)}\boldsymbol{c}^{(B)}\right| \cos\left(\arg\left(\boldsymbol{c}^{*(A)}\boldsymbol{c}^{(B)}\right)\right). \tag{2.2.67}$$

From this equation we have $\Phi^{\text{interferometer}} = \arg\left(\boldsymbol{c}^{*(A)}\boldsymbol{c}^{(B)}\right)$, and the contrast $\mathcal{C} = 2\left|\boldsymbol{c}^{(A)}\boldsymbol{c}^{(B)}\right|$.

These coefficients are given by the product of matrix elements of the pulses evolution operator. The specific matrix element depends both on the path and on the pulse index and are given by the matrix (2.2.21). Computing those coefficients, one should furthermore renormalize the wavefunction after the first Ramsey sequence since half of the coherences are removed with a resonant pulse. After some trigonometric simplification, we obtain:

$$\mathcal{C} = \frac{\sin\left(\theta_I\right)\sin\left(\theta_{II}\right)}{1-\cos\left(\theta_I\right)\cos\left(\theta_{II}\right)} \cdot \frac{\sin\left(\theta_{III}\right)\sin\left(\theta_{IV}\right)}{2} \tag{2.2.68}$$

In this equation, we observe that there is an asymmetry between the two Ramsey sequences. The term relative to the second Ramsey sequence is quite alike the

[4] One could expect $2^4 = 16$ paths. This number is reduced due to the recombinations at the interferometer output.

[5] We do not consider here the loss channels.

contrast terms of the Mach-Zehnder. Moreover, its maximum is reached when the pulse are perfect $\pi/2$ and evaluates to $1/2$. This result is expected considering the loss channels of the third pulse.

Concerning the first Ramsey sequence, when $\theta_I = \theta_{II}$, the term evaluates to 1. Indeed, even if not $\pi/2$, when the two first pulses are equilibrated, they only control the number of atoms that are transferred through the Ramsey sequence. Moreover, if we develop the formula around $\pi/2$ for the two pulse area, we find that this term is alike to $\cos\left(\theta_I - \theta_{II}\right)$, confirming the lower contrast sensitivity on the first Ramsey sequence than on the second.

Finally and similarly to the Mach-Zehnder discussion, if the pulse area variation have a common source, the contrast writes $\mathcal{C} = 1 - \delta\theta^2$, which shows that the Ramsey-Bordé interferometer is twice as less sensitive to pulse area variations than the Mach-Zehnder.

2.2.5 Sensitivity function approach: phase noise transfer function and pulses finite duration corrections

Earlier in the development, we discussed the impact of pulse area imperfections and translated their variation into contrast noise. Moreover we were able to show that this noise was not impacting the phase at the output of the interferometer.

However, phase noise contributes directly to the output of the interferometer and we can then anticipate that it is a major source of noise that needs to be controlled.

In order to estimate the sensitivity of our differential velocity sensor with respect to phase noise, we will use the formalism of the *sensitivity function*, developed in the frame of microwave clocks[Dick, 1987]. In this context where the frequency of a local oscillator is compared to a physical frequency, phase noise on the local oscillator may translate into systematic errors that damage the stability and accuracy of the clock. Because the clocks are made out of a Ramsey interrogation, the formalism extends immediately to atom interferometry.

Moreover, we will see that this formalism provides an alternative way to compute the output phase of the interferometer. Finally, our earlier analysis assumed infinitely short optical pulse. This approach will allow us to estimate corrections taking into account the duration of the pulses[6] and conclude on the validity of this approximation.

[6]but maintaining the hypothesis that the coupling Hamiltonian diagonal elements are negligible before its non-diagonal elements

2.2.5.1 Definition

The phase at the output of the differential velocity sensor can be written:

$$\Phi^0 = \phi_{IV} - \phi_{III} - \phi_{II} + \phi_I, \tag{2.2.69}$$

where the phases correspond to the absolute phases of the transitions and no assumptions are made on the atomic trajectories, or on the laser phase behavior. The sensitivity function is defined in the following way. Assume that an infinitely small phase jump $\delta\phi$ is applied to the Raman lasers at a time t. Then the output phase varies and we write the modified value $\Phi^0(\delta\phi, t)$. We can then write the sensitivity function g_ϕ:

$$g_\phi(t) = \lim_{\delta\phi\to 0} \frac{\Phi^0(\delta\phi, t) - \Phi^0}{\delta\phi} \tag{2.2.70}$$

This function is the impulse response of the interferometer phase. It is a real number by construction and finite from a continuity argument. In order to evaluate it, let us assume that $0 < t < T_{\text{Ramsey}}$. Then the phases of the second and following pulses are incremented by $\delta\phi$, such that we have:

$$\Phi^0(\delta\phi, t) = (\phi_{IV} + \delta\phi) - (\phi_{III} + \delta\phi) - (\phi_{II} + \delta\phi) + \phi_I \tag{2.2.71}$$

$$= \Phi^0 - \delta\phi \tag{2.2.72}$$

From such reasoning, we immediately deduce the sensitivity function:

$$g_\phi(t) = \begin{cases} 0 & \text{if} \quad t < 0 \\ -1 & \text{if} \quad 0 < t < T_{\text{Ramsey}} \\ 0 & \text{if} \quad T_{\text{Ramsey}} < t < T_{\text{delay}} \\ 1 & \text{if} \quad T_{\text{delay}} < t < T_{\text{delay}} + T_{\text{Ramsey}} \\ 0 & \text{else} \end{cases}. \tag{2.2.73}$$

We immediately observe that the interferometer is sensitive to phase noise only during the Ramsey sequences and with opposite sign for each of them. Thus, by setting the origin of time at the middle of the interferometer $t = (T_{\text{Ramsey}} + T_{\text{delay}})/2$, the function becomes odd, a property that will be useful.

2.2.5.2 Preliminary treatment

During the operation of the interferometer, the laser phase is not constant with time due to the atomic motion and the laser frequency sweeps. Using the definition of the sensitivity function, we can write the output phase of the interferometer[Cheinet, 2006]:

$$\Phi^0 = \int g_\phi(t) \mathrm{d}\phi(t) = \int_{-\infty}^{\infty} g_\phi(t) \frac{\mathrm{d}\phi}{\mathrm{d}t} \mathrm{d}t. \tag{2.2.74}$$

With the same notations as earlier, we have $\frac{\mathrm{d}\phi}{\mathrm{d}t} = k_e v(t) - \omega(t) = k_e v_0 - \omega_0 - k_e(g - g_0)t$. We compute the integral separately for the two Ramsey sequences. For one sequence:

$$\Phi^{\mathrm{Ramsey}} = \pm \int_0^{T_{\mathrm{Ramsey}}} \frac{\mathrm{d}\phi}{\mathrm{d}t} \mathrm{d}t \tag{2.2.75}$$

$$= \pm \left(T_{\mathrm{Ramsey}}(k_e v_0 - \omega_0) - \frac{k_e(g - g_0)T_{\mathrm{Ramsey}}^2}{2} \right) \tag{2.2.76}$$

We can parametrize the initial conditions as (v_0, ω_0) for the first Ramsey sequence and $(v_0 + \delta v, \omega_0 + \delta\omega)$ for the second, where δv correspond to

$$\delta v = \Delta v - g T_{\mathrm{delay}}. \tag{2.2.77}$$

Lastly, replacing the $\pm$ by the sign of the sensitivity function for each sequence, we find the same earlier result for the output phase of the interferometer (equation (2.2.66)).

In the presence of a sinusoidal perturbation[7] $\phi(t) = \mathcal{A}\cos(\omega t + \psi)$, the sensitivity function gives the phase shift induced by the perturbation:

$$\delta\Phi = -\mathcal{A}\omega\cos(\psi)\int_{-\infty}^{\infty} g_\phi(t)\sin(\omega t)dt, \tag{2.2.78}$$

where the origin of times has been defined such that the sensitivity function is odd, property which was used to eliminate the $\cos(\omega t)$ term from the development. For simplicity, we assume $\psi = 0$.

The above integral is related to the Fourier transform of the sensitivity function $\widetilde{g_\phi}(\omega)$:

$$\widetilde{g_\phi}(\omega) = -2i\int_0^{\infty} \sin(\omega t) g_\phi(t) dt, \tag{2.2.79}$$

where, again, we have taken advantage of the oddness of g_ϕ. We have that the transfer function of the perturbation on the interferometer phase $H(\omega) = |\delta\Phi/\mathcal{A}|$ is given by:

$$H(\omega) = \left|\omega\widetilde{g_\phi}(\omega)\right| \tag{2.2.80}$$

With the input of equation (2.2.73), we find:

$$H(\omega) = 4\left|\sin\left(\frac{\omega T_{\mathrm{Ramsey}}}{2}\right)\sin\left(\frac{\omega T_{\mathrm{delay}}}{2}\right)\right|. \tag{2.2.81}$$

[7]The development of this paragraph is based on the presentation of [Cheinet, 2006].

When $\omega \to 0$, *i.e.* for a constant perturbation, the transfer function tends to 0 as ω^2: the perturbation is canceled over the interferometer. This is not the only case for which it happens:

Let us consider a perturbation at a frequency $f = \omega/(2\pi)$. If the product $f \cdot T_{\text{Ramsey}}$ is an integer, then the accumulated phase over a Ramsey sequence sums up to zero and the perturbation is canceled. If the product $f \cdot T_{\text{delay}}$ is an integer, then the phase of the perturbation at the beginning of both sequences is identical such that the accumulated phase over the Ramsey sequences is also identical. Thanks to the oddness of the sensitivity function, the perturbation is then canceled.

On the other hand, if the considered product are half an integer, then the perturbation phase is whether maximally transmitted by a Ramsey sequence or changes sign over the two sequences. In these cases, the perturbation is fully transmitted to the interferometer output phase.

Product of two oscillating function whose periods are given by the characteristic durations of the interferometers, the transfer function exhibits that a perturbation needs to be out of phase with the interferometer to produce a phase shift. This is indicated by the factor 4 which corresponds to a addition on each pulse.

Finally, the transfer function allows us to evaluate the phase noise at the output of the interferometer as a function of the spectral power density of the input phase noise $S_\phi(\omega)$[Papoulis, 1991]:

$$\sigma^2_{\delta\Phi} = \int_0^\infty \frac{\mathrm{d}\omega}{2\pi} S_\phi(\omega) \left|H(\omega)\right|^2, \tag{2.2.82}$$

where we have taken into account the $\cos(\psi)$ term earlier ignored with $\langle \cos^2(\psi) \rangle = 1/2$.

2.2.5.3 Pulses finite duration

However, the sensitivity function on which we based our analysis is not continuous, which is not physical, and lead us to over estimate the phase noise in equation (2.2.82). In order to make it continuous, we need to refine the above treatment by considering the effect of a phase shift during a light pulse. The transfer function will then present a low-pass filter behavior.

If a phase shift occurs during a light pulse, the associated evolution operator is modified as the product of two evolution operators with different phases. In order to translate this modification into the sensitivity function, we use the complex coefficients associated to each path $\left\{\boldsymbol{c}^{(A)}, \boldsymbol{c}^{(B)}\right\}$ that we used for the study of the interferometer contrast. Using these coefficients we can write the phase of the interferometer: $\Phi^0 = \arg\left(\boldsymbol{c}^{*(A)}\boldsymbol{c}^{(B)}\right)$.

A phase jump during a pulse impacts those coefficients, and we write them with the same notation as the output phase: $\left\{\boldsymbol{c}^{(A)}\left(\delta\phi,t\right),\boldsymbol{c}^{(B)}\left(\delta\phi,t\right)\right\}$. We can write the sensitivity function with respect to those coefficients:

$$g_{\phi}\left(t\right)=\lim_{\delta\phi\to0}\frac{\arg\left(\boldsymbol{c}^{*(A)}\left(\delta\phi,t\right)\boldsymbol{c}^{(B)}\left(\delta\phi,t\right)\boldsymbol{c}^{*(A)}\boldsymbol{c}^{(B)}\right)}{\delta\phi}. \tag{2.2.83}$$

Thanks to the limit of $\delta\phi$ to 0, we can limit the calculation to the first order in $\delta\phi$. In particular, at this order and using the finite and real properties of the sensitivity function, we have:

$$\boldsymbol{c}^{*(A)}\left(\delta\phi,t\right)\boldsymbol{c}^{(B)}\left(\delta\phi,t\right)\boldsymbol{c}^{*(A)}\boldsymbol{c}^{(B)}=\mathcal{B}\left(1+ig_{\phi}\left(t\right)\delta\phi\right)+\mathcal{O}(\delta\phi^{2}), \tag{2.2.84}$$

where $\mathcal{B}$ is a real number, and we have immediately identified the sensitivity function out of the development.

We should now compute the modified coefficients. We start by computing the evolution operator associated with a pulse defined by an area θ during which a phase jump occurs. Its computation is based on the combination of two pulses with pulse areas θ' and $\theta-\theta'$ and phases ϕ and $\phi+\delta\phi$. With the input of equation (2.2.21), and at the order one in $\delta\phi$:

$$\begin{aligned}&U^{\text{phase jump}}(\theta,\theta',\phi,\delta\phi)=U(\theta-\theta',\phi+\delta\phi)\cdot U(\theta',\phi) \qquad (2.2.85)\\ &=\begin{pmatrix}\cos(\frac{\theta}{2})\left(1-\frac{i\delta\phi}{2}\left(1-\cos(\theta')-\sin(\theta')\tan(\frac{\theta}{2})\right)\right) & -ie^{-i\phi}\sin(\frac{\theta}{2})\left(1-i\delta\phi\frac{\cos(\theta'/2)\sin((\theta-\theta')/2)}{\sin(\theta/2)}\right)\\ -ie^{i\phi}\sin(\frac{\theta}{2})\left(1+i\delta\phi\frac{\cos(\theta'/2)\sin((\theta-\theta')/2)}{\sin(\theta/2)}\right) & \cos(\frac{\theta}{2})\left(1+\frac{i\delta\phi}{2}\left(1-\cos(\theta')-\sin(\theta')\tan(\frac{\theta}{2})\right)\right)\end{pmatrix}\end{aligned}$$

By treating the problem pulse per pulse, selecting the appropriate matrix elements and propagating the phase jump on the following transitions, one obtains the sensitivity function as a function of θ'. For each pulse:

$$g_{\phi}(\theta')= \tag{2.2.86}$$

$$\begin{cases}-1+\sin(\theta_{I}-\theta')/\sin(\theta_{I}) & \text{if the phase jump occurs during the first pulse}\\ -1+\sin(\theta')/\sin(\theta_{II}) & \text{" " " " " " " second "}\\ 1-\sin(\theta_{III}-\theta')/\sin(\theta_{III}) & \text{" " " " " " " third "}\\ 1-\sin(\theta')/\sin(\theta_{IV}) & \text{" " " " " " " forth "}\end{cases}$$

We now need to unify this equation and equation (2.2.73). The limits $\theta'\to0$ and $\theta'\to\theta$ ensure the continuity of the sensitivity function. However, this computation was made under the infinitely short pulse formalism, such that no explicit time dependence appear.

We assume that the four pulses share the same duration τ_p, such that θ' can be rewritten

$$\theta' = \theta_i \frac{t}{\tau_p} \quad \text{for } i = I, II, III \text{ or } IV \tag{2.2.87}$$

for each pulse. We can now write the sensitivity function for all times, which is plotted on figure (2.6):

$$g_\phi(t) = \begin{cases} 0 & \text{if} \quad t < 0 \\ -1 + \frac{\sin(\theta_I(1-t/\tau_p))}{\sin(\theta_I)} & \text{if} \quad 0 < t < \tau_p \\ -1 & \text{if} \quad \tau_p < t < T_{\text{Ramsey}} + \tau_p \\ -1 + \frac{\sin(\theta_{II} t/\tau_p)}{\sin(\theta_{II})} & \text{if} \quad T_{\text{Ramsey}} < t < T_{\text{Ramsey}} + \tau_p \\ 0 & \text{if} \quad T_{\text{Ramsey}} + \tau_p < t < T_{\text{delay}} \\ 1 - \frac{\sin(\theta_{III}(1-t/\tau_p))}{\sin(\theta_{III})} & \text{if} \quad T_{\text{delay}} < t < T_{\text{delay}} + \tau_p \\ 1 & \text{if} \quad T_{\text{delay}} + \tau_p < t < T_{\text{delay}} + T_{\text{Ramsey}} \\ -1 + \frac{\sin(\theta_{IV} t/\tau_p)}{\sin(\theta_{IV})} & \text{if} \quad T_{\text{delay}} + T_{\text{Ramsey}} < t < T_{\text{delay}} + T_{\text{Ramsey}} + \tau_p \\ 0 & \text{else} \end{cases} \tag{2.2.88}$$

Now that we have written an explicit duration for the laser pulses, we should notice that the phase of the transition is a dynamical parameter and the evolution operator of equation (2.2.21) cannot be used directly. Here, the sensitivity function reveals itself as a powerful tool as this framework allows to take into account phase variations all along the interferometer, and in particular during the pulses. Moreover, the behavior of the sensitivity function is not trivial with the pulse area. In particular, when it exceed $\pi/2$, the function changes sign during the pulses. As a consequence, we need to evaluate the effect of pulse area imperfections in this context.

Taking into account the modification induced by the pulses finite duration on the sensitivity function, we compute the output phase of the interferometer as earlier by integrating the product of the sensitivity function and the time derivative of the phase and obtain:

$$\begin{aligned} &\Phi^{\text{interferometer}} = \\ &\Big(k_e \delta v - \delta\omega\Big)\Big(T_{\text{Ramsey}} + \tau_p\Big(1 + f(\theta_{IV}) + f(\theta_{III}) - f(\theta_{II}) - f(\theta_I)\Big)\Big) \\ &-k_e\Big(g - g_0\Big)\tau_p\Big(\Big(T_{\text{Ramsey}}\left(f(\theta_{IV}) - f(\theta_{II})\right) \\ &\qquad + \tau_p\left(h(\theta_{IV}) - h(\theta_{III}) - h(\theta_{II}) + h(\theta_I)\right)\Big)\Big) \end{aligned} \tag{2.2.89}$$

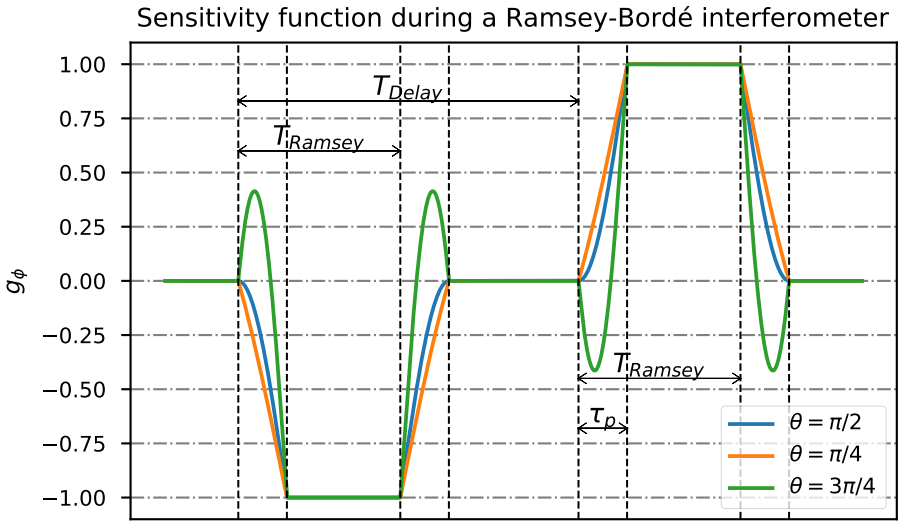

Figure 2.6: Plot of the phase sensitivity function for different pulse areas. The different time scales indicated with double arrows and no proper origin of times is defined. Indeed, depending on the calculation, we will either need to make the function odd (Fourier transform) or to split the function in two part, one for each Ramsey sequence (interferometer output phase). The ratio τ_p/T_{Ramsey} as been exaggerated for visualization purposes.

The computation is similar to the derivation of equation (2.2.76) and of the correction functions f and h are given by:

$$f(\theta) = \frac{cos(\theta) - 1}{\theta \sin(\theta)} \tag{2.2.90}$$

$$h(\theta) = \frac{\theta \cos(\theta) - 1}{\theta^2 \sin(\theta)} \tag{2.2.91}$$

Around $\theta = \pi/2$, we have $|f(\theta)|, |h(\theta)| \lesssim 1$. If the pulse areas remain constant along the interferometer, the f and h terms cancel, and the consideration of the pulses duration is reduced to a modification of the fringes periods through $T_{\text{Ramsey}} \leftarrow T_{\text{Ramsey}} + \tau_p$ which does not change the central fringe condition. Moreover, we typically have in our experiment $\tau_p/T_{\text{Ramsey}} \sim 10^{-2}$, such that this correction cannot be considered large.

Variations of the pulse area impacts the output phase in two different ways. First the term that is factor of $k_e\delta v - \delta\omega$ does not affect the position of the central fringe, and produce negligible displacements typically three order of magnitudes below the dominant term in T_{Ramsey}.

Secondly the term factor of $k_e(g-g_0)\tau_p$ produces an absolute phase shift. The dominant term is the one in T_{Ramsey}, such that estimating this term gives an order of magnitude of the phase shift. We assume that we can write all pulse areas as $\theta_\iota = \theta + \delta\theta_\iota$ with $\theta \sim \pi/2$. We then develop the expression around θ and find

$$\delta\Phi^{\text{interferometer}} = k_e(g-g_0)\tau_p T_{\text{Ramsey}} \left(\delta\theta_{IV} - \delta\theta_{II}\right) f_c(\theta), \tag{2.2.92}$$

where f_c is derived from f and evaluates to $\sim 10^{-1}$ around $\pi/2$. With $k_e g \sim 2\pi \cdot (25\ \text{MHz}\cdot\text{s}^{-1})$, and typical values $T_{\text{Ramsey}} = 10$ ms and $\tau_p = 200\ \mu$s, we have:

$$\delta\Phi^{\text{interferometer}} \sim 10 \cdot \pi \frac{g-g_0}{g} \left(\delta\theta_{IV} - \delta\theta_{II}\right). \tag{2.2.93}$$

The magnitude of this expression is controlled by the *a priori* knowledge of the gravitational acceleration. With $g - g_0 \sim 10^{-7} g$, it is completely negligible.

The analysis based on the sensitivity function allows to take into account the finite duration of the laser pulses. Apart from a variation of the fringes period, we exhibited the importance of controlling precisely the gravity compensation frequency ramp. This aspect was absent from the path integral based treatment. The precision of this control hence gives a criteria for the viability of neglecting the pulse duration in the treatment of the differential velocity sensor. For a phase shift < 1 mrad, and pulse area fluctuations $\sim 10\%$ around $\pi/2$ pulse areas, we find that the frequency ramp should be exact within a few 10^{-4} relative precision.

In our experimental conditions this precision is easily obtained, such that the criteria is met and the approximation is valid.

Let us move now to the transfer function of the interferometer with respect to phase noise. For simplicity, we assume that the four pulses have a common pulse area of $\pi/2$. As a consequence, the sensitivity function can be made odd and we can focus the discussion on the impact of taking the pulse finite duration into account.

As earlier, through the computation of the Fourier transform of the sensitivity function, we deduce the interferometer transfer function:

$$\begin{aligned} H(\omega) =& \frac{4\pi}{\left|4\tau_p^2\omega^2 - \pi^2\right|} \\ &\times \left|2\tau_p\omega\cos\left(\omega\frac{T_{\text{Ramsey}}-\tau_p}{2}\right) - \pi\sin\left(\omega\frac{T_{\text{Ramsey}}+\tau_p}{2}\right)\right| \\ &\times \left|\sin\left(\omega\frac{T_{\text{delay}}}{2}\right)\right|, \end{aligned} \tag{2.2.94}$$

where we find the infinitely short pulses expression of equation (2.2.81) when substituting τ_p by 0. Moreover, we find the infinitely short pulse result that a

constant perturbation cancels over the interferometer ($H(\omega) \sim \omega^2$, for $\omega \to 0$), as shown in figure (2.7).

Interpreting this equation from bottom to top, we first observe that the term associated to T_{delay} is unchanged with respect to the infinitely short pulse expression. This term cancels perturbations that are in phase with the two Ramsey sequences delay, which is not modified when accounting for the pulse duration.

However, the cancellation on a Ramsey sequence has been modified to be given by a sum of two oscillating terms whose period are now given by the duration between the pulses $T_{\text{Ramsey}} - \tau_p$ and to duration of the sequence with pulses $T_{\text{Ramsey}} + \tau_p$. This term exhibit that the phase sensitivity during a light pulse is not trivial when the perturbation is sinusoidal. This non trivial behavior was observed experimentally on the Mach-Zehnder interferometer in[Cheinet, 2008].

Finally, the top term seems to indicate a resonance at $\omega = \pi/(2\tau_p) = \Omega$, the Rabi frequency which is not observed on the plot. Indeed, at this point, the second term tends to 0. Combined, the two terms tend to a finite value, such that the transfer function evaluates:

$$H(\Omega) = \left|2\sin\left(\frac{\pi}{4\tau_p}(T_{\text{Ramsey}} + \tau_p)\right) - \pi\cos\left(\frac{\pi}{4\tau_p}(T_{\text{Ramsey}} + \tau_p)\right)\right| \times \left|\sin\left(\frac{\pi T_{\text{delay}}}{4\tau_p}\right)\right|. \tag{2.2.95}$$

At frequencies large compared to T_{Ramsey}^{-1} and T_{delay}^{-1}, the transfer function oscillates such that its behavior is better captured by taking its mean with respect to the trigonometric functions whose argument are whether ωT_{Ramsey} or ωT_{delay}. It is easily done by evaluating the square of the transfer function and we obtain:

$$H^2(\omega) = \frac{4\Omega^2\left(\Omega^2 + \omega^2 - 2\Omega\omega\sin\left(\frac{\pi\omega}{2\Omega}\right)\right)}{\left(\omega^2 - \Omega^2\right)^2}, \tag{2.2.96}$$

where, because it is the only duration parameter left, we have replaced τ_p by the Rabi frequency Ω which produces a simpler formula. From this equation, we deduce that the transfer function as a first order low pass filter. Indeed the high frequency limit of the above equation gives:

$$H(\omega) \underset{\omega\to\infty}{\sim} \frac{2\Omega}{\omega}. \tag{2.2.97}$$

When the frequency of the perturbation is large before the Rabi frequency, the effect of the perturbation is averaged many times over a single light pulse and therefore is not translated on the atomic wavefunction.

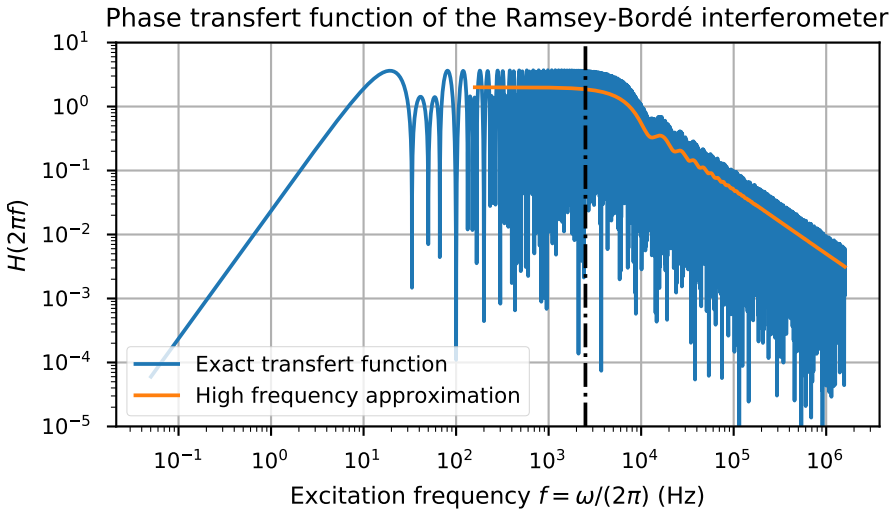

Figure 2.7: Plot of the Ramsey-Bordé phase transfer function (equation (2.2.94)) for $T_{\text{Ramsey}} = 20$ ms, $T_{\text{delay}} = 30$ ms and $\tau_p = 100$ μs. In blue, the exact function which display an oscillating figure. In orange, the average value that captures the high frequency behavior (equation (2.2.96)). The black vertical dashed dotted line marks $\omega = \Omega$.

2.2.6 Conclusion

We have developed our framework to model atom interferometry. This development led us to exhibit an effective Lagrangian that represents well the atomic trajectories including the velocity kicks induced by infinitely short light pulses. This formalism allows us to compute easily the effect of perturbations that can be modeled through perturbative Lagrangians.

Moreover, this effective Lagrangian exhibits the origin of the interferometric signal: *the laser phases at the light pulses moments*. These phases are controlled by two quantities, the atomic motion and the frequency control of the Raman lasers necessary to ensure the resonance condition of the pulses.

The former is governed by the physics of the system while the latter is an experimental parameter. Through its control, one operates the interferometer in order to determine the central fringe and extract information on the physical properties of the system. In particular, we discussed the Ramsey-Bordé interferometer in differential velocity sensor, paving the way to a recoil velocity measurement technique.

Finally, we discussed a complementary formalism to the Lagrangian mechanics treatment: the sensitivity function. This formalism enabled the determination of the behavior of the Ramsey-Bordé interferometer with respect to phase noise. In particular, its frequency cutoff is determined by the duration of the light pulses.

Moreover, the Lagrangian formalism was very effective since we considered infinitely short light pulses which allows us to model their effect as Dirac deltas velocity kicks associated with a phase shift. The sensitivity function formalism gave us the tools to evaluate the validity of the approximation and we showed that the criteria was easily verified in our experimental conditions.

Our treatment relies on the hypothesis that the diagonal terms of the total Hamiltonian are negligible with respect to its coupling terms. The effect of those diagonal terms is represented in the evolution operation (equation 2.1.32). The pulse areas are modified, but as we stated this does not impact the central fringe condition and produces small variations of the interferometer contrast. However, they also induce a phase shift whose physics is not straightforward. Their related study is postponed to section 4.2.

Finally, our toolbox for the recoil velocity measurement is not complete yet as we did not treat our method to transfer atomic recoils. This constitutes the next part of this dissertation.

2.3 Bloch Oscillations

The Ramsey-Bordé interferometer in differential velocity sensor configuration being our tool to measure the transferred velocity to the atoms in between the two Ramsey sequences, we need a tool to transfer a well defined number of atomic recoils.

One of the simplest solution we could imagine is multiple counterpropagating Λ transitions with atoms remaining in the same internal state. This would require two lasers whose frequency difference would be governed by Doppler effect ($\sim$ 30 kHz). At this frequency difference, and if we assume coherence between them, the laser beams would form a moving optical lattice.

We have displayed in figure (2.8) an energy momentum diagram of such a process. By applying a succession of laser pulses with incrementing frequency difference, one can transfers recoils by a succession of *Bragg* π pulses. This technique has been used to realize atom interferometers with a large enclosed space-time area using sequential multi-photon Bragg transitions as beam splitters[Chiow, 2011].

Alternatively, the principle of *Bloch Oscillations* (BO) is to trap the atoms in the optical lattice and linearly chirp the frequency difference between the two

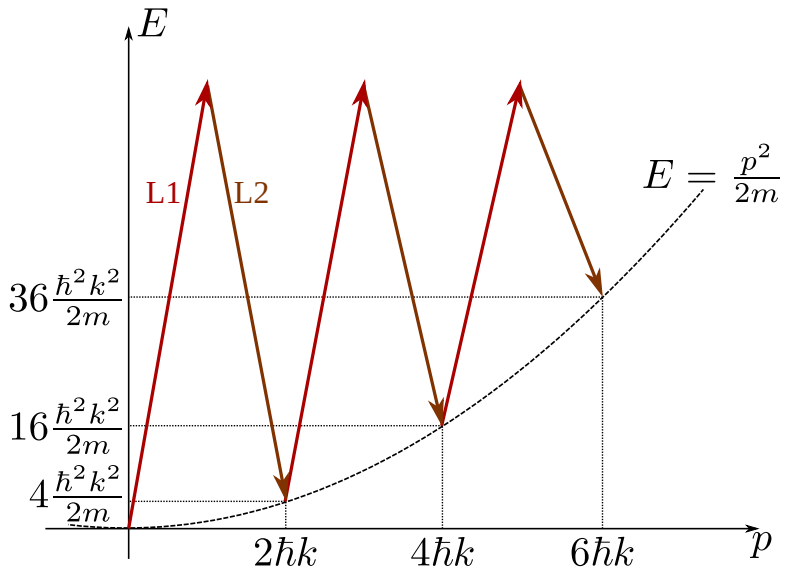

Figure 2.8: Energy momentum diagramm of repeated Raman transitions in the same internal state.

lasers that drive the lattice. The velocity transfer is then based on an adibatic passage and reaches higher efficiency.

We will first detail the potential induced by the optical lattice on the atoms, and write the eigenstates of the problem (known as the Bloch states). We will then present a treatment that takes into account the chirping of the lasers and describe the velocity transfer mechanism.

This development is inspired by previous treatments written in our team[Cadoret, 2008a; Cladé, 2015]. We refer the reader to these references for more details.

2.3.1 Optical lattice potential

We have seen when studying Raman transitions that detuned optical fields displace the atoms ground states energy levels through the non-resonant coupling mechanism. One can show[Grimm, 2000] that the light shift is given as a function of the laser intensity:

$$V(\vec{r}) = \frac{3\pi c^2}{2\omega_{\text{atom}}^3}\frac{\Gamma}{\Delta}I(\vec{r}), \tag{2.3.1}$$

where ω_{laser} is the frequency of the driving laser and the sign of the detuning $\Delta = \omega_{\text{laser}} - \omega_{\text{atom}}$ controls the sign of the potential. If the laser is blue detuned, *i.e* $\omega_{\text{laser}} > \omega_{\text{atom}}$, then the light shift behaves as a repulsive potential and the atoms are trapped at the minima of intensity. Inversely, a red detuned laser traps

the atoms at the intensity maxima. In our experiment, we use a blue detuned lattice to limit scattering processes with $\Delta \simeq 40$ GHz.

Studying two counterpropagating coherent monochromatic plane waves with scalar electric fields, with identical linear polarizations so that we can ignore them:

$$E^{\pm} = E_0 \exp\Big(i(\pm kz - \omega t + \phi)\Big), \tag{2.3.2}$$

the intensity pattern they produce presents a standing wave interference pattern

$$I(x, y, z) = I_0 \cos^2(kz)\,. \tag{2.3.3}$$

This laser configuration creates a one dimensional sinusoidal potential with spatial period $d = \lambda/2$.

The height of the lattice potential V_0 given by

$$V_0 = \frac{3\pi c^2}{2\omega_{\text{atom}}^3}\frac{\Gamma}{\Delta}4I_0 \tag{2.3.4}$$

is usually compared to the recoil energy

$$E_r = \frac{\hbar^2 k^2}{2m}, \tag{2.3.5}$$

which is the characteristic energy of the system as it corresponds to the kinetic energy acquired upon the absorption of a single photon.

When the *weak binding limit* $V_0 \ll 4E_r$ condition is fulfilled, the lattice potential can be treated as a perturbation to the free case.

Alternatively, in the *tight binding limit* when $V_0 \gg 4E_r$, the atoms are trapped in the potential wells.

2.3.2 States in a periodic potential

Let us study the problem addressed by F. Bloch in 1928[Bloch, 1928] which corresponds to the description of the state of a particle in a periodic potential in the frame of quantum mechanics. The case of an atom trapped in an optical lattice is included in the problem.

We restrict ourselves to the one-dimensional description of the system. Its Hamiltonian is given by:

$$H = \frac{p^2}{2m} + V(z) \tag{2.3.6}$$

$$\text{with } V(z) = V(z + d), \tag{2.3.7}$$

where d is the periodicity of the potential.

The spatial translation operator of the quantity d given by

$$\hat{T}_d = e^{i\frac{\hat{p}d}{\hbar}} \tag{2.3.8}$$

commutes with the above Hamiltonian according to Bloch theorem. As such, we can search eigenstates of the Hamiltonian that are also eigenstates of the translation operator.

Such states can be written as *Bloch waves* which are the product of a plane wave and of a d-periodic function:

$$\langle z|\Psi_q\rangle = e^{iqz} \cdot u_q(z) \tag{2.3.9}$$

$$\text{with } u_q(z) = u_q(z+d) \tag{2.3.10}$$

and where q is the quasi-momentum of the particle in the lattice. To avoid double counting of states, we restrict q to $\left]-\frac{\pi}{d}, \frac{\pi}{d}\right]$, which corresponds to the first Brillouin zone.

Evaluating the product of the Hamiltonian on such a state in z representation, we obtain the condition on u_q such that $|\Psi_q\rangle$ is an eigenstate of the periodic Hamiltonian:

$$H_q u_q(z) = \mathcal{E}_q u_q(z) \tag{2.3.11}$$

$$\text{with } H_q = \frac{(\hat{p}+\hbar q)^2}{2m} + V(z) \tag{2.3.12}$$

For a given value of q, because $u_q(z)$ is periodic, this equation provides an infinite discrete series of solutions $\left\{\mathcal{E}_n(q), u_{n,q}(z)\right\}$. For each solution, we write the quantum state: $|n,q\rangle$.

We can then diagonalize numerically the Hamiltonian and obtain its energy spectrum[Dalibard, 2013]. The result of such a procedure is displayed on figure (2.9). The spectrum is formed by *energy bands* well known in solid state physics. In particular, in the weak binding limit, we observe that the lattice potential only acts on the edges of the first Brillouin zone where the degeneracy between the states $|p = \pm\hbar k\rangle$ is lifted by the two photons coupling.

2.3.3 Principle of Bloch Oscillations

The Hamiltonian of Bloch Oscillations[Zener, 1934] is given by adding a force F to the Hamiltonian (2.3.6):

$$H = \frac{p^2}{2m} + V(z) - Fz \tag{2.3.13}$$

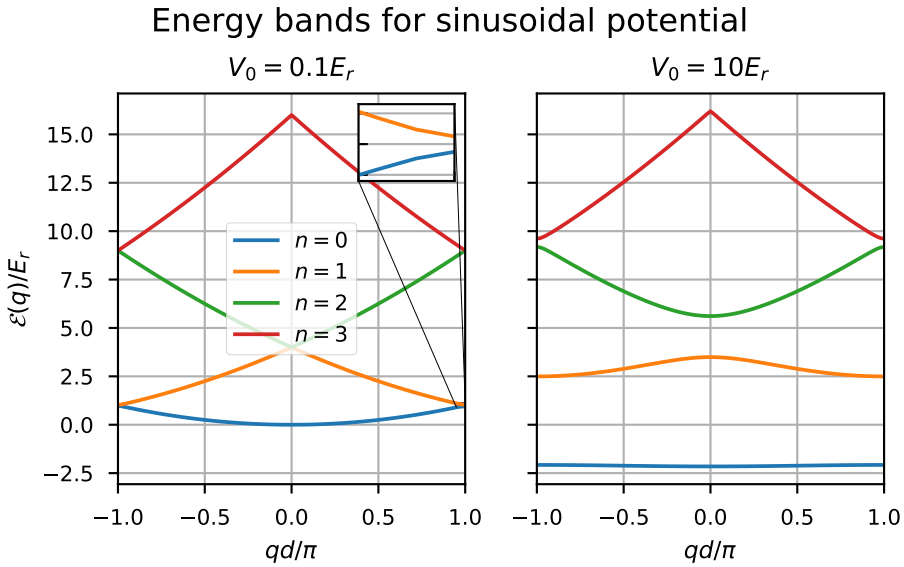

Figure 2.9: Energy spectrum of a particle trapped in a blue detuned lattice for two potential heights. We have reduced the horizontal axis to the first Brillouin zone.

With atom trapped in an optical lattice in vertical configuration, gravitational acceleration drives this Hamiltonian with $F = -mg$. Alternatively, to implement Bloch Oscillations, we chirp linearly the lasers frequency in opposite directions so that the two photons wavevector remains constant one obtains from equation (2.3.2):

$$E^{\pm} = E_0 \exp\Big(i(\pm(k \pm \delta\omega(t)/c)z - (\omega \pm \delta\omega(t))t + \phi)\Big), \tag{2.3.14}$$

where $\frac{\mathrm{d}\delta\omega}{\mathrm{d}t}$ is the chirping rate. We then obtain the interference pattern:

$$I = I_0 \cos^2\left(kz - \delta\omega(t)t\right), \tag{2.3.15}$$

from which one creates a moving optical lattice at a constant acceleration a:

$$a = \frac{d}{\pi}\frac{\mathrm{d}\delta\omega}{\mathrm{d}t}. \tag{2.3.16}$$

The frame where the lattice is at rest is not inertial. As such the Hamiltonian in this frame is given by the equation (2.3.13) with $F = ma$.[8]. Using this chirping principle, one can compensate the motion of the free falling atoms by setting

[8]The transformation that links the Hamiltonian in the laboratory frame written using the optical potential of equation (2.3.15) and the Hamiltonian in the frame in which the lattice is at rest is not trivial. It is detailed in [Cadoret, 2008a].

$a = -g$ and also take gravity into account during the acceleration of the lattice. This compensation is used on the experiment when performing BO.

The Hamiltonian (2.3.13) is no longer periodic. However, the commutator between the Hamiltonian and the translation operator evaluates to

$$[H, \hat{T}_d] = Fd\hat{T}_d, \tag{2.3.17}$$

from which one can show that the wavefunction of the atom can be described with wavefunctions similar to Bloch states:

$$\langle z|\Psi(t)\rangle = e^{iq(t)d}u(z,t), \tag{2.3.18}$$

where $u(z,t)$ is a periodic function of z with period d, and the quasi-momentum obeys to:

$$q(t) = q_0 + \frac{Ft}{\hbar}. \tag{2.3.19}$$

This equation remains valid regardless of the lattice height or of the strength of the acceleration. After a duration:

$$\tau_B = \frac{\hbar}{Fd}, \tag{2.3.20}$$

we have

$$q(\tau_B) - q(0) = 2\frac{\pi}{d}, \tag{2.3.21}$$

which corresponds to the same quasi-momentum in the first Brillouin zone.

The principle of Bloch Oscillations is represented in figure (2.10). An atomic wavefunction is loaded in the first energy band of the lattice:

$$|\Psi(0)\rangle = |0, q_0\rangle\,. \tag{2.3.22}$$

and follows adiabatically this energy band. The adiabatic condition yields an upper bound for the lattice acceleration[Ben Dahan, 1997]:

$$a \ll a_0\frac{\pi}{64}\left(\frac{V_0}{E_r}\right)^2 \quad \text{in the weak binding limit} \tag{2.3.23}$$

$$a \ll a_0\sqrt{2}\left(\frac{V_0}{E_r}\right)^{3/4} \text{ in the tight binding limit,} \tag{2.3.24}$$

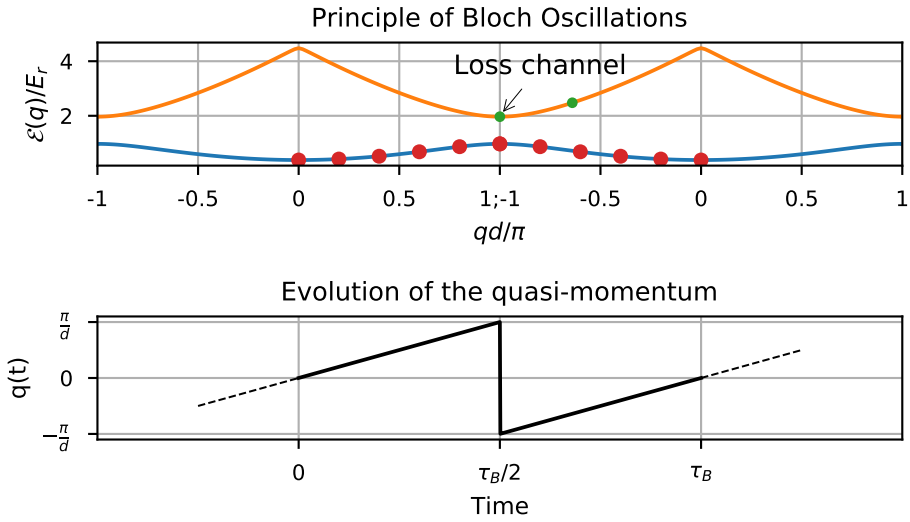

Figure 2.10: Top: band structure on two concatenated first Brillouin zones. Red dots: evolution of the state quasi-momentum with time, which reads from left to right. Green dots: interband transition which is a loss channel. Bottom: Evolution of the quasi-momentum in the first Brillouin zone. The dashed lines are placed for visualization.

where $a_0 = \hbar^2 k^3/m^2$ is a natural acceleration built from the system parameters and evaluates to 278 m·s^{-2} for ^{87}Rb. With our typical lattice depth $V_0 \sim 80E_r$, in the tight binding limit, we obtain a critical acceleration of $\sim 10^4$ m·s^{-2}.

If the adiabatic condition is respected, the duration τ_B represents the duration after which the system is back in its initial state, which justifies the term *Oscillations*. In the frame of the accelerated lattice, an atom initially in the first band $n = 0$ remains in this band, which means that the atom follows the lattice. In the laboratory frame, the atom is then accelerated through a two photon process, and it performed a Bloch Oscillation.

Experimentally, we choose the duration of one Bloch Oscillation $\tau_B \sim 12$ μs. As the atom is kicked by two atomic recoils during this duration, it corresponds to an acceleration $a = 2\hbar k/m\tau_B \sim 9.8 \cdot 10^2$ m·s^{-2} which is one order of magnitude below the critical acceleration.

Let us rapidly discuss the loss mechanism through interband transitions. In the weak binding limit, the optical lattice potential induces an avoided crossing at the edges of the Brillouin zone, where the interband transitions then preferentially

occur, as the gap between bands is minimal. The losses are then well captured through the Landau-Zener formula.

In the tight binding limit, the energy bands are almost flat (see figure (2.9, right)) such that the above analysis does not hold. Instead the efficiency is captured through a numerical simulation of the process. This work has been realized in our team[Cladé, 2017], and we comment it in the next section. In this regime, the gap between the band is higher and the adiabaticity criterion allows us to use stronger acceleration.

2.3.4 Bloch Oscillations in the tight binding regime

Because the lattice can only couple states separated by $2\hbar k$, one can show[Cadoret, 2008b] that a Bloch state can be decomposed on the plane wave basis $|\hbar q + 2l\hbar k\rangle$, where the l-s are integers. For example, in the first Bloch band:

$$|0, q\rangle = \sum_l \widetilde{\Phi}_0\Big(\hbar q + 2l\hbar k\Big) \, |\hbar q + 2l\hbar k\rangle \,, \tag{2.3.25}$$

The decomposition $\widetilde{\Phi}_0$ is not straightforward and is linked to the Wannier representation of the lattice eigenstates[Wannier, 1937; Dalibard, 2013]. In the following, we denote $\widetilde{\Phi}_0$ as the *Wannier function in momentum space*.

In the absence of a lattice ($V_0 = 0$), the Wannier function in momentum space evaluates to 1 in the first Brillouin zone and 0 else where. In the tight binding limit, the potential wells can be approximated by harmonic oscillators with frequency $\omega = 2\sqrt{|V_0|E_r}/\hbar$ and the Wannier function in momentum space is then proportional by the p-representation of the ground state of the harmonic oscillator:

$$\widetilde{\Phi}_0(p) \propto \left(\frac{1}{\pi m\hbar\omega}\right)^{1/4} \exp\left(-\frac{p^2}{2m\hbar\omega}\right). \tag{2.3.26}$$

As the initial state of the atom presents a single momentum component initially, it would be loaded in a superposition between bands if the lattice were to be turned on abruptly. Alternatively, we can increase linearly the lattice potential so that the atomic wavefunction follows adiabatically the first energy band $n = 0$. The evolution of the wavefunction has been represented in figure (2.11).

The duration τ of the linear ramp is constrained by the adiabatic condition that we obtain from[Ben Dahan, 1997]:

$$\tau \gg \frac{1}{32\sqrt{2}} \frac{\hbar}{E_r} \frac{V_0}{E_r} \qquad \text{in the weak binding limit} \tag{2.3.27}$$

$$\tau \gg \frac{1}{16\sqrt{2}} \frac{\hbar}{E_r} \left(\frac{E_r}{V_0}\right)^{1/2} \text{in the tight binding limit,} \tag{2.3.28}$$

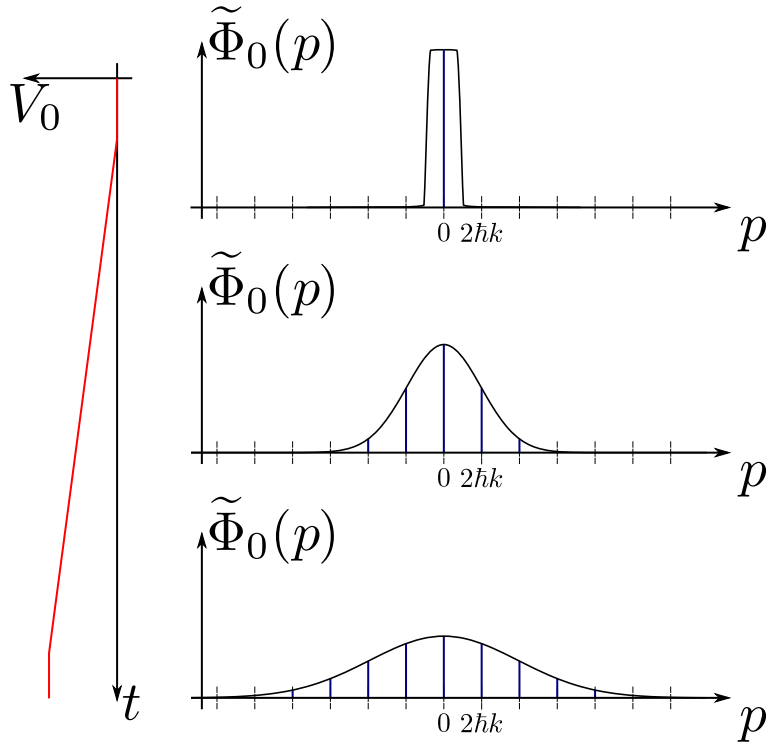

Figure 2.11: Adiabatic loading to the first Bloch band through linearly increase of the lattice potential from top to bottom. In red, linear ramp of the lattice height. In blue, momentum components of the wavefunction.
The figure can also be read from bottom to top with a time reversal and then represents the unloading of the atomic wavefunction from the lattice.
The Wannier functions have not been precisely computed and are illustrations of the concept.

Both criteria depend on the typical duration $\hbar/E_r \sim 42$ μs for Rubidium atoms. The dependence in V_0 changes with the binding limit, such that we estimate the duration at $V_0 = 4E_r$ and obtain 93 μs from the tight binding limit condition. During the loading, the optical lattice is not at rest in the laboratory frame but mimics the gravitational acceleration. We set the loading duration at 200 μs, by optimizing the unloading process (see below).

After the loading is completed, the acceleration is turned on and the quasi-momentum obeys equation (2.3.19), such that the state given by equation (2.3.25) evolves as:

$$|0, q(t)\rangle = \sum_l \widetilde{\Phi}_0\Big(\hbar q + Ft + 2l\hbar k\Big)\, |q + Ft + 2l\hbar k\rangle\,. \tag{2.3.29}$$

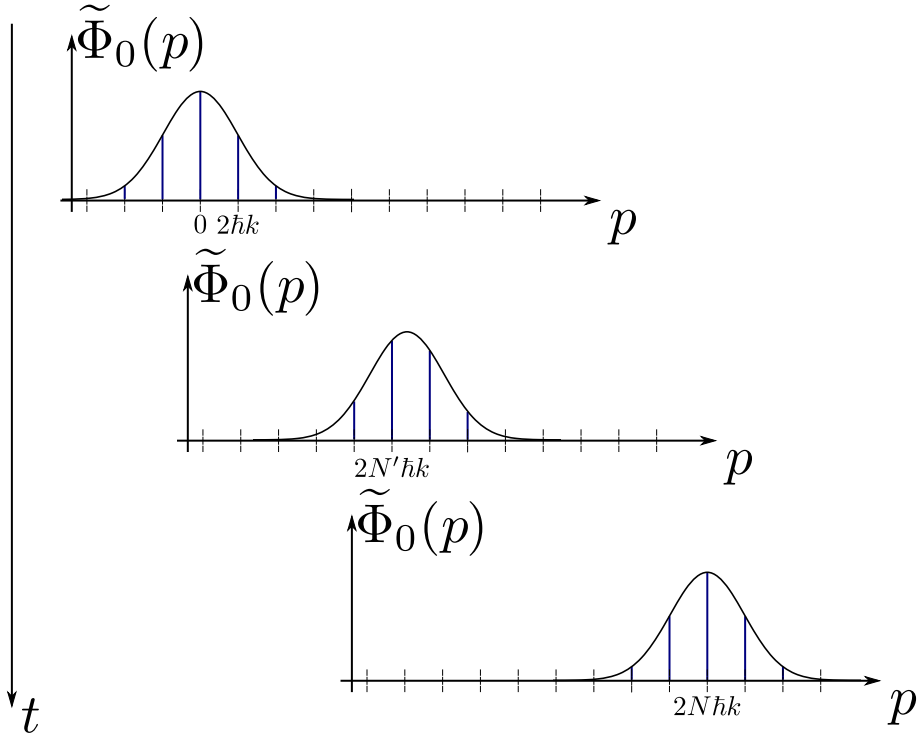

Figure 2.12: Evolution of the Bloch state during the acceleration through its decomposition on the plane wave basis. Top: after the adiabatic loading. Middle: during the acceleration. Bottom: after the acceleration, beginning of the adiabatic unloading.
The width of the Wannier function in momentum space as been artificially reduced. The horizontal displacements indicate that the origin of the horizontal axis is shifted towards increasing p from top to bottom.

The evolution of the wavefunction is represented on figure (2.12). The teeth components of the wavefunction are unchanged with the evolution, but the amplitude of each contribution varies accordingly with the evolving Wannier function.

Our team studied numerically the acceleration process in [Cladé, 2017] where they computed the evolution operator associated with one Bloch Oscillation using the time-independent Hamiltonian from equation (2.3.13):

$$U = \exp\left(-\frac{iH\tau_B}{\hbar}\right), \tag{2.3.30}$$

where the Hamiltonian is given by equation (2.3.13). An eigenstate of this operator with an eigenvalue of modulus 1 performs a Bloch Oscillation without losses. This study showed that in the tight binding limit the Bloch state is actually not an

eigenstate of the evolution operator and as a consequence is not optimal with respect to losses by interband transitions. The interpretation of this result is that when the acceleration starts, the local minima of the potential are slightly shifted because of the Fz term. Because of this, the trapped atoms exhibit a micro-motion at the bottom of the wells. Experimentally, we solve this issue by applying a phase shift to the laser beams during the acceleration, such that the minima with and without acceleration overlap.

At the end of the acceleration, *i.e.* after a duration $T_B = N\tau_B$, the wavefunction has been translated in momentum space by $2N\hbar k$. We then unload the atoms from the lattice with a linearly intensity ramp which is the time reverse of the loading ramp. The adiabatic unloading maps the final Bloch states on a single momentum component. It is by minimizing the number of atoms at $\pm 2\hbar k$ that we optimized the loading/unloading duration at 200 μs. These velocity components were observed using velocity selective Raman transitions.

2.3.5 Application to the h/m measurement

The usefulness of Bloch Oscillations comes from two properties

1. It performs a coherent acceleration, *i.e.* without scattering, such that they can be embedded in an atom interferometer

2. Their efficiency have been estimated to 99.97% per recoil[Cladé, 2006]. The limitation to this efficiency come from spontaneous emission and interband transitions. Nevertheless, it corresponds to an 86% survival probability over a 500 BO process.

As a consequence, we use them as the process in between the Ramsey sequences of the differential velocity sensor (section 2.2.4). The velocity transfer is given by:

$$\Delta v = 2N_B \frac{\hbar k_B}{m}, \tag{2.3.31}$$

where we denote the BO related quantities by the subscript B. The parameter N is well known, as it is controlled by the duration of one BO τ_B and the total duration of the acceleration T_B. Typically, for $N_B = 500$ and $\tau_B = 12$ μs, we have $T_B = 6$ ms, such that BO can be integrated in an atom interferometer. As a consequence, we obtain a signal that is proportional to h/m (gravity excluded) with a proportionality factor $2Nk_B$ which is precisely known. We will discuss precisely the h/m determination protocol in chapter 5.

A difficulty that can occur with BO is that for $N_B = 500$, the velocity of the atoms is shifted by 6 m·s^{-1}. As such, even with our one meter tall vacuum cell, it is easy to make the atoms reach a window. However, BO are also the solution to

this issue as a combination of two pulses allows to control both the position and velocities of the atoms:

For simplicity, we assume that the BO process happens in a infinitely short duration. We apply two Bloch pulses at times t_1, t_2 with N_1, N_2 BO each. We take here the convention the number of BO can be negative to mark accelerations in both direction. Assuming $z_0 = 0, v_0 = 0$ at $t = 0$, and that the atom is subjected to gravity g, we obtain that the velocity and positions obey for $t > t_2$:

$$v(t) = \Big(N_1 + N_2\Big)\frac{2\hbar k_B}{m} - gt \tag{2.3.32}$$

$$z(t) = \Big(N_1(t - t_1) + N_2(t - t_2)\Big)\frac{2\hbar k_B}{m} - \frac{gt^2}{2}. \tag{2.3.33}$$

We control the velocity of the atoms through the number of BO of each pulse and their position through the delay between the two pulses. This technique, called *atom elevators*, will be developed in detail for the study of systematic effects (section 6.1.2) for which the positioning of the atoms prior to the interferometry sequence is critical.

Our toolbox is now complete as we can transfer a large number of atomic recoils to the atoms (BO) and measure their velocities (Raman transitions, interferometry). The present thesis work was focused on implementing those tools on the new experimental setup, which is presented in the following section.

Chapter 3

Experimental implementation

The research interest towards measurements of the h/m ratio in the metrology team of the laboratory started in 1998. Since then, three versions of the experiment have been implemented. This work has been essentially focused on the third and last version of the experiment.

The previous setup issued the last determination of the team[Bouchendira, 2011] with a relative uncertainty on α of $6.6 \cdot 10^{-10}$. In order to improve this result, our group a built a new experimental setup. The construction of this setup started in 2013 and has been detailed in the PhD thesis of R. Jannin[Jannin, 2015a] and C. Courvoisier[Courvoisier, 2016].

It presents several improvements:

1. An improved control of the magnetic field during the interferometers
2. Higher-power laser sources
3. Ultracold atomic sources
4. A better control of vibration noise

In this chapter, we start by presenting the vacuum cell and the setup to produce atomic clouds. Then, we will turn to the presentation of the interferometry lasers implementation. This part describes one of the main contributions of my PhD work to the development of this setup. Finally, we will discuss the operation of the setup, in particular on two examples: the measurement of the magnetic field in the interferometry area and the measurement of the gravity gradient.

3.1 Atomic sample production

3.1.1 Vacuum cell

The vacuum cell design and preparation have been extensively detailed on the previous thesis[Jannin, 2015a; Courvoisier, 2016]. We start by recalling here its main features. A schematic presentation is displayed on figure (3.1): the vacuum cell is L-shaped with three distinct areas: the *corner*, or main chamber, where the atomic samples are prepared, the *horizontal* part which is responsible for loading atoms in the *corner* part and the *vertical* part which is the interferometry region.

The requirements for the vacuum cell were a pressure below 10^{-9} mbar in order to allow trapped atom lifetimes $\sim 10\ s$. Under this condition, no residual atomic vapor can be placed in the main chamber. In order to load atoms in the main chamber, the atomic source is placed at the tip of the horizontal part and a two dimensional magneto-optical trap (2DMOT) is responsible of primary trapping (see section 3.1.3). In between the 2D-MOT cell and the main chamber, a vacuum cross gives access to the cell for primary pumping, and continuous pumping with an ion pump.

In order to prevent a pollution of the main chamber by the rubidium vapor in the 2DMOT cell, the connections are made through two perforated disks whose holes diameter are ~ 4 mm, realizing a differential vacuum between the two parts of the chamber.

The vacuum cell was furthermore manufactured from titanium, an amagnetic material in order to avoid stray magnetic fields. Finally, the vertical part is a tube surrounded by a solenoid that defines a bias magnetic field along the vertical axis and a two layer cylindrical 2 mm thick μ-metal magnetic shield. The diameters of the shield cylinders are 12 and 16 cm. We used 3D-printed spacers to ensure the stability of the inner cylinder. The residual magnetic field has been estimated to 100 μG.

The tube and the main chamber are separated by a cubic cell which is used to detect the atoms. A detailed description of the vertical laser path and the detection is reserved for sections 3.2.4 and 3.3.2.

Finally, the vacuum cell is embedded in an aluminum profile system, and we have surrounded it with wood panels for environmental shielding. Pictures of the setup are shown in figure (3.2).

In order to maintain the vacuum inside the chamber, two *SAES NEXTorr D200-5* systems, combining an ion pump and a getter surface, are installed on the chamber.

The chamber was machined by the mechanical workshop of our lab. In particular, two crosses were welded under an Argon atmosphere. This noble gas saturates

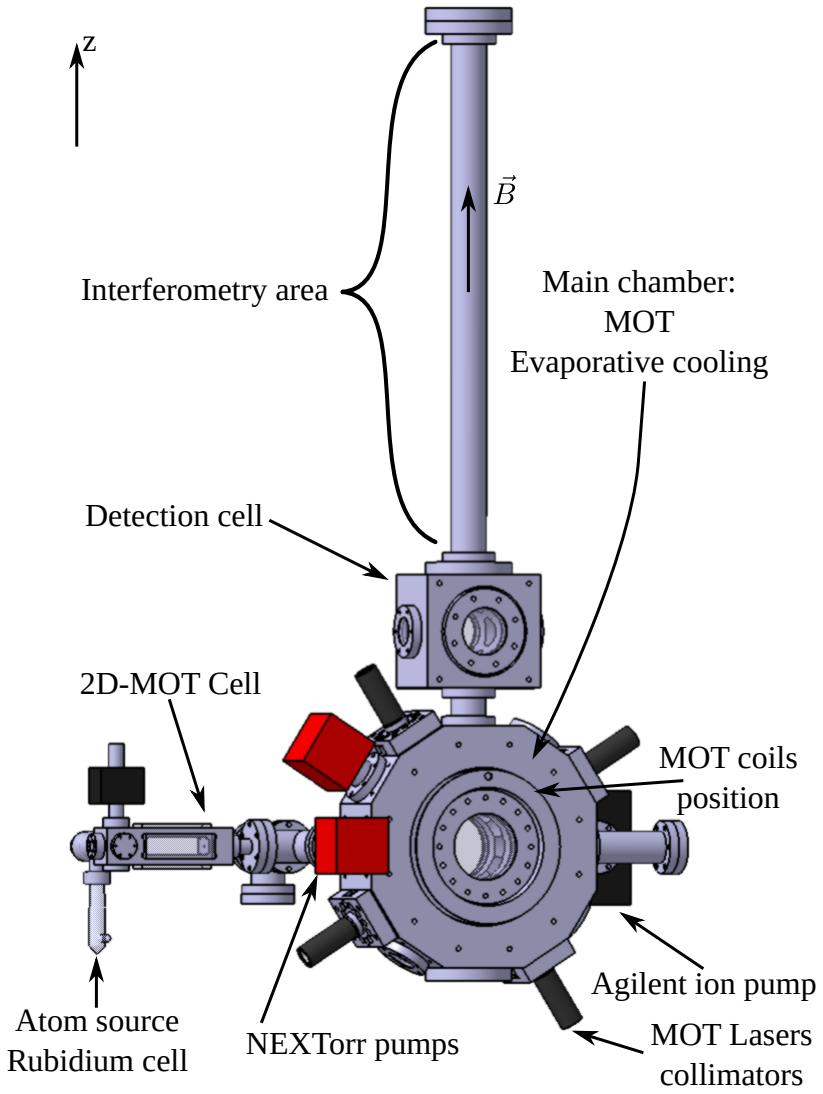

Figure 3.1: Schematics of the vacuum cell and its main components. The solenoid that generates a vertical bias magnetic field is wrapped around the tube of the interometry area. The magnetic shield surrounding it is not represented.

Figure 3.2: Pictures of the experimental setup. On the left: the wood panel box that shields to experiment from environment induced perturbation (mainly the air conditioning system). On the right: inside the wood panels: the interferometry area solenoid is hidden by the magnetic shield. Furthermore, the vacuum cell is surround by *Elcom* aluminum bars that allow for agile access.

the SAES NEXTorr pumps and leads to periodic sharp pressure increases. In order to prevent this *Argon instability*[Courvoisier, 2016], a supplementary *Agilent* ion pump was installed.

This system was in place at the beginning of this work. However, after a few months, the pressure in the vacuum chamber was unstable around a mean value of a few 10^{-9} mbar. This value was limiting our experiments with Bose-Einstein Condensates. In order to solve it, we have replaced one of the vacuum cross, the farthest from the Agilent pump, by a commercial cross which contained no Argon.

After re-baking the vacuum chamber for three weeks, we obtained a vacuum quality of $\sim 2 \cdot 10^{-10}$ mbar, continuously for now two years.

3.1.2 Atom trapping laser system

We use usual techniques based on *optical molasses* and *Sisyphus cooling* to produce cold atoms sources[Dalibard, 1989; Ungar, 1989], based on illuminating a given location with 6 laser beams, one for each direction.

The experimental implementation on atomic levels is based on a cycling transition ($|F = 2\rangle \rightarrow |F' = 3\rangle$ for ^{87}Rb) such that the atoms cannot fall back to $|F = 1\rangle$

and remain trapped. We denote the laser that excites this transition the *trapping* laser.

However, the $|F = 2\rangle \rightarrow |F' = 2\rangle$ transition is not forbidden, and from this level, atoms may decay to $|F = 1\rangle$, state which is not trapped. In order to avoid this process, a secondary laser, known as *repump*, is set resonant to the $|F = 1\rangle \rightarrow |F' = 2\rangle$ transition.

We then need two lasers with well controlled frequencies. Moreover, the properties of the trap can be controlled through the frequency of the trapping laser. For the preparation of the atomic sample, a dynamic control of this parameter is necessary.

3.1.2.1 Cooling laser system

The two lasers are generated through laser diodes (*Thorlabs L785P090*) in Extended Cavity Diode Laser (ECDL) configuration[Baillard, 2006]: the laser diode is embedded in a Fabry-Pérot cavity. One end of the cavity being a mirror and the other the diode itself. Inside the cavity, we place an interferential filter in order to choose a lasing mode at 780 nm because the nominal value of the diode wavelength is 785 nm. This systems output ~ 25 mW per diode.

The optical power passes through a Faraday isolator to protect the diode from feedback light and is then fiber coupled for further manipulation. This method of fiber coupling presents the drawback of power loss. However, it provides for modularity and for a better control of laser propagation mode. Indeed, collimating the output of a fiber tip produces a circular gaussian mode while the output of an ECDL produces an elliptical mode, harder to manipulate.

The frequency of each laser is set through three degrees of freedom:

1. The temperature of the diode, which is controlled by a Peltier device and stabilized through a PID lock.

2. The current of the diode, which provides a fast retroaction on the frequency.

3. A piezoelectric transducer placed on the mirror of the ECDL cavity which allow us to have a long-term frequency control.

The two lasers are then sent to a module where they are split and combined in order to achieve the control of their frequencies. From this module, they are also sent to an optical table where we prepare them for trapping.

This module is represented in figure (3.3). For compactness, the device (*Thorlabs FT114X149, PAF-X-5-B and derivatives*) was chosen. While its stability is

quite satisfying, its alignment is a long and hardly repeatable procedure as it is based on the precise positioning of fiber collimator lenses.

The system was modified since [Courvoisier, 2016] through the addition of mirror based fiber coupling. This modification reduced the long-term stability of the system, but simplified its alignment.

Let us first describe the optical paths. The trapping beam is simply split through a half-waveplate ($\lambda/2$) and Polarizing Beam Splitter (PBS) system. The main part of the power ($\sim$ 8 mW) is sent to the manipulation table, while the remaining part is sent to a fast photodiode on which we produce a beatnote with the repump beam.

Concerning the repump beam, it is directly split and $\sim$ 2 mW are sent for manipulation in the *auxiliary output*. Splitting very early in the propagation, we make sure that the trapping laser does not mix with this repump.

The remaining part ($\sim$ 8 mW) is further split in two. One part ($\sim$ 6 mW) is combined on a PBS with the trapping laser to be sent to the manipulation table, and the other part is sent to the frequency control systems. The part that is superposed to the trapping laser can be shut off through the use of a mechanical shutter. When this occurs, the repump auxiliary output controls what is sent to the atoms.

The other part of the repump is again split in two: one part contains almost exclusively repump beam and is sent to a saturated absorption spectroscopy[MacAdam, 1992] cell where we generate a signal to lock on the $|F = 1\rangle \rightarrow |F' = 1\rangle$ to the $|F = 1\rangle \rightarrow |F' = 2\rangle$ crossover.

The spectral difference between the levels $F' = 1$ and $F' = 2$ of the ^{87}Rb D_2 line is $\sim$ 160 MHz, such that the crossover lies 80 MHz below the $|F = 1\rangle \rightarrow |F' = 2\rangle$ transition. This 80 MHz difference is compensated through the Acousto-Optic Modulators (AOM) that we use to control the dynamical properties of the beams.

The second part is sent to the fast photodiode in order to produce a beatnote with the trapping laser. This beatnote is then phase locked with a variable reference signal such that we have a dynamic control on the trapping laser frequency. We refer the reader to [Courvoisier, 2016] for more details on the frequency locks and control.

3.1.2.2 Manipulation

The manipulations output of the splitting module (figure 3.3) is sent to the MOT optical table (figure 3.4). At the output of the fiber transport, the repump and trapping beam have orthogonal polarizations.

Those two beams pass through an optical isolator that prevents feedback to the lock system. Since an optical isolator allows only one linear polarization to

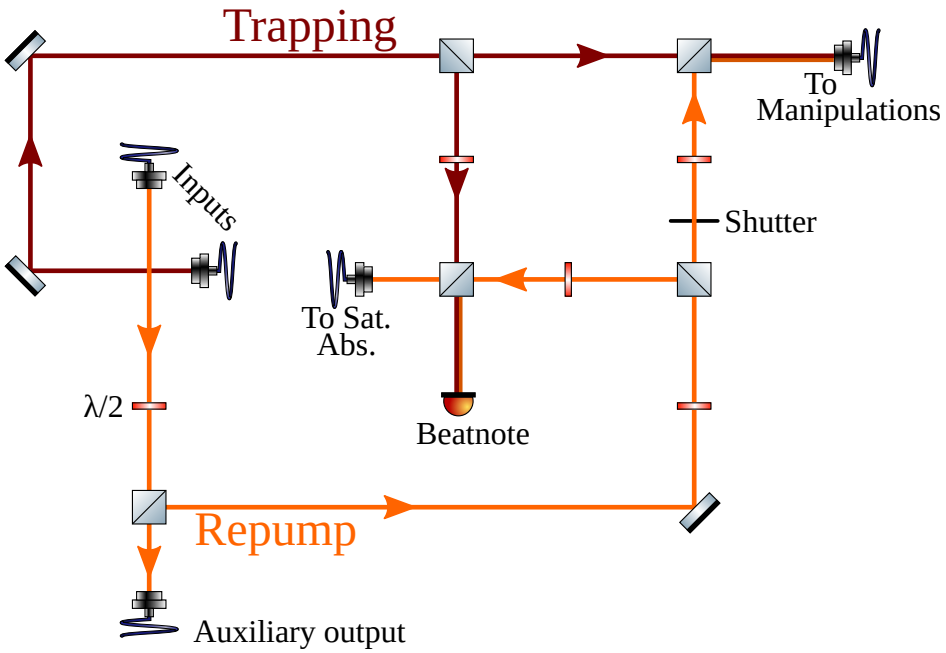

Figure 3.3: Module for trapping lasers frequency control. Two mirrors for the alignment of repump between its first splitting and the cube square are not represented. Also, the filtering polarizers right after the input fibers are absent from this schematic.

pass through, we place an half-waveplate before its input to balance the relative powers between trapping and repump.

After the isolator, the laser beams are amplified with a tapered amplifier. This system provides us with $\sim$ 700 mW of trapping laser and $\sim$ 200 mW of repump. The output of the amplifier is collimated with cylindrical lenses to correct its elliptical shape and is sent to a second isolator to protect the amplifier from feedbacks.

The remaining of the optical table consists firstly of splittings with half-waveplate and PBS module and AOM-control/fiber coupling. A first splitting feeds another splitter that outputs 6 beams for the 3D-MOT. A second splitting on the optical table divides the remaining power between the 2D-MOT and an auxiliary output. After each splitting, we placed an AOM for dynamical control of the laser beams.

The auxiliary repump comes in at this level. It passes through an AOM and is split with one output sent to the light sheets detection (section 3.3.2). The second output is superposed to the main beam auxiliary output.

The end-use of this auxiliary part of the beams is when the repump part of the main beam is shut off with the splitting module mechanical shutter. At this stage, we have temporal independent control of both the trapping beam and the repump

beam. The trapping laser can be set resonant so that it can be used whether to detect the atoms (section 3.1.4) or to blow them away (section 3.2).

The auxiliary combination cube provides two outputs. One is sent to the interferometry optical table (see section 3.2.5), while the other one is split in two to be sent to the two absorption imaging channels. Since the two lasers have orthogonal polarizations after the combination cube, this last splitting is quite constrained. However, the AOMs provide us with a fine tuning of the timings that compensate this imperfect splitting configuration.

Let us now zoom in on the 2D-MOT part of the table. As we will see in next section we need to sample a fraction of the light for the 2D-MOT pusher which is again performed with a half-waveplate/PBS splitting. Furthermore, the non diffracted order of the AOM is deflected by the edge of a mirror and passes through an another AOM. We also use this path to feed the light sheet detection (section 3.3.2) with resonant light.

Finally, we added on each path a mechanical shutter that ensures that no leakage light reach the atoms when the AOM is off. The response time of the shutters is $\sim$ 10 ms. Through their calibration, we can control their opening and closing with a precision of $\sim$ 1 ms. Thus, they are not meant to be used in conjunction with the AOMs but with the steps of the experimental sequence (molasse, evaporation, interferometry, ...)

3.1.3 Magneto-optical traps

Optical molasses allow to reach temperatures ~ 4 μK with ^{87}Rb atoms. However, because the atoms are not spatially trapped, the density of the gas they form is quite low. As a consequence, the atomic signal at the output of the experiment would be low, or maybe undetectable.

To reach higher density, one combines the laser cooling process with a magnetic field gradient[1], and circularly polarized beams. This forms a magneto-optical trap (MOT)[Dalibard, 1983; Raab, 1987]. This configuration allows for higher densities and trap loading rate, which also enables a reduction of the experimental cycle duration.

As the atoms are now trapped where the magnetic field cancels, the density of the gas is quite high. Furthermore, the laser cooling process induces series of spontaneous emissions. These photons may be reabsorbed by other atoms. As their direction is random, this reabsorption process is a heating mechanism that increases the equilibrium temperature of the gas.

[1] In fact, a quadrupole field

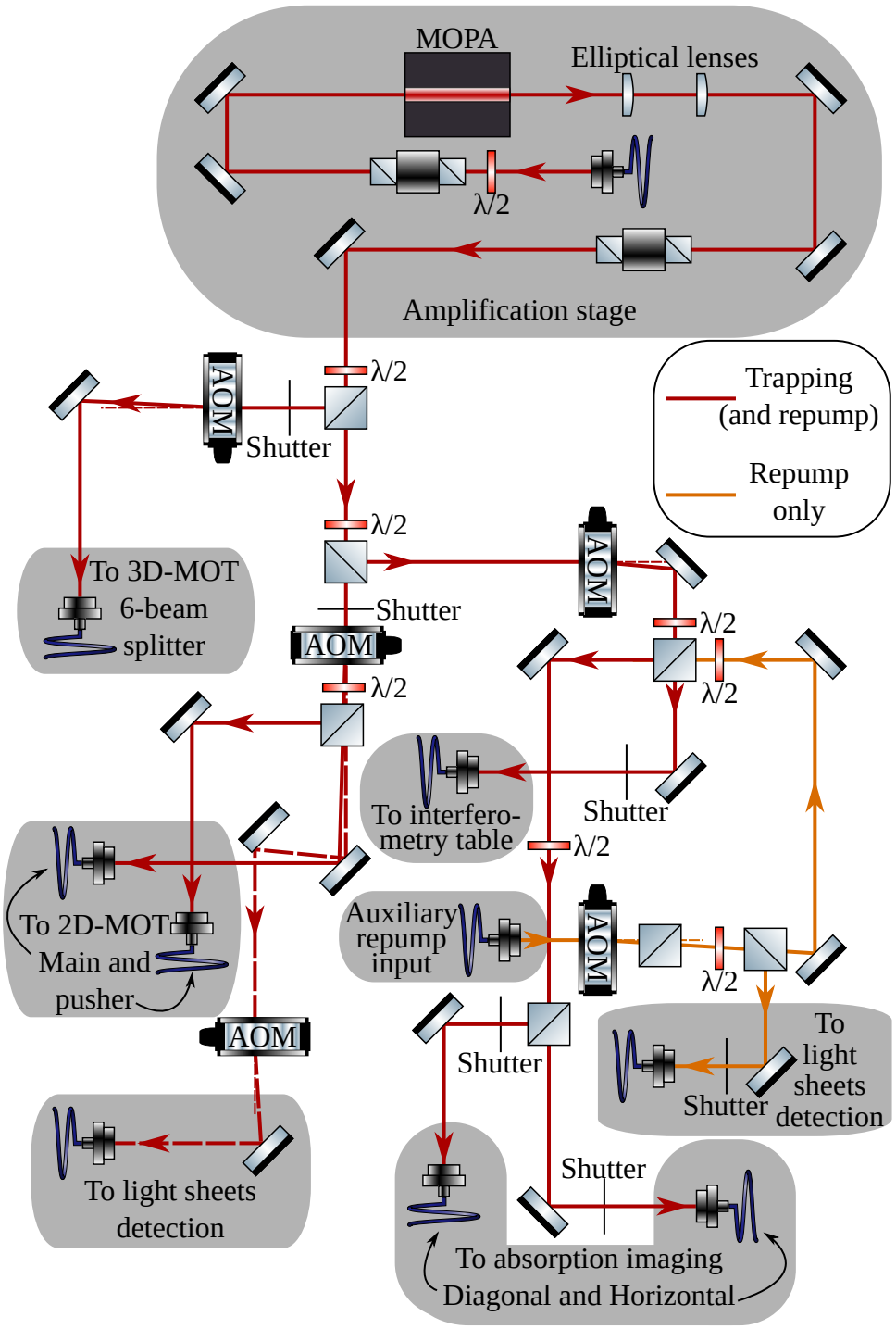

Figure 3.4: MOT beams manipulations table. The top of the figure displays the amplification setup. On the left-hand corner, from top to bottom: splitting of the main beams to the 3D-MOT, 2D-MOT and light sheet detection. On the right, mixing of the main beams with the auxiliary repump for use during interferometers and for absorption imaging.

In order to combine the advantages of both techniques, the loading of the MOT is followed by an optical molasses phase which produces a gas at a temperature ~ 4 μK, containing 10^8 atoms with a $1/e$ radius of 600 μm.

The magnetic field is generated from a pair of coils in anti-Helmholtz configuration, powered by a low response time power supply. The current through the coils is controlled by an analog signal, which allows to switch from the MOT to optical molasses.

At the output of the 6-beam splitter, the laser beams are collimated through a 4 lens system, which is followed by a quarter waveplate to produce circularly polarized beams. This collimator allows for a large beam (of waist ~ 5 mm) which enhances the trapping power of the MOT. The typical power in each of the beam is 12 mW.

The 3D-MOT is loaded by atom beam produced by a two dimensional magneto-optical trap (2DMOT)[Riis, 1990]: horizontally to the main chamber is placed a vacuum element (2DMOT chamber) connected to a rubidium cell. The 2DMOT chamber is hence filled with rubidium. We there produce a MOT in two dimensions, the third being used to push the atoms from the 2DMOT chamber to the main chamber. The optical setup around the vacuum cell to produce the 2DMOT is presented in figure (3.5).

3.1.3.1 Optical molasses operation

The conversion from a MOT to an efficient optical molasses sequence is performed through a few steps of manipulations. A scheme of these steps is presented on figure (3.6). The loading of the MOT takes ~ 600 ms and is limited by the programming duration of the sequence (see section 3.3.1), the detuning of the trapping laser with respect to the optical transition Δ is set to $\sim -1.9\Gamma$ while the magnetic field presents a gradient of ~ 9 G·cm^{-1}. For 5 ms, the magnetic field is ramped up to ~ 15 G·cm^{-1} while the laser is detuned by -3.3Γ. With these parameters, the cloud is slightly compressed. This compression stage lasts for 25 ms and maximizes the density of the atom cloud.

Subsequently, the magnetic field command is swept to 0 in ~ 20 ms. Simultaneously, the laser is detuned by $\sim -6\Gamma$. We now reach the molasse phase which lasts 20 ms and during which the laser is set to $\sim -22\Gamma$ in 5 ms. Finally, we shut down the lasers power and release the cloud by ramping down the lasers intensity to 15% of its maximum value in 10 ms, before an abrupt shutoff. The total duration of this stage is approximately 80 ms, such that we produce an atom gas from an optical molasse in ~ 700 ms.

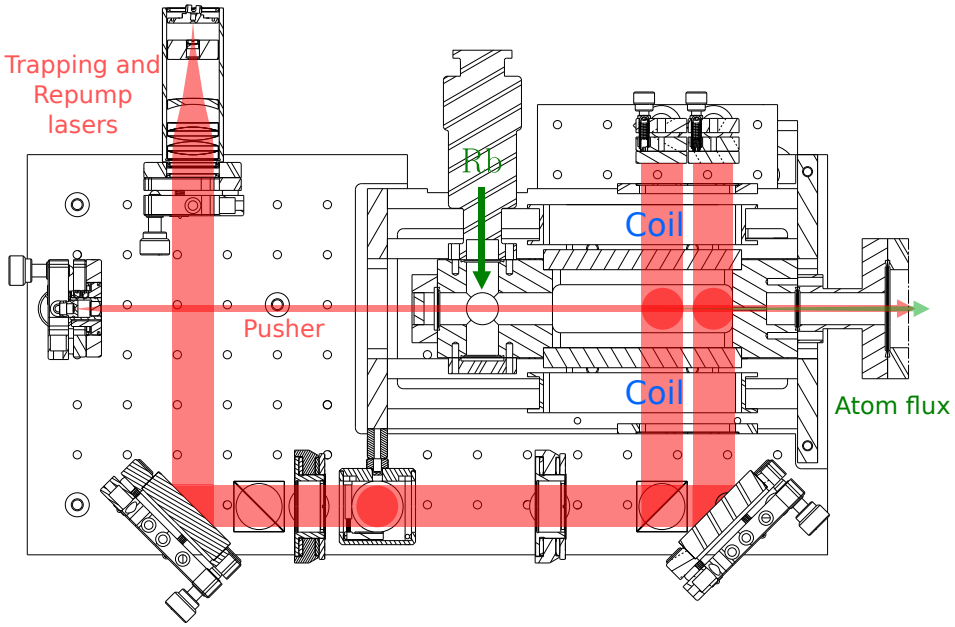

Figure 3.5: Top view of the 2DMOT. A large beam, with both trapping and repump, is split in two parts, an horizontal one and a vertical one (not represented). Then the beams are split in two to increase the 2DMOT captured range. The atoms that are cooled are pushed towards the main chamber with a pusher beam. Adapted from [Courvoisier, 2016].

After the production of the cloud, the atom cloud is positioned to the interferometry area with an elevator based on two Bloch Oscillations pulses (see section 2.3.5).

3.1.3.2 Residual magnetic field compensation

For the optical molasses process to take place at its utmost efficiency, the magnetic field at the position of the atom trap should be rigorously 0. Thus, three pairs of coils, each for one spatial direction and placed around the main chamber, produce a magnetic field that is aimed to compensate for the residuals magnetic field induced by either the Earth magnetic field or by our instruments.

The colder the atom cloud, the higher its density in velocity space, such that the higher the transmission through a narrow Raman pulse. Using this principle, we were able to optimize the magnetic field compensation and observe atom clouds with a temperature of ~ 4.3 μK, by a measurement of their velocity distribution, displayed on figure (3.7). The size of the atom clouds upon their release from the molasse is ~ 1 mm, which we extraced from absorption imaging (see next section).

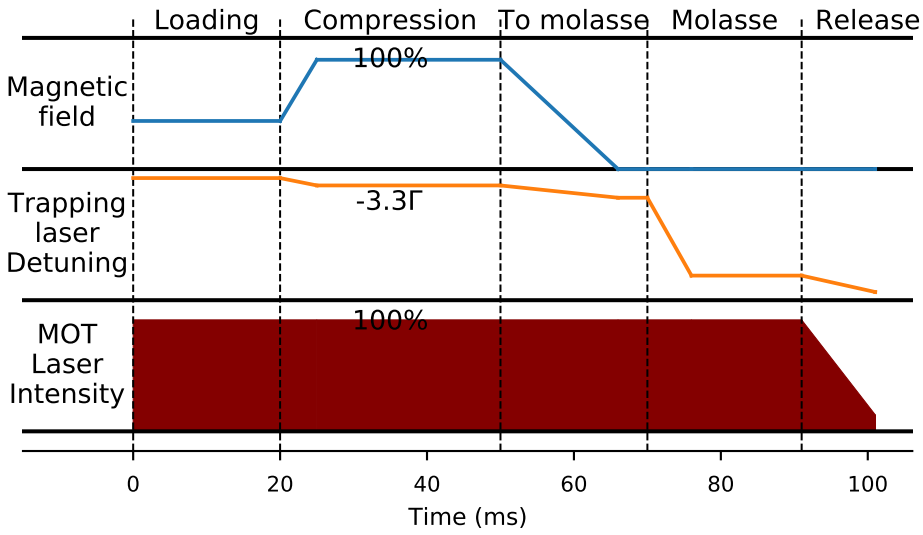

Figure 3.6: Sequential steps for the MOT to molasses conversion.

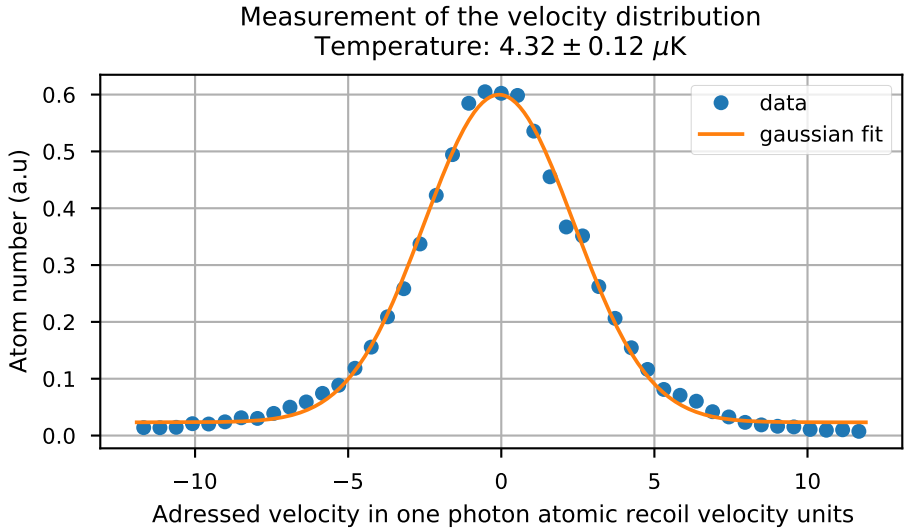

Figure 3.7: Velocity distribution at the output of the molasse stage. Data (blue dots) was taken by scanning the addressed velocity of an elevator-selection sequence (see section 3.3) and measuring the atom number at its output. Data is fitted by a gaussian (orange line), from which we extract a $1/e$ velocity width of ~ 3.5 one photon recoil velocity. This corresponds to a temperature of ~ 4.3 μK.

3.1.4 Absorption imaging

During the MOT stage of the experiment, the atoms experience cycles of absorption-emission. Because the direction of emission is random, the output photons of those cycles are observed with a simple lens-photodiode-amplifier setup, where the lens is placed at a window of the vacuum cell. This setup provides an observation signal that characterizes the MOT loading rate and the repeatability of experimental cycles.

As the cooling process advances to a molasse stage, the atom density and laser intensity get lower, and thus the signal onto this photodiode does as well, such that others observation techniques shall be used. In the experiment, two kind of observation process are set up:

1. Time of flight detection, based on the collection of the atomic fluorescence in laser sheets. This method is used to measure the number of atoms in each hyperfine levels ($|F = 1\rangle, |F = 2\rangle$), and thus its presentation (section 3.3.2) will be made after the interferometry setup has been introduced.

2. Imaging, which is based on the observation of the laser absorption by an atom cloud, and is detailed on the following paragraphs.

3.1.4.1 Principle

By exposing an atomic sample to a resonant laser probe beam, and imaging with a telescope system onto a CCD camera, one observes the absorption of the laser beam by the atoms. In the low saturation regime, where the laser intensity is small with respect to the addressed transition saturation intensity, the ratio between the input and output intensity are given by the Beer-Lambert law:

$$\frac{I_{out}(x,y)}{I_{in}(x,y)} = e^{-n(x,y)\sigma}, \tag{3.1.1}$$

where σ is the absorption cross section, and $n(x,y)$ the local density, integrated over the laser direction of propagation. The product of those two quantities is call *optical density*: $OD = n(x,y)\sigma$.

A second measurement with no sample allows to determine the input intensity, and as such the optical density. Through the knowledge of the cross section and the integration of the optical density over the camera region, one may estimate the detected number of atoms. Furthermore, this technique provides spatial information on the atomic sample.

3.1.4.2 Operation

On the experimental setup, we have two cameras available. One (*Sony XCD-V60*) and its telescope system are placed directly on a window of the vacuum cell. The telescope tube part *Thorlabs SM1NR1* allows a longitudinal displacement of the camera in order to perform clear images of the atomic sample. On the opposite window of the cell, we placed a collimator fed with one the auxiliary output of the MOT optical table. The direction of this imaging system is neither horizontal of vertical, so that we denote it *diagonal*.

The second system is placed on the optical tables surrounding the cell on a *horizontal* axis. The camera (*IDS UI-5240CP-NIR-GL*) is placed on two horizontal translation stages for fine positioning and focusing. The corresponding collimator is fed with another auxiliary output of the MOT table.

The laser feed of the two cameras provide a resonant (from the trapping laser) and repump beam. The former is used as the probe beam. As it is only resonant with atoms in $|F = 2\rangle$, the observation of atoms in $|F = 1\rangle$ is only enabled through a preliminary pulse of repump beam.

Due to the re-emission of the absorbed photons, the cloud is heated by the probe beam. As such the imaging technique is a destructive measurement. Moreover, when operating, we should limit this heating process that would damage the spatial information that could be extracted from the imaging process. To this end, the probe pulse duration are of the order of ~ 100 μs. The repump pulses duration is of the same order of magnitude and is placed as close as possible prior to the probe beam such that we do not observe the heating that it induces.

3.1.5 Evaporative cooling

In 2009, it was observed that that the transverse expansion of the cloud was a limiting factor to build a more complex and sensitive interferometer geometry based on Large Momemtum Transfer Beam Splitter combining Raman transitions and Bloch Oscillations[Cladé, 2009].

As such, the new experimental setup that we present in this thesis is equipped with an optical dipole trap in which the cloud is cooled by evaporation. The choice of an optical trap versus a magnetic trap is motivated by the absence of strong magnetic fields which can perturb the interferometers during their relaxation.

In our setup, the optical dipole trap is loaded from the MOT through specific cooling steps (see figure (4.1)). As a consequence, we can either perform experiments with cold atomic sources generated from optical molasses or ultracold sources produced by evaporative cooling. A comparison of the use of these two atomic sources in our experimental setup is presented in chapter 4.

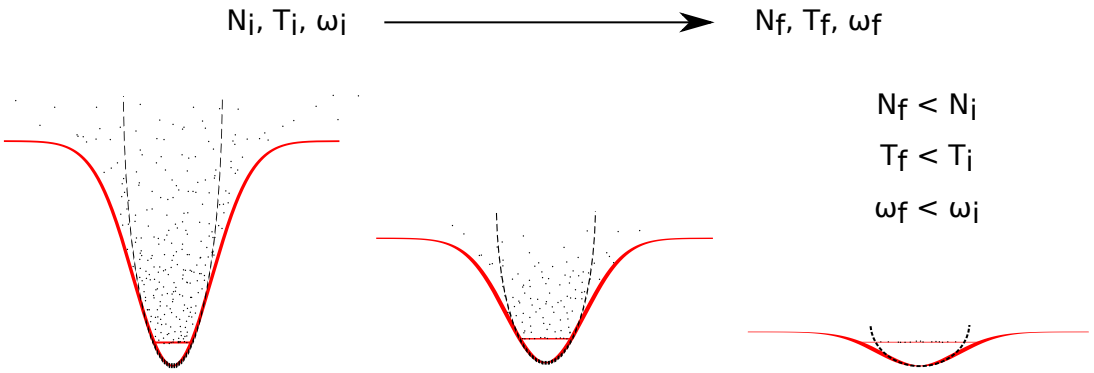

Figure 3.8: Potential landscape seen by the atoms with the evolution of the evolution process. The atom number in the trapped gas and its temperature are reduced, as well as the potential height and confinement frequency. Extracted from [Courvoisier, 2016]

The evaporation technique and the setup are presented in detail in [Jannin, 2015a] and [Courvoisier, 2016] and we present its main characteristics.

First, the principle of the evaporation in an optical dipole trap is presented in figure (3.8). An atom cloud is trapped in a harmonic trap generated by laser beams in a crossed configuration. The use of this configuration is motivated by the fact that the trap generated by a single laser beam does not provide strong confinement along its direction of propagation.

The evaporation cooling principle goes as follows: as the power of the laser beam is reduced, the more energetic atoms escape the trap. The total energy of the cloud is then lowered. Through a collisions mediated energy redistribution (or thermalization), the temperature of the cloud is then reduced.

One can show[CohenTannoudji, 1997; Courvoisier, 2016] that the evaporation process is governed by a power law:

$$\left(\frac{N_f}{N_i}\right)^{2q} = \frac{T_f}{T_i}, \tag{3.1.2}$$

where N represents the number of trapped atoms, T the temperature of the gas they form, and the subscripts i and f the initial and final states, respectively. Finally q represents the efficiency of the evaporation and depends on the configuration of the laser beams. The best performance of obtained on our setup is $2q \sim 1.5$.

As a consequence, the initial conditions of the evaporation govern its final state. In particular, a Bose-Einstein Condensate (BEC), where the atoms macroscopically populate the ground state of the harmonic trap, can be observed at

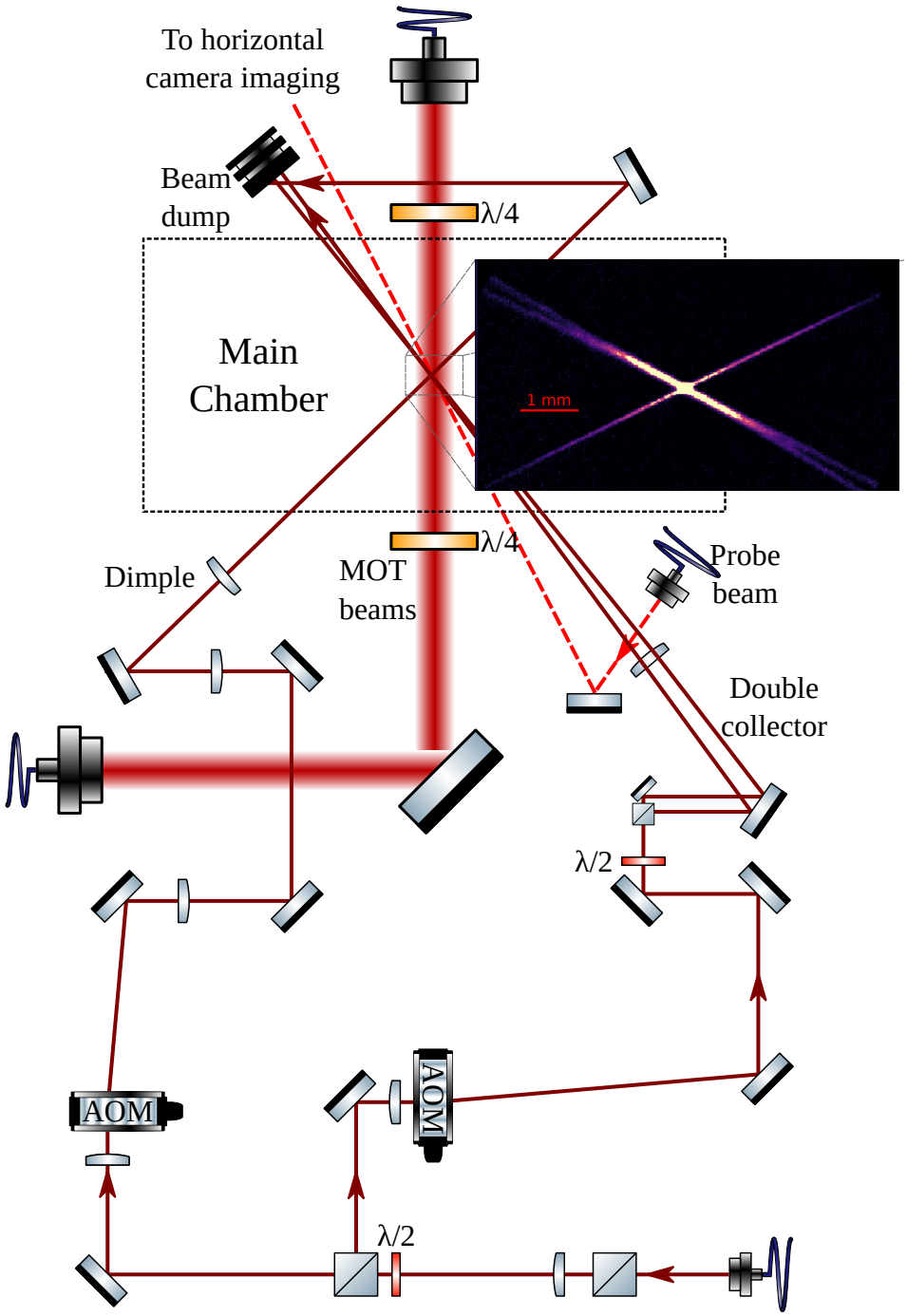

Figure 3.9: Schematic representation of the optical tables surrounding the main chamber (top view). The setup mainly correspond to the dipole beam setup for evaporative cooling (dark red lines), but also contains the horizontal MOT beams (large red) and the horizontal camera path (dashed red lines). Inset: image of the three dipole beams through the observation of atoms that are trapped at very short time of flight (1 ms). The image is saturated so that the tails of the trap are distinguishable.

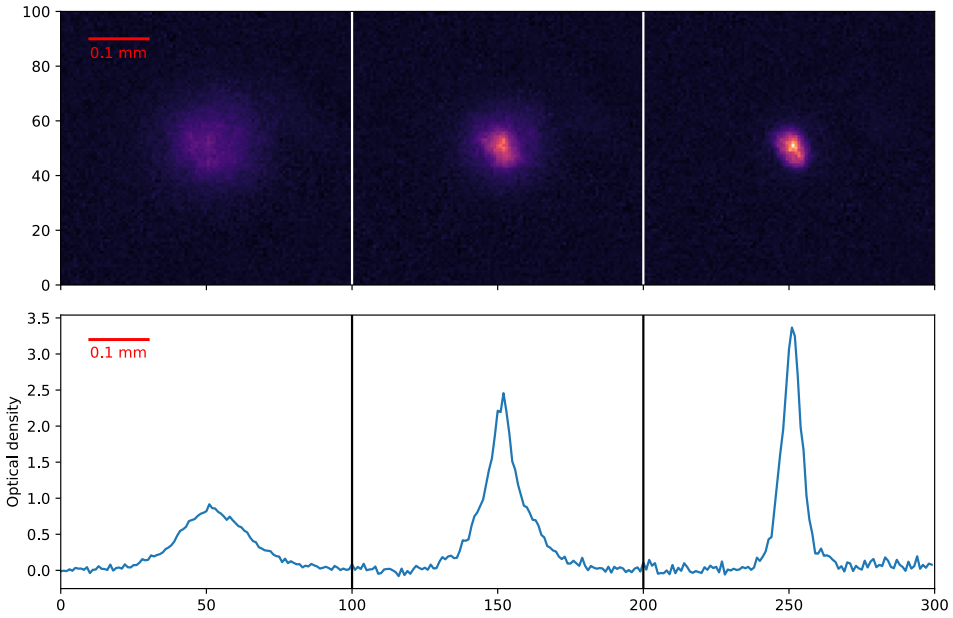

Figure 3.10: Images of the atom cloud at the end of the evaporation obtained after 18 ms time of flight. From left to right, the evaporation duration increases, so that we start with a thermal gas on the left. In the middle, the characteristic peak of a BEC appears with a thermal background. On the right picture, we observe only the BEC peak.

temperature below[Courvoisier, 2016]:

$$T_c = 0.94 \cdot \frac{\hbar\omega}{k} N^{1/3}, \tag{3.1.3}$$

where ω is the trap frequency and k is in this context the Boltzmann constant. The temperature of the transition scales with the remaining number of atoms in the trap, which indicates that the initial number of atoms is a critical parameter in order to produce BECs.

One of the challenges of evaporating in a optical dipole trap is the reduction of the trap frequency ω as the laser power is reduced. Indeed, the harmonic potential is an approximation of the gaussian potential created by the laser. The harmonic frequency deduced from the approximation scales linearly with the laser power. Finally, the collision rate γ inside the trap scales with its harmonic frequency[Dalibard, 2006]:

$$\gamma = \frac{m\sigma_{coll}}{2\pi}\omega^3 \frac{N}{kT}, \tag{3.1.4}$$

where $\sigma_{coll} = 6.5 \cdot 10^{-16}$ m^2 is the two body collision cross section for ^{87}Rb. The collision rate governs the thermalization rate, so that the higher the collision rate, the faster the thermalization.

Finally, both the transition temperature and the collision rate reduce as we proceed with the evaporation process. The constraints on the laser setup are then to provide a large number of atoms initially and maintain a large enough trap frequency. As the trap frequency scales as the inverse of the laser waist, but their capture range scales quadratically with it, we use a three beams setup with two collectors of large waist (~ 100 μm) and a *dimple* beam of smaller waist (~ 30 μm), in a crossed configuration.

The optical setup that produces this configuration is displayed on figure (3.9). We start from the output of a infrared IPG Photonics laser at 1070 nm that produces a power 50W. This beam is first split and collimated to a smaller size in order to increase the efficiency of the diffraction through the AOMs.

We use the order 1 and -1 of the AOMs to control the powers of the collectors and the dimple. As such, the frequencies of the beams are separated by 160 MHz, such that they do not interfere at their crossing points.

Then, the dimple beam passes through another telescope system that increases its waist, and is then focused by a lens on a translation stage which allows for a fine positioning of the laser waist. Secondly, the collector part is split in two on a PBS. The two parts have orthogonal polarization and then cannot interfere with each other. They are then made parallel and are focused similarly to the dimple beam at the center of the vacuum cell.

The laser arrangement can be observed in the vacuum cell thanks to absorption imaging of the trapped atoms, which we display as an inset on figure (3.9). Using this setup, we are able to observe BECs as shown in figure (3.10) which displays their formation as the laser power is reduced. In particular, one can observe the contrast between the width of the left picture (thermal cloud) and right picture (BEC).

At the beginning of this thesis work, the performance of the setup was the production of BEC of 50000 atoms at 35 nK within 4s of evaporation[Courvoisier, 2016]. The improvements that were made during this thesis on this part of the experiment, presented in section 4.1, allowed to double the number of atoms while dividing by 2 the evaporation duration. In the others parts of this chapter (mainly section 3.3.3), the results that we present were obtained with optical molasses solely.

3.2 Interferometry lasers

The *interferometry lasers* name includes all beams that are travelling along the vertical axis. There are four types of them and they share a dedicated optical table, which is represented on figure (3.21).

The lasers that we are to describe are:

1. The Raman lasers
2. The Bloch lasers
3. A blow away laser, derived from the MOT trapping laser
4. A repump laser, derived from the MOT repump laser

We start with a description of the laser production and frequency control of the Bloch and Raman lasers. We will then describe the vertical optical path. After discussing the laser manipulations on the optical table, we will present examples of experimental cycles in order to illustrate the role of each laser element.

The production of the Raman and Bloch lasers is derived from telecom technologies. We present it first.

3.2.1 Amplification and doubling technology

The laser production scheme is displayed on figure (3.11). We use amplifier-doubling modules seeded with a narrow bandwidth laser at 1560 nm. This configuration allows us to obtain high power at 780 nm.

The amplifier is an Erbium Doped Fiber Amplifier (EDFA)[Naji, 2011]: Erbium ions are placed as defects inside the glass of the fiber core and amplify an incoming laser through a stimulated emission process. The Erbium ion can be modeled as a three level system. The ions are excited by a pump at 980 nm, and decay to a lower lying excited state in ~ 1 μs through a non radiative transition. From this state, the ions may emit an infrared photon, falling back to its ground state.

However, the ions may also decay through a spontaneous emission process. Although the emission direction is random, some of the photons are guided through the fiber and are subsequently amplified. This process, known as Amplified Spontaneous Emission (ASE), produces a large noise spectrum.

The amplified laser beam is then sent to propagate along a Periodically Poled Lithium Niobate (PPLN), and is doubled through Second Harmonic Generation (SHG). For the conversion to occur both energy and momentum must be preserved. Inside the material, the dispersion relation (refractive index) governs momentum conservation, such that the temperature of the crystal should be carefully adjusted. This is also known as the phase matching condition.

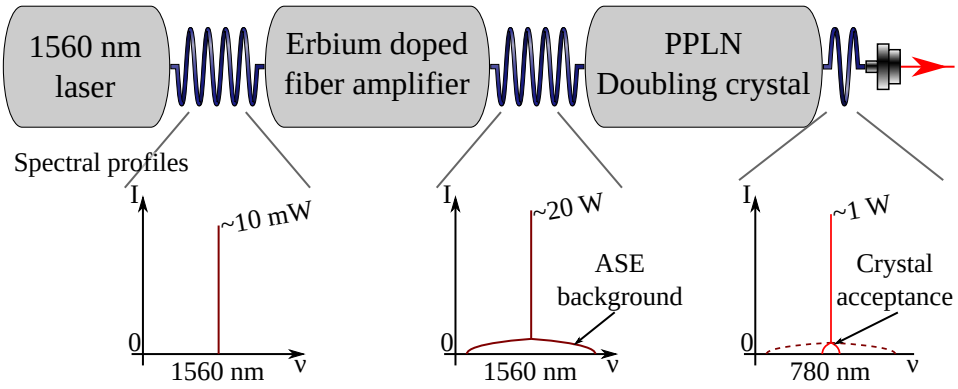

Figure 3.11: Scheme of the amplification and doubling of a 1560nm laser source to a high power 780 nm source. On the bottom of of the figure are represented an approximative power spectrum at each step which display the ASE background and its filtering by the doubling process.

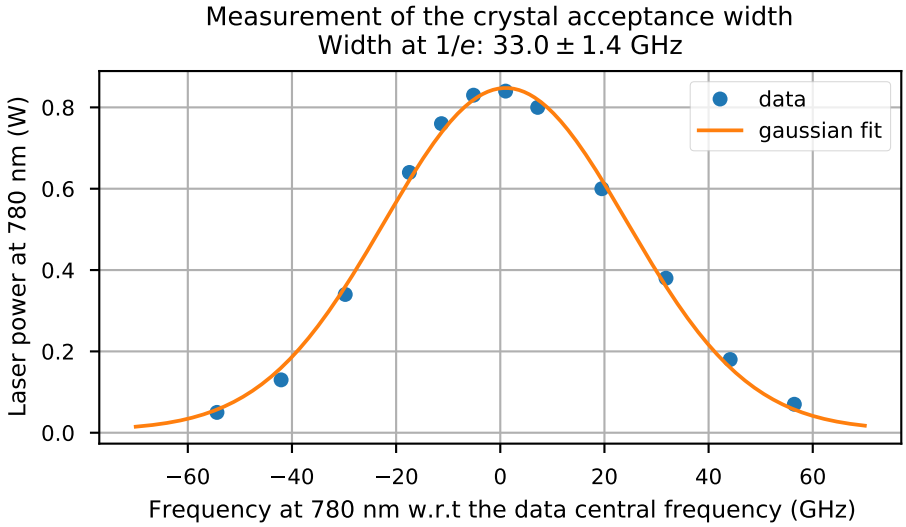

Figure 3.12: Output power of the amplifier-doubling module as a function of the seeder frequency (converted to 780 nm). The temperature of the doubling crystal is constant, such that this figure represent the width of the crystal acceptance.

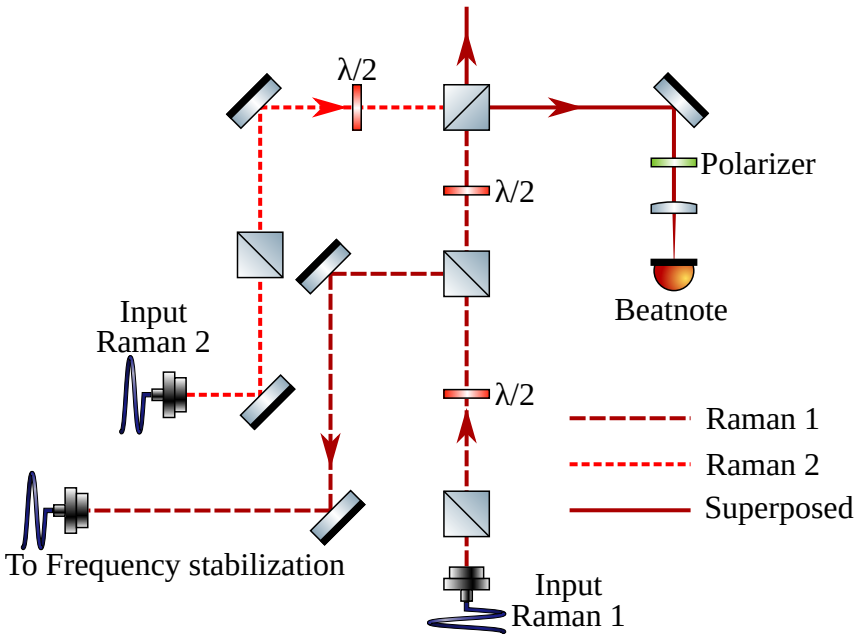

Figure 3.13: The two Raman lasers preparation, which constitutes a superposition for further manipulation (top middle arrow, unmarked), and a superposition for phase locking (right). The laser Raman 1 is furthermore picked off for absolute frequency stabilization.

The frequency width of the phase matching condition depends of the geometry of the crystal. We have performed a measurement of this quantity and found a width of $\sim$ 40 GHz (see figure (3.12)) for the modules that we use on the experiment, which were built by the company *MuQuans*. This figure is particularly interesting when estimating the impact of the ASE background on our experiments.

3.2.2 Raman Lasers

In order to perform Raman transitions, we need two lasers whose frequencies are separated by the hyperfine splitting. Additionally, the frequency of each laser should be controlled precisely as well as the phase between the two lasers.

One of the lasers is seeded with a NKT laser while the second with a RIO diode. I denote them respectively Raman 1 and 2. We phase lock Raman 2 to Raman 1. The RIO diode has a fast response time which meets the requirements to run an interferometer. On the other hand, the NKT laser presents a narrow frequency power spectrum. We lock the absolute frequency of this laser with techniques presented in section 3.2.6.

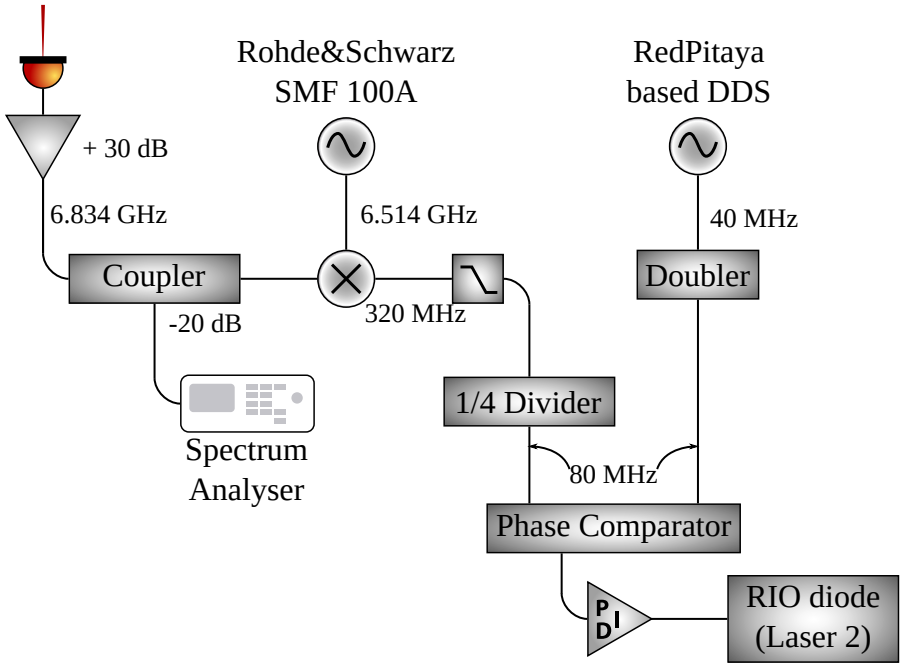

Figure 3.14: Raman Phase Lock Loop frequency chain. See text for detail. We did not represent the laser path between the RIO laser diode (bottom right-hand corner) and the photodiode beatnote (top left-hand corner).

The schematic of the Raman preparation is presented on figure (3.13). Both lasers are polarization filtered with PBS at the output of the lasers. Raman 1 is furthermore picked off with a half-waveplate/PBS combination. This picked off light is sent to the frequency stabilization module.

Finally, the two beams are combined on a PBS which provides two outputs with superposed Raman beams, with orthogonal linear polarizations, meeting the requirement we have stated in section (2.1.2.2). One the output is further manipulated before being sent to the atoms (see section 3.2.5). The other is sent to a fast photodiode for phase locking.

The frequency chain of the Raman Phase Lock Loop (PLL) is displayed on figure (3.14). The fast photodiode (*Hamamatsu G4176-03*) produces a signal at frequency $\sim$ 6.834 GHz, which is amplified by $\sim$ 35 dB. A small fraction (-20 dB) of the signal is sampled with a coupler and used for observation. We usually observe its trace on a spectrum analyser (figure (3.15)).

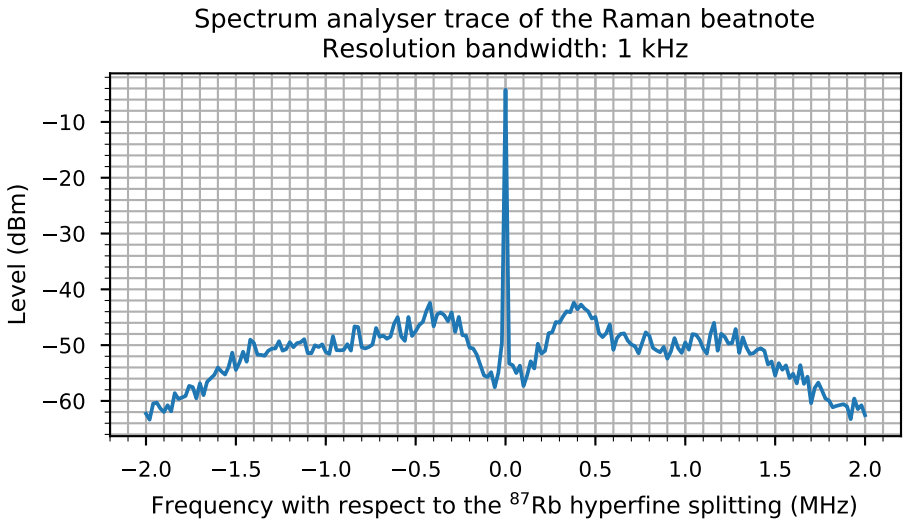

Figure 3.15: Typical trace of the Raman lasers beatnote obtained on a spectrum analyser.

In order to transport the main part of the signal with minimum losses, it is directly mixed with the output of Rohde&Schwartz SMF100A to lower its frequency at ~ 320 MHz. This signal is then divided by 4 and sent to the Phase Comparator device.

The synchronization input of the phase comparator is fed with a RedPitaya output set in direct digital synthesizer. This device outputs a 40 MHz signal which is frequency doubled. We obtain two 80 MHz signals to implement phase locking. The PLL is then completed with a PID controller to feedback on the RIO diode laser and lock its phase to the first Raman laser.

The PID parameters are carefully set to minimize the low frequency phase noise, as displayed in figure (3.15). Indeed, as we have developed when studying the sensitivity function (section 2.2.5), the transfer function of an atom interferometer behaves as a low pass filter whose cutoff frequency is given by the duration of the Raman pulses.

3.2.3 Bloch Lasers

For the Bloch lasers, we need two coherent laser beams at 780 nm whose frequencies can be controlled independently: when running the optical lattice inside the interferometer in order to measure the recoil velocity of an atom, it is required that the 2 photon recoil remains constant, *i.e.* the mean frequency of the two lasers is unchanged.

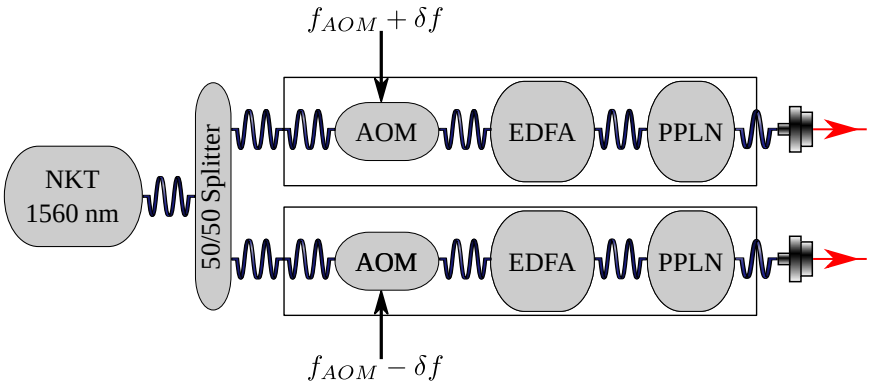

Figure 3.16: Laser system for the implementation of the Bloch Oscillation process. A single source feeds two amplification-doubling modules. The control of the frequency of the lasers at 780 nm is achieved by the frequency command of AOMs placed before the amplifiers.

The usual technique to achieve this control was to split the 780 nm source, and place a double pass AOM for each splitted beam. The double pass AOM allows a frequency shift without steering, and thus a constant coupling through a fiber collimator.

However, the efficiency of a double pass AOM is limited to 50%, and it depends on the AOM driving signal frequency. When operating a double pass AOM for Bloch Oscillations, the frequency of the driving signal changes by typically ± 10 MHz, which is slightly larger than the frequency range on which the AOM efficiency is flat. As a consequence, the optical power will not be constant over the Bloch Oscillations pulse.

In order to circumvent this issue, an AOM at 1560 nm is placed before the EDFA in the amplifier-doubling module. This AOM is single pass but the design by *MuQuans* was carefully made to minimize the impact of steering. Due to the fast response time of the EDFA output power lock, this system provides a 1.5 W laser with dynamically variable frequency and constant power over the frequency range. This system is represented in figure (3.16)

In order to run Bloch Oscillations, we have two of such modules and we seed them with a 50/50 splitted single source produced by a second NKT laser. The frequency of the lasers is given by

$$f_{Bloch} = 2\left(f_{NKT} + f_{AOM}\right) \tag{3.2.1}$$

We recall that the two photon Bloch frequency is made constant by changing the frequency of the two lasers by the same absolute value but with opposite sign.

As a consequence, we control the lasers frequency around a central value for the AOMs f^0_{AOM}:

$$f^{\pm}_{Bloch} = 2\left(f_{NKT} + f^0_{AOM} \pm \delta f\right) \tag{3.2.2}$$

During the Bloch Oscillations process in the interferometric sequence, if a part of the ASE background is resonant with an atomic transition, it will lead to spontaneous emission, which induces decoherence during an interferometric sequence. This decoherence leads to a dramatic decrease in the contrast of the interference fringes and reduces the sensitivity of the measurement. This phenomenon has been studied previously in our team[Andia, 2015b], and we apply the technique that was then implemented and characterized to overcome it: we place on the path of the lasers a heated cell that contains Rubidium atoms which absorbs the resonant part of the ASE spectrum. This preparation scheme is presented in figure (3.17).

Since the Bloch lasers are far detuned from the resonance ($\Delta \sim -40$ GHz), it is not attenuated by the heated cell. On the other hand, we checked the proper functioning of the cell by passing a beam resonant with Rubidium atoms through it. We observed an absorption or 99% of the beam power from a cell temperature of 40°C. In continous operation, the cell temperature is maintained around 85°C.

The reason why this filtering is necessary for the Bloch system and not for the Raman one is related to the duration of the light pulses: a few milliseconds for Bloch pulses and a fraction of millisecond for Raman pulses. Finally, this laser system, that produce optical lattices with variable velocities can also be used to perform Bragg transitions.

3.2.3.1 Relative frequency control

One of the main drawbacks of such a system is the RF generator discontinuations during frequency ramps which can result in a breakage of the laser system: during frequency ramps, some generators may stop for a duration of ~ 10 μs. During this period, the input AOM is shutoff, and no input light enters the EDFA. This duration is too short to be detected by the control photodiodes, and the EDFA accumulates excited Erbium ions. As soon as the input light comes back, these ions emit a strong light pulse that might damage the fiber itself or the doubling crystal.

In order to avoid such phenomenon, the 1560 nm AOMs are fed with the two fast output of a RedPitaya. Their programming ensures a fixed amplitude of the radiofrequency signal with controllable frequency.

3.2.3.2 Absolute Frequency control

The second drawback of this system is that the laser frequency at 780 nm is not constant with time, and in particular during the Bloch Oscillations pulse. Moreover, the stabilization process locks the NKT seeder laser frequency. In this context, it is preferable to sample a laser corresponding to twice the frequency of the NKT laser[2], without offset coming from the 1560nm AOM.

In order to meet such a requirement, we have picked off a fraction of one the lasers, similar to the Raman laser pickoff. However, before sending it the frequency stabilization setup, the laser beam goes through a double pass AOM system (see figure (3.17)), where the AOM is fed by the same frequency of the 1560 nm AOM. Moreover the alignment is set such that the laser is diffracted to the -1 order of the AOM, such that its output frequency evaluates to:

$$f = 2\left(f_{NKT} + f_{AOM}\right) - 2f_{AOM} = 2f_{NKT}. \tag{3.2.3}$$

This solution meets the requirement that we stated in the above paragraph. However, as we have exposed previously, the output frequency of a double pass configuration varies sharply with the input frequency of the AOM. Moreover, the frequency stabilization procedure is based on the Pound-Drever-Hall technique that slightly depends on the laser intensity. In the context of high precision measurement, this can lead to a systematic effect.

To circumvent this issue, we have set up a more expensive solution: we collect from the NKT laser 10% of its power and send this pickoff to another amplifier-doubling module and lock the NKT frequency with the output of this laser. This solution possesses the advantage on relying directly on a laser whose frequency $2f_{NKT}$ is constant.

In conclusion, we have presented a new laser system for the production of optical lattices at 780 nm based on amplification-doubling modules and where the frequency variation is performed before the amplification. Compared to usual double pass AOM systems, this one is compact and provides constant optical power at 780 nm over the whole frequency range. However, for applications demanding a frequency stabilization, this system requires an additional module. We have presented two solutions, one, cheaper based a double pass AOM that can be used if high accuracy in the knowledge of the laser frequency is not needed. The second, more expensive, based on the use of a third amplification-module system, is currently used on the experiment for the current work we are doing towards the measurement of the h/m ratio as it ensures accuracy on the laser frequency that is sent to the stabilization table.

[2] As our stabilization process is designed to work with signals at 780 nm

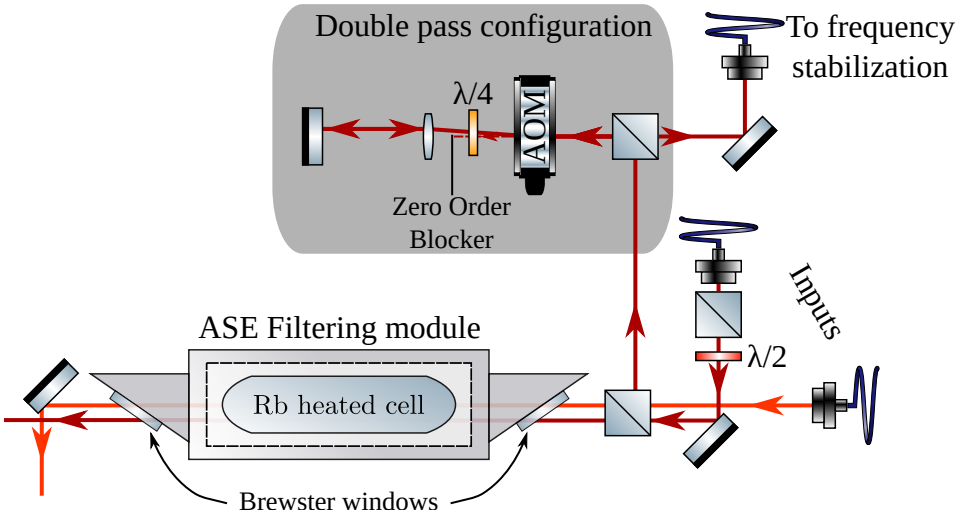

Figure 3.17: Schematics of the Bloch lasers preparation. The beam colors are meant for visualization purposes and do not represent the lasers frequency. One of the beam (in red) is picked off to a double pass AOM that erases the frequency shift induced by the 1560 nm AOM and can then be sent to frequency stabilization. Both beam pass through a Rubidium cell for ASE background filtering

3.2.4 Vertical path description

Before turning to the interferometry optical table design that aims to the final control of the lasers to interrogate atoms, we describe the optical path of those lasers in the vacuum chamber. This presentation will allow us to discuss the characteristic of the setup, and will exhibit the requirements for the interferometry lasers preparation. A schematics of this path is displayed on figure (3.18)

The choice of a vertical configuration for the interferometry lasers is guided by the fact that the atoms are subjected to the gravitational acceleration. As such, any horizontal configuration would be limited by this acceleration. With the vertical acceleration, we ensure that gravity does not move the atoms out of the laser beams.

Moreover, because Bloch Oscillations are implemented during the interferometer, we should ensure that the Bloch beams induce as little decoherence as possible. On top of the blue detuning that induces a trapping at the minima of intensity within the lattice, we should use a configuration that limits residual lattices as they would translate in a non zero mean intensity perceived by the atoms.

As a consequence, we use a configuration that makes each Bloch beam travel only once through the vacuum cell. The downwards going beam is deflected by

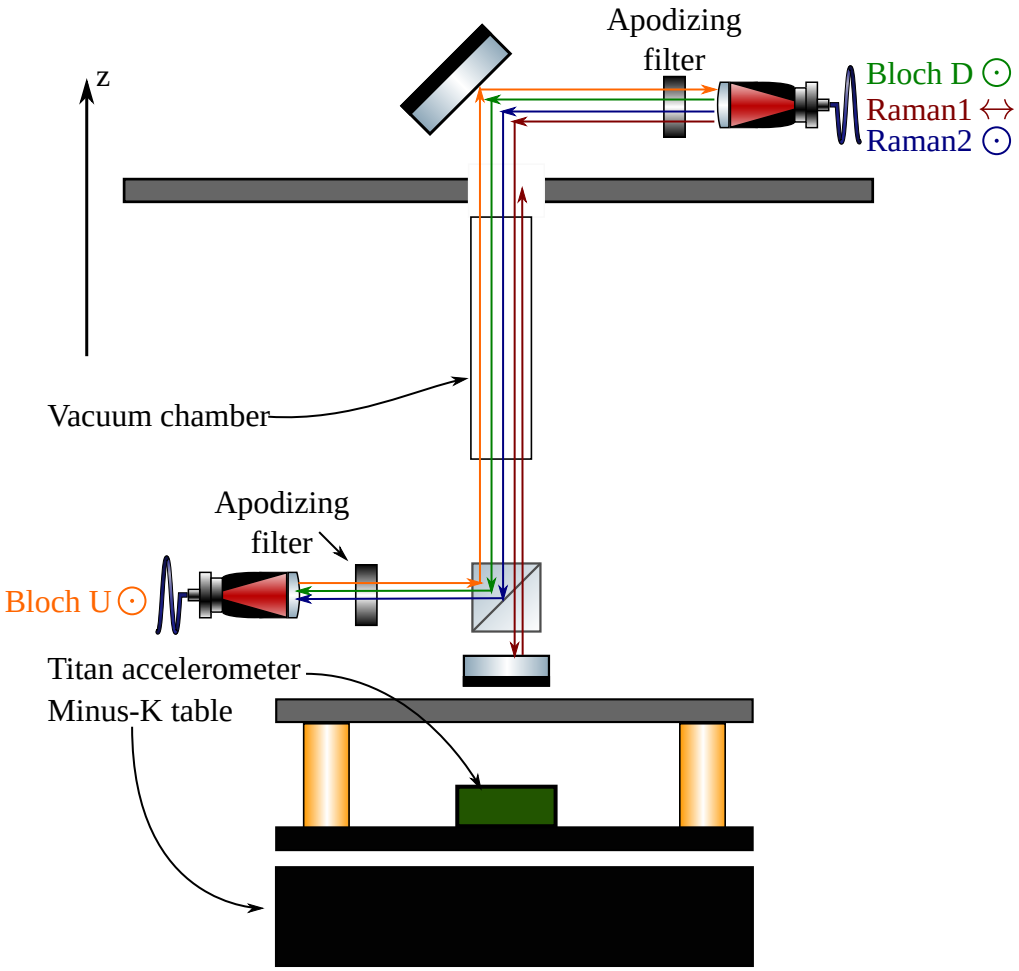

Figure 3.18: Scheme of the interferometry lasers path. The two Bloch beams are distinguished by their direction of propagation (Downwards (D) or Upwards (U)). Each interferometry beam is indicated next to its input fiber with its corresponding axis of linear polarization.

a PBS at the output of the vacuum cell and sent to the upwards going beam collimator to ensure proper alignment.

Moreover, the beams at the output of the collimators have a gaussian shape. In order to place ourselves in a configuration that is as close a possible to a plane wave, we need to use large beams. To achieve this, we use commercial (*SK 60FC-T-4-M75-02*) collimators that produce a beam with 6.25 mm waist. However, the beams are there not strictly gaussian as they present non-negligible intensity at their wings. In the interferometry region, which is a 5 cm diameter tube, these wings reflect on the edges producing parasitic reflections that induce decoherence of the atomic states during the interferometer.

We hence place reverse apodizing filters (*Thorlabs NDYR10A*) at the output of the collimators that cuts the beam wings and produce beams with a ~ 5 mm waist. Because these filter are metallic, they cause back reflections to the cell. This issue is solved by tilting the filters by a few degrees.

For the measurement of the recoil velocity, the beams alignments (counterpropagating condition) is an important parameter to be controlled within a few μrad. The alignment drifts will prevent us to reach such a precision over a extended period of time. We use PZT transducers on mirror mounts and the observation of the transmitted (or reflected) power through the input fiber. We set the PZTs at the maximum of observed power to ensure the best alignment possible between the different beams. This procedure is ran approximately every 45 minutes, so that the alignment is continuously optimized.

During the interferometers, Bloch acceleration is currently only used for common mode acceleration and we do not need phase coherence of the two beams. This is not the case for the Raman beams as their phase coherence is necessary to run the interferometer.

If the Raman beams were sent through different fibers, each fiber would induces a differential phase shift. This phase shift would not be constant over time as it would depend on environment fluctuations such as temperature. In the early stages of the experiments, a compensation of this phase noise was tried. However, it does not reach a sufficient stability.

As a consequence, the two Ramans beams should be sent to the vacuum cell through the same fiber. For counterpropagating configuration, we then need the beams to be retroreflected. Due to selection rules of the Rubidium atom, the polarization of the Raman beams should be orthogonal. As we use linear polarization, we may split the beams with a PBS. As such, above the retro reflecting mirror we place a PBS, in order to reflect only one of the Raman beams. As we have seen, this PBS is also used to send the upwards going Bloch beam and discard the

downwards going one, such that the polarization of the Bloch beams should be linear and is dictated by the PBS.

It should be noted that the presence of an additional beam increases the light shifts during the Raman pulses. Moreover, copropagating Raman transitions are also induced by the arrangement of the beams, which generates an additional energy level displacement. The effect of this displacement on the measurement of h/m is considered in section 6.3.1.3.

Let us now discuss the Raman phase noise of the system. The retroreflected beams travels an additional distance $2z$ induced by the back and forth in the cell. Any noise on z would then translate to the interferometric phase as $2k_\iota z$, where k_ι is the wavevector of the retroreflected Raman beam. This noise is related to the ground acceleration. We estimate its impact using the sensitivity function formalism and deduce the interferometer velocity sensitivity function g_v.

Indeed, we can measure the acceleration of the retroreflection mirror $a(t)$ and deduce from it $\mathrm{d}v = a(t)\mathrm{d}t$, and then compute an estimation the phase shift on the interferometer with:

$$\delta\Phi = \int_{-\infty}^{+\infty} g_v(t)\mathrm{d}v = \int_{-\infty}^{+\infty} g_v(t)a(t)\mathrm{d}t, \tag{3.2.4}$$

where g_v describes the impulsional response of the interferometer to a velocity jump of the retroreflecting mirror.

We recall that the interferometer phase shift with respect to a perturbation is given by:

$$\delta\Phi = \int_{-\infty}^{+\infty} g_\phi \frac{\mathrm{d}\phi}{\mathrm{d}t}\mathrm{d}t = \int_{-\infty}^{+\infty} g_\phi 2k_\iota \frac{\mathrm{d}z}{\mathrm{d}t}\mathrm{d}t \tag{3.2.5}$$

in our case. We can obtain the acceleration $\frac{\mathrm{d}^2 z}{\mathrm{d}t^2}$ through an integration by part and deduce the velocity sensitivity function:

$$g_v(t) = -2k_\iota \int_{-\infty}^{t} g_\phi(t')\mathrm{d}t' \tag{3.2.6}$$

For simplicity, we limit the discussion the to infinitely short pulse hypothesis, such that for the Ramsey-Bordé interferometer this function is given by (equation (2.2.73)):

$$g_v(t) = 2k_\iota \begin{cases} 0 & \text{if} \quad t < 0 \\ t & \text{if} \quad 0 < t < T_{\mathrm{Ramsey}} \\ T_{\mathrm{Ramsey}} & \text{if} \quad T_{\mathrm{Ramsey}} < t < T_{\mathrm{delay}} \\ T_{\mathrm{Ramsey}} - (t - T_{\mathrm{delay}}) & \text{if} \quad T_{\mathrm{delay}} < t < T_{\mathrm{delay}} + T_{\mathrm{Ramsey}} \\ 0 & \text{else} \end{cases}. \tag{3.2.7}$$

Considering the interferometer transfer function to a sinusoidal acceleration $a(t) = a_0 \cos(\omega t + \psi)$, we may obtain easily that $H_a(\omega) = |\widetilde{g_v}(\omega)|$. Moreover, from the properties of Fourier transform and derivatives, we have $\widetilde{g_v}(\omega) = -i(2k_\iota/\omega)\widetilde{g_\phi}(\omega)$, such that we have the simple relation:

$$H_a(\omega) = \frac{2k_\iota}{\omega^2} H(\omega), \tag{3.2.8}$$

because the phase transfer function of the interferometer writes $H(\omega) = |\omega\widetilde{g_\phi}(\omega)|$ (equation (2.2.81)). Thus, the velocity sensitivity function decreases sharply with the perturbation acceleration frequency. Indeed, considering a sinusoidal acceleration with constant amplitude a_0, as its frequency increases, it induces displacements that decrease as ω^{-2} from the integration of the equation of motion. As a consequence, the phase noise associated to this acceleration, proportional to the position shift of the mirror decreases with the same scaling factor.

For an explicit expression, we have from equation (2.2.81):

$$H_a(\omega) = \frac{8k_\iota}{\omega^2} \left| \sin\left(\frac{\omega T_{\text{Ramsey}}}{2}\right) \sin\left(\frac{\omega T_{\text{delay}}}{2}\right) \right|. \tag{3.2.9}$$

The limit $\omega \to 0$ yields

$$H_a(\omega) \underset{\omega\to 0}{=} 2k_\iota T_{\text{Ramsey}} T_{\text{delay}}. \tag{3.2.10}$$

We find here a result similar to the gravitational acceleration sensitivity of the output phase of the interferometer that takes into account the atomic motion. As such, a constant acceleration of the retroreflection mirror appears as a systematic shift in the determination of the central fringe. Moreover, because $2k_\iota \sim k_e$, the Raman effective wavevector, one may factorize the expression of the output phase in the presence of a constant acceleration a_0 from equations (2.2.66) and (3.2.4):

$$\Phi^{\text{interferometer}} = T_{\text{Ramsey}} \left(k_e(\Delta v - (g - a_0)T_{\text{delay}}) - \delta\omega \right). \tag{3.2.11}$$

As a consequence, the retroreflecting mirror can be seen as the referential in which the measurement is performed, and its control is of critical importance.

Furthermore, thanks to the limit in $\omega \to 0$ of the transfer function given by equation (3.2.10), we can obtain that the acceleration cutoff frequency is of the order of $f_c \sim \sqrt{T_{\text{Ramsey}} T_{\text{delay}}}^{-1}$. In practical purposes, we can assume that we are only sensitive to acceleration noise in the band $0 - 100$ Hz.

Unfortunately, this frequency band is quite populated in typical laboratory conditions. In order to isolate the retroreflecting mirror from this vibration noise, it is placed on a passive isolation table (*Minus-K BM4*), which has a cut-off frequency of 0.5 Hz when properly set.

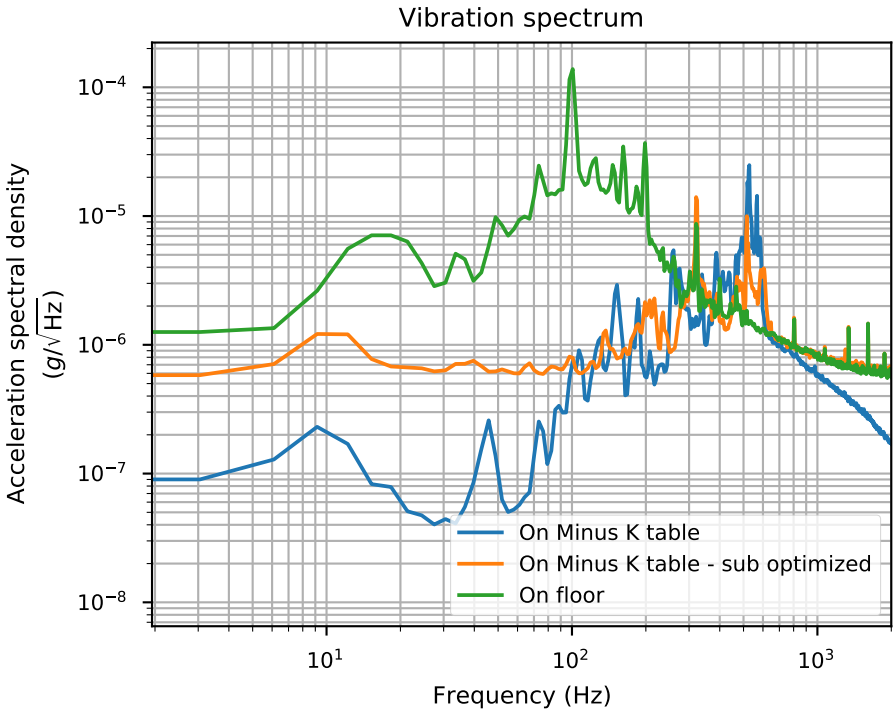

Figure 3.19: Acceleration power spectral density: without isolation (green), with sub optimized isolation (orange) and optimized isolation (blue). We obtained the data from an oscilloscope measurement. The high frequency ($\gtrsim$ 1 kHz) component of these power density is attributed to electronic noise.

In order to get the best isolation possible, a minimal number of optical elements are placed onto the table. However, because of this choice, the isolation platform is quite light and a such very sensitive to air flow from the air conditioning system. To reduce this sensitivity, the whole vacuum cell is embedded in a wood panels box that shield in particular from air flow.

Moreover, we place on the isolation table, beneath the retroreflecting mirror, an accelerometer (*Nanometrics Titan*) from which we can obtain the acceleration power spectral density, displayed in figure (3.19). This plot shows the importance of the adjustment of the isolation table. We estimate the phase noise induced by the acceleration noise to ~ 7 mrad using equation (2.2.82), with this data at optimal adjustement.

This phase noise is not negligible and we use the accelerometer to measure the vibrations during the interferometer and compensate them in the phase computation using the sensitivity function (equation (3.2.7)). The difficulty in such

a method is the calibration of the accelerometer. Currently, we use an *ad hoc* calibration constant based on minimizing the statistical uncertainty of a large interferometer fringes dataset.

Now that we have discussed the main source of noise in the phase induced by the Raman beams during the interferometer, we may discuss less important sources of phase noise. The top collimator from which both Raman beams are inputted to the vacuum cell is not isolated from environmental vibrations. However, the phase noise that these vibrations induce scales with an effective wavevector $|k_1 - k_2|$, which correspond to a sensitivity 10^{-5} less important than the retroreflection induced noise. The common propagation mode reduction is actually better than the isolation table!

Moreover, because the Raman beams are sent through the same fiber, one may expect that this cancels all transport phase noise. However, we send two beams with orthogonal polarization through a polarization maintaining fiber. The core of this kind of fiber is birefringent such that they do not share a common refractive index, either a common sensitivity to environmental perturbations. In order to limit phase noise from this effect, we place the fiber in a thermal sheath. Moreover, thermal fluctuations also affect the polarization at the output tip of the fiber. Concerning the Bloch beams, this translates as fluctuations of the main lattice height and creation of a residual lattice.

To conclude this description, we also need a blow-away that removes atoms in the $|F = 2\rangle$ hyperfine state and a repump that transfer all atoms in $|F = 1\rangle$ to $|F = 2\rangle$. These beams are obtained from the MOT optical table (see figure 3.4), and their polarization are orthogonal, similarly to the Raman beams case. In order to meet the behavior described, the blow away polarization is chosen so as that the beam is transmitted by the PBS. As a consequence, the repump is retroreflected and heats the atoms, unlike the blow away that pushes them.

3.2.5 Interferometry preparation

After the basic operations that we presented in sections 3.2.2 and 3.2.3, the laser beams should be manipulated in order for them to reach in a dynamically controlled way the vertical path described in the last section.

The bottom collimator is quite straightforward as it is the path of only one Bloch beam. However, the top collimator is fed with the second Bloch beams, the Raman beams, the blow-away and the repump lasers which correspond to three separated laser paths. Moreover, in the latter paths are superposed laser beams with orthogonal polarizations. As such, the beam superposition cannot be made with PBSs.

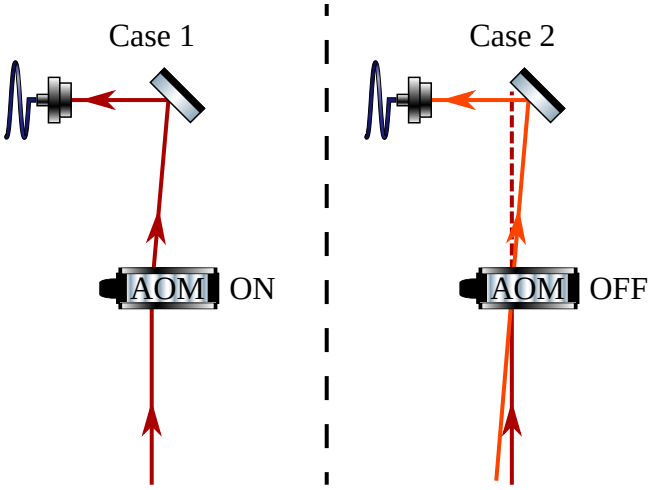

Figure 3.20: Principle of temporal superposition of two beams with an AOM.

Alternatively we can superpose beams in an AOM. The principle of the technique is displayed in figure (3.20). On the left we have displayed the usual AOM use as a switch. On the right, the AOM is off but we added a second beam that travels on the diffracted order path. Then both beams are superposed, and for example can be coupled to the same fiber port, but cannot be used simultaneously. This temporal separation is not an issue to us as the interferometer we perform rely on separate operation of Bloch Oscillations, Raman transitions and other manipulations.

We use this technique twice on the alignment towards the top collimator as can be seen in figure (3.21) that summarizes the manipulations made on the interferometry lasers. The top Bloch beam is diffracted through an AOM and then coupled. The Raman beams are diffracted with their own AOM, and the diffracted order is aligned to the Bloch diffracted path. Finally, the blow-away and repump lasers, obtained from the MOT table (figure (3.4)), are there controlled with their own AOM, and their path is superposed to the diffracted order of the Raman AOM.

Finally, in the superposed Raman beams path, we place a movable half-waveplate that rotates the polarization by 90°. This waveplate is placed on a translation stage whose motion is controlled by a servo motor. On the vertical path, this waveplate controls the beam that is deflected by the bottom PBS and as a consequence the Raman direction.

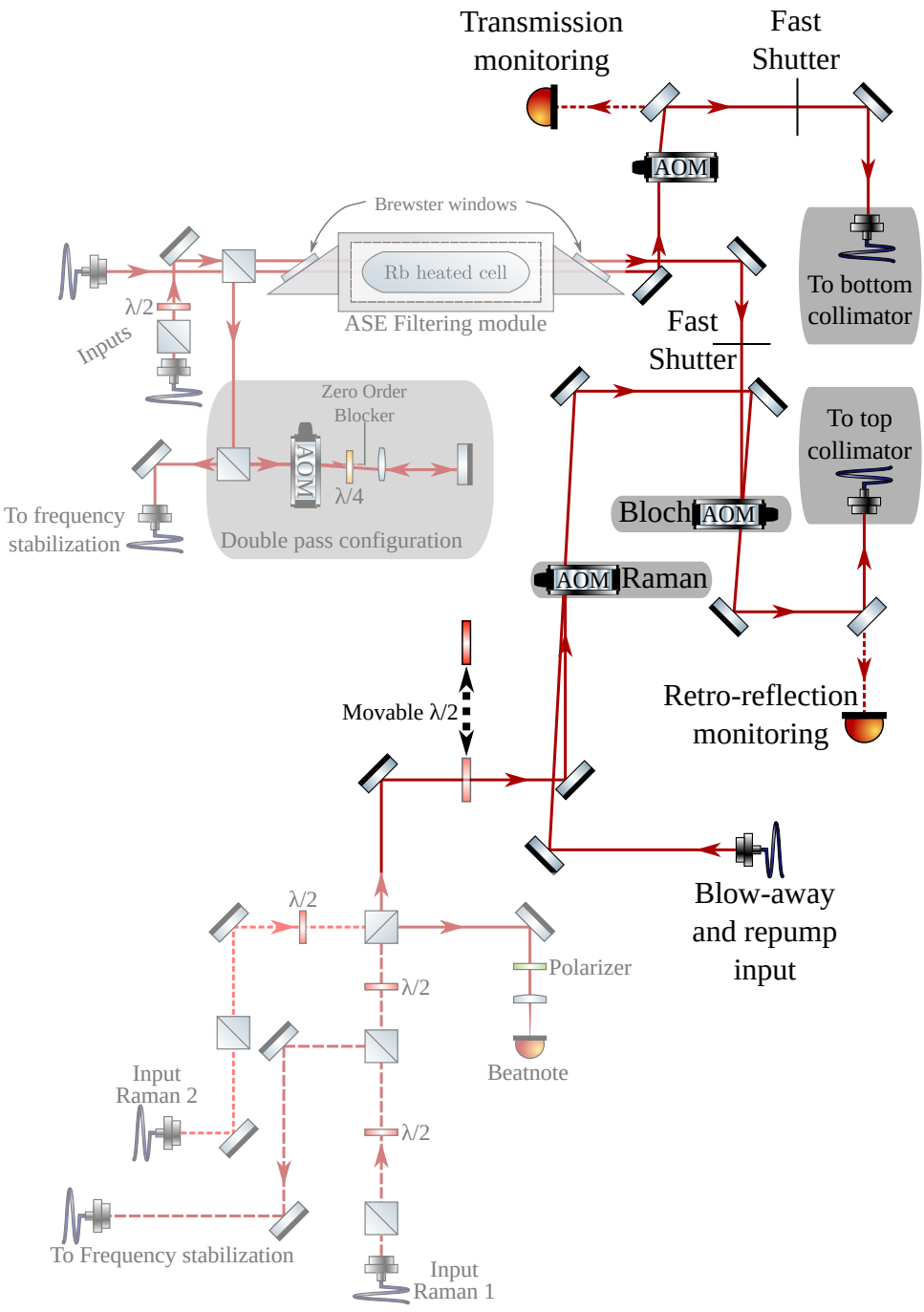

Figure 3.21: Interferometry optical table. The shaded parts have been described in figures (3.13) and (3.17) and are put for comprehensiveness of the table description. The remaining of the table feed the vertical path collimators with the necessary beams.

3.2.6 Frequency stabilization

The measurement of the h/m ratio requires a perfect knowledge of the Raman and Bloch lasers frequencies. The first step is to stabilize their frequencies, and then measure them.

The stabilization process has been described in [Jannin, 2015a] and is based on Pound-Drever-Hall technique on an ultra stable cavity which is itself locked to a two photon transition of ^{85}Rb.

The measurement process is based on the comparison with a frequency comb[Diddams, 2000] located on the second floor of the Jussieu building thanks to a fiber link between our laboratory and the frequency comb platform. We send in both lasers thanks to a fiber power splitter that we use as a combiner. Thanks to the agility of the frequency comb parameters, we can obtain separable beatnote RF signals for each laser, and measure them independently.

The time reference for this measurement is obtained from a 100 MHz signal issued by the SYRTE laboratory from their atomic microwave clock. This signal locks a quartz oscillator that outputs a 10 MHz signal which is used as a reference for the frequency counters. We also use this reference signal in our lab to control precisely the output frequency of our generators.

3.3 Operation of the experimental setup

3.3.1 Sequence programming

We have detailed in the last two sections the setup that produces cold atom gases and the laser system to interrogate them. We now describe the control system that synchronizes these elements.

Our control computer is connected to a National Instrument card that has 32 Digital Outputs (DO), 4 Analog Outputs (AO) and 4 Analog Inputs (AI), which we use to record the atomic time of flight signal that are described in the following section. The high number of DOs allow us to synchronize all the instruments, however the 4 AOs are not sufficient to run the experiment. As such, we have second NI card with 2 AOs. We also use its AIs for laser power monitoring purposes.

The dynamical control of the interferometry laser intensities (AOMs at 780 nm) and relative frequencies (phase lock for Raman, AOMs at 1560nm for Bloch) is performed through the use of Direct Digital Synthesizer (DDS) based on *RedPitaya* modules developed by Pierre Cladé. These DDS are agile and thus give us the possibility to change easily the experimental parameters.

Finally, we program the instruments with an interface based on the *Python* language. The back-end of this interface consists in the definition of the instruments

and the creation of the tools to manipulate them. On the front-end program, we build experimental sequences through a series of instructions based on the definitions in the back-end. These instruction are read and sent to the instruments by the Python interface within a few hundreds of milliseconds. The loading of the MOT is done during this dead time, in order to optimize the efficiency of the setup.

Once all the instruments are ready, the experiment can start. After the execution of the instructions, the program is read again with possible parameter change.

3.3.2 Light sheets detection

After the laser pulses have been applied to the atomic cloud, we have to detect their internal state. To this end, we use a setup based on the collection of fluorescence photons emitted by the atoms in a resonant laser field. A scheme of the setup is displayed on figure (3.22)).

In order to present its operation, let us assume that a cloud of atoms passes through it. In the cloud, some atoms are in $|F = 2\rangle$ and the others in $|F = 1\rangle$. The first sheet that the atoms encounter as they fall down is set to be resonant with the cycling transition $|F = 2\rangle \rightarrow |F' = 3\rangle$, and as such is circularly polarized with a quarter waveplate. It does not affect atoms in $|F = 1\rangle$. The beam is furthermore reflected, which places the atoms in conditions close to an optical molasse and extends their lifetime in the beams and as a consequence, increases the fluorescence signal.

At the bottom of the sheet, a cache blocks the reflection and atoms in $|F = 2\rangle$ are blown away from the detection system. The photons that were emitted during their travel are collected with a simple imaging system: we use two *Thorlabs AC508-080-B* achromatic lenses to limit aberrations with present a 50 mm diameter in order to maximize the solid angle of the collection. At the focal point of the system, in a $4f$ configuration for compact size, we place a large photodiode (10 mm square side, *Hamamatsu S1337-1010BR*) whose output current is then amplified and converted to a voltage with a transimpedance amplifier with an operational amplifier.

The remaining atoms in $|F = 1\rangle$ then pass through a repump sheet, resonant with the $|F = 1\rangle \rightarrow |F' = 2\rangle$ transition that transfer the atoms to $|F = 2\rangle$. They are furthermore detected in the third light sheet and a second photodiode, similar the first sheet setup, which allows for close detection characteristics for both internal states.

An example of signal is plotted on figure (3.23). The top plot shows the raw data produces by the two photodiodes. In order to reduce the noise on those

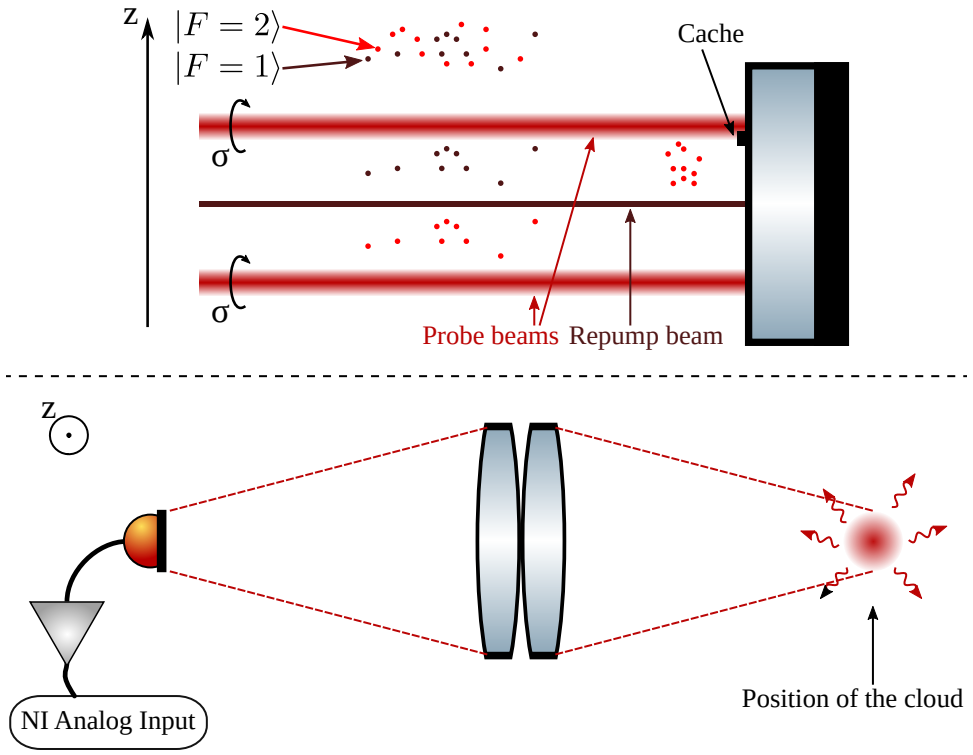

Figure 3.22: Scheme of the detection setup. On top, a view from the side that shows the counterpropagating circularly polarized light sheets. As the atom falls, the figure reads from top to bottom. The atoms in $|F = 2\rangle$ are detected in the first light sheet and blown away thanks to the cache on the retroreflecting mirror. The remaining atoms, in $|F = 1\rangle$, are then repumped and detected. On the bottom, a view of the imaging system from the top: the atom cloud is imaged on photodiodes (one for each state, only one is represented), whose signals are then amplified and recorded.

signal, we analyse the difference of the two which eliminates common noise on the two photodiodes. The differential signal is then fitted with a gaussian difference:

$$\text{fit}(t) = -a_2 \exp\left(-\frac{(t-t_{0,2})^2}{w_2^2}\right) + a_1 \exp\left(-\frac{(t-t_{0,1})^2}{w_1^2}\right) + \text{offset}, \tag{3.3.1}$$

from which we extract the relative populations of atoms. In particular, we find that the width of the signal are similar $w_1 \sim w_2$ so that we assimilate the amplitudes a_1 and a_2 to the atom number.

Currently, the main source of noise on the interferometer readout comes from frequency noise on the stabilization of the *repump* and *cooling* lasers. As the sensitivity we obtain with this limitation is satisfying, we did not yet reworked the stabilization system.

3.3.3 Operation and characterization

We have presented the building blocks of our experiment. With them, we can manipulate the atoms in order to extract information. We usually start an experimental sequence with a launch pulse 10 ms after the release of the molasse. This launch pulse is made of 650 BO, and the atoms reach the interferometry area within ~ 100 ms. We can then position them precisely with a second Bloch pulse.

Furthermore, we can also perform a longitudinal velocity selection (see figure (3.26)). At the output of the molasse, the atoms are distributed on the Zeeman sublevels of $|F = 2\rangle$. We apply a counterpropagating Raman π pulse that transfers atoms in $|F = 2, m_F = 0\rangle$ to $|F = 1, m_F = 0\rangle$, provided their longitudinal velocity satisfies the resonance condition. The remaining atoms in $|F = 2\rangle$ are blown away with resonant light. The atoms that were transferred by the Raman pulse are then transferred back with a second Raman π pulse.

This set of pulses constitutes also a Zeeman sublevel selection. Using copropagating transitions, we can select the Zeeman sublevel without performing a velocity selection. With counterpropagating transitions, the width of the velocity selection is controlled by the duration of the first π pulse, that we can change easily through the amplitude of the radiofrequency signal sent to the AOM.

We give below two characterizations that illustrate these techniques: the measurement of the magnetic field inside the interferometry area and the measurement of the gravity gradient.

3.3.3.1 Magnetic field measurement

When running interferometers, we use the magnetically insensitive Zeeman sublevels $m_F = 0$. On the other hand, the measurement of the magnetic field

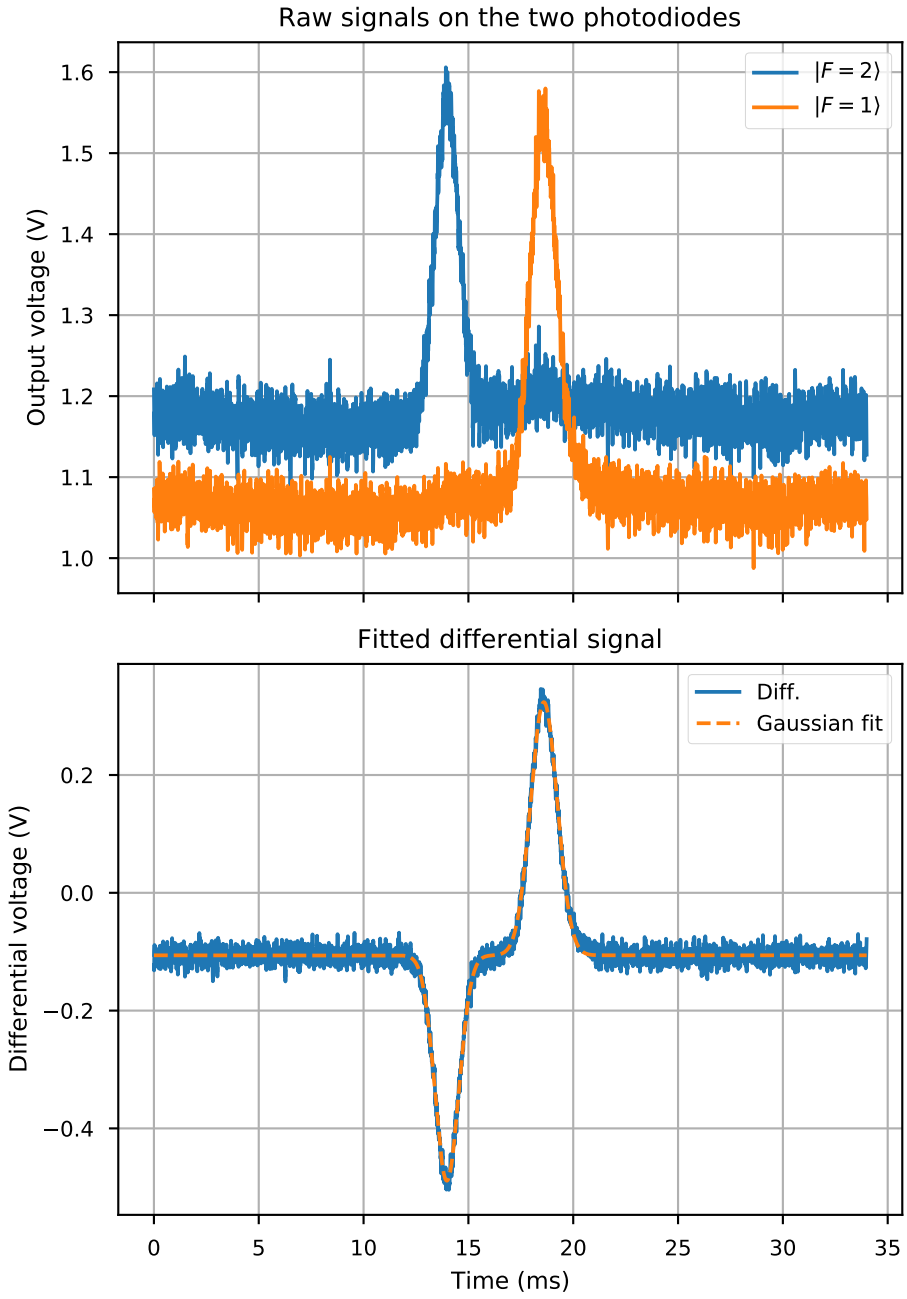

Figure 3.23: Signals obtained with the light sheets detection. Top: raw signals of each photodiodes. Bottom: differential signal for processing and its fit with two gaussians.

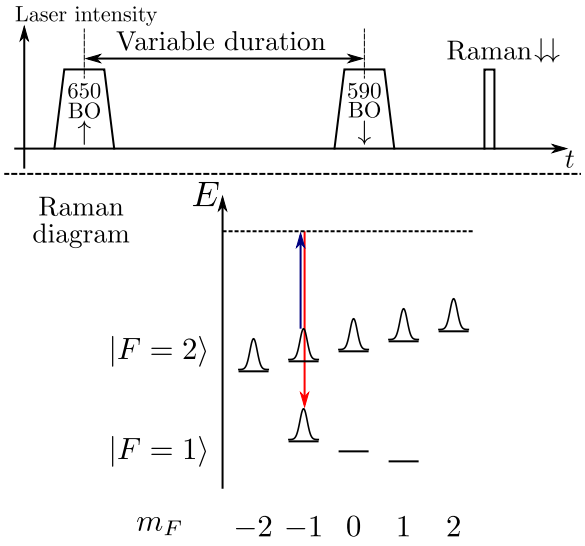

Figure 3.24: Measurement of the magnetic field. Top: laser pulses arrangement. The Bloch and Raman intensity scales are different for visibility. Bottom: Zeeman sublevels population and addressed transition. The horizontal axis represents the longitudinal velocity distribution.

requires a transition on magnetically sensitive states. The crossed linear polarization of the Ramans beam and selection rules in Rubidium atom impose that the transitions can only occur between state of same m_F. Finally, since the Landé g-factors of the ^{87}Rb hyperfine have opposite signs, the transitions $|F=1, m_F=\pm 1\rangle \rightarrow |F=2, m_F=\pm 1\rangle$ are sensitive to the magnetic field with a sensitivity of 1.4 MHz·G^{-1}[Steck, 2001].

We chose to address the $m_F=-1$ transition. A scheme of the protocol is described on figure (3.24). The atoms are placed with two Bloch pulses, which work as an *elevator*. Over the repetition of the measurements, the number of Bloch Oscillations is unchanged, but the timing of the second Bloch pulse controls the altitude of the atoms at the Raman pulse, placed at a fixed timing. As a consequence, the parameters of the cloud (size, velocity, ...) during the Raman pulse are independent of its position.

In order to measure the magnetic field, we use copropagating transitions, whose Doppler sensitivity is highly suppressed. As we aim to measure the transition in the $m_F=-1$ states performing an internal state selection is difficult as it demands an *a priori* knowledge of the magnetic field. We use instead the output of the molasses where all the sublevels of $|F=2\rangle$ are populated.

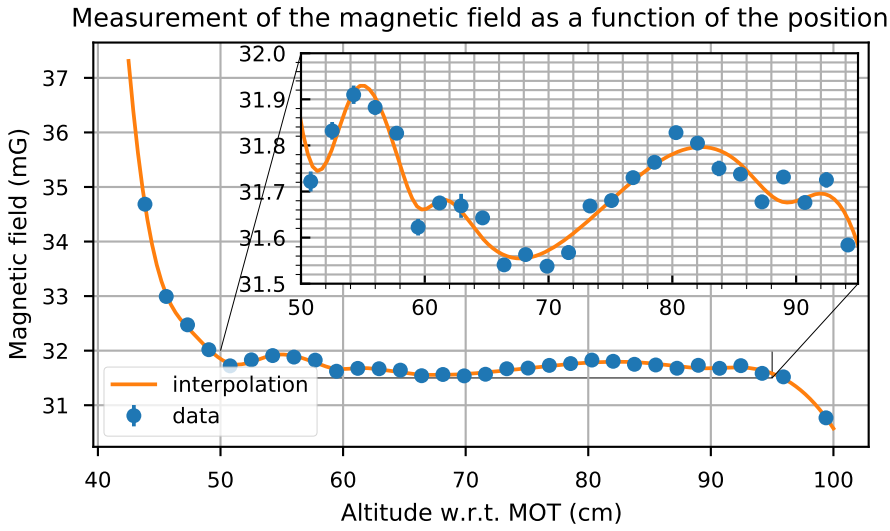

Figure 3.25: Measurement (blue dots) of the magnetic field as a function of the position. The orange line corresponds to an interpolation of the data by an univariate spline. As explained in the text, the absolute value of the magnetic field estimation is perturbed by systematic errors. In the plot, the displayed uncertainty does not takes them into account to exhibit the estimation of the magnetic field inhomogeneities. The error bars are smaller than the points for most data.

We then scan the frequency difference of the Raman lasers at each position, performing a Rabi spectra. From the fit of these spectra, we deduce the resonance condition and as such a magnetic field estimation. However, the accuracy of the measurement is limited by the lack of knowledge on the light shifts during the Raman pulses that displaces the resonance condition. As a consequence, the absolute value of the magnetic field indicated on figure (3.25) is precise within 5%.

Nevertheless, the systematic errors induced by light shifts are independent of the position, and we can use these data to estimate the magnetic field gradients within the setup. The results are displayed in figure (3.25).

On the edges of the interferometry area, and as such of the solenoid and of the magnetic shield, the magnetic field exhibit large variations. However, in the center of this area, in a 45 cm long distance, we have a well controlled magnetic field with local gradients less than 4 mG·m^{-1}.

In particular, the lower region (50-60 cm altitude) presents the higher inhomogeneities. If we exclude this region, then the local gradients can be estimated as less than 2 mG·m^{-1}. The source of these gradient is attributed to variations of the coil density in the solenoid.

This study exhibits one the improvements of the new experimental setup. On the previous setup, a detailed study of the effect of the magnetic field was performed[Andia, 2015a]. On this setup, the magnetic field gradients reached 4 $\mathrm{G{\cdot}m^{-1}}$ at their maximal value. Moreover, a detailed confrontation between experiments on the previous and appropriate simulations showed a discrepancy. This discrepancy was interpreted as the signature of a transverse magnetic field.

If the direction of the magnetic field is not parallel to the Raman lasers propagation direction, then their effective polarization is modified, and as such the selection rules. In particular, the $m_F = 0 \rightarrow m_F = \pm 1$ transitions may be observed. In the new setup, prior to installing the magnetic shield, we were able to observe such transitions. After the installation, they are forbidden.

As a conclusion, we have demonstrated that the magnetic field in the interferometry area is longitudinal, and that its value is well controlled. In particular, we can run the experiments with magnetic field gradients three order of magnitude smaller than on the previous setup.

3.3.3.2 Gravity gradient measurement

When we treated interferometry, we computed the phase difference between the two arms if the gravitational acceleration depends linearly with the altitude. We obtained that in the presence of gravity gradient γ such that $g(z) = g_c - \gamma z$, the phase difference between the two arms scales linearly with the position (equation (2.2.60)). In particular, comparing interferometers at different altitude but with the same initial velocity, we expect to observe a linear variation of the measured acceleration.

This reasoning holds with a differential velocity sensor interferometer. Moreover, thanks to the elevator technique based on Bloch Oscillations, we are able to run interferometers which differ only by their altitude. We were then able to measure the linear gravity gradient using the pulse arrangement displayed on figure (3.26).

After the elevator sequence, we perform a differential velocity sensor with $T_{\mathrm{Ramsey}} = 45$ ms and $T_{\mathrm{delay}} = 50$ ms in order to enhance the sensitivity to g. Moreover, we place two Raman π pulses that perform a velocity selection. The diagram at the bottom of figure (3.26) shows the evolution of the atomic states along the selection pulses. In particular, the Rabi frequency of the first Raman pulse is reduced in order to perform a narrow velocity selection. The Rabi frequency of the second pulse is then increased in order to ensure a very high efficiency for transferring back the atoms to $|F = 2, m_F = 0\rangle$.

We plotted the results of this study in figure (3.27), which indeed display a linear decrease of the gravitational acceleration with the altitude. In particular,

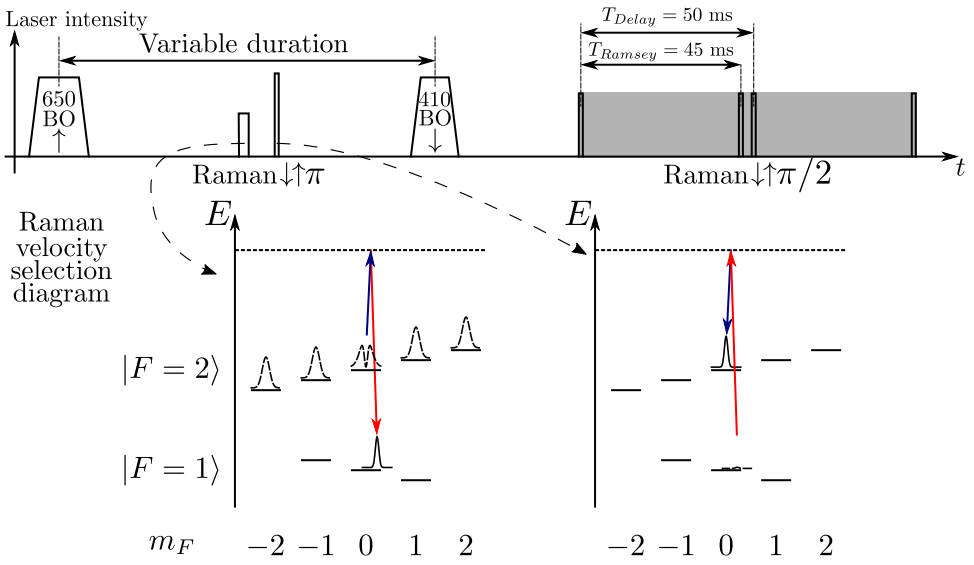

Figure 3.26: Measurement of the gravity gradient. Top: lasers pulses arrangement. A Raman based velocity selection sequence is placed in between of a Bloch based atom elevator. This sequence is then followed by an atom interferometer (in gray). Bottom: Zeeman sublevels population during the velocity selection. The horizontal axis represents the longitudinal velocity displayed. Solid lines of the velocity distribution represent the transfer by Raman pulses. Dashed lines represent the remaining atoms that are eliminated by a blow away (left) or a repump pulse (right)

the gravity gradient is estimated to

$$\gamma = (2.24 \pm 0.15) \cdot 10^{-6} \text{ s}^{-2}. \tag{3.3.2}$$

This value is in disagreement with the prediction obtained by developing Newton's law $F = -GmM_{\odot}/R_{\odot}^2$ above the Earth surface[3] which yields $\gamma \sim 3 \cdot 10^{-6}$ s^{-2}. Obtaining a prediction of the gravity gradient is a difficult task because it requires a precise knowledge of the laboratory environment.

However, we can note that in a spherical model of the Earth, the gravity gradient is discontinuous at its surface. Such an observation was performed in this study [Bidel, 2013], where the authors placed a gravimeter based on atom interferometry in an elevator and observed such a discontinuity at the basement transition. This study shows a lower gradient in the underground, with a value of $\gamma = (2.626 \pm 0.016) \cdot 10^{-6}$ s^{-2}, attributed to the mass of the soil above the measurement points.

[3]The $\odot$ indicates Earth related quantity. The centrifugal acceleration is negligible in this context.

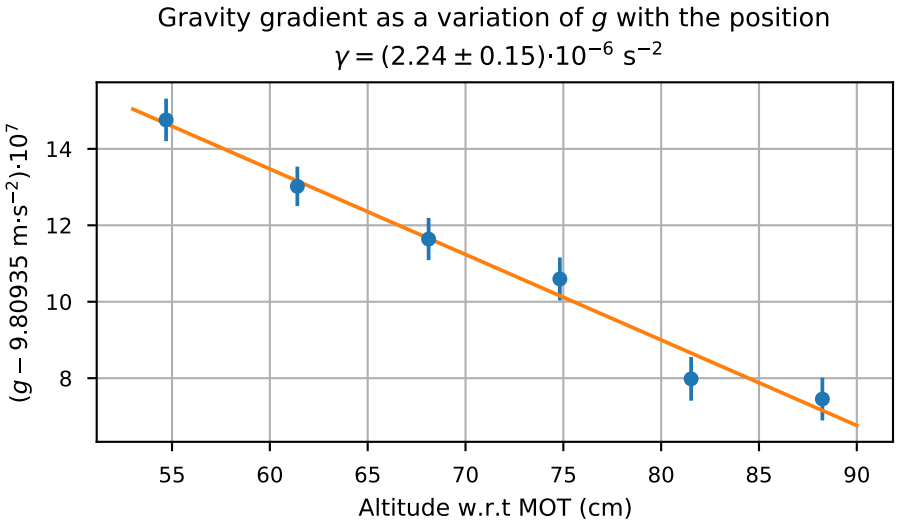

Figure 3.27: Variation of the measured gravity with respect to the altitude (blue dots). We can estimate the gravity gradient parameter γ from the linear fit (in orange). The relative precision on this parameter is 6.7%.

Even if our laboratory is located in the basement of the Jussieu campus, with a five-story building above, the lower value of the gravity gradient we obtained is a surprising result. We did not investigate this measurement further. Moreover, the relative precision of the measurement 6.7% limits our ability to correct the perturbation induced by the gravity gradient.

As we will see in section 6.2, we developed a protocol to cancel the systematic error induced by the gradient of gravity in the determination of h/m. The development of this protocol was motivated by the fact that our experimental setup is not adapted to a very precise measurement of the gravity gradient. The application of this protocol relies on the assumption of a constant gravity gradient, as observed in this study.

Following the presentation of the experimental setup, we detailed its operation. In particular, we showed two characterizations that enabled us to present our techniques to prepare the atoms before the interferometer: the atom elevator based on Bloch Oscillations and the velocity selection based on Raman pulses. Moreover, these studies allowed us to draw to conclusions:

1. The magnetic field in the interferometry area is well controlled, which is a dramatic improvement with respect to the previous setup.

2. The linear gravity gradient is not easy to measure with a high precision in our setup and should be canceled using a suitable experimental protocol.

The new experimental setup features several additional improvements with respect to the setup used for the 2011 measurement[Bouchendira, 2011]: the technology derived from 1560 nm has been used to provide an agile laser with constant output power for Bloch Oscillations. Moreover, we can produce gases in a large temperature range $\sim 40\ nK$—$\sim 4\ \mu$K thanks to the optical dipole trap. However, our current studies are limited to the two limits of the range.

We will now turn the presentation of the operation of this setup. We will start with the optimization of the condensation process and its application to the investigation of inter-atomic interactions in a BEC. This work has been performed in the main chamber of the vacuum cell and not in the interferometry area. Then we will describe the results that we obtained by elevating thermal gases produced by optical molasses in the interferometry area. We will explicit velocity dependent phase shift with Raman transitions and how we have taken advantage of them to compensate for the expansion of the molasse.

Finally, we set up the protocol for the h/m measurement which features unprecedented sensitivity and advance on the study of related systematic effects.

Part II

Results

Chapter 4

Atom sources comparison

As we have announced in the introduction and seen in last chapter, the experiment can produce cold atom sources either at low temperature ($\sim \mu$K) from optical molasses or ultra-cold at lower temperature (a few tens of nK) through evaporative cooling. With the latter process, we can achieve BEC regime.

The choice of the atom source is critical for the h/m measurement. On the one side, running interferometers for precision measurements with a BEC as an atom source requires to deal with some challenges. Among them, the number of atoms must be sufficiently high. In theory, in a BEC, phase space density has been highly increased so that the question of the signal-to-noise ratio remains open.

Moreover, in precision measurements, the statistical uncertainty is limited by the production rate of the atomic source. As the evaporation process takes a few seconds, it is the limiting factor of the experiment cycle time. Finally, in a BEC, atom-atom interactions are not negligible, and should be evaluated precisely.

On the second side, running interferometers with optical molasses has the advantage of a better integration potential as the production process takes place in less than a second.

However, the duration between the production of the cloud and the start of the interferometer is $\gtrsim 150$ ms. In this context, the cloud has expanded and the interferometer phase might be sensitive to the reduction of the mean intensity seen by the atoms.

We have seen in section 2.2.5 that the interferometer phase can be considered insensitive to intensity variations along the interferometer if the Raman transitions can be considered resonant. This is however not the case because of the one-photon light shifts induced by the lasers driving the Raman transitions. In this chapter, we present a theoretical and experimental study of the contributions of resonance mismatch during Raman transitions to the interferometer output phase.

This chapter is composed of two parts. The first part is devoted to the optimization of the BEC production in an optical dipole trap. At this stage of the experimented, the setup was not equipped with interferometry lasers sources. We have then realized Ramsey sequences based on microwave transitions between the two hyperfine states of ^{87}Rb. This work was motivated by a model previously developed in our team based on the Gross-Pitaevskaii equation to evaluate the contribution of the interactions at the output of an atom interferometer sequence[Jannin, 2015b].

After installing the interferometry lasers setup, we tested the experiment with optical molasses. We obtained rapidly a better sensitivity on h/m (section 5) than the one of the last measurement ($4.4 \cdot 10^{-10}$ in 15h[Bouchendira, 2011]). At this point, we investigated the impact of the expansion of the cloud on the interferometer.

I would like to point out that I have chosen to present these two surveys together to discuss the choice of atomic source. This remains a non-exhaustive study.

4.1 Optimization of the Bose Einstein Condensates production process

4.1.1 Sequence for the production of a BEC

4.1.1.1 Dipole trap loading

Performing an optical molasse and loading atoms into a dipole trap are related has they both start from a MOT, and use the same laser system[1]. However, the setting of the lasers parameters are quite different.

The output atomic hyperfine state of the optical molasses that we produce is $|F = 2\rangle$, but we choose to load atoms in $|F = 1\rangle$ in the dipole trap. The choice of $|F = 1\rangle$ is guided by the fact that atoms in $|F = 2\rangle$ can decay to $|F = 1\rangle$ through non elastic two-body collisions that liberates energy, and as a consequence heats the trapped gas[Grimm, 2000].

As a consequence, the loading of the dipole trap requires specifics cooling steps that are displayed on figure (4.1). It starts similarly as the molasse preparation with a compression stage, which is followed by two molasses stages during which the dipole trap laser is turned on. When this appends, the repump beam that gets amplified in the MOPA of the MOT table (figure 3.4) is mechanically shut, and the repump amplitude is controlled through the auxiliary channels shared with the imaging system. This amplitude gets lowered in the final stage of the loading such

[1] At the exception of the high power infrared laser that generates the dipole trap

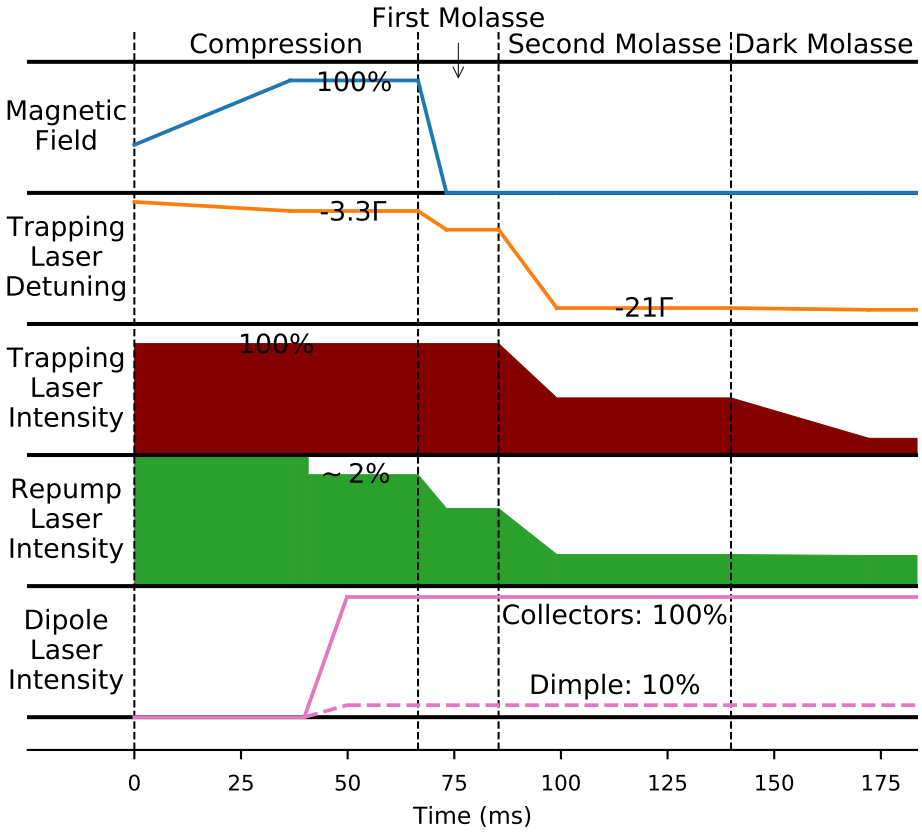

Figure 4.1: Steps sequence for the efficient loading of the dipole trap. At the end of the sequence, the trapping and repump laser are abruptly shut off while the dipole laser powers are then ramped for the evaporation sequence.

that atoms fall in $|F = 1\rangle$, trapped in the dipole trap and no longer sensitive to the cooling laser.

4.1.1.2 Genetic algorithm

The parameters of this sequence need to be carefully adjusted. Moreover, their number, 27, is quite large, and we found empirically that they are highly correlated among them. As a consequence, it is highly probable that the parameters space presents a large number of local minima that we may mistaken with an optimal setting during a manual search.

In order to circumvent this issue, we developed the implementation of an optimization of the setup based on a *genetic algorithm*. The choice of a genetic algorithm was guided by the fact that it is relatively simple compared to machine

learning based method[Wigley, 2016], and by the fact that it relies on random numbers to explore maximally the parameters space.

The principle of the algorithm goes as follow:

1. A collection of parameter sets $\left\{X^{(J)} = \left\{x_k^{(J)}\right\}_k\right\}$ is randomly generated from initial conditions.

2. Each of these parameters set is tested on the experiment. From a combination of observables, we determine a *fitness* of the parameters set $\mathcal{F}^{(J)}$ that should be maximized[2]. The parameters set are sorted by their fitness.

3. The generation of a new collection of parameters set starts with a selective *breeding* phase. We randomly choose two parameter sets $X^{(J_1)}$ and $X^{(J_2)}$. The higher the fitness, the higher the probability to be chosen. We then draw a random number linearly distributed in $[-\beta, 1+\beta]$ with $\beta > 0$,[3] from which we perform a linear interpolation to generate a new parameter set:

$$X^{(\text{new})} = \left\{\beta x_k^{(J_1)} + (1-\beta)x_k^{(J_2)}\right\}_k \tag{4.1.1}$$

   Because $\beta \neq 0$, the interrogation of the parameters space is made larger. Finally, this renewal of the collection is not total, as we usually keep the $\sim 40\%$ best sets in the population.

4. Once the breeding phase is performed, we enter the *mutation* phase during which each parameter of the sets might be altered *individually*. We use a 20% probability that the mutation occur, and use gaussian distribution on the alteration value. This phase is critical to ensure a large scan of the parameters space.

5. Go back to step 2.

When running the algorithm, the choice of the fitness function is critical. As we have seen in section 3.1.5, the evaporation is governed by a power law such the initial number of atoms N should be as high as possible and the sample temperature T as low as possible. We chose to use:

$$\mathcal{F} = \frac{N}{T}. \tag{4.1.2}$$

Because of the power law scaling, one may consider fitness function as N/T^γ. Empirically, we observe no improvement when setting $\gamma \neq 1$.

[2] Another formulation for algorithm is to describe the *fitness* as a *cost function* of the parameter set. The difference between the two is that the cost function should be minimized

[3] We use $\beta = 0.4$

In order to extract the number of trapped atoms and the temperature of the gas, we load the dipole trap with the parameter set, then wait for 200 ms such that the atoms that were not trapped fall under the effect of gravity. We then release the cloud, let it expand for 18 ms and observe it with an imaging sequence. The typical image that reconstruct from this process is displayed on figure (4.2, left). The images are fitted with a two dimensional asymmetric gaussian fit from which we extract estimator for the atom number and the temperature.

The results of the algorithm are given on figure (4.2, right), where the algorithm was left to run for an hour. At the beginning of the algorithm, we observe a sharp rise of the fitness function in ~ 10 minutes. After this duration, the improvement of the algorithm determination happens at a slower rate. After an hour, it seems that it has not converged yet. We can draw some conclusions from these considerations.

First, upon clearly suboptimal parameters, one may run the algorithm for a few minutes to get improved parameters. Although not optimal, those parameters may be sufficient for some procedures on the experiment. This feature is particularly interesting in the hypothesis of a sudden change of the experimental parameters (for example a loss of laser power). By running the algorithm and comparing the new parameter set to the old one, one may rapidly get insight on the experimental issue that occurred.

Secondly, the algorithm needs more than an hour (and a thousand repetitions) to converge. This confirms that the parameters space of the dipole trap loading present a complex structure, and shows that the parameters of the algorithm are set so that it does not converge too rapidly to a local minima of the parameter space.

After a few hours of algorithm interrogation (which can be performed over night), we obtain a set of parameters that allow us to load typically $1.5 \cdot 10^7$ atoms at $\sim 25\mu$K in the dipole trap. Compared to previous results, we double the number of atoms loaded at the same temperature. As a consequence, the performance of the condensation process has been improved as we are able to produce BEC with $120,000$ atoms at ~ 40 nK.

Moreover, we applied the algorithm on the evaporation ramps sequence with the objective of reducing the duration of the evaporation. The algorithm provided with two seconds long ramps with the same atom number in the BEC at their output. Loading the MOT and the dipole trap takes also ~ 1.5 seconds, such that the performance of the setup is the production of $120,000$ atoms BECs every 3.5 seconds.

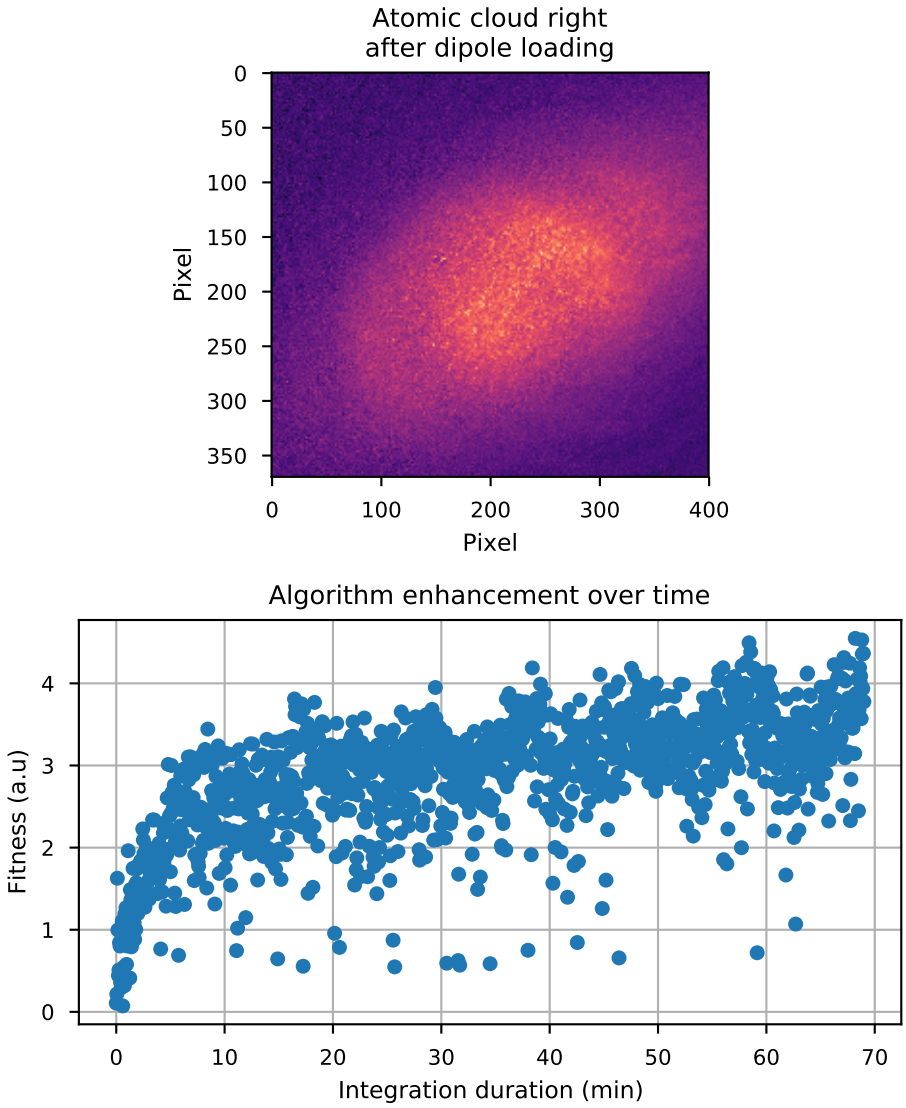

Figure 4.2: Top: Image of the cloud loaded in the dipole trap after 18 ms time of flight with parameters obtained with genetic optimization. The maximum optical density is 1. Bottom: Results of the algorithm on the loading of the dipole trap as a function of time. After a sharp rise in the setup performance, the algorithm based-enhancement increases of the hour timescale.

4.1.2 Atom-atom interactions phase shift

4.1.2.1 Spin distillation

The optimization of the production process paved the way to the observation of phase shifts induced by atom-atom interactions. However, an optical dipole trap is insensitive to the hyperfine Zeeman sublevels. As a consequence the three $m_F = 0, \pm 1$ levels are present in the trap.

Performing a Stern-Gerlarch experiment by applying a magnetic field gradient with the MOT coils at the end of the evaporation sequence, we are able to separate the three hyperfine states. We present a set of images taken doing such an experiment in figure (4.3).

When performing atom interferometry, we prefer to work with the magnetically insensitive sublevel $m_F = 0$. If the three Zeeman sublevels are populated, the contrast of the interferometric signals will be reduced. More importantly, as we can see in figure (4.3), the relative population between the sublevels varies shot to shot with fluctuations up to $\pm 30\%$ of the mean atom number. As a consequence, we will face high contrast noise in the fringes signal.

We have chosen to use the technique of spin distillation([Couvert, 2008]). The idea of spin distillation, represented in figure (4.4), is to apply a magnetic field gradient during the evaporation that lowers the depth of the trap selectively for the magnetically sensitive states. As such, these states are preferentially evaporated, and we can optimize the value of the gradient and its time of application to be left only with atoms in $m_F = 0$ at the end of the evaporation and thus obtain polarized BECs. Similarly to the Stern and Gerlarch experiment, we use the MOT coils to implement the gradient.

We will present our method to reconstruct interferometer fringes with the BEC setup in the next section. However, we can already observe the performance of the spin distillation technique in figure (4.5, right) where we can observe an almost perfect contrast on an interferometer fringe, indicating a complete polarization of the BEC.

4.1.2.2 Microwave-based Ramsey interferometry

At the time at which the work that we present here was done, the experimental setup was not as complete as presented in chapter 3. There was neither no Raman nor Bloch laser systems, such that the observation of the BEC state was constrained to remain in the main chamber of the vacuum system. Moreover, as Raman beams were not available, we performed interferometry with microwave transitions mediated with a *Rohde&Schwarz SMF100A* generator connected to a wire half-wave antenna placed close to the vacuum chamber.

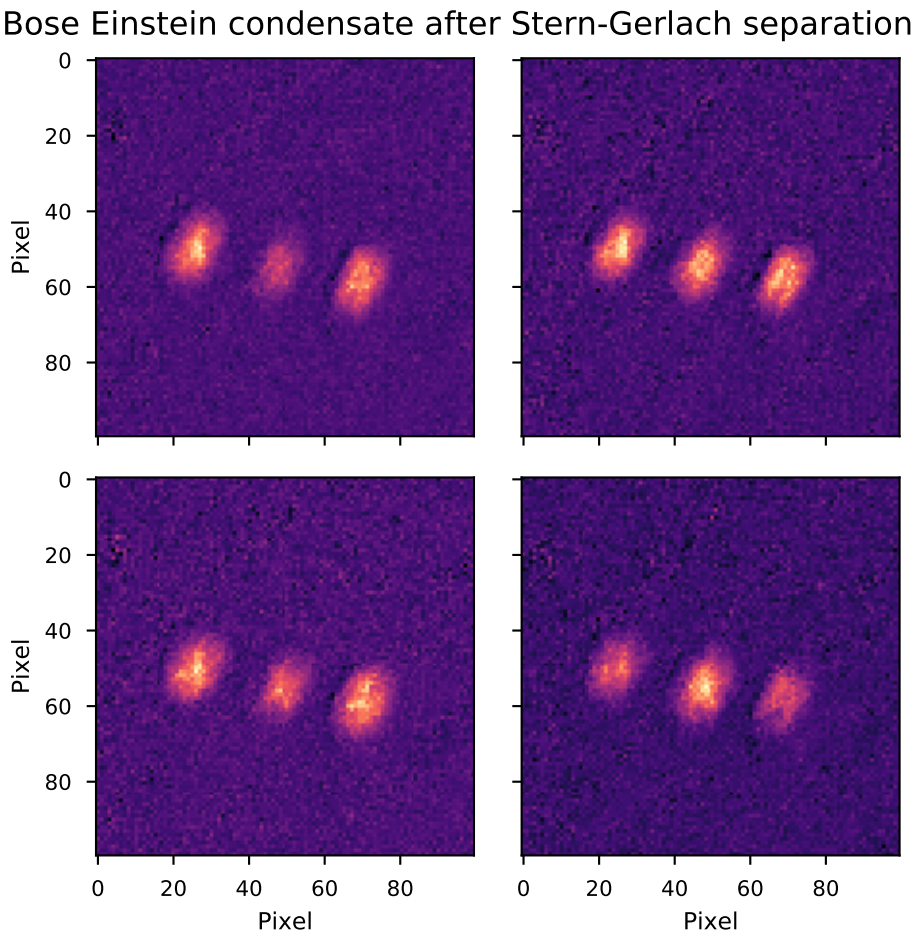

Figure 4.3: Images of the BEC after a Stern-Gerlach experiment that spatially separates the hyperfine Zeeman sublevels. The four images are sequential shots of the experiment. In particular, one can observe that the relative population in each sublevels varies shot to shot.

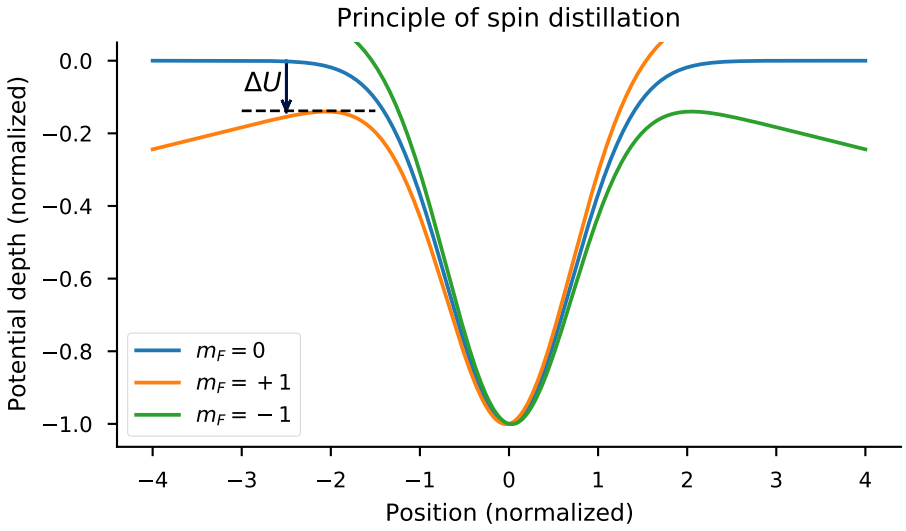

Figure 4.4: Principle of the spin distillation technique. Adding a magnetic field gradient does not change the shape of the potential for atoms in $m_F = 0$ (in blue, solid), but does for magnetically sensitive states and lowers the potential height by an amount ΔU

Unlike the case of light-pulse based interferometry, where the wavepackets are separated by $2\hbar k_{\text{optique}}$, with microwave interferometry the atom trajectories do not depend on their internal state. This feature poses a challenge for the detection of the interferometer output state. Indeed, we are able to observe the spatial distribution of the atoms, but if atoms in $|F = 1\rangle$ and $|F = 2\rangle$ are overlapped, we cannot distinguish them.

In order to spatially separate them, we set up an imaging technique based on taking two images in a short duration ($\sim$ 5 ms). The delay between images with a CCD camera is limited by the duration in which the CCD transfers the pixels information to the computer. Thanks to the *Area Of Interest* feature of the horizontal camera, we can reduce the area over which the image is taken, and as such reduce the delay between images.

The imaging process then goes as follow. A pulse of resonant light with the $|F = 2\rangle$ state is sent to the imaging path. The atoms in $|F = 1\rangle$ are not affected, so that we observe only atoms in $|F = 2\rangle$. These atoms are then removed from the camera range with a second pulse resonant with $|F = 2\rangle$. Finally, a repump pulse transfers the remaining atoms from $|F = 1\rangle$ to $|F = 2\rangle$, which are then observed similarly to the atoms initially in $|F = 2\rangle$. Typical images resulting from this process are displayed in figure (4.5, left).

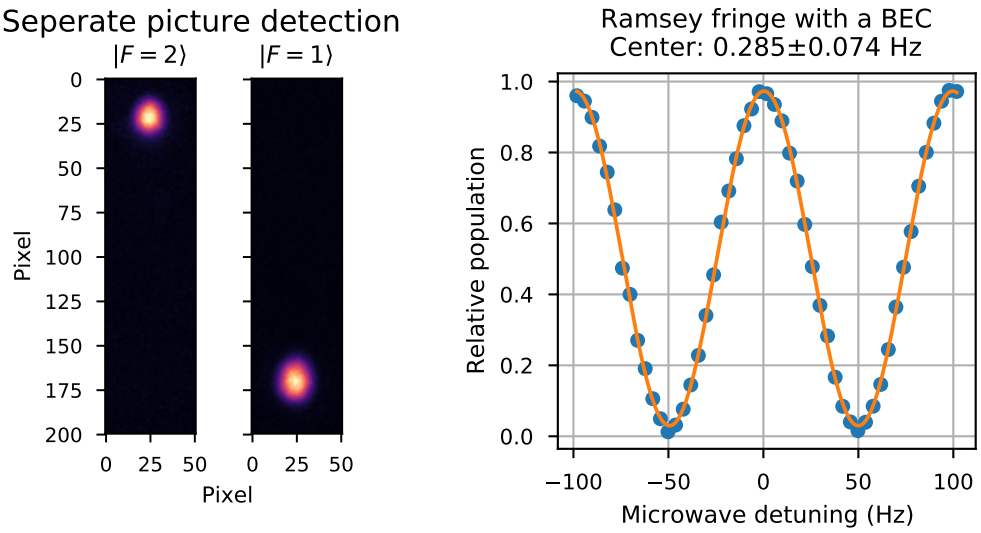

Figure 4.5: Left: separate images of the BEC output state of a microwave pulse sequence. First, atoms in $|F=2\rangle$ are observed and subsequently removed. Then a second image is taken $\sim$ 5 ms after which detects atoms in $|F=1\rangle$. Right: through the analysis of set of images, one can reconstruct Ramsey fringes.

As a final remark on this technique, one may notice the similarity with the light sheets time of flight technique (section 3.3.2). Indeed, both of them are based on a detection→blow away→repump→detection sequence.

Thanks to this technique, we are able to reconstruct the relative population of the BEC at the output of an interferometric sequence. The limitations here a related to the atom fall in the gravitational field. The maximal time of flight between the release from the dipole trap and the observation was 18 ms. This duration is sufficient to run Ramsey sequences with interfringe $\lesssim$ 100 Hz. We plot the result of such an interrogation performed by scanning the frequency of the microwave generator on figure (4.5). The precision on this fringe center is 74 mHz, which allowed us to study the contribution of atom-atom interactions with such a pulse sequence.

4.1.2.3 Interaction in the context of a Ramsey sequence

We present in this paragraph the effect of atom-atom interaction in the context of a microwave based Ramsey sequence. This presentation is based on the detailed study that our team published[Jannin, 2015b]. This study was devoted to the more general context of light-pulse based interferometry and the model takes into account interactions between atoms in the same internal state (*self interactions*),

and in different internal states (*mutual interactions*), as well as cloud expansion and overlapping between the superposed clouds along the interferometer duration. Here, we restrict ourselves to presentation of the conclusions that are useful for us.

First, this study showed that the effect of the interactions is negligible during the interferometer pulses, and that it is sufficient to consider their effect during the free evolution period. The effect of the interactions is to displace the energy levels.

For simplicity, we assume that the beam splitter pulses are perfect $\pi/2$. As the clouds overlap, the phase shift induced by mutual interactions between the hyperfine states cancels. We also write $|F = i, m_F = 0\rangle = |i\rangle$ for $i = 1, 2$, which can also be written as subscript. Then, at the output of the first beam splitter, the wavefunction of the atoms can be written:

$$|\Psi\rangle = \frac{1}{\sqrt{2}} \left(|1\rangle + |2\rangle\right) \tag{4.1.3}$$

and the atom-atom interactions perturbations can be described by (equations (2) and (7) of [Jannin, 2015b]):

$$\langle i| H^{\text{pert}} |j\rangle = \delta_{ij} \frac{1}{2} \hbar \frac{N}{\hbar\sqrt{\pi} w} \sum_{k=1,2} \frac{2\hbar^2 a_{ik}}{m w^2} \tag{4.1.4}$$

$$= \delta_{ij} \frac{\hbar^2}{\sqrt{\pi} m} \frac{N}{w^3} \sum_{k=1,2} a_{ik}, \tag{4.1.5}$$

where δ_{ij} is the Kronecker symbol, N is the number of atoms in the BEC, w its $1/e$ radius assuming it can be represented by an isotropic gaussian ansatz, and the a_{ik} are the s-wave scattering length. They depend on the internal states with $a_{11} \sim 100a_0$, $a_{22} \sim 95a_0$ and $a_{12} = a_{21} \sim 98a_0$, where a_0 is the Bohr radius[Egorov, 2013]. This expression shows through the N/w^3 that the perturbation is proportional to the atomic density in the BEC.

One may then compute the differential phase shift induced by the interactions in a Ramsey sequence and obtain, as the mutual interaction ($\propto a_{12}$) terms compensate:

$$\phi_{\text{pert}} = \frac{\hbar}{\sqrt{\pi} m} N \left(\int_0^{T_{\text{Ramsey}}} \frac{1}{w^3(t)} dt \right) (a_{22} - a_{11}) \tag{4.1.6}$$

The difficulty in the theoretical estimation of the phase shift comes from the integration of the cloud size w over the Ramsey sequence, as its initial parameters and evolution are not straightforward to determine experimentally. Indeed the expansion rate of a BEC is governed by the repulsive interactions that the atoms experience. When the atom density is high at the output of the dipole trap, the

BEC expands at a high rate. Then, its density reduces and the expansion rate as well.

It is necessary to improve the experimental model of the cloud expansion to perform precise *a priori* evaluations. However, the phase shift is proportional to the number of atoms, such that by changing the atom number without modifying the shape of the cloud, one may observe a simple behavior of the perturbation phase shift.

In order to obtain such a process, we apply a microwave pulse at the output of the BEC release. This pulse has a variable area, and subsequently to it, we apply a blow away pulse resonant with atoms in $|F = 2\rangle$. This pulse does not affect atoms in $|F = 1\rangle$ such that the shape of the remaining cloud is unchanged. Through the variation of the pulse area of the microwave pulse, we have an experimental parameter to scan the number of atoms in the BEC.

However, as we remove atoms from the BEC, we also reduce the signal that we observe and as such are more sensitive to noise in the measurement process. The interrogation beam being a laser, a highly-coherent source, interference patterns appear on the CCD images. In our setup, the beam collimator and the camera are placed on two separate tables, such that vibrations of the setup translate into shifts of these fringe patterns and cause noise on the detection process.

In order to reduce this noise, we have treated the images with a Fringe Removal Algorithm[Ockeloen, 2010], which is based on defining a large set of reference images[4]. Then, we consider the image on which the atom cloud was detected and reconstruct an optimal reference image from the set. The result of this technique can be seen in figure (4.6), as the uncertainty in the fringe determination has been divided by 2 at the lowest atom number parameter.

After the atom removal process, we apply a Ramsey sequence with $T_{\text{Ramsey}} = 13$ ms and measure the central frequency of the interferometric process. Indeed, equation (4.1.6) can be interpreted as an energy shift and as we discussed in section 2.2.1, a Ramsey sequence can be interpreted as a comparison between the internal energy difference of the atoms and the frequency of driving generator. As a consequence, this measurement is directly sensitive to the energy difference induced by the atom-atom interactions.

Moreover, as $a_{22} < a_{11}$, we expect that the higher the effect of the interactions, the lower the energy splitting between the two hyperfine levels. This is the behavior that we observe when running such an experiment. Its results are displayed on figure (4.6). We obtain that the data (blue dots) agree with a linear law. From a fitting procedure, we can obtain an extrapolation of the resonance frequency

[4] *i.e.* images without atoms

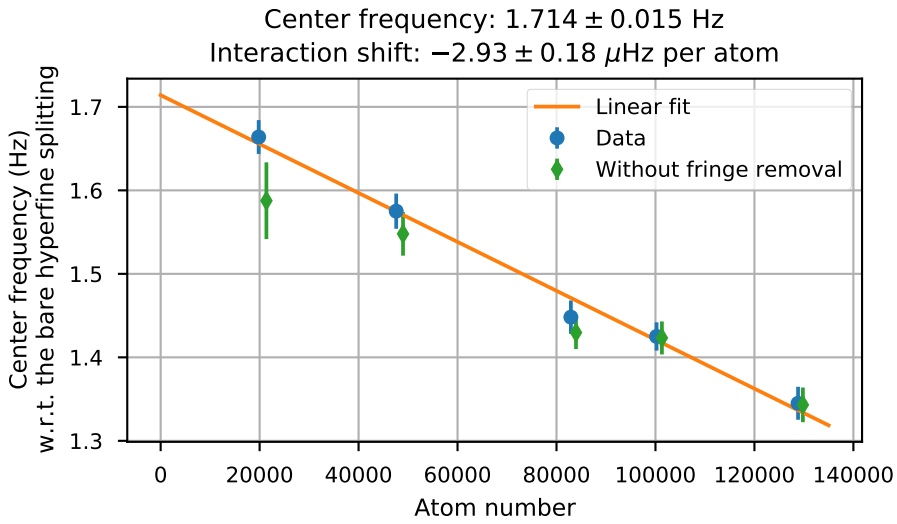

Figure 4.6: Variation of the resonance frequency of Ramsey sequence with the number of atoms in a BEC. The raw data (green diamonds) presents more noise than the data treated with a Fringe Removal Algorithm on the absorption images (blue dots). We observe a good agreement with a linear from which we extract the frequency shift per atom in the BEC.

without the effect of interactions. Moreover, we can estimate the energy shift induced by a single atom from the slope. With 130,000 atoms in the BEC we observe a displacement of the fringe center by −400 mHz, or −2.93 μHz per atom in the BEC. Inverting equation (4.1.6) and assuming a mean size $\langle w \rangle$ and $a_{22} - a_{11} = 5a_0$, we obtain that $\langle w \rangle \sim 18$ μm, compatible with the imaging observations.

4.1.2.4 Conclusion

This observation of the atom-atom interaction induced phase shift confirmed that this perturbation should be carefully treated in order to perform accurate precision measurements. However, our experiment was performed right at the output of the dipole trap with no implementation of any technique that increases the size of the BEC. As such, the effect of the interactions was exalted by our experimental conditions.

The performance of our evaporation setup with the production of 120000 atoms in a BEC with a 3.5s cycle time (1.5 second loading of the MOT, 2s evaporation) does not match the performance obtained with evaporation setups based on atom chips[Rudolph, 2015], but compares to performance of similar setups based on

optical dipole trap[5]. It is conceivable to enhance the perfomance of our setup using the technique described in [Roy, 2016], based on dynamically shaping the dipole trap through time-averaging of the potential created by a laser beam moving rapidly.

Moreover, one of the main drawback of the BEC production system is its reliability as it requires daily adjustements. Since using a BEC comes with a supplementary error source, we oriented our work towards studying the possibility of using clouds produced by optical molasses. Indeed this production protocol is shorter ($\sim$ 700 ms in our experiment) and its adjusment is very reliable as they are stable over several months.

4.2 Resonance mismatch during light pulses

Compared to using a BEC and its low velocity dispersion, the main drawback of using clouds produced by optical molasses originates from the expansion of the cloud during the interferometer which induces a reduction of the intensity seen by the atoms over the interferometer.

This phenomenon was already identified as a limitation to build beam splitters combining Raman transitions and Bloch Oscillations[Cladé, 2009]. In the context of beam splitters based on a single Raman transition, we were able to demonstrate an experimental calibration of the cloud expansion. By increasing the intensity of the Raman driving lasers along the interferometers, we reduced the variations of the intensity seen by the atoms.

In order to understand one of the implications of the cloud expansion on the interferometer phase, we make a detour through a finer modeling of the interferometer beam splitters.

4.2.1 Phase shifts

The earlier treatment of the interferometers was made under the assumption of that $\delta \ll \Omega$, where Ω is the coupling Rabi frequency and δ the energy difference between the two levels. In our experimental conditions, this requirement does not hold because the differential light shift, which contributes to δ is of the order of magnitude of Ω.

[5]See figure 6 of [Rudolph, 2015].

Let us first model the two level system $\left\{ |\alpha\rangle\,,\ |\beta\rangle \right\}$ with its free and coupling Hamiltonians:

$$H_0 = \hbar \begin{pmatrix} \delta/2 & 0 \\ 0 & -\delta/2 \end{pmatrix} \tag{4.2.1}$$

$$H_c = \hbar \begin{pmatrix} 0 & \Omega e^{-i\phi} \\ \Omega e^{i\phi} & 0 \end{pmatrix}, \tag{4.2.2}$$

where all quantities are real. Ω is the Rabi frequency between of the coupling and δ the bare energy diffenrence between the two levels. In the context of counter-propagating Raman transitions, it corresponds to the Doppler shift.

We first assume that the coupling does not induce energy shift for clarity. We can the deduce the evolution operators associated the free Hamiltonian and to the total Hamiltonian $H = H_0 + H_c$:

$$U_0(\tau) = \begin{pmatrix} \exp\left(-i\frac{\delta\tau}{2}\right) & 0 \\ 0 & \exp\left(i\frac{\delta\tau}{2}\right) \end{pmatrix} \tag{4.2.3}$$

$$U(\tau) = \cos\left(\frac{\Omega_e\tau}{2}\right)\mathbf{1} - i\frac{\sin\left(\frac{\Omega_e\tau}{2}\right)}{\Omega_e} \begin{pmatrix} \delta & \Omega e^{-i\phi} \\ \Omega e^{i\phi} & -\delta \end{pmatrix}, \tag{4.2.4}$$

Taking into account the energy splitting contribution to the evolution operator translates as a modification of the amplitudes of the projection of the wavefunction onto the atomic states. We have seen that the absolute values of these amplitudes impacts the contrast of the fringes without inducing a shift of the central fringe. However, as the interferometric signal originates from the phase difference between those amplitudes, perturbations of the amplitude phases shift the central fringe.

From equation (4.2.4), the phase of the off-diagonal elements is the same for infinitely short and finite duration pulses. However, the diagonal terms carry an additional pure imaginary number that induces a phase shift.

Since we are interested in the phase shift induced by the transition, we compare the phase of the total evolution operator matrix element to the free evolution one:

$$\delta\phi_{|\alpha\rangle\to|\alpha\rangle} = \arg\left(\langle\alpha|\,U(\tau)\,|\alpha\rangle\,/\,\langle\alpha|\,U_0(\tau)\,|\alpha\rangle\right) \text{ and} \tag{4.2.5}$$

$$\delta\phi_{|\beta\rangle\to|\beta\rangle} = \arg\left(\langle\beta|\,U(\tau)\,|\beta\rangle\,/\,\langle\beta|\,U_0(\tau)\,|\beta\rangle\right). \tag{4.2.6}$$

Putting the reference to the free evolution case isolates the contribution of the coupling.

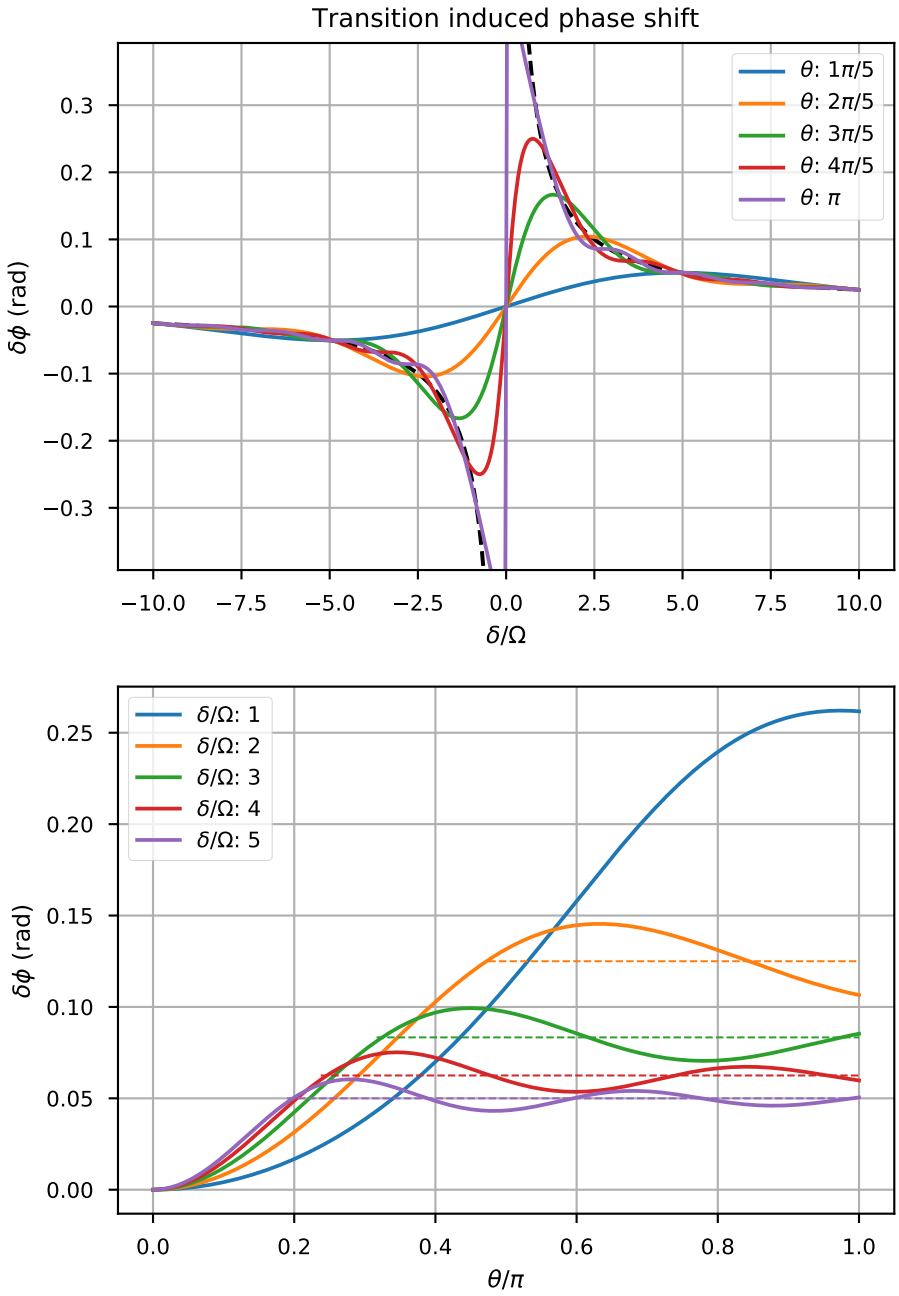

Figure 4.7: Plot of equation (4.2.9). Top plot: phase shift as a function of the reduced detuning for different pulse areas. Bottom plot: phase shift for a given reduced detuning as a function of the pulse area. On each plot, the dashed lines represent the prediction of first order perturbation theory

With the input of equations (4.2.3) and (4.2.4), we get:

$$\delta\phi_{|\alpha\rangle\to|\alpha\rangle} = -\arctan\left(\frac{\delta}{\Omega_e}\tan\left(\frac{\Omega_e\tau}{2}\right)\right) + \frac{\delta\tau}{2} \tag{4.2.7}$$

$$\delta\phi_{|\beta\rangle\to|\beta\rangle} = +\arctan\left(\frac{\delta}{\Omega_e}\tan\left(\frac{\Omega_e\tau}{2}\right)\right) - \frac{\delta\tau}{2} \tag{4.2.8}$$

The two phase shifts have opposite sign, which is also the case if we consider free evolution only and their dependency in δ exhibit the shape of a dispersion relation (see figure (4.7) top).

In order to get some insight of this formula, we reexpress equation (4.2.8) with adimensional parameters: the reduced detuning $\delta' = \frac{\delta}{\Omega}$ and the pulse area $\theta = \Omega\tau$.

$$\delta\phi = \arctan\left(\frac{\delta'}{\sqrt{1+\delta'^2}}\tan\left(\frac{\theta\sqrt{1+\delta'^2}}{2}\right)\right) - \frac{\delta'\theta}{2} \tag{4.2.9}$$

For $\delta' \to 0$, *i.e.* in the infinitely short pulse assumption, we find as expected $\delta\phi \to 0$.

Moreover, for $\delta' \gg 1$, we can develop the arctan in equation (4.2.9) in two steps which yields $\delta\phi \sim \frac{\Omega^2}{4\delta}\tau$ that corresponds to the result obtained from the computation of the energy displacement in the first order perturbation theory framework. This correspondence shows that what we calculated as a phase shift can also be seen as an energy shift induced by the coupling.

The behavior for intermediate cases is represented in figure (4.7). The top figure shows the behavior by scanning the detuning for different pulse areas. The width of the dispersion figure scales inversely with the pulse duration, which can be interpreted as a consequence of the time-energy equivalent Heisenberg principle ($\Delta\delta\Delta\tau = \Delta\delta'\Delta\theta > 1/2$): as the pulse duration (θ) increases, its resonance frequency gets defined with a better precision.

We notice a discontinuity at $\theta = \pi$: assuming the initial state is $|\psi\rangle = |\alpha\rangle$, when doing a resonant $(\delta' = 0)\pi$ pulse, the amplitude of the wavefunction projection to the initial state $\langle\alpha|\psi\,(\theta = \pi)\rangle$ reaches 0 and thus its phase cannot be defined.

The bottom plot displays the behavior of the phase shift with respect to the pulse area for different reduced detunings. At small pulses area, the phase shift increases with the pulse area for all reduced detunings. However, as the pulse area keep increasing, and for large reduced detuning, the phase shift oscillates around the prediction obtained by a perturbative approach.

As we have developed previously, the parameter that is not kept constant during the interferometer is the pulse area through variations of the laser intensity induced by the atom cloud expansion. This plot shows the sensitivity of this phase shift with pulse area variations. In particular, around $\theta = \pi/2$, we notice that this sensitivity is highly dependent of the detuning.

4.2.1.1 Effect of diagonal terms in the coupling

Revoking the assumption that the coupling Hamiltonian diagonal terms are zero, we can rewrite it:

$$H_c = \begin{pmatrix} \delta_{|\alpha\rangle} & \Omega e^{-i\phi}/2 \\ \Omega e^{i\phi}/2 & \delta_{|\beta\rangle} \end{pmatrix} \tag{4.2.10}$$

$$= \delta_m \mathbf{1} + \frac{\delta_c}{2}\sigma_z + \frac{\Omega}{2}\left(\cos(\phi)\sigma_x + \sin(\phi)\sigma_y\right), \tag{4.2.11}$$

$$\text{where } \delta_m = \frac{\delta_{|\alpha\rangle} + \delta_{|\beta\rangle}}{2}, \text{ and } \delta_c = \delta_{|\alpha\rangle} - \delta_{|\beta\rangle} \tag{4.2.12}$$

When treating the case of Raman transitions δ_c corresponds to the differential light shift: $\delta_c = \Omega^{\text{LS}}_{\text{diff}}$.

The evolution operator of the total Hamiltonian is then modified:

$$U(\tau) = e^{-i\delta_m\tau}\mathbf{1}\left(\cos\left(\frac{\Omega_e\tau}{2}\right)\mathbf{1} - i\frac{\sin\left(\frac{\Omega_e\tau}{2}\right)}{\Omega_e}\begin{pmatrix} \delta+\delta_c & \Omega \\ \Omega & -\delta-\delta_c \end{pmatrix}\right), \tag{4.2.13}$$

$$\text{with} \quad \Omega_e = \sqrt{\Omega^2 + \left(\delta+\delta_c\right)^2}. \tag{4.2.14}$$

The global phase term can be safely ignored in the context of interferometry as it modifies globally the phase function. However, as we compare the coupling case to the free case, this phase term appears as a leftover.

In the formula (4.2.8), the presence of diagonal terms in the coupling operator modifies the argument of the arctan function in which the δ should be replaced by $\delta + \delta_c$:

$$\delta\phi = \arctan\left(\frac{\delta+\delta_c}{\Omega_e}\tan\left(\frac{\Omega_e\tau}{2}\right)\right) - \frac{\delta\tau}{2}, \tag{4.2.15}$$

the term $\delta\tau/2$ being unchanged since it represents the evolution without the coupling.

The effect of this modification is plotted on figure (4.8). The coupling operator displaces differently the two levels, which has two consequences: first, the relative phase evolution between the to levels is changed which induces a vertical displacement of the dispersion figure. Secondly, this changes also the resonance condition which results to an horizontal displacement of the figure.

4.2.1.2 Conclusion

We have treated in detail the effect of phase shifts induced by the transitions when their duration can not be modeled as infinitely short.

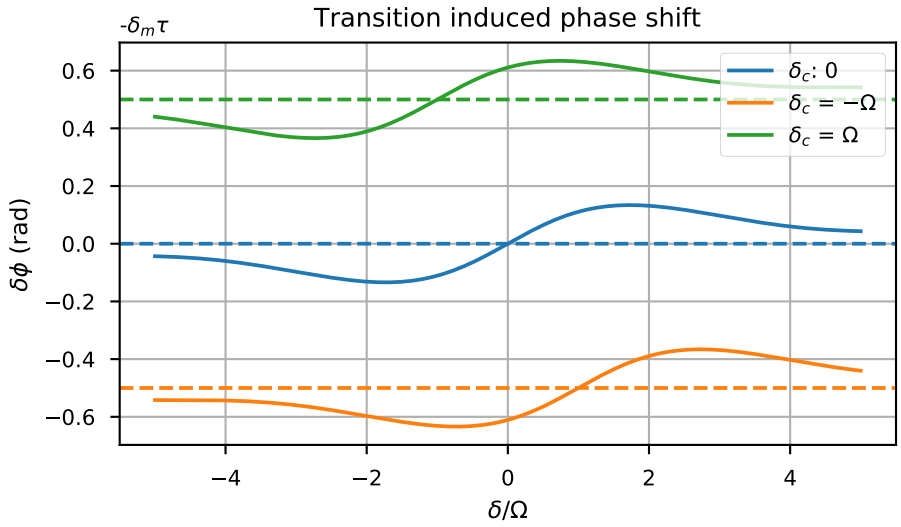

Figure 4.8: Phase shift as a function of the reduced detuning for different differential energy shifts induced by the coupling. We notice both a vertical and horizontal displacement of the dispersion figure.

These phase shifts, induced by the diagonal terms of the evolution operator exhibit a non trivial behavior with the resonance deviation, either when scanning the pulse area or when considering the energy shifts induced by the coupling.

4.2.2 Application to atom interferometry

4.2.2.1 Counterpropagating Raman transitions

In order to discuss the impact of these phase shifts to our interferometers, we recall the expression of the Rabi frequency and of the light shifts as a function of the lasers intensity:

$$\Omega = \frac{\Gamma^2}{16\Delta}\frac{\sqrt{I_1 I_2}}{I_S} \tag{4.2.16}$$

$$\Omega_i^{\mathrm{LS}} = \frac{\Gamma^2}{8\Delta}\frac{I_i}{I_S}, \tag{4.2.17}$$

where the index i references the laser beams.

If the lasers are well equilibrated ($i.e\ I_1 = I_2$), the light shift on a single level is twice as big as the Rabi frequency! Fortunately, the light shift applies on the two hyperfine levels, where the difference is only controlled by the detuning which

differs by ω_{HFS}. As a consequence, the differential light shift for a single laser beam is given by:

$$\Omega^{\mathrm{LS}}_{\mathrm{diff},i} = \frac{\Gamma^2}{8\Delta}\frac{I_i}{I_S} \times \frac{\omega_{HFS}}{\Delta} \tag{4.2.18}$$

With our parameters, $\Delta = 65$ GHz, the differential light shift is typically ten times smaller than the direct light shift. Since we apply three laser beams to the atoms, the order of magnitude of the light shift is then 60 percent of the effective Rabi frequency, which is far from negligible.

In the following of the development, we assume that the differential light shift is proportional to the Rabi frequency.

As we have seen during the presentation of counterpropagating Raman transitions, these are sensitive to Doppler effect.

Thus, to identify terms of the modelization presented above to the experimental terms, we have:

$$\delta \leftrightarrow \delta_{Doppler} = (\vec{v} - \vec{v_0}) \cdot \vec{k_e} \tag{4.2.19}$$

$$\delta_c \leftrightarrow \Omega^{\mathrm{LS}}_{\mathrm{diff}} = \sum_i \Omega^{\mathrm{LS}}_{\mathrm{diff},i}, \tag{4.2.20}$$

where $\vec{v_0}$ correspond to the velocity class addressed by the Raman transition.

4.2.2.2 Effect in a Ramsey-Bordé interferometer

The interferometric signal of an atom interferometer comes from the non-diagonal terms of the evolution operator. Since the correction induced by the finite duration of the pulse applies to the diagonal terms of this operator, we deduce that the total phase shift over a Ramsey-Bordé interferometer is given by:

$$\delta\phi^{\mathrm{finite}} = -\delta\phi_{IV} + \delta\phi_{III} + \delta\phi_{II} - \delta\phi_I \tag{4.2.21}$$

Over the Ramsey sequences, the diagonal term that we should consider switch from pulse to pulse. Since the correction changes sign with the matrix element of

the evolution operator (see equation (4.2.8)), we obtain:

$$\begin{aligned}\delta\phi^{\text{finite}} = &- \arctan\left(\frac{\delta_{Doppler}+\Omega^{\text{LS}}_{\text{diff},IV}}{\Omega_{e,IV}}\tan\left(\frac{\Omega_{e,IV}\tau}{2}\right)\right)\\ &- \arctan\left(\frac{\delta_{Doppler}+\Omega^{\text{LS}}_{\text{diff},III}}{\Omega_{e,III}}\tan\left(\frac{\Omega_{e,III}\tau}{2}\right)\right)\\ &+ \arctan\left(\frac{\delta_{Doppler}+\Omega^{\text{LS}}_{\text{diff},II}}{\Omega_{e,II}}\tan\left(\frac{\Omega_{e,II}\tau}{2}\right)\right)\\ &+ \arctan\left(\frac{\delta_{Doppler}+\Omega^{\text{LS}}_{\text{diff},I}}{\Omega_{e,I}}\tan\left(\frac{\Omega_{e,I}\tau}{2}\right)\right),\end{aligned} \tag{4.2.22}$$

where we have identified with a pulse index the parameters that depend on the laser intensity and are then assumed to vary over the interferometer.

First, we observe that if the laser intensity is kept constant along the interferometer then all terms cancel and this effect can not be observed.

4.2.2.3 Velocity dependence

Each term of equation (4.2.22) behaves as a dispersion relation, such that we expect to observe a dispersion relation at the output of the Ramsey-Bordé.

The experimental result is displayed on figure (4.10). The Ramsey duration T_{Ramsey} was 10 ms and the delay between the Ramsey sequences was 70 ms.

In order to observe the dispersive nature of equation (4.2.22), we scanned the initial mean velocity of the atom cloud on which the interferometric sequence was applied. This is performed through the setting of the addressed velocity class of the preselection pulse by changing the frequency of the Raman selection pulse. The experimental conditions are presented in figure (4.9).

The Rabi frequency was $2\pi\cdot(2.5\text{ kHz})$, and the initial velocity was scanned on a $[-6.0, 7.0]$ kHz in Doppler shift units, with a 1 kHz step. The velocity distribution full width at the output of the preselection sequence was estimated to be less than 1 kHz. The consequence of this large velocity scan with respect to the Rabi frequency is that we performed interferometry with low contrast.

Moreover, when presenting the Ramsey-Bordé interferometer, we have seen that the natural variable to scan was the frequency of the second Ramsey sequence. However, in these conditions, the Rabi spectra that is probe by the atomic velocity distribution may vary sharply with the pulse frequency. Hence, by scanning the frequency, the Rabi spectra shape may induce an additional shift of the central fringe. In order to prevent this effect, we scanned the phase of the last pulse.

On figure (4.10), the experimental data was fitted with equation (4.2.22), with the following parameters: the initial Rabi frequency, a ramp parameter character-

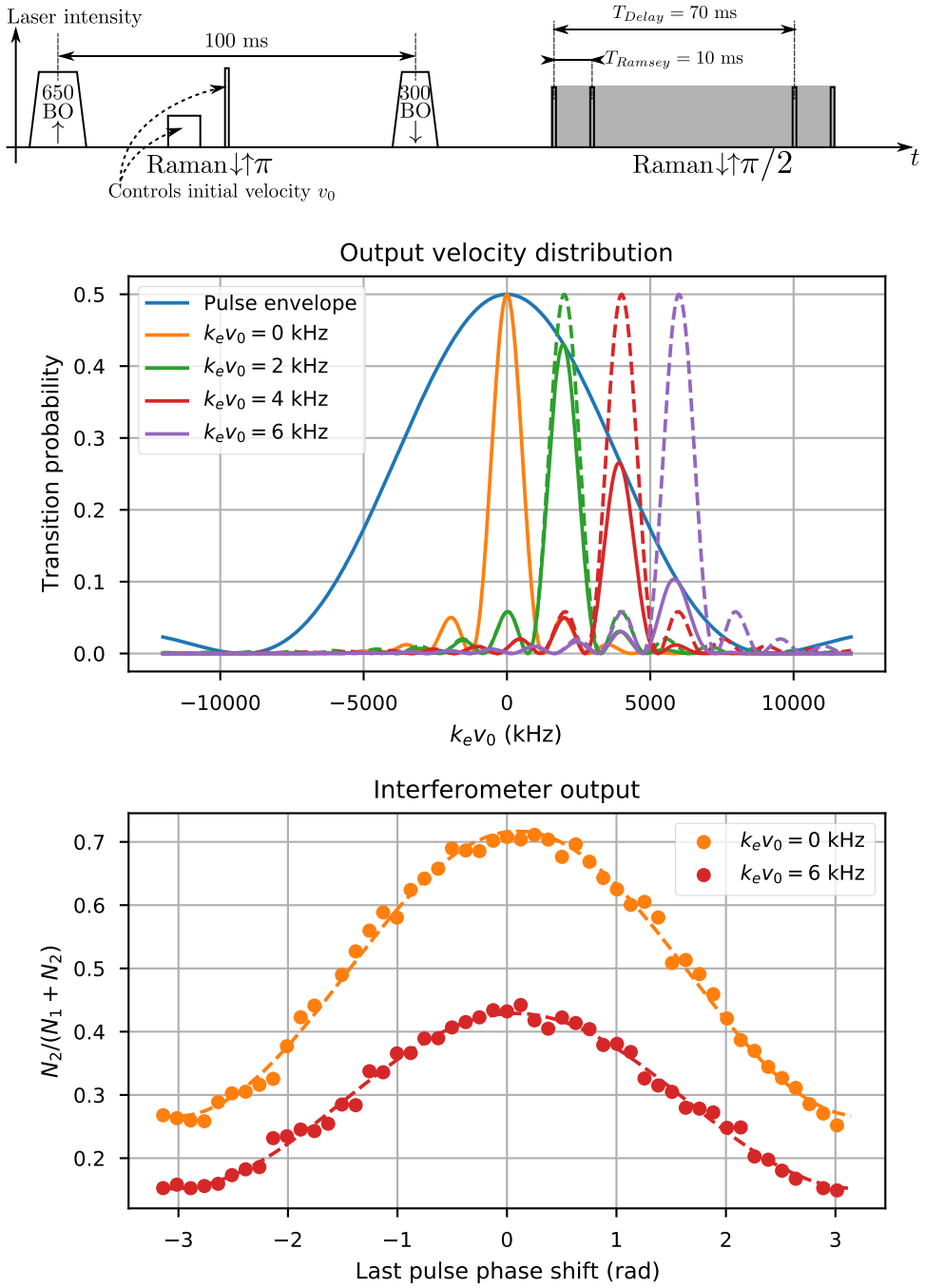

Figure 4.9: Experiment to observe the phase shift predicted by equation (4.2.22). Top: pulses arrangement. The frequency of velocity selection in between the atom elevator is our parameter to change the velocity of the atoms in the interferometer. Middle: In blue, interferometer pulses Rabi envelope (without light shifts). The dashed curves represents initial velocity distribution, and the solid curve their selection by the interferometer pulses. Bottom: interferometer signal at the output of the light pulses sequence. When the Doppler shift associated to the atomic velocity reaches the edge of the Rabi enveloppe (middle plot, blue curve), the fringe contrast is degraded (middle and bottom plots, red curves).

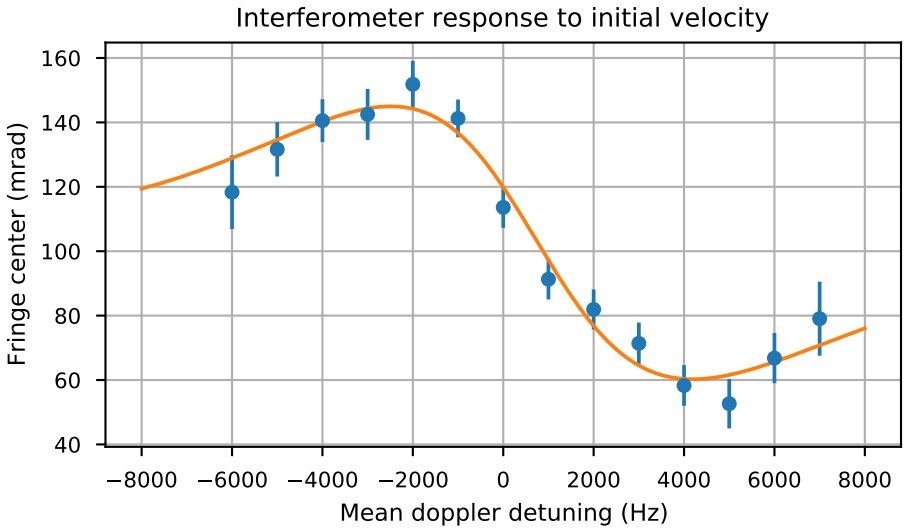

Figure 4.10: Dispersion behavior of the output phase of a Ramsey-Bordé interferometer by scanning the initial velocity of the atoms. The orange line corresponds to a fit with equation (4.2.22), with an intensity variation over the interferometer.

izing the reduction of the Rabi frequency over time and a proportionality constant C so that $\Omega_{\text{diff}}^{\text{LS}} = C\Omega$.

The fitted Rabi frequency is 10% higher than the one obtained through a estimation based on Rabi Oscillations. However the reduction of the Rabi frequency is estimated to 2% over 50 ms, which is far from the value expected from considerating a 4 μK expanding gas ($\simeq$ 20%). We can attribute this discrepancy as a consequence of the large velocity scan:

As the atoms are further from resonance when performing the interferometer, their contribution to the interferometer signal is not uniform over their velocity distribution. Because of this the mean Doppler detuning on the horizontal axis might be overestimated, and as such the amplitude of the dispersion curve underestimated.

Even though the experimental conditions to observe (4.2.22) are challenging to put in place because of the width of the Rabi spectra, we are able to confirm the dispersive nature of the finite pulse duration correction.

4.2.2.4 Calibration of the intensity variation

As we have seen above, the dependence in initial velocity displays a dispersive behavior. Additionally, if we were to reduce the intensity variation over the pulses, we would observe a decrease in the dispersion curve amplitude.

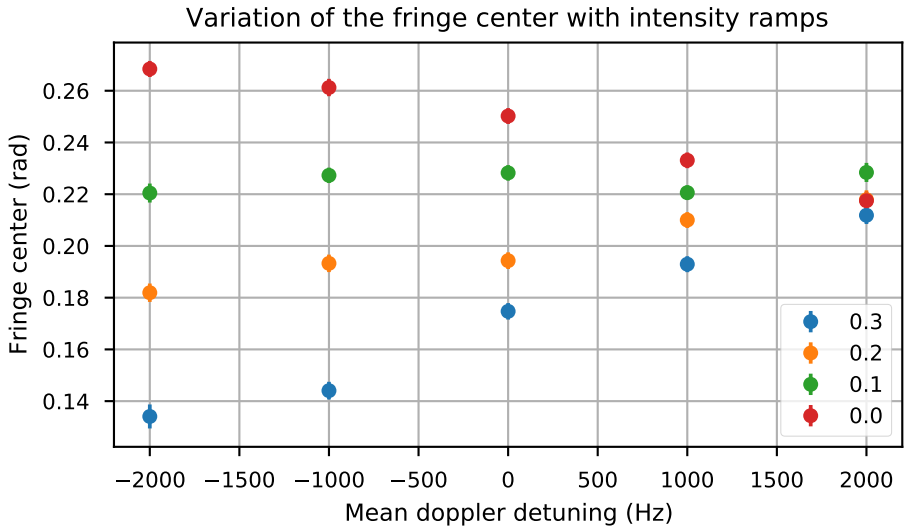

Figure 4.11: Center phase of a Ramsey Bordé interferometer with intensity ramps on the interferometry pulses. The green points displays a compensation of the intensity variation induced by the expansion of the atom cloud. The labels of each data set correspond the intensity reduction of the first interferometer pulse. For example, for the blue points, the intensity of the first pulse was 30% smaller that for the last pulse. The intensity of the pulses is then swept linearly with respect to time.

By applying an intensity ramp during the interferometer, *i.e.* increasing the Raman power to compensate for the cloud expansion, we can compensate experimentally such a reduction of the intensity variation.

We scanned the output phase of a Ramsey Bordé interferometer without Bloch Oscillations between the Ramsey sequences. In order to place ourselves as close as possible to the h/m measurement interferometer, T_{Ramsey} was set to 20 ms and the delay between the Ramsey sequences T_{delay} was 30 ms such that the total interferometer duration was 50 ms.

Two parameters were changed: the initial velocity of the atoms and the amplitude of the linear intensity ramp. The result of this experiment is displayed on figure (4.11). We observe that when the intensity sent to the vacuum chamber is 10% smaller for the first pulse than for the last pulse, the slope of the variation with the initial velocity is greatly reduced by $\sim 80\%$, and as such the systematic error induced by such phase shifts.

4.2.3 Conclusion

Drawbacks and advantages of both kind of atomic sources have been studied. It must be pointed out that the phase shift studied using optical molasses is present when using BECs. However it is greatly reduced thanks to the lower transverse expansion rate.

Using a BEC as an atom source involves an additional systematic effect and that their production reduces the cycling rate of the experiment and are more elaborated, thus less stable.

These considerations, combined with the fact that we were able to calibrate the intensity variations over the cloud expansion, led us to choose clouds produced by optical molasses for the h/m determination.

Finally, as we will see in section 6.5.2, local fluctuations of the intensity profile can shift the interferometric output phase. This effect, firstly reported in [Andia, 2015a], was explained in [Bade, 2018]. This effect has been studied experimentally with optical molasses on the new setup (section 6.5.2).

Because of the local intensity sensitivity, it is necessary to average out the intensity fluctuations. In this context, optical molasses appears as a better production process than the evaporative cooling to Bose Einstein Condensation.

Chapter 5

Determination of the h/m_{Rb} ratio

The principle of the measurement of the atom recoil velocity was exposed in chapter 2, with the combination of atom interferometry and Bloch Oscillations.

In this chapter, we describe in detail the experimental and analysis protocols that aims to the determination of the h/m_{Rb} ratio. We then discuss the implementation of these protocol and present the performance of the experimental setup.

To simplify the notations, we drop the subscript of the Rubidium atom mass symbol.

5.1 Experimental protocol

Let us start with a brief reminder of the previously exposed measurement principle. Bloch Oscillations allows to transfer to atoms an arbitrary number of atom recoil $2v_B = 2\hbar k_B/m$, where k_B is the Bloch beams wavevector. Thus, with a process of N_B Bloch Oscillations, one transfers the following velocity:

$$\Delta v = N_B \cdot 2v_B = 2N_B \frac{\hbar}{m} k_B \tag{5.1.1}$$

By embedding the process in a differential velocity sensor Ramsey-Bordé interferometer, which is characterized by the 2 photons wavevector of the Raman based beam splitters k_R and its two durations, T_{Ramsey} the Ramsey sequences duration and T_{delay} the delay between the two Ramsey sequences, one obtains an atom interferometer whose output phase shift is given by:

$$\Phi^{\text{interferometer}} = T_{\text{Ramsey}} \left(k_R \left(\epsilon_B 2N_B \frac{\hbar}{m} k_B - g T_{\text{delay}} \right) - \delta\omega \right), \tag{5.1.2}$$

where $\delta\omega$ is the Raman beams detuning shift between the two Ramsey sequences and $\epsilon_B = \pm 1$ describes the direction of the acceleration. Figure (5.1) displays a schematic of such an interferometer.

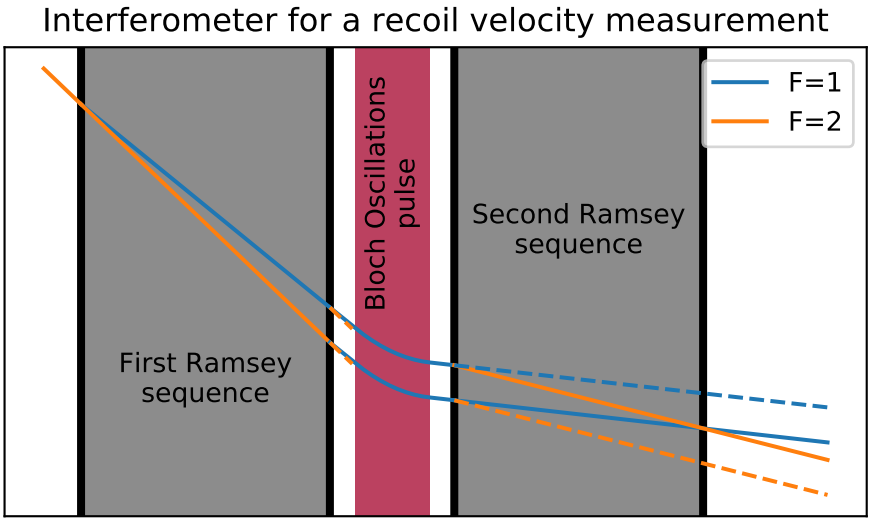

Figure 5.1: Bloch Oscillations embedded in a differential velocity sensor. For clarity, gravity was not represented and the beam splitter recoil was exaggerated. The dashed lines represent the loss channels.
At the input of the interferometer, the atoms are in $|F = 2\rangle$. After the first Ramsey sequence, a blow away pulse removes the $|F = 2\rangle$ coherences. After the Bloch Oscillations process, a second Ramsey sequence is applied. The central fringe condition corresponds to a maximum $|F = 1\rangle \rightarrow |F = 2\rangle$ transfer probability by the second Ramsey sequence.

We typically set the interferometer parameters to $N_B = 500$, and $T_{\text{Ramsey}} = 20$ ms. We discuss the choice of those parameters in section 5.1.4.

5.1.1 Gravity elimination

The determination of the fringe center defined by $\Phi^{\text{interferometer}} = 0$, and the $\delta\omega_c$ parameter that realizes it allows to deduce the velocity shift between the two Ramsey sequences. By building a single interferometer one gets a signal that depends on gravity. However, by combining the two Bloch acceleration directions, one may eliminate the impact of the gravitational acceleration and obtains the h/m ratio:

$$\frac{h}{m} = \frac{\pi\left(\delta\omega_c(\epsilon_B = +1) - \delta\omega_c(\epsilon_B = -1)\right)}{2N_B k_R k_B}. \tag{5.1.3}$$

This formula displays the critical importance of the determination of the effective wavevectors of both the Bloch and Raman transitions.

5.1.2 Raman inversion technique

However, equation (5.1.2) describes an ideal situation where the atomic systems are unperturbed. The interferometer treatment of chapter 2 exhibited that the phase induced by the internal energy difference of the atomic levels would cancel, but it was made under the implicit assumption that this energy difference is constant over the entire interferometer. As such magnetic field inhomogeneities produces an additional phase shift.

Moreover, we have seen in section 4.2 that the Raman transition induced light shifts that also add a phase shift to the output of the interferometer. As a consequence we should add to the right hand side of equation (5.1.2) an additional phase $\delta\phi$.

The Bloch velocity transfer inside the interferometer reaches $\sim 6\ \mathrm{m}\cdot\mathrm{s}^{-1}$ for 500 Bloch Oscillations. This high amount leads to quite different atom trajectory (see figure (5.3) below) as a function of the Bloch direction such that the phase shift $\delta\phi$ depends on ϵ_B. Thus they do not cancel in equation (5.1.2).

The technique to compensate these phase shifts is to invert the Raman direction, *i.e.* alternatively diffract atoms upwards or downwards with the light pulses. In the equations, this corresponds to replacing k_R with $\epsilon_R k_R$, with $\epsilon_R = \pm 1$, similarly to the Bloch direction.

The light shifts induced by the Raman beams are independent of the transition direction. Moreover, inverting the direction slightly displaces the atomic trajectories, such that we can assume with a good approximation that the effect of magnetic field inhomogeneities is unchanged with the Raman inversion. We hence assume that $\delta\phi$ depends only on ϵ_B.

The measurements of the central fringe parameter on the four situations yield four equations derived from equation (5.1.2):

$$0 = T_{\mathrm{Ramsey}}\left(\epsilon_R k_R\left(\epsilon_B 2N_B\frac{\hbar}{m}k_B - gT_{\mathrm{delay}}\right) - \delta\omega_c\left(\epsilon_R,\epsilon_B\right)\right) + \delta\phi\left(\epsilon_B\right)$$
$$\text{for } \epsilon_R = \pm 1,\ \epsilon_B = \pm 1. \tag{5.1.4}$$

Combining these four equations, we obtain:

$$\frac{h}{m} = \frac{\pi}{4N_B k_B k_R}\sum_{\epsilon_R,\epsilon_B}\epsilon_R\epsilon_B\delta\omega_c\left(\epsilon_R,\epsilon_B\right) \tag{5.1.5}$$

In terms of systematic effects, without performing the Raman inversion, we would need to estimate the phase shifts $\delta\phi(\epsilon_B)$ to ensure the accuracy of the measurement. Thanks to this inversion technique, we only have to estimate the

difference of light shifts between the two Raman directions. This estimation will be treated in a dedicated section 6.3.

With these four measurements, we can also estimate the gravity acceleration g and the phase shifts $\delta\phi(\epsilon_B)$

$$g = -\frac{1}{4k_R T_{\text{delay}}} \sum_{\epsilon_R,\epsilon_B} \epsilon_R \delta\omega_c\left(\epsilon_R, \epsilon_B\right) \tag{5.1.6}$$

$$\delta\phi\left(\epsilon_B\right) = \frac{T_{\text{Ramsey}}}{2} \sum_{\epsilon_R} \delta\omega_c\left(\epsilon_R, \epsilon_B\right) \tag{5.1.7}$$

5.1.3 Fringe extraction procedure

The measurement of the central fringe condition, and as such the determination of $\delta\omega_c$, goes as follow. From the initial knowledge of the phase formula parameters, we deduce an estimation of $\delta\omega_c$. We then scan the parameter $\delta\omega$ around this value in order to obtain phase shifts in the $[-\pi, \pi]$ interval. This correspond to $\delta\omega/(2\pi)$ in $[-1/T_{\text{Ramsey}}, +1/T_{\text{Ramsey}}]$ around $\delta\omega_c^{est}/(2\pi)$. We use for the measurement $T_{\text{Ramsey}} = 20$ ms, and we check that we are indeed close to the central fringe by changing this parameter.

In order to extract the fringe pattern, we perform 51 evenly spaced measurements within this interval. At the output of the interferometer, we measure the atom numbers in the two hyperfine states N_1 and N_2 from which we obtain the relative population in $|F = 2\rangle$: $y_2 = N_2/(N_1+N_2)$. At the central fringe condition, we have a constructive interference that maximizes y_2.

We then fit the fringe pattern with a sinusoidal function and extract an estimation of the $\delta\omega_c$ parameter with its associated uncertainty. The result of such a protocol is displayed in figure (5.2).

Because we have to build four fringe patterns in order to estimate h/m, a single run is 204 points. The sampling of these points is performed randomly in order to avoid drifts during the data collection. Finally, we measure the acceleration of the retroreflecting mirror during the interferometer and apply a correction on the x-axis of the fringe in order to compensate the vibration noise.

5.1.4 Discussion

From the plot of the fringes (figure (5.2)), we see that the values of $\delta\omega_c/(2\pi)$ are within the range of 15 MHz: an atom recoil velocity transfer results into a 15

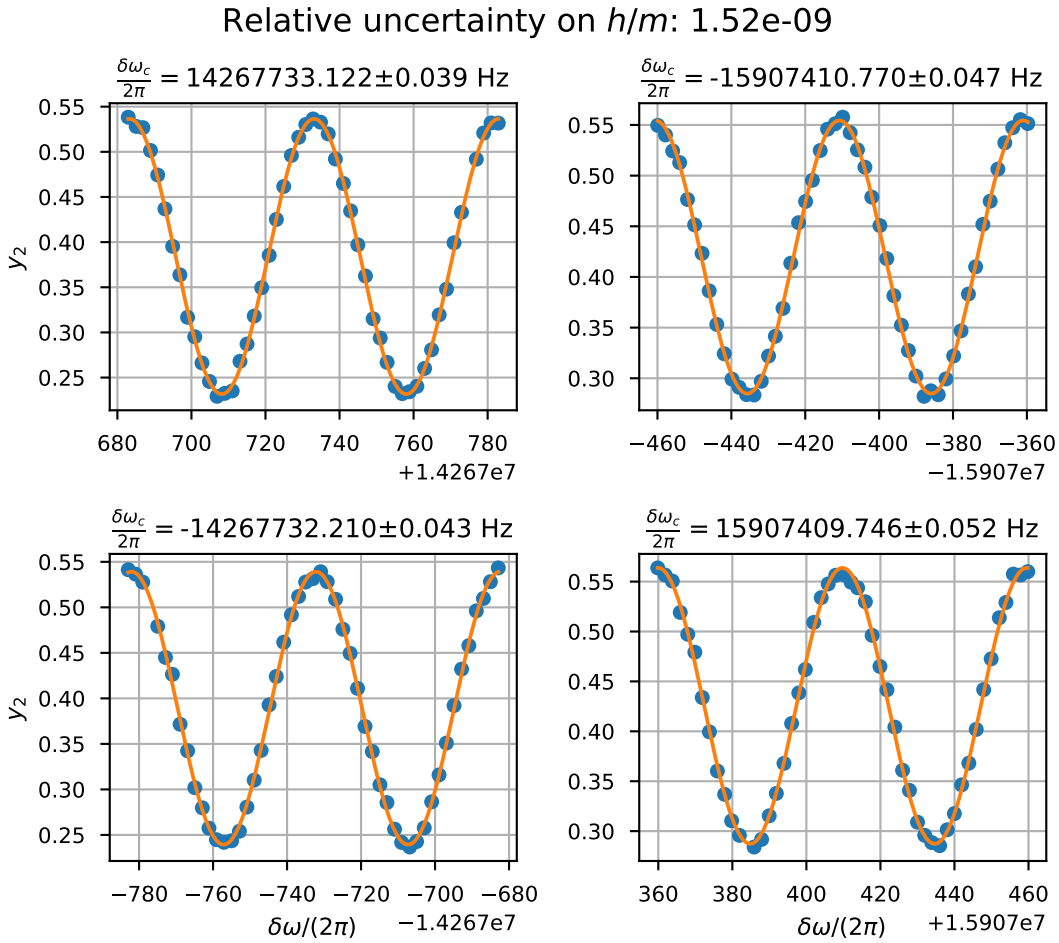

Figure 5.2: Typical spectra set for a determination of the h/m ratio. The left column corresponds to $\epsilon_B = 1$ and the top row to $\epsilon_R = 1$. The data is plotted as blue dots. The uncertainty on the central fringe condition is deduced from the fitting procedure, whose output is plotted as orange solid lines. We do not estimate uncertainty of the y_2 measurement. From the combination of the four spectra, we deduce a value of h/m with an estimated $1.5 \cdot 10^{-9}$ uncertainty.
The data points are not evenly spaced on the horizontal axis because of the vibration correction.

kHz Doppler shift for the Raman beams. Here, we transferred a thousand recoils through 500 Bloch Oscillations.

For each spectra, the typical uncertainty ~ 50 mHz gives a relative uncertainty of a few 10^{-9} and the combination of the four spectra subsequently divides by a factor ~ 2 the one spectra relative uncertainty for the h/m determination.

Finally, in order to increase the precision of the measurement, one would imagine increasing the number of Bloch Oscillations. However, this number is limited by two factors. First, the frequency range of the lasers and the fact that we cannot cross the zero velocity during the interferometer because of a residual lattice that damages the interferometer coherence and washes the fringes. Secondly, one needs to obtain well controlled experimental conditions along the entire interferometer trajectory. Its minimal extension in space along the vertical direction is approximately given by

$$2N_B\frac{\hbar k_B}{m}T_{\text{Ramsey}} + \frac{g}{2}\left(T_{\text{Ramsey}} + T_{\text{delay}}\right)^2, \tag{5.1.8}$$

which for our experimental parameters evaluates to ~ 15 cm. However, the real extension is larger:

We have plotted in figure (5.3) the typical atom trajectories for the h/m measurement. After the release from the optical molasses stage, the atoms, in $|F = 2\rangle$, are subjected to a 650 Bloch Oscillations pulse upwards in order for them to reach the interferometry region. A second Bloch pulse closes the atom elevator and is responsible for the precise positioning of the atom cloud during the interferometer sequence. We thus prepare the atoms at a given altitude $z_0(\epsilon_B)$ and at a velocity $v_0(\epsilon_B)$.

This positioning is important for the control of some systematic effects:

1. The atoms should remain in the area where the magnetic field is well controlled (~ 45 cm height) during the interferometer (see section 6.3.2).

2. The trajectories corresponding to the two Bloch acceleration directions should be carefully placed in order to reduce the effect of gravity gradient (see section 6.2).

3. The copropagating transition induces an additional coupling that shifts the energy levels during the Raman pulses. Their effect scales inversely with the atom velocities (see section 6.3.1.3). As such, the trajectories cannot feature velocities close to zero during the interferometric process.

These three reasons extend the minimal size required for running our h/m determination protocol. The required spatial extension over the vertical direction

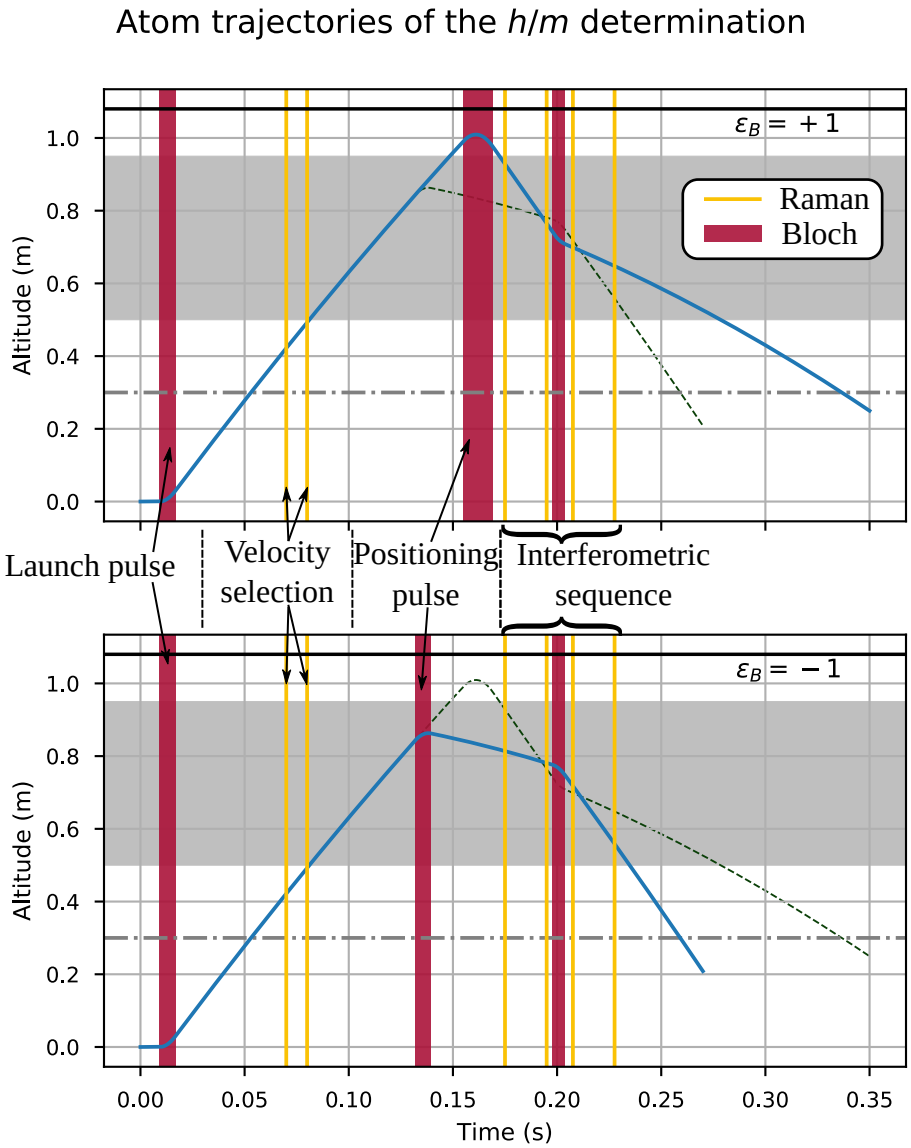

Figure 5.3: Trajectories of the atom clouds for the two Bloch accelerations directions (top: $\epsilon_B = +1$, bottom: $\epsilon_B = -1$). We separated the plots to highlight the differences between the two cases. The blue line corresponds to the trajectory of the Bloch direction indicated in the title. The green dashed line corresponds to the other and has been plotted to ease the comparison.
The red area indicate the Bloch Oscillations pulses and the yellow lines the position of the Raman pulses. The first two correspond to the preselection stage. The four other form the interferometer.
Finally, the horizontal dashed-dotted line indicates the altitude of the detection device and the black line the ceiling of the vacuum cell. The gray area is the region in which we estimate that the control of the magnetic field is optimal.

is made $\sim$ 40 cm, almost the full extension of the interferometry area. As such 500 Bloch Oscillations appear as a limit that will be difficult to overcome.

Alternatively, at constant phase sensitivity, the precision of the $\delta\omega_c$ determination scales inversely with T_{Ramsey}. As we have seen in section 3.2.4, the low frequency vibration noise sensitivity scales linearly with T_{Ramsey} (equation (3.2.10)). As a consequence, increasing T_{Ramsey} requires an increased precision in the vibration measurement. Furthermore, the spatial extension of the interferometers also scales with T_{Ramsey}, which is ultimately the main limitation to the tuning of this parameter.

Finally, in between those two elevator Bloch pulses, we use a long Raman π pulse ($\sim$ 500 μs) that selects a narrow longitudinal velocity class. The selected atoms are thus placed in $|F = 1\rangle$ and the non selected atoms are removed with a blow away pulse. The selected atoms are subsequently placed in $|F = 2\rangle$ with a shorter π pulse. This preselection stage reduces the impact of velocity dependent phase shifts with Raman transitions as it reduces inhomogeneous phase shifts on the atomic sample and as such preserves contrast.

5.1.5 Raman wavevector variation

To obtain equation (5.1.5), we assumed that the wavevector of the Raman transitions was constant along the interferometric sequence. However, the Doppler shift varies by 15 MHz between its beginning and end, resulting in a variation of the Raman wavevector that must be considered to extract h/m from the measurements of the four central fringes $\delta\omega_c(\epsilon_R, \epsilon_B)$. We will then use the Lagrangian formalism to account for these variations. This treatment leads to an explicit definition of the Raman wavevector, given in equation (5.1.17), to use in equation (5.1.5) for the h/m determination.

We recall that with regard to the Bloch Oscillations process, the two lasers are chirped symmetrically so that the two photon wavevector remains constant. This is not the case for Raman transtions where the frequency of a single laser is changed.

We write $\vec{u}$ the normal vector pointing upwards, opposite to the gravity acceleration. For the Raman transitions we have two lasers:

$$\begin{cases} \omega_1, & \vec{k}_1 = \epsilon_R \frac{\omega_1}{c} \vec{u} \\ \omega_2, & \vec{k}_2 = -\epsilon_R \frac{\omega_2}{c} \vec{u} \end{cases}. \tag{5.1.9}$$

We recall that the effective wavevector of the transition writes $\vec{k}_R = \left(\vec{k}_1 - \vec{k}_2\right) = \epsilon_R \vec{u}\,(\omega_1 + \omega_2)/c$. In our experiment, ω_1 is a fixed parameter while ω_2 is set to a specific frequency using the frequency chain described in section (3.2.2). We use a frequency ramp at a rate β to compensate for gravity during the Ramsey sequences

$\omega_{\text{off}}/(2\pi)$	6 834 847 522.277	Hz
$\beta/(2\pi)$	25 148 419.694	Hz/s
$\delta^0(\epsilon_B = 1)/(2\pi)$	−18 449 959.483	Hz
$\delta^0(\epsilon_B = -1)/(2\pi)$	−3 362 388.127	Hz
$\delta\omega(\epsilon_B = 1)/(2\pi)$	14 292 881 ± 50	Hz
$\delta\omega(\epsilon_B = -1)/(2\pi)$	−15 882 261 ± 50	Hz

Table 5.1: Raman frequency parameters for an experimental sequence with 500 Bloch Oscillations during the interferometer.

and a frequency jump $\delta\omega$ to maintain the resonance after the Bloch Oscillations pulse.

More precisely, the sequence program into the synthesizer is:

$$\omega_2(t) = \omega_1 - \omega_{\text{off}} - \delta\omega_2(t), \tag{5.1.10}$$

with

$$\delta\omega_2(\epsilon_R, \epsilon_B, t \in [t_I, t_{II}]) = \epsilon_R(\delta_0(\epsilon_B) - \beta(t - t_I)) \tag{5.1.11}$$

and

$$\delta\omega_2(\epsilon_R, \epsilon_B, t \in [t_{III}, t_{IV}]) = \epsilon_R(\delta_0(\epsilon_B) + \delta\omega - \beta(t - t_{III})), \tag{5.1.12}$$

where t_I, t_{II}, t_{III} and t_{IV} are the times of the four $\pi/2$ Raman pulses.

In order to be resonant with the atoms, one should have:

$$\omega_{\text{off}} \simeq \omega_{HFS} + \omega_{\text{rec}} \tag{5.1.13}$$
$$\delta_0(\epsilon_B) \simeq k_R v_0(\epsilon_B) \tag{5.1.14}$$
$$\beta \simeq k_R g \tag{5.1.15}$$
$$\delta\omega \simeq k_R(2\epsilon_B N_B v_B - g T_{\text{delay}}), \tag{5.1.16}$$

where $\omega_{rec} = \frac{\hbar^2 k_R^2}{2m}$ corresponds to the recoil energy.

In the time sequence, approximate values are used to calculate these first three parameters, as well as $\delta\omega$ which is scanned around the estimated value. Table 5.1 compiles the numerical values used for the sequences presented in figure (5.3).

In the calculation of the interferometer phase, two terms appear, the terms in ωt and kz (see section 2.2.3.2). It is important to note that when calculating the term in ωt, the δ_0, ω_{off} and β quantities cancel out and do not have any effect.

In the following paragraph, we evaluate the corrections related to the term in kz. It should be noted that what is relevant in the calculation is the synthesized experimental value.

The (kz) term in the phase of the lasers writes:

$$\phi(z) = \epsilon_R(k_1 + k_2)z = \epsilon_R(k_R + \delta k_2(t))z, \tag{5.1.17}$$

where

$$k_R = \frac{2\omega_1 - \omega_{\text{off}}}{c} \tag{5.1.18}$$

$$\delta k_2(t) = -\frac{\delta\omega_2(t)}{c} \tag{5.1.19}$$

We define the Lagrangian of equation (2.2.49) with a constant Raman wavevector $k_e = \epsilon_R k_R$. The term $\epsilon_R \delta k_2(t) z$ leads to a perturbation of this Lagrangian:

$$\delta\mathcal{L} = \epsilon_R \sum_{\text{pulses}} \delta k_2(t) z(t) \delta(t - t_{\text{pulse}}) \tag{5.1.20}$$

With this formalism, we do not have to calculate the perturbation to the trajectories due to the change in the recoil, and we simply obtain the phase shift induced by this perturbative Lagrangian:

$$\Delta\Phi(\epsilon_R, \epsilon_B) = \epsilon_R \frac{-\delta\omega_2(t_I) z_I + \delta\omega_2(t_{II}) z_{II} + \delta\omega_2(t_{III}) z_{III} - \delta\omega_2(t_{IV}) z_{IV}}{c} \tag{5.1.21}$$

In order to calculate the phase shift of the interferometer, it should be noted that the same linear sweep is used between t_I and t_{II} as well as between t_{III} and t_{IV}. We then have $\delta\omega_2(t_{II}) - \delta\omega_2(t_I) = \delta\omega_2(t_{IV}) - \delta\omega_2(t_{III})$. Thus, the phase shift is independent of the initial position of the atoms.

From the atom trajectories, we can calculate this correction. We can notice that $\delta\omega_2$ changes sign with ϵ_R while the atom positions do almost not change. $\Delta\Phi$ is then almost constant when the Raman direction is changed, and thus cancels out in the calculation of h/m.

More precisely, we have:

$$\Delta\Phi(\epsilon_R, \epsilon_B) = T_{\text{Ramsey}}\zeta(\epsilon_B) - \epsilon_R \frac{T_{\text{Ramsey}}\beta}{c} \Delta z, \tag{5.1.22}$$

where the main part is $T_{\text{Ramsey}}\zeta(\epsilon_B)$, with:

$$\begin{aligned}\zeta(\epsilon_B) = -\frac{1}{c}\Big(&\big(2\epsilon_B N_B v_B - g T_{\text{delay}}\big)\big(\delta_0(\epsilon_B) + \beta T_{\text{Ramsey}}\big) + \beta\delta z_m(\epsilon_B) \\ &+ \delta\omega\Big(v_0(\epsilon_B) + 2\epsilon_B N_B v_B - g T_{\text{delay}} - \frac{g T_{\text{Ramsey}}}{2}\Big)\Big),\end{aligned} \tag{5.1.23}$$

where $\delta z_m(\epsilon_B)$ is the variation of position between the two Ramsey sequences, averaged over the inversion of the Raman direction:

$$\delta z_m = \frac{(z_{III}(\epsilon_R = 1) - z_I(\epsilon_R = 1)) + (z_{III}(\epsilon_R = -1) - z_I(\epsilon_R = -1))}{2} \quad (5.1.24)$$

This term proportional to $\zeta(\epsilon_B)$ cancels in the calculation of h/m.

The second part is proportional to the distance $\Delta z = 2T_{\text{delay}} v_R$, where v_R is the two photon Raman recoil. This term evaluates to $\sim 10^{-5}$ rad and is therefore negligible.

With this approximation, equations (5.1.5) and (5.1.6) remain valid provided that the Raman wavevector is defined by equation (5.1.17). The equation to use to determine the phase shift is now

$$\delta\phi(\epsilon_B) = T_{\text{Ramsey}} \left(\frac{\sum_{\epsilon_R} \delta\omega_c(\epsilon_R, \epsilon_B)}{2} - \zeta(\epsilon_B) \right). \quad (5.1.25)$$

The interferometer is no longer closed, since the recoil is not the same with each Raman pulse. As as a consequence, the phase depends on the initial velocity $v_0(\epsilon_B)$ of the atoms. It is therefore necessary to evaluate it precisely in order to estimate the phase shift.

The effect of the Raman wavevector variation is illustrated in figure (5.4). We have recorded the four spectra with different number of Bloch Oscillations during the interferometer. From each measurement we extracted the phase using either equation (5.1.7) or (5.1.25), on respectively the top and bottom plots.

The solid line on the top plot is an estimation of the $T_{\text{Ramsey}}\zeta(\epsilon_B)$ derived from the *a priori* knowledge of the trajectory parameters.

We have presented the measurement protocol for the h/m determination. The discussion treated the improvement possibilities in term of parameter set to increase to sensitivity and we showed that we are exploiting fully the potential of the experimental setup. Moreover, we studied in detail the output phase of the interferometers and extracted precise formulas for the h/m ratio, the gravitational acceleration and the common perturbations over the Raman direction inversion.

Finally, we have displayed an example of the four spectra fringes, but we did not discussed in detail the sensitivity performance of the setup. We turn to the treatment of this point now.

5.2 Statistical performance

We have seen that performing four spectra we can reach a typical relative precision of $\sigma = 2 \cdot 10^{-9}$ on h/m. In order to gain an order of magnitude we repeat the

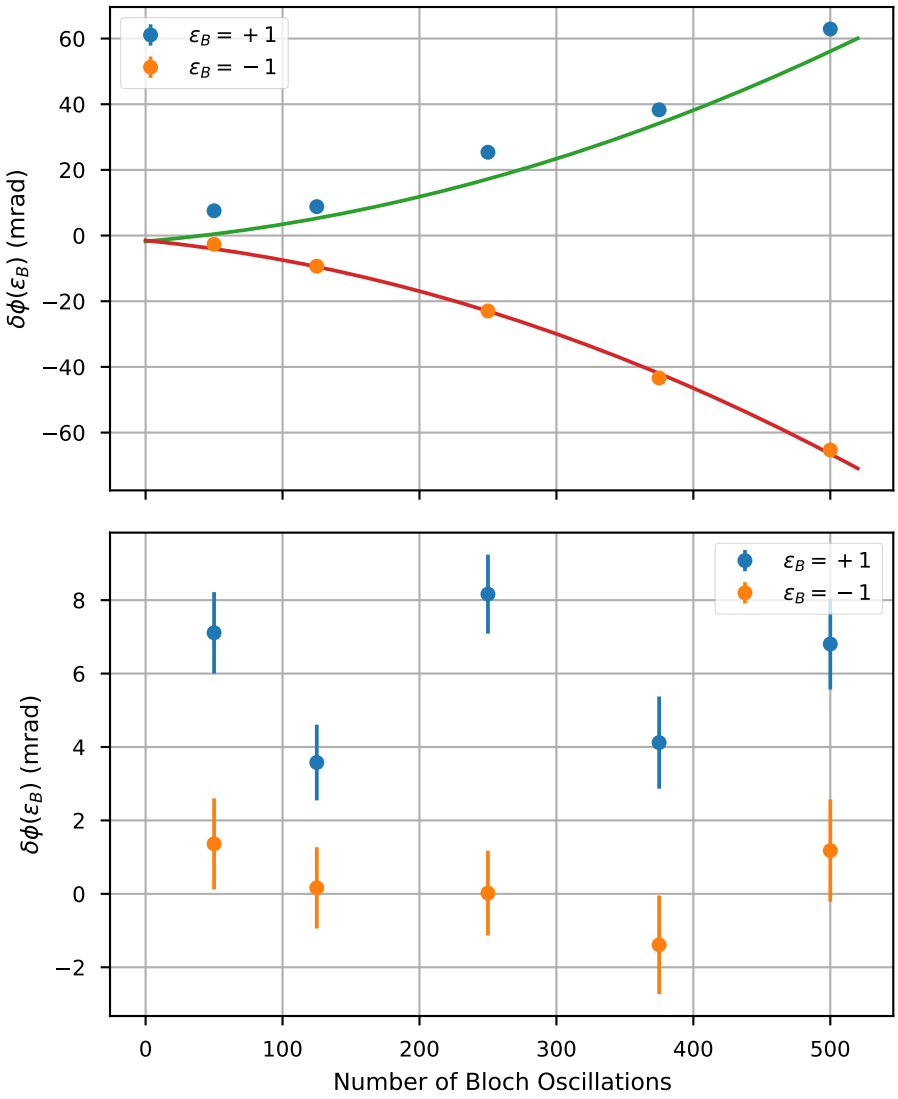

Figure 5.4: Observation of the phase shift induced by Raman wavelength variation. Top: For different number of Bloch Oscillations during the interferometer, we recorded the four spectra. The dots represent the phase $\delta\phi(\epsilon_B)$ obtained using equation (5.1.7). The errorbars are smaller than the dots. The solid line is the evaluation of $T_{\text{Ramsey}}\zeta(\epsilon_B)$.
Bottom: Residuals, which correspond to evaluating $\delta\phi(\epsilon_B)$ with equation (5.1.25).

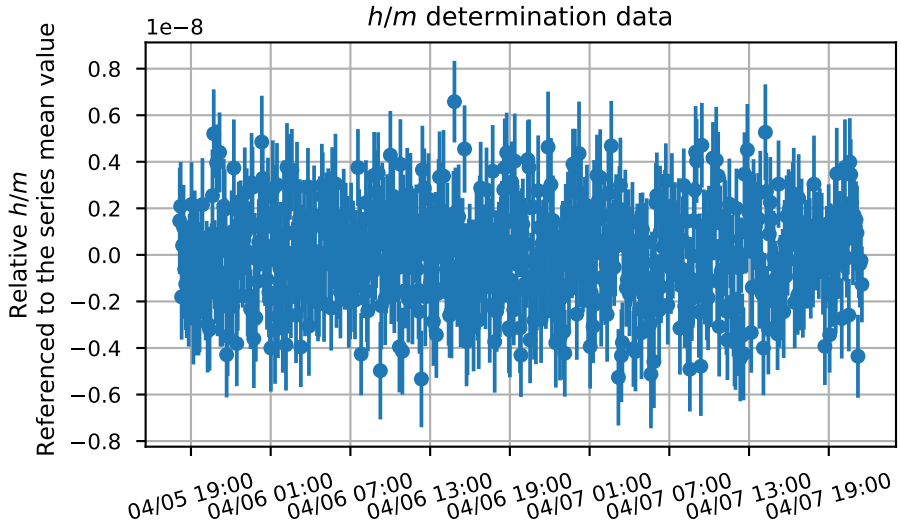

Figure 5.5: Set of h/m 678 determinations taken over a week-end. Each point correspond to ~ 5 minutes of integration.

experiment. After N repetitions of the experiment, and provided that the determinationof the h/m value are independent and identically distributed, we have that the precision over the integration is given by:

$$\sigma_{total} = \frac{\sigma}{\sqrt{N}} \tag{5.2.1}$$

In order to present the statistical performance of our setup, we present the result of a 48 hours integration that was performed over a week-end. The data set is composed of $N = 678$ determinations of h/m, which are collected in figure (5.5). This data set was obtained with $T_{\text{Ramsey}} = 20$ ms and 500 Bloch Oscillations for the acceleration.

The Allan deviation $\sigma_y(\tau)$ of the values is a powerful tool to study the statistical distribution of the determinations. Introduced to characterize the stability of atomic clocks, the Allan deviation is also an accurate tool to observe drifts of the experimental apparatus. For a measured quantity y, it is defined as:

$$\sigma_y^2(\tau) = \frac{1}{2}\left\langle (\bar{y}_{n+1} - \bar{y}_n)^2 \right\rangle, \tag{5.2.2}$$

where $\langle \dots \rangle$ designs the mean operation, and $\bar{y}_n$ the n-th determination of y obtained over an integration duration τ. We obtain these values by performing packets of determination and taking the mean value of those packets. It is possible to show that if the determinations are independent and identically distributed,

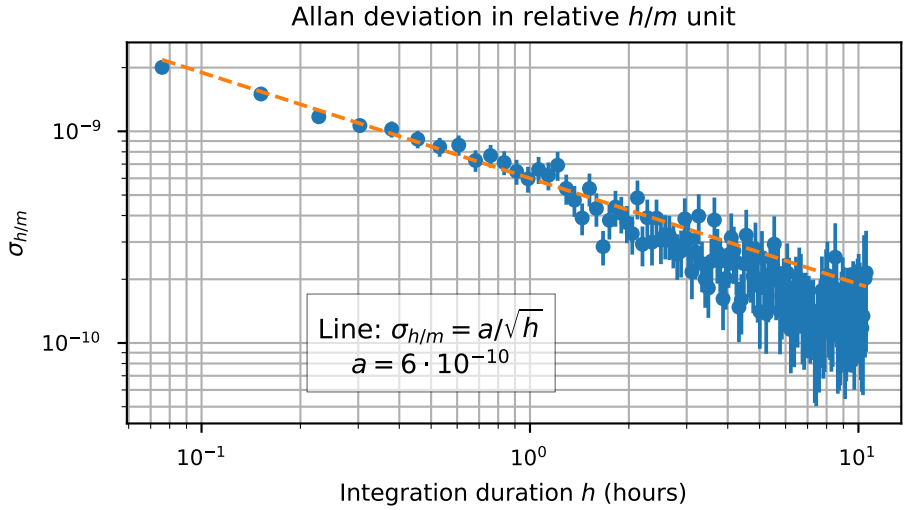

Figure 5.6: Comparison between the data Allan deviation and the expected behavior in the case of a white noise induced data distribution.

then the Allan deviation will scale with $1/\sqrt{\tau}$. In this context, it can be seen as a standard deviation averaged over time.

We plotted in figure (5.6) the Allan deviation of the data set. It behaves with the power law of a white noise so that we can estimate the performance of the experimental setup to a relative precision of $1.7 \cdot 10^{-10}$ on h/m over 12 hours of integration. One of the limit of the Allan deviation span is that it is limited to a quarter of the total integration duration. As a consequence, it cannot be use to characterize the full data set.

However, we may split the data set in 4 subsets that corresponds to 12 hours of integration each. From the Allan deviation, we have that the distribution of the 4 weighted mean values of the subsets are governed by a white noise. These four values are plotted in figure (5.7). As they agree with each other, we obtain the raw value of the h/m determination by taking the weighted mean of these four values. We then obtain a relative precision of $8.5 \cdot 10^{-11}$ on h/m over 48 hours of integration.

Compared to the precedent determination of our team with a statistical uncertainty of $4.4 \cdot 10^{-10}$ and the statistical uncertainty of the recent Berkeley determination of $3.2 \cdot 10^{-10}$, the performance of our setup is particularly interesting to provide a new determination of the fine structure constant.

Using the same dataset, we extract the determinations of g using equation (5.1.6). The results of these determinations are plotted in figure (5.8). The solid

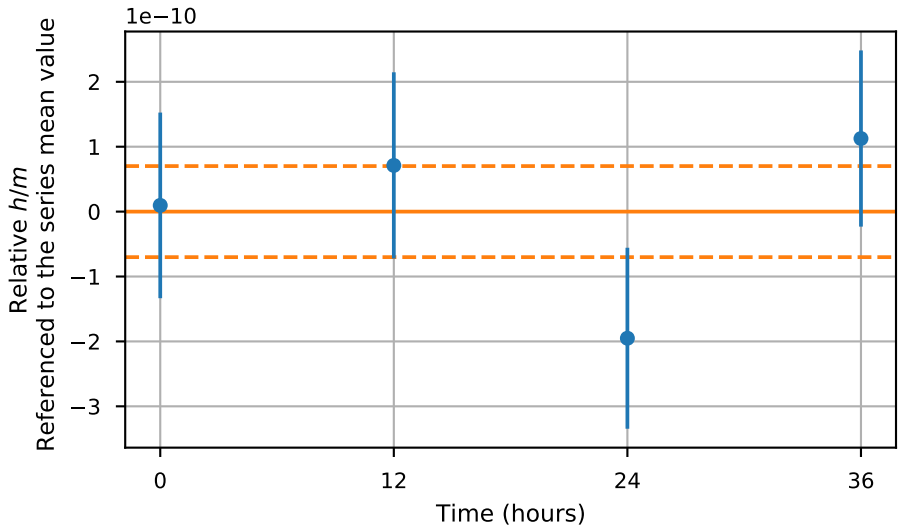

Figure 5.7: Four integrated h/m values. Each points corresponds to 12h of integration.

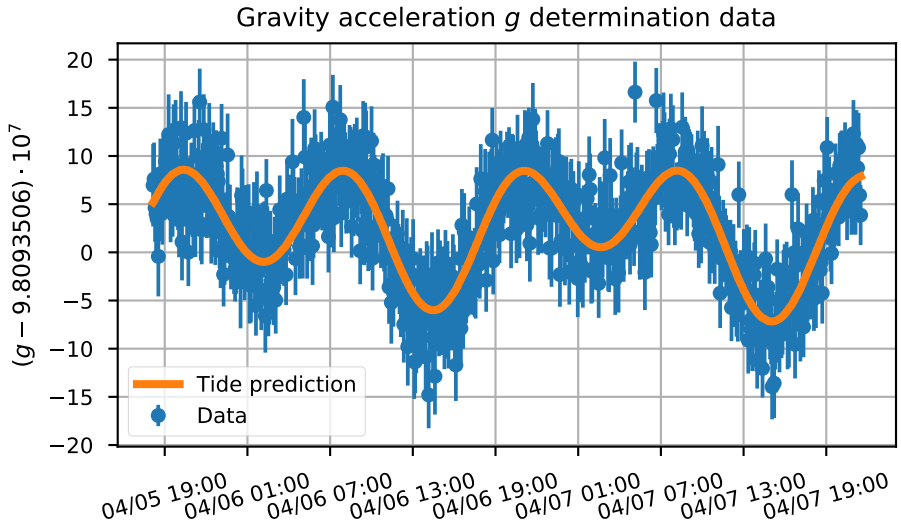

Figure 5.8: Determination of g extracted from the same dataset as figure (5.5). Blue dots: experimental determinations. Orange line: Predictions obtained from a model of Earth's tides.

line has been obtained using PETGTAB software which models Earth's tides, and our measurements are in agreement with this model.

By subtracting the tidal effect from our dataset, we compute the Allan variance of the g measurements. We then obtain a sensitivity of about $5{\cdot}10^{-6}$ $\mathrm{m{\cdot}s^{-2}{\cdot}Hz^{-1/2}}$. This performance is about 100 times worse than the best sensitivity obtained with a gravimeter based on atom interferometry reported in [Hu, 2013]. This performance ratio corresponds roughly to the phase sensitivity ratio between the two interferometers. It should be noted, however, that to achieve this performance on our experimental setup, it is necessary to control vibrations much better than is currently the case.

Thanks to our sensitivity on h/m, we have run various parameters scans that are represented in figure (5.9). As it can be observed, the current status of the experiment is at the identification of systematic error sources, either technical or fundamental. For example, the fast shutters presented in figure (3.21) were implemented to prevent leakage from the Bloch beams, diffracted by a residual RF signal in the AOMs.

Besides this experimental surveys, we have also developed a theoretical analysis of the systematic effects that will be accounted for in the error budget of the determination. This theoretical analysis constitutes the following and final part of this thesis.

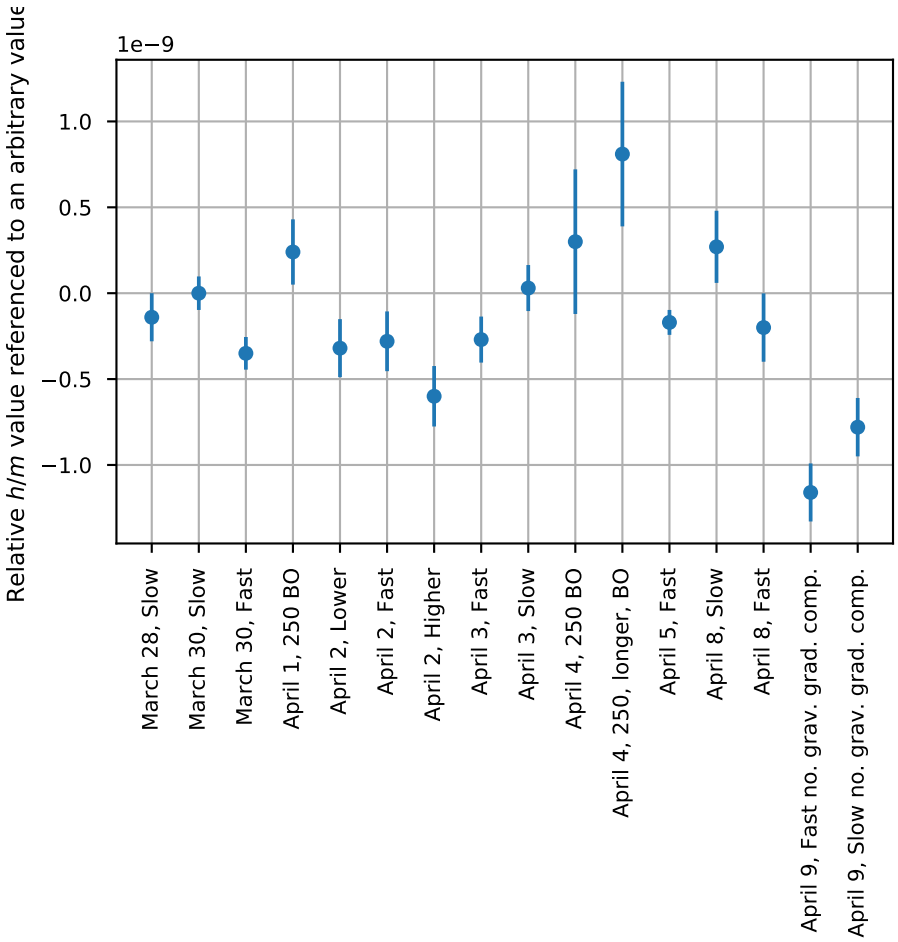

Figure 5.9: Collection of h/m determination for ten days some with parameter change.

Chapter 6

Analysis of systematic effects

6.1 Introduction

6.1.1 General considerations

The analysis of systematic error sources requires a careful method towards their estimation. Indeed, an error source may induce a correction, which has to be carefully estimated, with its associated uncertainty.

Let us present the framework of this analysis. We recall that the central fringe condition that we used for the derivation of the h/m formula was obtained by computing the difference between the phase of path (B) and the one on path (A)[1]. As a consequence, evaluating the effect of a perturbation that induces a path dependent perturbation ϕ_{pert}, the central fringe condition becomes:

$$0 = T_{\text{Ramsey}}\Big(k_R\delta v(\epsilon_B) - \delta\omega_c(\epsilon_R,\epsilon_B)\Big) + \phi^{(B)}_{\text{pert}}(\epsilon_R,\epsilon_B) - \phi^{(A)}_{\text{pert}}(\epsilon_R,\epsilon_B) \qquad (6.1.1)$$

Unlike the above development on the treatment of the four spectra, the variation of the wavevector is here not represented. Indeed, we have seen that by choosing the appropriate Raman wavevector k_R defined by equation (5.1.18), then the wavevector variation effect in cancel on h/m. It will not be considered in the following.

To simplify the notations, we write

$$\delta\phi_{\text{pert}}(\epsilon_R,\epsilon_B) = \phi^{(B)}_{\text{pert}}(\epsilon_R,\epsilon_B) - \phi^{(A)}_{\text{pert}}(\epsilon_R,\epsilon_B). \qquad (6.1.2)$$

Performing the four spectra weighted sum of equation (6.1.1), we obtain:

$$\sum_{\epsilon_R,\epsilon_B} \epsilon_R\epsilon_B\delta\omega_c(\epsilon_R,\epsilon_B) = \frac{4N_Bk_Rk_B}{\pi}\frac{h}{m} + \frac{1}{T_{\text{Ramsey}}}\sum_{\epsilon_R,\epsilon_B}\epsilon_R\epsilon_B\delta\phi_{\text{pert}}(\epsilon_R,\epsilon_B) \qquad (6.1.3)$$

[1]Path (B) being the one that correspond to a transition at the first beam splitter.

We can from this equation deduce a correction to h/m. Let us first define them: from the four spectra set, we deduce a raw value of h/m given by equation (5.1.5). However, because of the perturbation, this value is displaced from the *true* h/m:

$$\left(\frac{h}{m}\right)_{\text{raw}} = \frac{h}{m} - \Delta\left(\frac{h}{m}\right). \tag{6.1.4}$$

Inversely, knowing the correction induced by a perturbation and the raw value, we can estimate the *true* value by summing the two:

$$\frac{h}{m} = \left(\frac{h}{m}\right)_{\text{raw}} + \Delta\left(\frac{h}{m}\right). \tag{6.1.5}$$

We can now give the formula for a correction induced by a differential phase shift on the interferometer arms from equation (6.1.3):

$$\Delta\left(\frac{h}{m}\right) = -\frac{\pi}{4N_B k_R k_B}\frac{\sum_{\epsilon_R,\epsilon_B}\epsilon_R\epsilon_B\delta\phi_{\text{pert}}(\epsilon_R,\epsilon_B)}{T_{\text{Ramsey}}}. \tag{6.1.6}$$

We can also express the relative correction:

$$\frac{\Delta\left(\frac{h}{m}\right)}{\frac{h}{m}} = -\frac{\sum_{\epsilon_R,\epsilon_B}\epsilon_R\epsilon_B\delta\phi_{\text{pert}}(\epsilon_R,\epsilon_B)}{T_{\text{Ramsey}}\sum_{\epsilon_R,\epsilon_B}\epsilon_R\epsilon_B\delta\omega_c(\epsilon_R,\epsilon_B)}. \tag{6.1.7}$$

Setting in this equation the weighted sum of the pulsation centers to $\Big(2\pi\Big)\cdot 4\cdot\Big(15\text{ MHz}\Big)$, and with $T_{\text{Ramsey}} = 20$ ms, we obtain that for a control of the residual phase at 1 mrad, the relative precision of the h/m determination is limited to $\sim 1.3\cdot 10^{-10}$, which is the order of magnitude that we aim.

Moreover, the sum of the phase shifts weighted by the product of the Raman and Bloch direction exhibit the cancellation potential of our protocol: even if an effect changes sign with the Bloch direction, it will be compensated if it remains constant with the Raman direction, and inversely.

Of course, all the error sources that we have to estimate are not computed through a phase perturbation. However, in these cases, which mostly correspond to a correction to the effective wavevector of the laser beams, the sign of the correction is usually unambiguous.

Nevertheless, through equations (6.1.5) and (6.1.7), we defined the framework of our analysis.

6.1.2 Description of the trajectories

The knowledge of the atomic trajectories during the interferometric sequences is a prerequisite to the estimation of some systematic effects. In order to lighten the discussion of the systematic effect estimation, we choose to present the trajectories and their parametrization at first.

6.1.2.1 Beginning of the interferometer

In between the end of the optical molasses stage and the beginning of the interferometer, the atoms a prepared with two Bloch Oscillations pulse to position them and two counterpropagating Raman pulses, positioned in between the Bloch pulses, that perform a velocity selection.

We can model a Bloch pulse as a succession of velocity kicks. However, the manipulation of such kicks as a sum can be cumbersome and one can show that it is strictly equivalent to model the Bloch Oscillations as an additional acceleration a_B applied for a duration T_B with:

$$a_B = \epsilon_B \frac{v_B}{\tau_B} \text{ and } T_B = N_B \tau_B, \tag{6.1.8}$$

where v_B is the two-photon atomic recoil $v_B = 2\hbar k_B/m$, and τ_B the duration of a Bloch Oscillation, N_B the number of Bloch Oscillations and ϵ_B its direction.

We denote the first Bloch pulse as the *launch* pulse, characterized by the number of Bloch Oscillations N_l and its time of application t_l. Its direction is upwards ($\epsilon_l = +1$), and it is common to the four spectra.

We then obtain, by setting the position reference at the position of the molasse stage, the position and velocity after the launch pulse:

$$v(t) = -gt + N_l v_B \tag{6.1.9}$$

$$z(t) = -\frac{gt^2}{2} + N_l v_B \Big(t - (t_l + T_l/2)\Big) \tag{6.1.10}$$

where the last line shows that in term of position, after the Bloch pulse, it can be modeled as a single velocity kick placed at the middle of its duration.

We now move to the description of the velocity *selection*, also common to the four spectra. At a time t_s, a Raman pulse is applied to the atoms. On top of transferring a narrow velocity class of the atomic distribution, it kicks the velocity by $-\epsilon_R v_R$,[2] where v_R is the two photon Raman recoil. After a duration T_s, we apply a second Raman pulse that transfers back the atoms and kick them by $\epsilon_R v_R$.

[2]The minus signs is induced by the fact that the atoms are in $|F = 2\rangle$ at the end of the molasses stage

As a consequence, the velocity of the atoms is unchanged but their position has been displaced by $\Delta z_0 = -\epsilon_R v_R T_s$.

Finally, the *positioning* Bloch pulse depends on the direction of acceleration during the interferometer ϵ_B in terms of number of oscillations $N_p(\epsilon_B)$ and timing $t_p(\epsilon_B)$ but is always directed downwards: $\epsilon_p = -1$. We finally obtain that the equation of motion after the preparation stage is given by:

$$v(t) = -gt + \Big(N_l - N_p(\epsilon_B)\Big)v_B \tag{6.1.11}$$

$$z(t) = -\frac{gt^2}{2} + v_B\bigg(\Big(N_l - N_p(\epsilon_B)\Big)t - N_l t'_l + N_p(\epsilon_B)t'_p(\epsilon_B)\bigg) - \epsilon_R v_R T_s \tag{6.1.12}$$

where we have compacted the timing of the Bloch pulses with $t'_k = t_k + T_k/2$ for each of them. These equation shows that the velocity at the beginning of the interferometer depends only on the Bloch acceleration direction during the interferometer. Furthermore, the corresponding position depends also mainly on ϵ_B, with a correction depending only on ϵ_R. As a consequence, at the beginning of the interferometer t_{start}, the initial position and velocity are given by $z = z_0(\epsilon_B) - \epsilon_R \Delta z_0$ and $v = v_0(\epsilon_B)$.

The following tables give typical parameters of this preparation stage, and values of the initial position and velocities, which were also used to present the trajectories during the previous chapter in figure (5.3).

Parameter	t_l	N_l	t_s	T_s
Value	9 ms	650	70 ms	10 ms
Parameter	$t_p(\epsilon_B = +1)$	$N_p(\epsilon_B = +1)$	$t_p(\epsilon_B = -1)$	$N_p(\epsilon_B = -1)$
Value	155 ms	1185	131 ms	635

Parameter	t_{start}	Δz_0
Value	175 ms	120 μm
Parameter	$z_0(\epsilon_B = +1)$	$z_0(\epsilon_B = -1)$
Value	93 cm	81 cm
Parameter	$v_0(\epsilon_B = +1)$	$v_0(\epsilon_B = -1)$
Value	-8.1 $\mathrm{m \cdot s^{-1}}$	-1.5 $\mathrm{m \cdot s^{-1}}$

6.1.2.2 During the interferometer

The two arms of the interferometer can be described independently with position $z^{(A)}(t)$ and $z^{(B)}(t)$, but we rather adopt a description through the mean position

$z_m(t)$, and position difference $\delta z(t)$ given by:

$$z_m(t) = \frac{z^{(A)}(t) + z^{(B)}(t)}{2} \tag{6.1.13}$$

$$\delta z(t) = z^{(B)}(t) - z^{(A)}(t) \tag{6.1.14}$$

The position difference can be obtained immediately:

$$\delta z(t) = \begin{cases} -\epsilon_R v_R t & \text{if } t < T_{\text{Ramsey}} \\ -\epsilon_R v_R T_{\text{Ramsey}} & \text{if } t < T_{\text{delay}} \\ -\epsilon_R v_R (T_{\text{delay}} + T_{\text{Ramsey}} - t) & \text{else} \end{cases} \tag{6.1.15}$$

The trajectories separate continuously during the first Ramsey sequence. In between the two, their respective velocities are the same and the position difference remains constant, and is finally linearly reduced to 0 during the second Ramsey sequence.

The mean position on the other hand obeys the evolution law of a particle subjected to the gravitational field with initial position $z_0'(\epsilon_R, \epsilon_B) = z_0(\epsilon_B) - \epsilon_R \Delta z_0(\epsilon_R)$ and velocity $v_0(\epsilon_B) - \epsilon_R v_R/2$ because of the velocity kick of the first beam splitter. We should also take into account the Bloch pulse in between the Ramsey sequences and obtain:

$$z_m(t) = z_0'(\epsilon_R, \epsilon_B) + v_0(\epsilon_B)t - \frac{gt^2}{2} \tag{6.1.16}$$

$$+ \begin{cases} \epsilon_R \frac{v_R}{2} t & \text{if} \quad 0 < t < T_{\text{Ramsey}} \\ \epsilon_R v_R \left(t - \frac{T_{\text{Ramsey}}}{2}\right) & \text{if} \quad T_{\text{Ramsey}} < t < t_B \\ \epsilon_R v_R \left(t - \frac{T_{\text{Ramsey}}}{2}\right) & \\ + \frac{\epsilon_B a_B (t - t_B)^2}{2} & \text{if} \quad t_B < t < t_B + T_B \\ \epsilon_R v_R \left(t - \frac{T_{\text{Ramsey}}}{2}\right) & \\ + \epsilon_B a_B T_B \left(t - t_B'\right) & \text{if} \quad t_B + T_B < t < T_{\text{delay}} \\ \epsilon_R \frac{v_r}{2} \left(t + T_{\text{delay}} - T_{\text{Ramsey}}\right) & \\ + \epsilon_B a_B T_B \left(t - t_B'\right) & \text{else} \end{cases},$$

where t_B is the time at which the Bloch acceleration starts, and $t_B' = t_B + T_B/2$ its middle point.

Finally, the decomposition of the trajectories in mean position and position difference can be extended over the Raman direction inversion with the definitions:

$$Z_m(t) = \frac{z_m(\epsilon_R = 1, t) + z_m(\epsilon_R = -1, t)}{2} \tag{6.1.17}$$

$$\Delta Z(t) = z_m(\epsilon_R = 1, t) - z_m(\epsilon_R = -1, t) \tag{6.1.18}$$

whose expression can be easily deduced from the above equations. In particular, we find that:

$$\Delta Z(t) = -2\Delta z_0 - \begin{cases} v_R t & \text{if} \quad 0 < t < T_{\text{Ramsey}} \\ 2v_R \left(t - \frac{T_{\text{Ramsey}}}{2}\right) & \text{if} \quad T_{\text{Ramsey}} < t < T_{\text{delay}} \\ v_r \left(t + T_{\text{delay}} - T_{\text{Ramsey}}\right) & \text{else} \end{cases}, \tag{6.1.19}$$

which shows that the interferometer mean trajectories deviate from each other with linear branches over the interferometer duration as we invert the Raman direction. This behavior may limit the effectiveness of the Raman inversion technique.

One may notice the contrast on the level of details for the trajectories description between the extraction of the interferometric signal and the treatment of systematic effects. This is because the four terms $\vec{k_e} \cdot \vec{z}$ term over one interferometer do not retain information on the initial conditions of the atomic motion. However, this information can no longer be discarded when analyzing systematic error sources.

We now turn to these estimations. We start by the effects that we can control through the positioning of the interferometer: gravity gradients, then light shift (in particular, the one induced by copropagating transitions) and then the effect of magnetic field inhomogeneity.

We will then turn to the estimation of the lasers effective wavevector, which constitutes of the measurement of their frequency, the corrections induces by the non plane wave profile of the beam and their relative alignment. Because it is technically linked to this last point, we will also discuss the compensation of the Earth rotation. Finally, we will discuss phase shifts induced by the Raman phase lock device.

For numerical applications, we use the interferometer presented in figure (5.3), for which the Ramsey duration is $T_{\text{Ramsey}} = 20$ ms, the delay between the Ramsey sequences is $T_{\text{delay}} = 32.6$ ms, and the number of Bloch Oscillations is $N_B = 500$, with a duration per oscillation $\tau_B = 12$ μs.

6.2 Effect induced by the gradient of gravity

We have already presented the gradient of gravity in two contexts: first as a perturbation on the interferometer output phase in section 2.2.3 and secondly as a measured quantity in the characterization of the experimental setup in section 3.3.3.2.

The latter gives us an estimation of the gravity gradient that we should account for and the former the method to compute phase shift that it induces. However, in the context of the determination of h/m, as we perform spectra with inverted Bloch acceleration direction in order to cancel the gravity acceleration, we show that we can place precisely the interferometers with respect to one another in order to cancel the phase shift induced by gravity gradients.

First, we start by recalling that the expression of the phase shift induced by gravity gradients expresses as:

$$\phi^{\text{grav. grad}} = \frac{m\gamma}{\hbar}\int_{\text{interferometer}} z_m(t)\delta z(t)dt, \tag{6.2.1}$$

where γ is the linear correction to the constant gravity. We may already notice that the position difference δz changes sign with the Raman direction inversion, such that the phase shifts add on the h/m determination. As a consequence, the cancellation can only occur over the Bloch direction inversion.

Feeding the trajectories information into equation (6.2.1), we obtain:

$$\begin{aligned}\phi^{\text{grav. grad}} = &-\epsilon_R\frac{m\gamma T_{\text{Ramsey}}v_R}{12\hbar}\times \\ &\Bigg(\epsilon_B T_B a_B\left(\frac{T_B^2}{2}+2T_{\text{Ramsey}}^2+6(T_{\text{delay}}-t'_B)(T_{\text{Ramsey}}+T_{\text{delay}}-t'_B)\right) \\ &+6T_{\text{delay}}\left(T_{\text{delay}}(v_0-\epsilon_R v_R)+T_{\text{Ramsey}}v_0+2z_0\right) \\ &-2gT_{\text{delay}}\left((T_{\text{Ramsey}}+T_{\text{delay}})^2-\frac{T_{\text{Ramsey}}T_{\text{delay}}}{2}\right)\Bigg),\end{aligned} \tag{6.2.2}$$

where we have replaced $t_B + T_B/2$ by t'_B to simplify the notations. We simplify formally the notations of this equation in order to compute the four spectra combination. Noting that only z_0 and v_0 depend of ϵ_B, we rewrite it:

$$\phi^{\text{grav. grad}}(\epsilon_R,\epsilon_B) = \epsilon_R A\Big(\epsilon_B B + C(\epsilon_B) + \epsilon_R D + E\Big). \tag{6.2.3}$$

For the h/m determination, we perform the sum of each central frequency weighted by the product of the Bloch and Raman direction, such that the effective phase

shift induced by the gravity gradient can be written:

$$\phi_{h/m}^{\text{grav. grad}} = \sum_{\epsilon_R,\epsilon_B} \epsilon_R\epsilon_B\phi^{\text{grav. grad}} \tag{6.2.4}$$

$$= 2A\Big(2B + C(\epsilon_B = 1) - C(\epsilon_B = -1)\Big). \tag{6.2.5}$$

Taking into account the four spectra, we see that half of the terms cancel. We can now undo the formal identification, and by writing $\Delta z_0 = z_0(\epsilon_B = 1) - z_0(\epsilon_B = -1)$ and $\Delta v_0 = v_0(\epsilon_B = 1) - v_0(\epsilon_B = -1)$, we obtain:

$$\phi_{h/m}^{\text{grav. grad}} = -\frac{2m\gamma T_{\text{Ramsey}} T_{\text{delay}} v_R}{\hbar} \times \tag{6.2.6}$$

$$\left(\frac{T_B a_B}{6T_{\text{delay}}}\left(\frac{T_B^2}{2} + 2T_{\text{Ramsey}}^2 + 6(T_{\text{delay}} - t'_B)(T_{\text{Ramsey}} + T_{\text{delay}} - t'_B)\right)\right.$$

$$\left. + \frac{1}{2}(T_{\text{Ramsey}} + T_{\text{delay}})\Delta v_0 + \Delta z_0\right).$$

As a consequence, we can cancel the effect of the gradient of gravity by carefully positioning the two interferometer trajectories with respect to each other. In particular, we have put the above expression in a form that is the product of a prefactor in mrad·m^{-1} multiplied by a distance.

Using our typical values for the interferometer, and $\gamma = 3 \cdot 10^{-6}$ s^{-2} we can estimate the prefactor to 64 mrad·m^{-1}, which correspond to a systematic error on h/m of $8.5 \cdot 10^{-9}$ m^{-1}. As a consequence, in order to cancel the effect induced by the gradient of gravity it is sufficient to control the positioning of the interferometer at the level of the mm.

In order to achieve such a control, we use the positioning pulses and we set the number of oscillations of each pulse as well as the timing of one of them and cancel equation (6.2.6) with the timing of the second one, with a precision of 1 μs, which correspond to a positioning precision at the level of 10 μm. This allows us to cancel the gravity gradient error below 10^{-13} in relative h/m unit.

6.3 Effects on the atomic energy levels

6.3.1 Phase shift during Raman pulses

We have treated in detail phase shifts induced by a resonance deviation during the atom-laser coupling in section 4.2. The estimation of the detuning of the transition is hence fundamental. We described the contribution of the light shifts induced by one photon transitions and of the Doppler effect. However, the Ramans lasers

configuration is such that a far off resonance copropagating Raman coupling is applied to the atoms. This two photons coupling leads to an internal energy shift that we also estimate.

6.3.1.1 One-pulse phase shift

We start by recalling the formula that gives the phase shift that applies on the non diffracted arm of the interferometer for one Raman pulse:

$$\delta\phi = \arctan\left(\frac{\delta}{\Omega_e}\tan\left(\frac{\Omega_e\tau}{2}\right)\right), \tag{6.3.1}$$

where δ is the detuning of the transition and Ω_e its effective Rabi frequency.

In our case, the detuning is given by Doppler effect δ_{Doppler} and the one photon and two photons light shifts ($\Omega^{\text{LS}}_{\text{diff}}$ and $\delta_{2ph.}$, with $\Omega^{\text{LS}}_{\text{diff}} \gg \delta_{2ph.}$). The two photons light shift is induced by copropagating transitions and will be introduced shortly (section 6.3.1.3).

We assume $\delta_{\text{Doppler}} = 0$, which corresponds to treating only the center of the velocity distribution, and that the one photon light shift is proportional to the Rabi frequency: $\Omega^{\text{LS}}_{\text{diff}} = C\Omega$. Finally, we develop the pulse area $\Omega_e\tau$ around $\pi/2$. The phase shift now writes:

$$\delta\phi = \arctan\left(\frac{C\Omega + \delta_{2ph.}}{\Omega\sqrt{1+C^2}}\tan\left(\frac{\pi}{4} + \frac{\delta\theta}{2}\right)\right), \tag{6.3.2}$$

formula that we develop with $\delta\theta$ and $\delta_{2ph.}$ to obtain:

$$\delta\phi = \arctan\left(\frac{C}{\sqrt{1+C^2}}\right) + \frac{\sqrt{C^2+1}}{2C^2+1}\left(C\delta\theta + \frac{\delta_{2ph.}}{\Omega}\right). \tag{6.3.3}$$

The constant term in arctan describes the phase induced by the one photon light shift if the pulse area is perfectly $\pi/2$, and cancels over the four pulses of the interferometer. The second term gives the sensitivity to pulse area fluctuations and to the two photons light shift. In particular, we can separate their treatment.

6.3.1.2 One-photon light shifts

Measuring the frequency centers of Rabi spectra for different Rabi frequency, we estimated:

$$C = 0.337 \pm 0.013 \tag{6.3.4}$$

which is a mean value over the four spectra. Indeed, as we invert the Raman direction, C is slightly modified as the retroreflected beam is inverted. By a careful balancing of the laser powers, we are able to limit the variation δC below 5%.

Moreover, using the technique of section 4.2.2.4 to reduce beams intensity variations along the interferometer, we estimate that the pulse area fluctuations are contained with $\epsilon_\theta = 3\%$ of a $\pi/2$. By estimating the effect over the four interferometer pulses, we obtain:

$$\phi^{1\gamma} = \frac{C\sqrt{C^2+1}}{2C^2+1}\left(\delta\theta_I + \delta\theta_{II} - \delta\theta_{III} - \delta\theta_{IV}\right) \tag{6.3.5}$$

$$= \frac{C\sqrt{C^2+1}}{2C^2+1}\frac{\pi}{2}\epsilon_\theta. \tag{6.3.6}$$

which yields phase shifts of ~ 15 mrad.

Assuming that C depends on ϵ_R with $C(\epsilon_R) = C + \epsilon_R \delta C$, we obtain:

$$\phi_{2\,\text{spectra}}^{1\gamma}(\epsilon_B) = \frac{\delta C}{\sqrt{C^2+1}(2C^2+1)^2}\frac{\pi}{2}\epsilon_\theta \tag{6.3.7}$$

The numerical application yields residual phase shifts over the Raman inversion of ~ 700 μrad.

Finally, the compensation with the Bloch inversion is not straightforward. In particular, the number of BO in the preparation of the two Bloch acceleration direction differs by 500, which can cause a modification of the cloud shape. In particular, we do not know the sign of ϵ_θ which might change. As a consequence, we treat the two Bloch direction as independent variables, and we obtain a final formula:

$$\phi_{h/m}^{1\gamma} = \frac{\sqrt{2}\delta C}{\sqrt{C^2+1}(2C^2+1)^2}\frac{\pi}{2}\epsilon_\theta \tag{6.3.8}$$

We then obtain the correction on h/m, with formula (6.1.7):

$$\frac{\Delta\left(\frac{h}{m}\right)}{\frac{h}{m}} = 0 \pm 1.3 \cdot 10^{-10} \tag{6.3.9}$$

The uncertainty associated with the one photon light shift coupled to pulse area fluctuations is quite large. In order to reduce it, we plan to study the compensation over the Bloch direction with Monte Carlo simulations to estimate more precisely the contribution of this effect.

6.3.1.3 Two-photon light shifts

Counterpropagating Raman pulses couple the subspace $\mathcal{A} = \left\{ |F=1,\vec{p}\rangle, \left|F=2,\vec{p}+\hbar\vec{k}_R\right\rangle \right\}$. On the other hand, copropagating transitions act in the subspace $\left\{ |F=1,\vec{p}\rangle, |F=2,\vec{p}\rangle \right\}$, where we neglected their recoil velocity equivalent to a microwave photon. Those transitions are present because the Raman lasers are brought with the same fiber.

As a consequence, each state of $\mathcal{A}$ experience a coupling to the other hyperfine state with the same velocity, described by the Hamiltonian:

$$H = \hbar \begin{pmatrix} \delta/2 & \mathbf{\Omega}/2 \\ \mathbf{\Omega}^*/2 & -\delta/2 \end{pmatrix}, \tag{6.3.10}$$

where the Rabi frequency Ω is expected to be the same as the counterpropagating transition one. The detuning of transition is given by $\delta = \omega_1 - \omega_2 - \omega_{HFS}$ which is governed experimentally as we set the laser frequency so that the counterpropagating transition is resonant. We then have

$$\delta = \epsilon_R k_R v + \frac{\hbar k_R^2}{2m} \tag{6.3.11}$$

The recoil term in this equation $\frac{\hbar k_R^2}{2m}$ ($\sim$ 15 kHz) is negligible compared to the Doppler term, which evaluates to a few MHz. Moreover, we then have $\Omega \ll \delta$ such that we treat the copropagating coupling with perturbation theory.

This treatment yields that the state $|F=1,\vec{p}\rangle$ experiences an energy displacement of $-\hbar\delta_{2ph.}/2$, while the energy of $\left|F=2,\vec{p}+\hbar\vec{k}_R\right\rangle$ is displaced by the opposite amount $\hbar\delta_{2ph.}/2$ with:

$$\delta_{2ph.} = -\frac{\Omega^2}{2\delta}, \tag{6.3.12}$$

which clearly displays that as the atoms get slower the light shift induced by the copropagating transition increases as its resonance deviation decreases. The velocity of the atoms changes by a large amount during the interferometers such that this effect does not compensate. In particular $\delta_{2ph.}$ evaluates to typically $2\pi \cdot 5$ Hz for an atom moving at 1 m $\cdot$ s^{-1}.

We expect from this order of magnitude phase shifts of the order of a few mrad. Furthermore, equation (6.3.11) shows that this effect changes sign as the Raman direction is inverted. As a consequence, it is not compensated over the four spectra.

Approximating δ to $\epsilon_R k_R v$, we find that the contribution of this term to a single spectra is given by:

$$\phi^{2\gamma} = -\epsilon_R \frac{\sqrt{C^2+1}}{2C^2+1} \frac{\Omega}{2k_R} \left(\frac{1}{v_I} + \frac{1}{v_{II}} - \frac{1}{v_{III}} - \frac{1}{v_{IV}} \right) \tag{6.3.13}$$

As we have already stated, the slower the atoms, the greater the phase shift. In particular, when inverting the Bloch direction, the most contributing terms are also inverted, so that this effect adds on the four spectra.

The total phase contribution to h/m is given by:

$$\phi^{2\gamma}_{h/m} = -\frac{\sqrt{C^2+1}}{2C^2+1}\frac{\Omega}{k_R}\sum_{\epsilon_B=\pm 1}\epsilon_B\left(\frac{1}{v_I(\epsilon_B)}+\frac{1}{v_{II}(\epsilon_B)}-\frac{1}{v_{III}(\epsilon_B)}-\frac{1}{v_{IV}(\epsilon_B)}\right) \tag{6.3.14}$$

The sources of uncertainty in this formula come from C and Ω. We have given the former in equation (6.3.4), known with a 4% precision, while the latter evaluates to:

$$\Omega = 2\pi \cdot 2.07 \pm 0.10 \text{ kHz}, \tag{6.3.15}$$

which corresponds to a 5% precision. From the knowledge of the atomic trajectories, we can compute the effect of the two photons light shifts. For example on the atomic trajectories presented in chapter 5 and section 6.1.2 we obtain a shift of:

$$\frac{\Delta\left(\frac{h}{m}\right)}{\frac{h}{m}} = +(7.07 \pm 0.39)\cdot 10^{-11} \tag{6.3.16}$$

Finally, there are other two-photon transitions that we have not taken into account, as their contribution is negligible. First, the energy displacements associated with the $|F=1, m_F=0\rangle \leftrightarrow |F=2, m_F=\pm 2\rangle$ transitions are negligible as stated in section 2.1.2.2. Secondly, there are two other counterpropagating transitions that couple the states $|F=1, m_F=0, \vec{p}\rangle$ to $|F=2, m_F=0, \vec{p}-\hbar k_R\rangle$ and $|F=2, m_F=0, \vec{p}+\hbar k_R\rangle$ to $|F=1, m_F=0, \vec{p}+2\hbar k_R\rangle$. However, these transitions are off resonance by the hyperfine splitting (~ 6.8 GHz) and produce negligible light shifts in the mHz range.

6.3.2 Magnetic field inhomogeneities

Our interferometer is insensitive to the atom internal states energies by its symmetry. However, magnetic field inhomogeneities over the atom trajectories during the interferometer break this symmetry.

In our experimental setup, we have an interferometry region where the magnetic field control is driven by a solenoid, which is furthermore embedded in a magnetic shield. We can then treat it as a scalar and we develop it around its mean value:

$$B(z) = B_0 + b(z), \tag{6.3.17}$$

where $B_0 = 31.7$ mG and $|b(z)| < 200$ μG.

Since we perform interferometers with atoms in the $m_F = 0$ Zeeman sublevels, only sensitive to the second order Zeeman effect, we have:

$$\Delta E(z) = \pm \frac{hK}{2} B^2(z), \tag{6.3.18}$$

where the shift is positive for atoms in $|F = 2\rangle$ and negative for $|F = 1\rangle$. The result of the following treatment is that the contribution of this term in negligible on the h/m determination, so that we do not make particular care for its sign.

Developing the square of the magnetic field with expression (6.3.17), and putting the constant term in the energy levels, we obtain that the magnetic field inhomogeneities can be treated with the perturbative Lagrangian:

$$\mathcal{L}_{\text{mag}} = \mp hKB_0 b(z) \tag{6.3.19}$$

In order to obtain the phase shift over a trajectory, we should integrate the above expression. However, as we are sensitive to the phase shift difference between the two arms, we first describe the two trajectories. We can put them in the form:

$$z^{(A)}(t) = z_m(t) - \delta z(t)/2 \tag{6.3.20}$$

$$z^{(B)}(t) = z_m(t) + \delta z(t)/2, \tag{6.3.21}$$

where z_m is the mean trajectory and the position difference δz reads: We then develop the effective Lagrangian around the mean trajectory, and obtain:

$$\mathcal{L}_{\text{mag}} = \mp hKB_0 \left(b(z_m) \pm \frac{\delta z}{2} \frac{\mathrm{d}b}{\mathrm{d}z}(z_m) \right), \tag{6.3.22}$$

where the $\pm$ in the parenthesis depends on the trajectory. Provided that the magnetic field gradients are sufficiently small, we can restrict the development to the leading order and neglect the term proportional to the position difference δz.

We decompose the interferometer in its three phases: the first Ramsey sequence, the duration in between the two Ramsey sequences and the second Ramsey sequences.

During the first Ramsey sequence, path (B) corresponds to atoms in $|F = 1\rangle$. As a consequence, we have:

$$\mathcal{L}^{(B)}_{\text{mag}} = +hKB_0 b(z_m) \tag{6.3.23}$$

$$\mathcal{L}^{(A)}_{\text{mag}} = -hKB_0 b(z_m) \tag{6.3.24}$$

We recall that the phase shift induced by a perturbative Lagrangian is given by:

$$\phi_{\text{pert}} = \frac{1}{\hbar} \int \mathcal{L}_{pert} dt, \tag{6.3.25}$$

such that the phase shift during the first Ramsey sequence is given by:

$$\delta\phi_{mag}^{\mathrm{Ramsey}_1} = 2\pi K B_0 \int_0^{T_{\mathrm{Ramsey}}} b(z_m(t))dt. \tag{6.3.26}$$

Immediately, we have that the phase shift during the second Ramsey sequence is given by:

$$\delta\phi_{mag}^{\mathrm{Ramsey}_2} = -2\pi K B_0 \int_{T_{\mathrm{delay}}}^{T_{\mathrm{delay}}+T_{\mathrm{Ramsey}}} b(z_m(t))dt. \tag{6.3.27}$$

Inversely, in between the Ramsey sequences, the two paths correspond to atoms in $|F = 1\rangle$, and the two term cancel.

In the worst case scenario where the two phase shift add, we find a contribution to the output interferometer phase $\lesssim 1$ mrad. Moreover, the phase shifts compensate over the Raman direction inversion, such that we can expect a negligible contribution to the h/m determination.

The imperfect compensation of the magnetic field originates from the slight difference between the atomic trajectories when inverting the Raman directions. Using equations (6.1.17) and (6.1.18), we obtain that the phase contribution of the two spectra:

$$\begin{aligned}\delta\phi_{mag}(\epsilon_B) = 2\pi K B_0 \Big(&\int_0^{T_{\mathrm{Ramsey}}} \Delta Z(t) \frac{\mathrm{d}b}{\mathrm{d}z}\left(Z_m(t)\right) \\ &- \int_{T_{\mathrm{delay}}}^{T_{\mathrm{delay}}+T_{\mathrm{Ramsey}}} \Delta Z(t) \frac{\mathrm{d}b}{\mathrm{d}z}\left(Z_m(t)\right) \Big).\end{aligned} \tag{6.3.28}$$

Assuming the worst case scenario of a constant gradient with opposite sign with the two Ramsey sequences, we have from equation (6.1.19):

$$\delta\phi_{mag}(\epsilon_B) = -4\pi K B_0 \frac{\mathrm{d}b}{\mathrm{d}z}\left(2\Delta z_0 + v_R T_{\mathrm{delay}}\right) T_{\mathrm{Ramsey}}. \tag{6.3.29}$$

With our interferometer parameters and a magnetic field gradient at 4 mG·m^{-1}, we obtain residual phase shifts of ~ 10 μrad. Then, again in the worst case scenario where the shifts do not compensate over the Bloch direction inversion, we obtain a total contribution of ~ 20 μrad, which correspond to a relative error on h/m of $2.6 \cdot 10^{-12}$.

This corresponds to a dramatic reduction of the contribution of the second order Zeeman effect compared to the previous setup of our team[Bouchendira, 2011].

The precise computation using equation (6.3.28), equations (6.1.17) and (6.1.19) for the trajectories and results from section 3.3.3.1 for the magnetic field characteristics, we obtain an phase contribution to h/m of 6.6 μrad, we corresponds to:

$$\frac{\Delta\left(\frac{h}{m}\right)}{\frac{h}{m}} = -8.8 \cdot 10^{-13}. \tag{6.3.30}$$

This contribution is indeed negligible. We set a conservative uncertainty at 10^{-12} and apply no correction.

6.4 Effect induced by the rotation of the Earth

The terrestrial referential in which our experiment takes place is not strictly Galilean because of the rotation of the Earth. This imperfection is well captured through the Coriolis acceleration:

$$\vec{a}_C = 2\vec{\Omega}_E \times \vec{v}, \tag{6.4.1}$$

where $\vec{\Omega}_E$ is the vector describing the Earth rotation. In the lab frame, this vector possesses both a vertical and horizontal component. Let us choose a normal vector set $\left\{\vec{u}_x, \vec{u}_y, \vec{u}_z\right\}$ to describe our problem. The vector $\vec{u}_z$ represents the direction of the Raman beams, on which the differential velocity measurement is performed. We furthermore choose the orientation of the remaining axis such that:

$$\vec{\Omega}_E = \Omega_{E,x}\vec{u}_x + \Omega_{E,z}\vec{u}_z, \tag{6.4.2}$$

where x corresponds the East-West direction and y to South-North. Since we are only sensitive to the $\vec{u}_z$ component of a_C, we deduce that we have to account for an additional acceleration that depends on the transverse velocity along $\vec{u}_y$ which reads:

$$a_{C,z} = \vec{a}_C \cdot \vec{u}_z = 2\Omega_E v_y. \tag{6.4.3}$$

As the effect of the Earth rotation expresses as an acceleration, it translates on the output as of the interferometer as:

$$\delta\phi^{\text{Coriolis}}(\vec{v}) = k_R T_{\text{Ramsey}} T_{\text{delay}} a_c(\vec{v}) \tag{6.4.4}$$

$$= 2k_R T_{\text{Ramsey}} T_{\text{delay}} \Omega_E v_y. \tag{6.4.5}$$

As a consequence, a phase shear appears on the cloud velocity distribution along the y axis. As our detection method of the atomic cloud is insensitive to spatial information, such a phase inhomogeneity may wash out the fringes especially

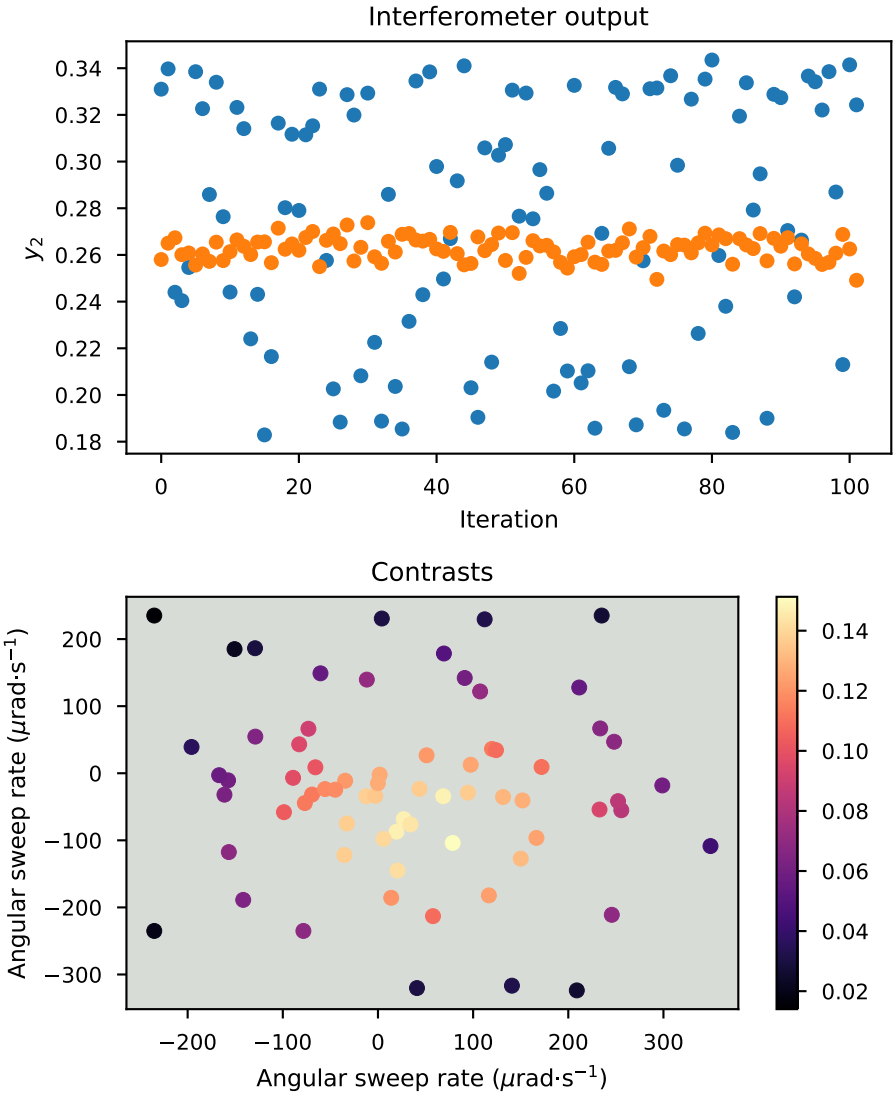

Figure 6.1: Top: relative populations at the output of the interferometer for two PZT ramps. Bottom: fringes contrast as a function of the two axis ramps amplitudes.

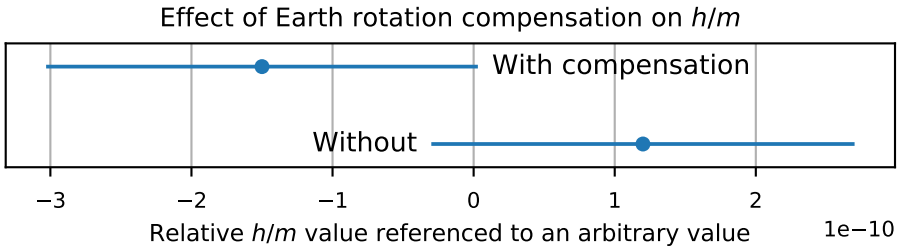

Figure 6.2: Integrated h/m raw determinations with and without Earth rotation compensation. Each point correspond to 400 sets of 4 spectra. The total interrogation duration is 60 hours.

if the interferometer sensitivity (in our case $\propto T_{\mathrm{Ramsey}} T_{\mathrm{delay}}$) is large[Lan, 2012; Sugarbaker, 2013].

With $\Omega_E = 48\ \mu\mathrm{rad}{\cdot}\mathrm{s}^{-1}$, our typical interferometer durations ($T_{\mathrm{Ramsey}} = 20$ ms, $T_{\mathrm{delay}} = 33$ ms), we obtain a Coriolis acceleration induced phase of:

$$\delta\phi^{\mathrm{Coriolis}} \sim 500\mathrm{mrad}/\left(\mathrm{m}\cdot\mathrm{s}^{-1}\right). \tag{6.4.6}$$

The typical width of the velocity distribution of the atoms that participate to the interferometer being of the order of 1 $\mathrm{cm}\cdot\mathrm{s}^{-1}$, we estimate that the amplitude of the phase shear to 5 mrad.

In principle this effect should average over the velocity distribution. At the time of the detection, the atoms positions depends mostly on their velocities. As such, any inhomogeneous spatial efficiency of the detection translates in a not perfect averaging over the velocity distribution.

Moreover, as we eliminate gravity with the Bloch direction inversion, we also eliminate any supplementary acceleration. However, any change in the detection process over the Bloch inversion translates in a systematic shift. In particular, and as can be seen in figure (5.3) that describes the atomic trajectories, the time of the detection varies over the Bloch direction inversion, and as such the spatial distribution of the cloud.

As the spatial dependence of the detection efficiency is a difficult quantity to evaluate, we have turned to a method that allows us to compensate experimentally the phase shear induced by Coriolis acceleration. We take advantage of the fact the retroreflection mirror is driven by PZTs to dynamically mimic the Earth rotation[Lan, 2012]. This corresponds to slightly misaligning the Raman beams which also induces a phase shear proportional to the atomic transverse velocity (see section 6.5.1).

In order to extract the rotation rate of the mirror that compensate the Earth's rotation, we use the phase shear property of the effect. Using $T_{\text{Ramsey}} = 350$ ms and $T_{\text{delay}} = 355$ ms, we increase the output phase sensitivity to the Earth rotation. Here, we are not interested in a accurate determination of the fringe center so that the effect of vibration noise is not a limitation.

However, we can process the atomic relative populations $y_2 = N_2/(N_1 + N_2)$ to extract the contrast of the fringes. We obtain a sample of the y_2 distribution by repeating the experiment a hundred times. On figure (6.1, top), we have plotted results of such a procedure for efficient and inefficient Coriolis compensations.

Because the experiment is rotated with respect to the cardinal direction canvas[3], we need to rotate the mirror along its two axis X and Y. Estimating the contrast for a two dimensional random sampling of (X, Y), we obtain the plot of figure (6.1, bottom).

Fitting the results with a two dimensional gaussian, we obtain the sweep rates to apply to maximize the fringe contrast and as such the compensation of Earth rotation induced phase shifts. We estimate the error on these sweep rates by repeating the fitting procedure on data subsets. We obtain sets of estimates, whose standard deviations give an estimate of the error on the sweep rates. We find that their relative errors are below 5%. Treating each axis of the PZT as an independent variable, we estimate the accuracy of the compensation that we apply to 7%.

Finally, we have measured h/m with the compensation of Earth rotation and without. The results of this survey on figure (6.2). The discrepancy between the two values being at worst $5.7 \cdot 10^{-10}$. As we apply experimentally the compensation for the h/m measurement, we apply no correction. The uncertainty on the Earth rotation compensation is estimated by the product of this discrepancy and the estimated accuracy of the compensation. We finally obtain:

$$\frac{\Delta\left(\frac{h}{m}\right)}{\frac{h}{m}} = 0 \pm 4 \cdot 10^{-11} \tag{6.4.7}$$

6.5 Effects on the lasers wavevectors

6.5.1 Beams misalignment

The treatment of the interferometers assumed perfect alignment between the lasers beams. If the beams are not perfectly aligned, as represented in figure (6.3) then

[3]because of the orientation of the Jussieu campus

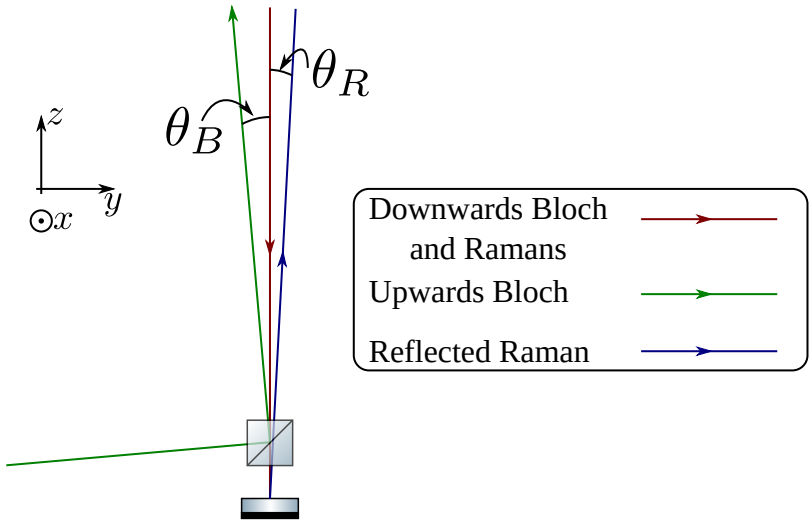

Figure 6.3: Beam alignment notations. The z axis is defined by the downwards going beams, and the y axis by the plane formed by those beams and the reflected Raman beam. The out of plane angle ϕ_B of the upwards Bloch beam is not represented.

the Raman wavevector is changed to:

$$\vec{k}_R = \frac{k_R}{2}\Big((1+\cos(\theta_R))\vec{u}_z + \sin(\theta_R)\vec{u}_y\Big), \tag{6.5.1}$$

where we have performed the simplification $k_1 \simeq k_2 \simeq k_R/2$. Then, the phase imprinted to the atoms during the interferometer Raman pulses is changed to:

$$\vec{k}_R \cdot \vec{r} = \frac{k_R}{2}\Big(1+\cos(\theta_R)\Big)z + \frac{k_R}{2}\sin(\theta_R)y \tag{6.5.2}$$

Similarly, the velocity transferred with Bloch Oscillations writes:

$$\overrightarrow{\Delta v} = \Delta v\left(\frac{1+\cos(\theta_B)}{2}\vec{u}_z + \frac{\sin(\theta_B)}{2}(\cos(\phi_B)\vec{u}_x + \sin(\phi_B)\vec{u}_y)\right) \tag{6.5.3}$$

with $\Delta v = N_B v_B$ and ϕ_B describes the relative angle between the wavevectors of the upwards going Bloch and the upwards going Raman in the horizontal plane $(\vec{u}_x, \vec{u}_y)$.

By combining equation (6.5.2) and the equations of motion, one obtains in the leading order in θ_R, θ_B, the relative correction on h/m with given angles:

$$\frac{\Delta\left(\frac{h}{m}\right)}{\frac{h}{m}} = \frac{+\theta_R^2 + \theta_B^2 - \theta_R\theta_B\sin(\phi_B)}{4}. \tag{6.5.4}$$

The beams alignment is ensured through continuous optimization with PZT transducers on mirror mounts. From the calibration of the PZT and the shot to shot variations on the optimization procedure we obtain:

$$\theta_R < 3 \quad \mu\text{rad} \tag{6.5.5}$$

$$\theta_B < 4.5 \ \mu\text{rad} \tag{6.5.6}$$

Because ϕ_B is unknown, the maximal correction is given by the worst case scenario $\phi_B = \pi$ which corresponds to opposite angles on the Bloch and Raman upwards going beams. The minimal correction is given by perfectly aligned beams $\theta_R = \theta_B = 0$, such that the alignment correction on h/m is given by:

$$\frac{\Delta\left(\frac{h}{m}\right)}{\frac{h}{m}} = +(5.34 \pm 5.34) \cdot 10^{-12}. \tag{6.5.7}$$

The compensation of the Earth rotation induces a supplementary misalignment on the Raman wavevector as the angle between the two Raman beams is linearly ramped:

$$\theta_R(t) = \theta_R + \beta\left(t - \frac{T_{\text{Ramsey}} + T_{\text{delay}}}{2}\right), \tag{6.5.8}$$

where β is the angular sweep rate. The ramp is symmetrized with respect to the interferometer duration such that the maximal angle between the Raman beams is minimized. We have assumed that the misalignment θ_R is placed along the ramp direction. The more general calculation does not change the following result.

Computing the output phase of the interferometer with the equations of motion the time dependent misalignment, we first find a single term in v_y, the initial atom velocity along the y-axis:

$$\delta\phi = k_R T_{\text{Ramsey}} T_{\text{delay}} \beta v_y, \tag{6.5.9}$$

which explains that applying a linear ramp on the Raman beams angle can compensate Coriolis phase shift (equation (6.4.5)).

The other terms, in the first order in β, yield an additional correction to h/m:

$$\frac{\Delta\left(\frac{h}{m}\right)}{\frac{h}{m}} = \frac{\beta}{2}\left(\left(\theta_R - \frac{\theta_B \sin(\phi_B)}{2}\right)\left(\frac{T_{\text{Ramsey}}}{2} + \frac{3T_{\text{delay}}}{2} - t'_B\right) + 2T_{\text{delay}}\theta_R\frac{v_z}{\Delta v}\right), \tag{6.5.10}$$

where we recall that t'_B is the middle point of the Bloch acceleration. Embarrassingly, the calculation yields a term that depends on the initial velocity of the

atoms of the same order of magnitude than the other terms. Computing this term with the parameters of our interferometer parameters and the ramp that we apply $\beta = 66\ \mu\text{rad}\cdot\text{s}^{-1}$, we obtain:

$$\frac{\Delta\left(\frac{h}{m}\right)}{\frac{h}{m}} = +(5.42 \pm 5.42) \cdot 10^{-12}. \tag{6.5.11}$$

Combining the alignment correction (equation (6.5.7)) and the ramp corrections, we obtain the final correction of the effect induced by beam misalignment:

$$\frac{\Delta\left(\frac{h}{m}\right)}{\frac{h}{m}} = +(1.08 \pm 1.08) \cdot 10^{-11}. \tag{6.5.12}$$

6.5.2 Beam profile corrections

So far, we have assumed a well define wavevector k for the laser beams. This is only correct in the case of plane waves. Experimentally, we use gaussian beams of finite size. This part is devoted to the estimation of the relative correction to the wavevector $\delta k/k$ induced by the beam profile.

Note that this correction applies on both the Raman and Bloch wavevectors such that the correction on h/m writes:

$$\frac{\Delta\left(\frac{h}{m}\right)}{\frac{h}{m}} = -2\frac{\delta k}{k} \tag{6.5.13}$$

This work has not been finalized yet. As it will be explained in the conclusion of this chapter, we observe discrepancies on the measured h/m upon changing experimental parameters. However, the correction induced by the beam profile is not modified as we change these parameters. As a consequence, we have focused our work on the study of those discrepancies rather than on the completion of the beam profile correction estimation.

6.5.2.1 Ideal gaussian beam

With a gaussian beam, the effective wave vector along its direction of propagation z is given by[Cladé, 2005]:

$$k_z^{eff}(r,z) = k - \frac{2}{kw^2(z)}\left(1 - \frac{r^2}{w^2(z)}\right) - \frac{kr^2}{2R^2(z)}, \tag{6.5.14}$$

where k is the plane wave wavevector, r and z are respectively the transverse and longitudinal positions, $w(z)$ is the waist of the beam and $R(z)$ its radius of curvature at position z.

The waist $w(z)$ obeys:

$$w(z) = w_0\sqrt{1+\left(\frac{z}{z_R}\right)^2}, \tag{6.5.15}$$

where w_0 is the minimal waist of the beam and z_R its Rayleigh length defined by:

$$z_R = \frac{kw_0^2}{2}. \tag{6.5.16}$$

In our experimental conditions with $w_0 \sim 5$ mm, the Rayleigh length evaluates to $\sim 40 \cdot 10^3$m. As we implement our interferometers over distances of a few tens of centimeters, we can neglect the variations of the waist with the position.

Finally, the radius of curvature is given by:

$$R(z) = z\left(1+\left(\frac{z_R}{z}\right)^2\right). \tag{6.5.17}$$

In equation (6.5.14), the relevant parameters are the waist and the radius of curvature at the position of the interaction with the atoms. We estimate the waist using images from a CCD camera (see figure 6.5), and the radius of curvature from the interference pattern obtained with a shearing interferometer[Riley, 1977] which yielded $R > 1$ km.

From the correction term independent of the transverse position r, we obtain the order of magnitude of the correction:

$$\frac{\delta k}{k} = \frac{k_z^{eff}-k}{k} = -\frac{2}{k^2w_0^2} \tag{6.5.18}$$

$$= -1.2 \cdot 10^{-9}. \tag{6.5.19}$$

This number should be corrected with the other terms that depend on the mean value of the cloud size $\langle r^2\rangle$. The estimation of this quantity relies on the knowledge of the initial size of the cloud, of its temperature and of the spatial filtering induced by the elevator-velocity selection sequence. We use a Monte-Carlo simulation to evaluate such a term.

Finally, the motivation for a Monte-Carlo simulation comes also from the necessity to estimate the impact of wavefront distortions.

6.5.2.2 Effective wavevector in a distorted wavefront

In the latest measurement of our team[Bouchendira, 2011], the contribution of the gaussian wavefront correction to the systematic errors was one of the main limiting factors. The waist of the laser beam was then 3.6 mm. By increasing the waist by $\sim 40\%$ to 5 mm, the effect is decreased by a factor ~ 2.

After setting up more powerful lasers sources (see section 3.2) with larger beams, our team discovered a new systematic effect that appeared when reducing the Bloch lasers intensity. The relative effect was of the order of 2.10^{-8} for a 25% reduction of the Bloch pulse efficiency, ten times higher than the gaussian wavefront correction[Andia, 2015a].

This effect was then interpreted as a manifestation of the wavefront distortion[Bade, 2018]. In particular, in this reference, our team generalized the formula (6.5.14) to the case of a laser field ansatz:

$$\vec{E}(\vec{r},t) = \vec{E_0}(\vec{r})e^{i(\Phi(\vec{r})-\omega t)}, \tag{6.5.20}$$

where $\vec{E_0}(\vec{r})$ is the local amplitude of the laser field and $\Phi(\vec{r})$ its spatial phase.

The effective momentum of the photon can be deduced from the spatial phase with $\vec{p} = \hbar\overrightarrow{\nabla}\Phi$[Antognozzi, 2016]. Using Helmholtz equation with the ansatz of equation (6.5.20) one can extract the wavevector correction:

$$\delta k = -\frac{1}{2k}\left\|\overrightarrow{\nabla}_\perp\Phi\right\|^2 + \frac{1}{k}\frac{\Delta_\perp I}{I}, \tag{6.5.21}$$

where $I = \left\|\vec{E_0}\right\|^2$ is the local intensity of the field and $\overrightarrow{\nabla}_\perp$ and $\Delta_\perp$ are respectively the transverse gradient and Laplacian at a fixed position z_0.

The second term, that depends on intensity variations, induces negative corrections to the wavevector at local intensity maxima and positive corrections at positive intensity maxima. Moreover, the first term which corresponds to local fluctuations of the phase has been found negligible with respect to the second term[Bade, 2018].

The efficiency of Bloch Oscillations depends on the local laser intensity. At the output of the interferometer, we are sensitive to the average $\langle\delta k\rangle$ over the atoms that survived the Bloch pulse. Writing $P(I)$ this survival probability (or efficiency), we can obtain the average wavevector correction with a spatial integration:

$$\langle\delta k\rangle = \frac{\langle\delta k(\vec{r})P(I(\vec{r}))\rangle}{\langle P(I(\vec{r}))\rangle} \tag{6.5.22}$$

Assuming that we are not limited by spontaneous emission, the efficiency increases with the intensity. By lowering the intensity of the Bloch lasers, one filters preferentially atoms placed at local maxima of intensity, and observe a negative shift.

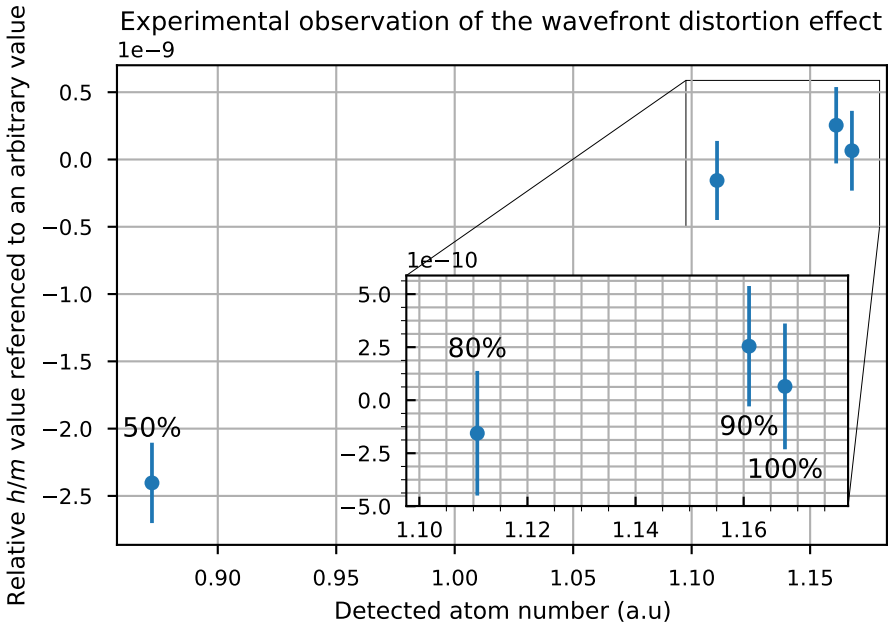

Figure 6.4: Relative h/m obtained by changing the intensity of the Bloch lasers for interferometer pulse. The text indicate the setpoint for each value.

6.5.2.3 Effect on h/m

The effect of the wavefront distortion scales with the square of the intensity fluctuations amplitude, as both the correction and the local variations of efficiency scale with it. Secondly, the short-scale fluctuations are dominant in equation (6.5.21) but are filtered out by the propagation in free space. As a consequence we increase as much as possible the distance between the interferometry lasers collimators and the atoms up to ~ 2 meters.

We display in figure (6.4) the variation of h/m obtained when reducing the laser power of the Bloch pulse during the interferometer. At a 75% efficiency, we observe a negative effect of $2.5 \cdot 10^{-9}$, which corresponds to a reduction by a factor of 10 of the initially observed effect[Andia, 2015a]. Moreover, at higher power, there is no resolvable shift between the data at a relative precision of $2.5 \cdot 10^{-10}$.

The evaluation of this effect requires precise knowledge of the beam profile, which we obtain with a CCD camera (*IDS UI-5340CP-NIR-GL*). We avoided the problem of interference fringes that form on the camera by using a laser diode below its threshold. We present on figure (6.5) a typical image obtained using this method, and the local wavevector correction using equation (6.5.21). We took

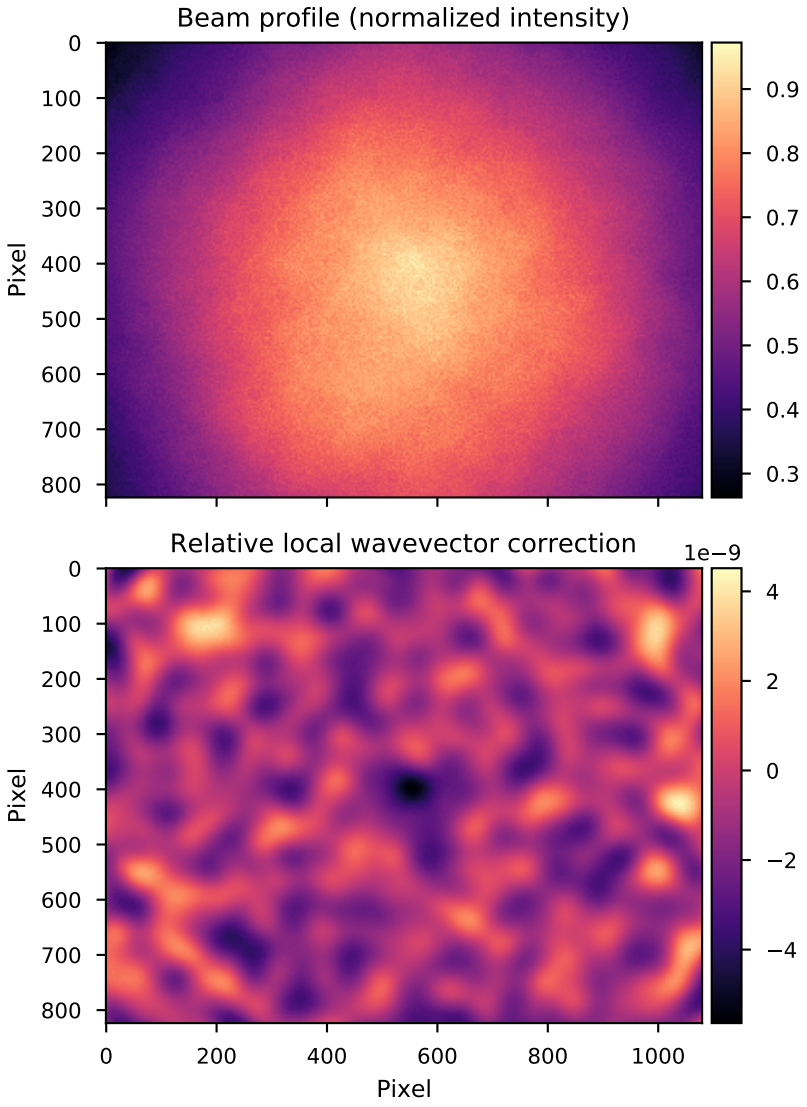

Figure 6.5: Top: Image of the beam profile obtained with a CCD camera. Bottom: relative wavevector correction deduced from the image.

several images at different positions to consider the beam profile at the distance at which they interact with the atoms.

Our team has developed a Monte-Carlo simulation that uses these images. I present our preliminary results displayed in figure (6.6), obtained with the laser profile presented in figure (6.5). The simulation program uses the local wavevector correction obtained from formula (6.5.21) and evaluates a mean correction using equation (6.5.22).

The bottom plot of figure (6.6) shows that the relevant parameter to extract the correction is the efficiency of the Bloch pulse independently of the Bloch potential depth. Comparing these predictions and the experimental observations of figure (6.4), there is a discrepancy as experimentally at 75% efficiency we observe a $-2.5 \cdot 10^{-9}$ that is not reproduced by the Monte Carlo simulation.

We expect from our experimental parameters: $P = 350$ mW per beam and $\Delta = -40$ GHz, $V_0 \sim 65\ E_r$. This expectation is supported by the fact that the survival probability decreases by $\sim 25\%$ when the lasers intensity is divided by two. The discrepancy might be due to an additional dust that has been deposited on an optical element in between the time the picture was taken and the data (~ 4 months).

Nevertheless, we can estimate a provisional recoil correction from figure (6.6) with:

$$\frac{\delta k}{k} = (-1.0 \pm 0.1) \cdot 10^{-9}. \tag{6.5.23}$$

Further work is planned in the operation of the Monte Carlo simulation in order to confirm this number. For example, we intend to reproduce the results of section 4.2 that exhibited the dispersive nature of the Raman pulses. Such a work will also be useful to reduce the contribution of one-photon light shifts in the final error budget.

Finally, because it is based on equation (6.5.21) which a generalization of the Gaussian beam correction (6.5.14), the above correction can be used for Bloch and Raman wavevectors, so that we obtain the provisional correction on h/m:

$$\frac{\Delta\left(\frac{h}{m}\right)}{\frac{h}{m}} = +(2.0 \pm 0.2) \cdot 10^{-9} \tag{6.5.24}$$

This number does not take into account errors in the beam profile image analysis related to the CCD characterization, and as such should be considered with caution because it is likely to be modified by subsequent analysis. It is however an indicator of the final accuracy that we expect on this effect.

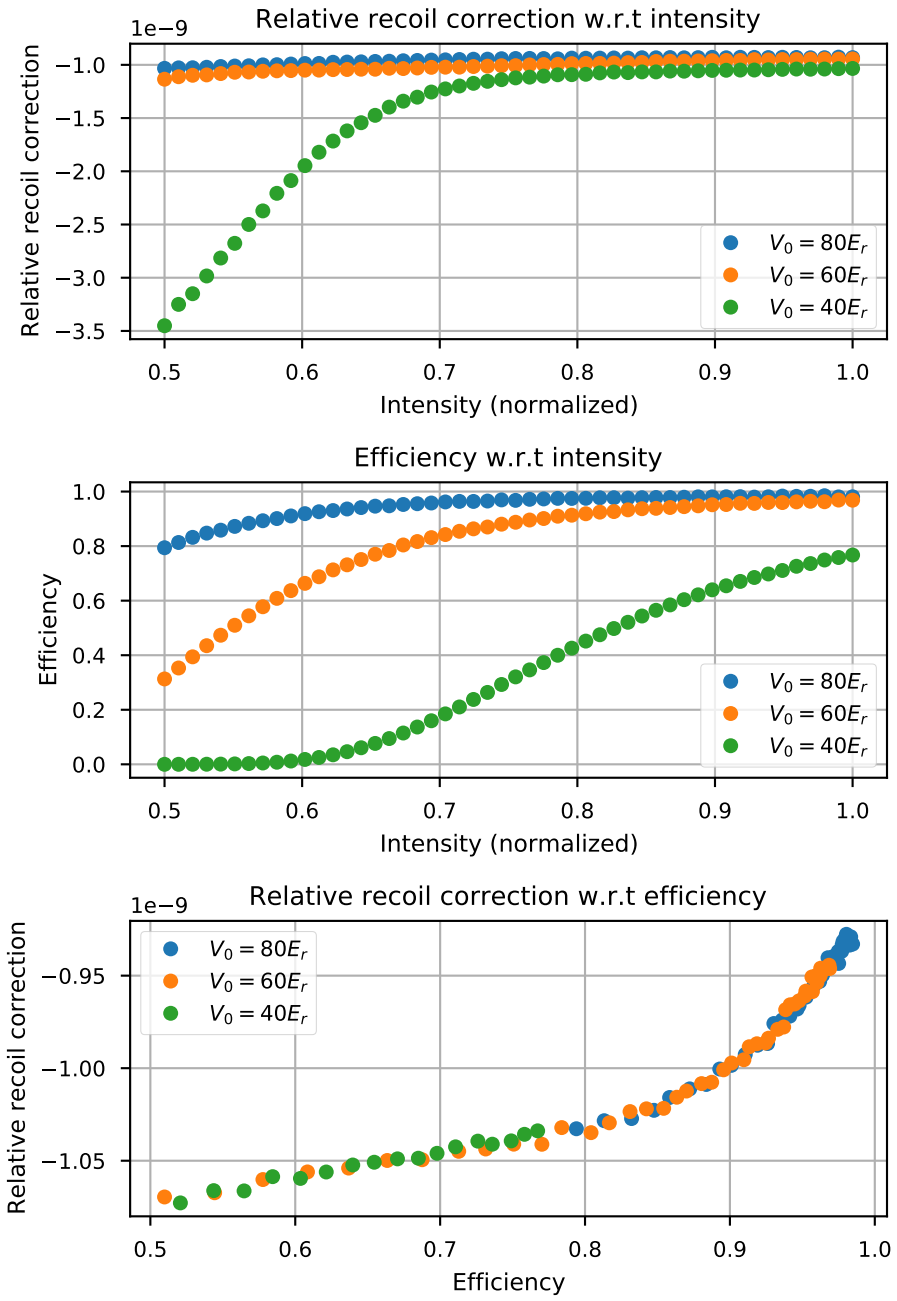

Figure 6.6: Preliminary results of the Monte Carlo simulation. Top: Variations of the averaged effective recoil with respect the laser intensity. Middle: predicted of the global efficiency of the Bloch pulse with respect to laser intensity. Bottom: plot of the effective recoil with respect to the Bloch pulse efficiency. On each plot we display result for three Bloch-lattice potential height.

6.5.3 Laser frequencies

The knowledge of the lasers frequencies is critical as they are used to determine the bare wavevector. R. Jannin presented in is PhD thesis[Jannin, 2015a] improvements of the laser frequency stabilization setup with a relative short term precision at $1.5 \cdot 10^{-11}$ on the frequencies which correspond to a 6 kHz precision.

However, we tracked the frequencies of our lasers with the frequency comb setup and observed long term variations of the lasers frequencies by $\sim$ 10 kHz, which induces an error source of

$$\frac{\Delta\left(\frac{h}{m}\right)}{\frac{h}{m}} = 0 \pm 5.2 \cdot 10^{-11} \tag{6.5.25}$$

From the short term performance of the stabilization system, we expect that we can reduce this number by a factor ~ 2. Two strategies can be applied, together or not: implement additional improvements on the stabilization system to reach better long term stability and continuously measure the lasers frequencies during the h/m measurement.

6.6 Phase shift in Raman radiofrequency chain

As we have presented in section 3.2.2, the Raman PLL works through the comparison of $\omega_{\text{beatnote}} - \omega_{\text{MW}}$, the frequency difference between the lasers beatnote and a microwave generator, and ω_{RF} generated by a RedPitaya around 40 MHz. Accounting for the frequency manipulations, the beatnote angular frequency is given by

$$\omega_{\text{beatnote}} = \omega_{\text{MW}} + 8\omega_{\text{RF}} \tag{6.6.1}$$

$$= \omega_{HFS} + \epsilon_R k_R v + \frac{\hbar k_R^2}{2m}. \tag{6.6.2}$$

During an interferometer, ω_{MW} is kept constant and ω_{RF} is the dynamical parameter used to compensate gravity and implement the frequency jump $\delta\omega$ for the h/m determination.

There is a low-pass filter with a 1 GHz cutoff in the RF part of the PLL frequency chain. Such a filter can produce a phase shift of a few mrad during the frequency ramps along a single Ramsey sequence. This phase shift depends on the start ω_{start} and stop point ω_{stop} of the ramp and on its duration. Since we use a single duration for all ramps, we ignore this dependence and write the phase shift:

$$\phi_{\text{RF}}(\omega_{start}, \omega_{stop}) \tag{6.6.3}$$

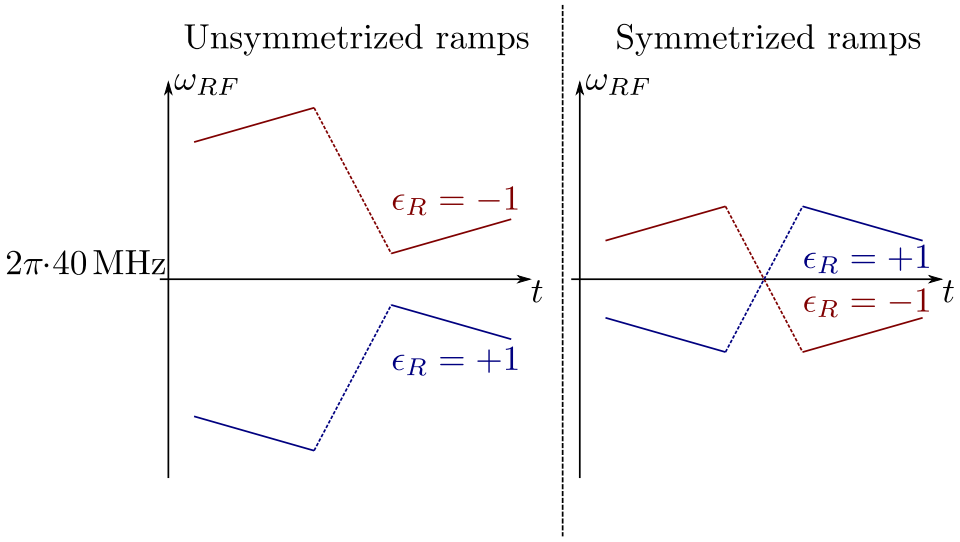

Figure 6.7: Frequency ramps performed by the RedPitaya generator for $\epsilon_B = 1$. Left: ω_{MW} is constant with the Raman inversion and the ω_{RF} ramps are not symmetric. Right: ω_{MW} is shifted when inverting the Raman direction such the ω_{RF} ramps are symmetric.

Thanks to time reversal symmetry, we can assume:

$$\phi_{\mathrm{RF}}(\omega_{start}, \omega_{stop}) = -\phi_{\mathrm{RF}}(\omega_{stop}, \omega_{start}) \tag{6.6.4}$$

We then obtain the interferometer shift induced by this effect with:

$$\phi = \phi_{\mathrm{RF}}(\omega_{III}, \omega_{IV}) - \phi_{\mathrm{RF}}(\omega_{I}, \omega_{II}) \tag{6.6.5}$$

Keeping ω_{MW} constant for the four spectra, then the ω_ι parameters of the ramp are not symmetric as displayed in figure (6.7, left). In these conditions, the phase shift (6.6.5) must be estimated.

Recording the beatnote and demodulating it with the frequency ramp commands, we were able to estimate these phase shifts to $\sim \pm 60$ mrad for two spectra and ~ 0 for the others for the $T_{\mathrm{Ramsey}} = 20$ ms, $N_B = 500$ interferometer. These shifts compensated on h/m so that it would have been possible to correct them with a precision of the order of the mrad. It required however a careful characterization of the phase shift estimation setup. Moreover, for example with $N_B = 250$, these phase shifts did not compensate anymore.

As a consequence, we preferred to put in place symmetric ramps that takes advantage of the property of equation (6.6.4) to enhance the compensation over

the Raman direction inversion. The condition for the compensation of the phase (6.6.5) is deduced from equation (6.6.4) and given by:

$$\omega_I(\epsilon_R) = \omega_{IV}(-\epsilon_R) \tag{6.6.6}$$
$$\omega_{II}(\epsilon_R) = \omega_{III}(-\epsilon_R) \tag{6.6.7}$$

Such a condition is achieved by changing ω_{MW} with the Raman direction. Experimentally, we ensure that the mean value of ω_{RF} is the same for the two Raman directions, as displayed in figure (6.7, right).

The modification of ω_{RF} occurs with a frequency jump, that is placed ~ 250 ms before the interferometer. We checked that no modification of the measured phase shift occurred by reducing this duration by 100 ms. We estimate the uncompensated phase shift to ± 500 μrad using the demodulation of the beatnote signal. This yields on h/m:

$$\frac{\Delta\left(\frac{h}{m}\right)}{\frac{h}{m}} = 0 \pm 6.6 \cdot 10^{-11} \tag{6.6.8}$$

6.7 Current error budget and survey of systematic effects

We have listed and estimated various error sources that we have compiled in the provisional table (6.1). The main contributions to the final uncertainty are the beam profile, then the one photon lights shifts and the laser frequencies. We expect to reduce the first two using a Monte-Carlo simulation and the last with experimental improvements.

The final expected relative uncertainty is currently $2.7 \cdot 10^{-10}$. Considering the fine structure constant α, we can expect a relative precision of $1.4 \cdot 10^{-10}$, which would make our determination the most accurate. However, this table is not complete as we are still running surveys to check for systematic errors. Uncovering a previously non considered error could reduce the accuracy of our determination.

In order to check for systematic effects, we perform parameters variations on the measurements. Some of those surveys are displayed in figure (6.8), for different parameters. We have a relatively good agreement when changing T_{Ramsey}. However, the integration duration was not there sufficient and we plan to repeat this interrogation. One of the difficulties with changing T_{Ramsey} is that we reduce the sensitivity of the measurement, which in turn requires a longer period of integration.

Moreover, upon identifying a new error source, we may not be able to correct the previous surveys. Lately, we uncovered the issue of phase shift in Raman

radiofrequency chain (section 6.6). Before the modification of the experimental protocol to reduce this effect, we did not observe an agreement between the two values for different T_{Ramsey} at this level of precision.

Similarly, the treatment of this effect reduces the disagreement between $N_B = 250$ and $N_B = 500$. However, this survey still exhibits a slight discrepancy. Furthermore, we resolve another discrepancy when changing the initial velocity of the atoms (third plot of the figure). The initial velocity is here changed only for two spectra ($\epsilon_B = +1$), by 50 BO which corresponds to $\sim 0.6\ \mathrm{m \cdot s^{-1}}$. We are currently investigating this discrepancy to identify its origin. This particular surveys exhibits the versatility of the technique of atom elevators through which we control the position and velocities of the atom. Indeed, we use it to eliminate the gravity gradient effect and to investigate the exactness of our measurement.

Finally, we also change the duration of Bloch Oscillations. This cannot be done at $N_B = 500$ with a large amplitude for practical reasons, which is why we run it at $N_B = 250$. This parameter modifies the efficiency of Bloch Oscillations and as such indicates if the effect induced by beam distortions is well understood.

As a conclusion on the systematic errors analysis, the current estimation of the error budget is quite promising. We have extended the protocol for the h/m determination such that some effects (gravity gradient, Earth rotation) are compensated.

However, this work has not yet been concluded. For example, the correction accounting for the beam profile requires additional studies. As we observe discrepancies with respect to some parameter modifications for which the contribution of the beam profile is identical, we are delaying this estimation in favor of the identification of the remaining error sources.

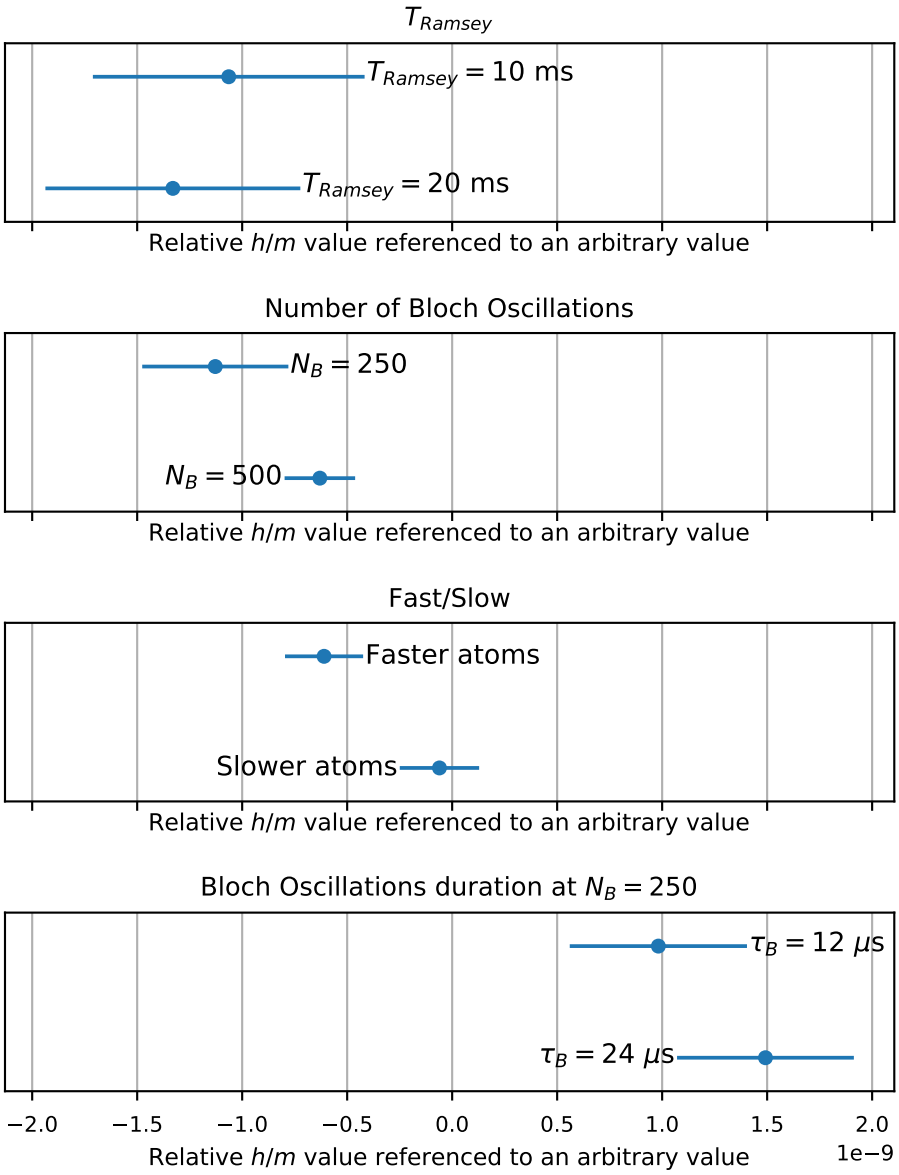

Figure 6.8: Check for systematic errors through parameter change. The values are corrected for systematic shifts. The reference is arbitrary but common to the four plots. Common error sources such as laser frequencies or beam profile has not been propagated such that the discrepancies that we observe are preserved.
The bottom plot has been taken from a different series than the others. For example, the error induced by the Raman frequency chain was not yet identified and cannot be corrected, which explains the discrepancy between this set of data and the others.

Systematic error source	Relative correction ($\times 10^{-11}$)	Relative uncertainty ($\times 10^{-11}$)
Gravity gradient	0	0.01
One photon light shifts	0	13
Two photons light shifts	+7.07	0.39
Second order Zeeman effect	0	0.10
Earth rotation	0	4.0
Beams alignment	+1.08	1.08
Beams profile	+200	20
Laser frequencies	0	5.2
Raman frequency chain	0	6.6
Total systematic errors	208	26
Statistical uncertainty (48h)		8.5
Total uncertainty		27

Table 6.1: Provisional error budget on h/m. We have highlighted in red the contribution of the beam profile for which the estimation has not been finalized.

Conclusion and outlooks

We have presented in this manuscript our work on the new experimental setup of our team. We implemented atom interferometry techniques and Bloch Oscillations of cold atoms on the setup. We applied the combination of the two techniques to the measurement of h/m for the determination of the fine structure constant α.

We demonstrated an excellent control of the magnetic field over a 45 cm long area which, combined with a better control of vibration noise. This allowed to increase the interferometer duration and as a consequence to reach unprecedented sensitivity on this measurement with statistical relative uncertainty on h/m of $8.5 \cdot 10^{-11}$ with 48 hours of integration.

Simultaneously, we have developed the analysis of systematic error sources which relies on two approaches. Firstly, a fine modeling of the interferometer and the atomic trajectories. Secondly, we have taken advantage of the setup sensitivity to perform experimental surveys. In particular, the latter exhibits that the assessment of the error budget is not finished as we can still observe unexplained discrepancies upon experimental parameter variations (number of Bloch Oscillations, initial velocity of the atoms).

The completion of this measurement campaign will be a milestone for the experimental setup as it goes with the control of systematic errors at the 10^{-10}. Moreover, we will then contribute to the test of the Standard Model through the α/a_e comparison.

Furthermore, we have improved the production protocol of ultra-cold atom sources based on evaporative cooling in an optical dipole trap. We demonstrated the ability to produce Bose Einstein Condensates (BEC) in a single magnetically insensitive hyperfine sublevel with 120000 atoms. Such ultra-cold sources, characterized by a smaller transverse expansion, would be used in the future to implement more sensitive interferometer geometries with large separation between the two arms.

After the measurement of h/m with cold atom clouds, the short term perspectives of the setup are the study of interferometry with a BEC source and in particular the development of experimental methods to measure the shift induced

by atom-atom interactions. We have performed such a study with microwave pulse based Ramsey sequences, which will be extended to interferometers based on light pulses.

Once the finalization of the error budget of the h/m measurement is completed, we plan to use the sensitivity of our setup to measure the phase shift induced by atom-atom interaction in a BEC using a Ramsey-Bordé interferometer. Following this work, we will reproduce the h/m measurement with colder atom sources. Finally we will check the comprehensiveness of the error budget by using ^{85}Rb for the measurement of h/m.

Bibliography

[ACME Collaboration, 2018] ACME Collaboration. "Improved Limit on the Electric Dipole Moment of the Electron". *Nature* 562.7727 (2018), pp. 355–360. DOI: 10.1038/s41586-018-0599-8 (Cited on page 4).

[Andia, 2015] Manuel Andia. "Oscillations de Bloch d'atomes ultra-froids: application aux mesures de haute précision." *PhD Thesis* (2015), p. 213 (Cited on pages 15, 107, 137, 179, 180).

[Andia, 2015] Manuel Andia, Étienne Wodey, François Biraben, Pierre Cladé, and Saïda Guellati-Khélifa. "Bloch Oscillations in an Optical Lattice Generated by a Laser Source Based on a Fiber Amplifier: Decoherence Effects Due to Amplified Spontaneous Emission". *Journal of the Optical Society of America B* 32.6 (2015), p. 1038. DOI: 10.1364/JOSAB.32.001038 (Cited on pages 6, 89).

[Antognozzi, 2016] M. Antognozzi, C. R. Bermingham, R. L. Harniman, S. Simpson, J. Senior, R. Hayward, H. Hoerber, M. R. Dennis, A. Y. Bekshaev, K. Y. Bliokh, and F. Nori. "Direct Measurements of the Extraordinary Optical Momentum and Transverse Spin-Dependent Force Using a Nano-Cantilever". *Nature Physics* 12.8 (2016), pp. 731–735. DOI: 10.1038/nphys3732 (Cited on page 179).

[Aoyama, 2019] Tatsumi Aoyama, Toichiro Kinoshita, and Makiko Nio. "Theory of the Anomalous Magnetic Moment of the Electron". *Atoms* 7.1 (2019), p. 28. DOI: 10.3390/atoms7010028 (Cited on page 3).

[Bade, 2018] Satyanarayana Bade, Lionel Djadaojee, Manuel Andia, Pierre Cladé, and Saïda Guellati-Khelifa. "Observation of Extra Photon Recoil in a Distorted Optical Field". *Physical Review Letters* 121.7 (2018). DOI: 10.1103/PhysRevLett.121.073603 (Cited on pages 137, 179).

[Baillard, 2006] X. Baillard, A. Gauguet, S. Bize, P. Lemonde, Ph. Laurent, A. Clairon, and P. Rosenbusch. "Interference-Filter-Stabilized External-Cavity Diode Lasers". *Optics Communications* 266.2 (2006), pp. 609–613. DOI: 10.1016/j.optcom.2006.05.011 (Cited on page 69).

[Battesti, 2003] Rémy Battesti. "Accélération d'atomes Ultrafroids ; Mesure de h/M". *PhD Thesis* (2003), p. 156 (Cited on pages 15, 19, 21).

[Ben Dahan, 1997] Maxime Ben Dahan. "Transport et relaxation d'atomes de césium: oscillations de Bloch et résonance de diffusion". *PhD Thesis* (1997), p. 252 (Cited on pages 57, 59).

[Bidel, 2013] Yannick Bidel, Olivier Carraz, Renée Charrière, Malo Cadoret, Nassim Zahzam, and Alexandre Bresson. "Compact Cold Atom Gravimeter for Field Applications". *Applied Physics Letters* 102.14 (2013), p. 144107. DOI: 10.1063/1.4801756 (Cited on page 108).

[Bloch, 1928] Felix Bloch. "Uber die Quantenmechanik der Elek ronen in Kristallgittern." *Zeitschrift für Physik* 52.555 (1928), p. 46 (Cited on page 54).

[Bouchendira, 2011] Rym Bouchendira, Pierre Cladé, Saïda Guellati-Khélifa, François Nez, and François Biraben. "New Determination of the Fine Structure Constant and Test of the Quantum Electrodynamics". *Physical Review Letters* 106.8 (2011). DOI: 10.1103/physrevlett.106.080801 (Cited on pages 1, 3, 6, 65, 110, 114, 170, 179).

[Bouchendira, 2012] Rym Bouchendira. "Mesure de l'effet de Recul de l'atome de Rubidium Par Interférométrie Atomique : Nouvelle Détermination de La Constante de Structure Fine Pour Tester l'électrodynamique Quantique". *PhD Thesis* (2012) (Cited on page 15).

[Cadoret, 2008] Malo Cadoret. "Application Des Oscillations de Bloch d'atomes Ultra-Froids et de l'interférométrie Atomique à La Mesure de h/m et à La Détermination de La Constante de Structure Fine". *PhD Thesis* (2008) (Cited on pages 53, 56).

[Cadoret, 2008] Malo Cadoret, Estefania de Mirandes, Pierre Cladé, Saïda Guellati-Khélifa, Catherine Schwob, François Nez, Lucile Julien, and François Biraben. "Combination of Bloch Oscillations with a Ramsey-Bordé Interferometer: New Determination of the Fine Structure Constant". *Physical Review Letters* 101.23 (2008). DOI: 10.1103/physrevlett.101.230801 (Cited on pages 23, 59).

[Cheinet, 2006] P Cheinet. "Conception et réalisation d'un gravimètre à atomes froids". *PhD Thesis* (2006), p. 191 (Cited on pages 43, 44).

[Cheinet, 2008] P. Cheinet, B. Canuel, F. Pereira Dos Santos, A. Gauguet, F. Yver-Leduc, and A. Landragin. "Measurement of the Sensitivity Function in a Time-Domain Atomic Interferometer". *IEEE Transactions on Instrumentation and Measurement* 57.6 (2008), pp. 1141–1148. doi: 10.1109/TIM.2007.915148 (Cited on page 50).

[Chiow, 2011] Sheng-wey Chiow, Tim Kovachy, Hui-Chun Chien, and Mark A. Kasevich. "102 $\hbar$ k Large Area Atom Interferometers". *Physical Review Letters* 107.13 (2011). doi: 10.1103/PhysRevLett.107.130403 (Cited on page 52).

[Cladé, 2005] Pierre Cladé. "Oscillations de Bloch d'atomes ultrafroids et mesure de la constante de structure fine". *PhD Thesis* (2005), p. 233 (Cited on pages 15, 177).

[Cladé, 2006] Pierre Cladé, Estefania de Mirandes, Malo Cadoret, Saïda Guellati-Khélifa, Catherine Schwob, François Nez, Lucile Julien, and François Biraben. "Determination of the Fine Structure Constant Based on Bloch Oscillations of Ultracold Atoms in a Vertical Optical Lattice". *Physical Review Letters* 96.3 (2006). doi: 10.1103/physrevlett.96.033001 (Cited on pages 23, 62).

[Cladé, 2009] Pierre Cladé, Saïda Guellati-Khélifa, François Nez, and François Biraben. "Large Momentum Beam Splitter Using Bloch Oscillations". *Physical Review Letters* 102.24 (2009). doi: 10.1103/physrevlett.102.240402 (Cited on pages 6, 78, 126).

[Cladé, 2015] Pierre Cladé. "Bloch Oscillations in Atom Interferometry". *La Rivista del Nuovo Cimento* 38.4 (2015), pp. 173–207. doi: 10.1393/ncr/i2015-10111-3. arXiv: 1405.2770 (Cited on page 53).

[Cladé, 2017] P. Cladé, M. Andia, and S. Guellati-Khélifa. "Improving Efficiency of Bloch Oscillations in the Tight-Binding Limit". *Physical Review A* 95.6 (2017). doi: 10.1103/PhysRevA.95.063604 (Cited on pages 59, 61).

[CohenTannoudji, 1997] Claude Cohen-Tannoudji. "Atoms Ultra-Froids - Piègeage Non Dissipatif et Refroidissement Évaporatif". *Notes de cours, Collège de France* (1997) (Cited on page 79).

[CohenTannoudji, 2001] Claude Cohen-Tannoudji, Jacques Dupont-Roc, and Gilbert Grynberg. *Processus d'interaction Entre Photons et Atomes*. OCLC: 57230878. Les Ulis [France]; Paris: EDP Sciences ; CNRS Éditions, 2001 (Cited on page 17).

[Courvoisier, 2016] Clément Courvoisier. "Condensat de Bose-Einstein par refroidissement évaporatif dans un piège dipolaire pour la métrologie par interférométrie atomique". *PhD Thesis* (2016), p. 181 (Cited on pages 6, 65, 66, 68, 70, 75, 79, 81, 82).

[Couvert, 2008] A. Couvert, M. Jeppesen, T. Kawalec, G. Reinaudi, R. Mathevet, and D. Guéry-Odelin. "A Quasi-Monomode Guided Atom Laser from an All-Optical Bose-Einstein Condensate". *EPL (Europhysics Letters)* 83.5 (2008), p. 50001. doi: 10.1209/0295-5075/83/50001 (Cited on page 119).

[Dalibard, 1983] J. Dalibard, S. Reynaud, and C. Cohen-Tannoudji. "Proposals of Stable Optical Traps for Neutral Atoms". *Optics Communications* 47.6 (1983), pp. 395–399. doi: 10.1016/0030-4018(83)90314-0 (Cited on page 72).

[Dalibard, 1989] J. Dalibard and C. Cohen-Tannoudji. "Laser Cooling below the Doppler Limit by Polarization Gradients: Simple Theoretical Models". *Journal of the Optical Society of America B* 6.11 (1989), p. 2023. doi: 10.1364/JOSAB.6.002023 (Cited on page 68).

[Dalibard, 2006] Jean Dalibard. "Atomes Ultra-Froids". *Notes de cours, Ecole Normale Supérieure* (2006) (Cited on page 81).

[Dalibard, 2013] Jean Dalibard. "Des Cages de Lumière Pour Les Atomes : La Physique Des Pièges et Des Réseaux Optiques". *Notes de cours, Collège de France* (2013) (Cited on pages 55, 59).

[Dick, 1987] G John Dick. "Local Oscillator Induced Instabilities in Trapped Ion Frequency Standards". *Proceedings of Precise Time and TIme Interval* (1987), pp. 133–147 (Cited on page 42).

[Diddams, 2000] Scott A. Diddams, David J. Jones, Jun Ye, Steven T. Cundiff, John L. Hall, Jinendra K. Ranka, Robert S. Windeler, Ronald Holzwarth, Thomas Udem, and T. W. Hänsch. "Direct Link between Microwave and Optical Frequencies with a 300 THz Femtosecond Laser Comb". *Physical Review Letters* 84.22 (2000), pp. 5102–5105. doi: 10.1103/PhysRevLett.84.5102 (Cited on pages 5, 100).

[Egorov, 2013] M. Egorov, B. Opanchuk, P. Drummond, B. V. Hall, P. Hannaford, and A. I. Sidorov. "Measurement of s -Wave Scattering Lengths in a Two-Component Bose-Einstein Condensate". *Physical Review A* 87.5 (2013). doi: 10.1103/PhysRevA.87.053614 (Cited on page 123).

[Feynman, 1965] R. P. Feynman and A. R. Hibbs. *Quantum Mechanics and Path Integrals*. New York: McGraw-Hill, 1965 (Cited on page 33).

[Gabrielse, 2019] G. Gabrielse, S. E. Fayer, T. G. Myers, and X. Fan. "Towards an Improved Test of the Standard Model's Most Precise Prediction" (2019). doi: 10.3390/atoms7020045 (Cited on page 4).

[Grimm, 2000] Rudolf Grimm, Matthias Weidemüller, and Yurii B. Ovchinnikov. "Optical Dipole Traps for Neutral Atoms". Ed. by Benjamin Bederson and Herbert Walther. Vol. 42. Advances In Atomic, Molecular, and Optical Physics. Academic Press, 2000, pp. 95–170. doi: https://doi.org/10.1016/S1049-250X(08)60186-X (Cited on pages 53, 114).

[Grynberg, 2010] Gilbert Grynberg, Alain Aspect, and Claude Fabre. *Introduction to quantum optics: from the semi-classical approach to quantized light*. New York, NY: Cambridge Univ. Press, 2010 (Cited on page 16).

[Hanneke, 2008] D. Hanneke, S. Fogwell, and G. Gabrielse. "New Measurement of the Electron Magnetic Moment and the Fine Structure Constant". *Physical Review Letters* 100.12 (2008). doi: 10.1103/PhysRevLett.100.120801 (Cited on pages 2, 3).

[Hu, 2013] Zhong-Kun Hu, Bu-Liang Sun, Xiao-Chun Duan, Min-Kang Zhou, Le-Le Chen, Su Zhan, Qiao-Zhen Zhang, and Jun Luo. "Demonstration of an Ultrahigh-Sensitivity Atom-Interferometry Absolute Gravimeter". *Physical Review A* 88.4 (2013). doi: 10.1103/PhysRevA.88.043610 (Cited on page 154).

[Huntemann, 2014] N. Huntemann, B. Lipphardt, Chr. Tamm, V. Gerginov, S. Weyers, and E. Peik. "Improved Limit on a Temporal Variation of m_p/m_e from Comparisons of Yb + and Cs Atomic Clocks". *Physical Review Letters* 113.21 (2014). doi: 10.1103/PhysRevLett.113.210802 (Cited on page 4).

[Jannin, 2015] Raphaël Jannin. "Interférométrie atomique avec un condensat de Bose-Einstein : effet des interactions internes". *PhD Thesis* (2015), p. 183 (Cited on pages 6, 65, 66, 79, 100, 184).

[Jannin, 2015] Raphaël Jannin, Pierre Cladé, and Saïda Guellati-Khélifa. "Phase Shift Due to Atom-Atom Interactions in a Light-Pulse Atom Interferometer". *Physical Review A* 92.1 (2015). doi: 10.1103/physreva.92.013616 (Cited on pages 6, 114, 122, 123).

[Kruger, 1999] E Kruger, W Nistler, and W Weirauch. "Re-Evaluation of a Precise Measurement of h/m_n". *Metrologia* 36 (1999), pp. 147–148. doi: 10.1088/0026-1394/36/2/9 (Cited on page 2).

[Lan, 2012] Shau-Yu Lan, Pei-Chen Kuan, Brian Estey, Philipp Haslinger, and Holger Müller. "Influence of the Coriolis Force in Atom Interferometry". *Physical Review Letters* 108.9 (2012). doi: 10.1103/PhysRevLett.108.090402 (Cited on page 173).

[MacAdam, 1992] K B MacAdam, A Steinbach, and C Wieman. "A Narrowband Tunable Diode Laser System with Grating Feedback, and a Saturated Absorption Spectrometer for Cs and Rb". *American Journal of Physics* 60.1098 (1992), p. 15 (Cited on page 70).

[Ménoret, 2018] Vincent Ménoret, Pierre Vermeulen, Nicolas Le Moigne, Sylvain Bonvalot, Philippe Bouyer, Arnaud Landragin, and Bruno Desruelle. "Gravity Measurements below $10^{-9}g$ with a Transportable Absolute Quantum Gravimeter". *Scientific Reports* 8.1 (2018). doi: 10.1038/s41598-018-30608-1 (Cited on page 36).

[Mohr, 2016] Peter J. Mohr, David B. Newell, and Barry N. Taylor. "CODATA Recommended Values of the Fundamental Physical Constants: 2014". *Journal of Physical and Chemical Reference Data* 45.4 (2016), p. 043102. doi: 10.1063/1.4954402 (Cited on page 1).

[Naji, 2011] A W Naji, B A Hamida, X S Cheng, M A Mahdi, S Harun, S Khan, W F AL-Khateeb, A A Zaidan, B B Zaidan, and H Ahmad. "Review of Erbium-Doped Fiber Amplifier". *Int. J. Phys. Sci.* 6.20 (2011), pp. 4674–4689 (Cited on page 83).

[Ockeloen, 2010] C. F. Ockeloen, A. F. Tauschinsky, R. J. C. Spreeuw, and S. Whitlock. "Detection of Small Atom Numbers through Image Processing". *Physical Review A* 82.6 (2010). doi: 10.1103/PhysRevA.82.061606 (Cited on page 124).

[Papoulis, 1991] A Papoulis. *Probability, Random Variables and Stochastic Processes*. McGraw-Hill International, 1991 (Cited on page 45).

[Parker, 2018] Richard H. Parker, Chenghui Yu, Weicheng Zhong, Brian Estey, and Holger Müller. "Measurement of the Fine-Structure Constant as a Test of the Standard Model". *Science* 360.6385 (2018), pp. 191–195. doi: 10.1126/science.aap7706 (Cited on pages 1–3).

[Peters, 1998] Achims Peters. "High Precision Gravity Measurements Using Atom Interferometry". *PhD Thesis* (1998) (Cited on page 38).

[Raab, 1987] E. L. Raab, M. Prentiss, Alex Cable, Steven Chu, and D. E. Pritchard. "Trapping of Neutral Sodium Atoms with Radiation Pressure". *Physical Review Letters* 59.23 (1987), pp. 2631–2634. doi: 10.1103/PhysRevLett.59.2631 (Cited on page 72).

[Riis, 1990] Erling Riis, David S. Weiss, Kathryn A. Moler, and Steven Chu. "Atom Funnel for the Production of a Slow, High-Density Atomic Beam". *Physical Review Letters* 64.14 (1990), pp. 1658–1661. doi: 10.1103/PhysRevLett.64.1658 (Cited on page 74).

[Riley, 1977] M. E. Riley and M. A. Gusinow. "Laser Beam Divergence Utilizing a Lateral Shearing Interferometer". *Applied Optics* 16.10 (1977), p. 2753. doi: 10.1364/AO.16.002753 (Cited on page 178).

[Roy, 2016] Richard Roy, Alaina Green, Ryan Bowler, and Subhadeep Gupta. "Rapid Cooling to Quantum Degeneracy in Dynamically Shaped Atom Traps". *Physical Review A* 93.4 (2016). doi: 10.1103/PhysRevA.93.043403 (Cited on page 126).

[Rudolph, 2015] Jan Rudolph, Waldemar Herr, Christoph Grzeschik, Tammo Sternke, Alexander Grote, Manuel Popp, Dennis Becker, Hauke Müntinga, Holger Ahlers, Achim Peters, Claus Lämmerzahl, Klaus Sengstock, Naceur Gaaloul, Wolfgang Ertmer, and Ernst M Rasel. "A High-Flux BEC Source for Mobile Atom Interferometers". *New Journal of Physics* 17.6 (2015), p. 065001. doi: 10.1088/1367-2630/17/6/065001 (Cited on pages 125, 126).

[Safronova, 2018] M. S. Safronova, D. Budker, D. DeMille, Derek F. Jackson Kimball, A. Derevianko, and Charles W. Clark. "Search for New Physics with Atoms and Molecules". *Reviews of Modern Physics* 90.2 (2018). doi: 10.1103/revmodphys.90.025008 (Cited on page 4).

[Steck, 2001] Daniel Steck A. "Rubidium 87 D Line Data" (2001) (Cited on pages 12, 20, 21, 105).

[Storey, 1994] Pippa Storey and Claude Cohen-Tannoudji. "The Feynman Path Integral Approach to Atomic Interferometry. A Tutorial". *Journal de Physique II* 4.11 (1994), pp. 1999–2027. doi: 10.1051/jp2:1994103 (Cited on pages 35, 36).

[Sturm, 2014] S. Sturm, F. Köhler, J. Zatorski, A. Wagner, Z. Harman, G. Werth, W. Quint, C. H. Keitel, and K. Blaum. "High-Precision Measurement of the Atomic Mass of the Electron". *Nature* 506.7489 (2014), pp. 467–470. doi: 10.1038/nature13026 (Cited on page 1).

[Sugarbaker, 2013] Alex Sugarbaker, Susannah M. Dickerson, Jason M. Hogan, David M. S. Johnson, and Mark A. Kasevich. "Enhanced Atom Interferometer Readout through the Application of Phase Shear". *Physical Review Letters* 111.11 (2013). doi: 10.1103/PhysRevLett.111.113002 (Cited on page 173).

[Ungar, 1989] P. J. Ungar, D. S. Weiss, E. Riis, and Steven Chu. "Optical Molasses and Multilevel Atoms: Theory". *Journal of the Optical Society of America B* 6.11 (1989), p. 2058. doi: 10.1364/JOSAB.6.002058 (Cited on page 68).

[Wang, 2017] Meng Wang, G. Audi, F. G. Kondev, W.J. Huang, S. Naimi, and Xing Xu. "The AME2016 Atomic Mass Evaluation (II). Tables, Graphs and References". *Chinese Physics C* 41.3 (2017), p. 030003. doi: 10.1088/1674-1137/41/3/030003 (Cited on page 1).

[Wannier, 1937] Gregory H. Wannier. "The Structure of Electronic Excitation Levels in Insulating Crystals". *Physical Review* 52.3 (1937), pp. 191–197. doi: 10.1103/PhysRev.52.191 (Cited on page 59).

[Wicht, 2002] Andreas Wicht, Joel M Hensley, Edina Sarajlic, and Steven Chu. "A Preliminary Measurement of the Fine Structure Constant Based on Atom Interferometry". *Physica Scripta T* (2002), p. 8. doi: 10.1238/Physica.Topical.102a00082 (Cited on pages 2, 23).

[Wigley, 2016] P. B. Wigley, P. J. Everitt, A. van den Hengel, J. W. Bastian, M. A. Sooriyabandara, G. D. McDonald, K. S. Hardman, C. D. Quinlivan, P. Manju, C. C. N. Kuhn, I. R. Petersen, A. N. Luiten, J. J. Hope, N. P. Robins, and M. R. Hush. "Fast Machine-Learning Online Optimization of Ultra-Cold-Atom Experiments". *Scientific Reports* 6 (2016), p. 25890. doi: 10.1038/srep25890 (Cited on page 116).

[Wolf, 2011] Peter Wolf, Luc Blanchet, Christian J Bordé, Serge Reynaud, Christophe Salomon, and Claude Cohen-Tannoudji. "Does an Atom Interferometer Test the Gravitational Redshift at the Compton Frequency?" *Classical and Quantum Gravity* 28.14 (2011), p. 145017. DOI: 10.1088/0264-9381/28/14/145017 (Cited on page 35).

[Zener, 1934] C. Zener. "A Theory of the Electrical Breakdown of Solid Dielectrics". *Proceedings of the Royal Society A: Mathematical, Physical and Engineering Sciences* 145.855 (1934), pp. 523–529. DOI: 10.1098/rspa.1934.0116 (Cited on page 55).

Interférométrie à haute sensibilité sur onde de matière : vers une détermination de la constante de structure fine au niveau de 10^{-10}

Résumé : La constante de structure fine α peut être déterminée à partir de la mesure du rapport h/m entre la constante de Planck h et la masse d'un atome m. La comparaison de la valeur expérimentale de l'anomalie du moment magnétique de l'électron ou du muon à leurs valeurs théoriques prédites par le Modèle Standard et utilisant cette valeur de α permet d'accomplir un test très précis de ce modèle.
Mon travail de thèse a porté principalement sur la mesure du rapport h/m de l'isotope 87 du rubidium en utilisant un nouveau dispositif expérimental conçu pour produire une source ultra-froide par évaporation dans un piège dipolaire tout-optique chargé par une mélasse optique. Nous avons optimisé les paramètres du dispositif à l'aide d'un algorithme génétique, ce qui nous a permis de produire un condensat de Bose Einstein, contenant 120.000 atomes, polarisé dans l'état $|F = 1, m_F = 0\rangle$, avec un temps de cycle de 3,5 secondes.
Nous avons ensuite installé le dispositif laser d'interférométrie atomique, pour interroger un nuage d'atomes froids produit dans une mélasse optique. En combinant un interféromètre utilisant des transitions Raman et la technique des oscillations de Bloch, nous avons démontré une sensibilité sans précédent sur la mesure de h/m correspondant à une incertitude statistique relative de $8{,}5 \cdot 10^{-11}$ en 48h de temps d'intégration, soit $4{,}3 \cdot 10^{-11}$ sur α.
Cette sensibilité nous a permis d'étudier expérimentalement de nombreux effets systématiques. Nous avons de plus mené un travail de modélisation qui a contribué à la mise en place de protocoles visant à compenser les biais induits par les effets systématiques. Nous présentons un bilan provisoire du budget d'erreurs associé à ces effets.

Mots clés : Métrologie, atomes froids, interférométrie atomique, constante de structure fine, transitions Raman, oscillations de Bloch

High sensitivity matter-wave interferometry: towards a determination of the fine structure constant at the level of 10^{-10}

Abstract: The fine structure constant can be determined from the measurement of the ratio h/m between the Planck constant, h, and the mass of an atom, m. The comparison of the experimental value of the anomalous magnetic moment of the electron or the muon with their theoretical values predicted by the Standard Model using this value of the fine structure constant allows a very precise test of this model.
My thesis work focused principally on the measurement of the h/m ratio of rubidium-87 using a new experimental device. This device has been designed to produce an ultra-cold source by evaporation in an all-optical dipole trap loaded from optical molasses. We optimized the parameters of the experimental device using a genetic algorithm, which allowed us to produce a Bose Einstein condensate, containing 120,000 atoms, polarized in the state $|F = 1, m_F = 0\rangle$, with a cycle time of 3.5 seconds.
We then installed the laser device for atom interferometry, to interrogate a cloud of cold atoms produced by optical molasses. Combining an interferometer using Raman transitions and the technique of Bloch Oscillations, we demonstrated an unprecedented sensitivity on the measurement of h/m corresponding to a relative statistical uncertainty of $8.5 \cdot 10^{-11}$ in 48 hours of integration, or $4.3 \cdot 10^{-11}$ on the fine structure constant. This sensitivity has allowed us to study experimentally a variety of systematic effects. We simultaneously carried out modelling work that contributed to the implementation of protocols to compensate for the biases induced by systematic effects. We present a preliminary assessment of the error budget associated with these effects.

Keywords : Metrology, cold atoms, atom interferometry, fine structure constant, Raman transitions, Bloch Oscillations